Airgap-based MEMS optical filters

For the ultraviolet-visible spectrum

Ghaderi, Amir

DOI
10.4233/uuid:7db0bc2e-9a7d-46fe-8108-2a63efcd3908

Publication date
2016

Document Version
Final published version

Citation (APA)
Ghaderi, A. (2016). *Airgap-based MEMS optical filters: For the ultraviolet-visible spectrum*. [Dissertation (TU Delft), Delft University of Technology]. https://doi.org/10.4233/uuid:7db0bc2e-9a7d-46fe-8108-2a63efcd3908

Airgap-based MEMS optical filters

For the ultraviolet-visible spectrum

Airgap-based MEMS optical filters

For the ultraviolet-visible spectrum

Proefschrift

ter verkrijging van de graad van doctor
aan de Technische Universiteit Delft,
op gezag van de Rector Magnificus prof. ir. K.C.A.M. Luyben,
voorzitter van het College voor Promoties,
in het openbaar te verdedigen op maandag 20 juni 2016 om 12:30 uur

door

Mohammadamir Ghaderi

Master of Science in Laser Physics,
Shahid Beheshti University, Tehran, Iran
geboren te Birjand, Iran.

This dissertation has been approved by the

promotor: Prof. dr. A. J. P. Theuwissen
copromotor: Dr. ir. R. F. Wolffenbuttel

Composition of the doctoral committee:

Rector Magnificus	chairman
Prof. dr. ir. A. J. P. Theuwissen	Delft University of Technology
Dr. ir. R. F. Wolffenbuttel	Delft University of Technology
Independent members:	
Prof. dr. G. V. Vdovine	Delft University of Technology
Prof. dr. P. French	Delft University of Technology
Prof. dr. H. Latifi	Shahid Beheshti University
Prof. dr. P. Enoksson	Chalmers University of Technology
Prof. dr. J. H. G. Correia	University of Minho

Keywords: Optical filter, CMOS-compatible, Silicon-based, Residual stress, air-gap optical filter.

Front: Structural coloring (optical interference) in a deformed ultra-thin membrane (retouched image).

Back, Top: A word cloud representation of the relative repetition of the technical words in this thesis in terms of the relative typeface sizes.

Back, Bottom: Spectral reflectance of a large area free-standing airgap-based MEMS Optical filter.

ISBN 978-94-028-0232-0

An electronic version of this dissertation is available at
http://repository.tudelft.nl/.

I dedicate this thesis to
my mother and father
for their constant support
and unconditional love.

Amir

Contents

Summary

Combining the batch processing of silicon wafers that is commonplace in microelectronics with the mechanical properties of silicon and its oxides and nitrides results in low cost and reliable sensors and actuators for many applications. Optical MEMS is a variation of the mainstream MEMS taking advantage of the optical properties of silicon-based materials. This dissertation investigates the optical design and the process to fabricate large-area optical filters, inspired by the photonic crystal structures in the 'Morpho blue' butterfly, for application in the ultraviolet (UV) and visible spectrum. The emphasis is put on the CMOS-compatibility of the fabrication process of these optical filters for applications in ultraviolet microspectrometers for gas sensing.

An airgap-based optical filter is an optical system in which the interference of light that is incident onto the structure of free-standing membranes brings the intended functionality to the device. However, it is also a mechanical system, as it is composed of free-standing membranes, supporting structures, and sacrificial release access holes. Moreover, the optical and mechanical characteristics are intertwined. The optical design, on the one hand, places limitations over the materials that can be used for a specific spectrum. The mechanical design, on the other hand, ensures that the forces within the structures can be sustained, thus yielding a stable free-standing structure that can actually perform the intended optical functionality. Finally, there are functional constraints to consider, such as maximum fill factor and CMOS-compatibility. These issues limit the choice of materials and possible processes for fabrication of such an optical MEMS structure.

A detailed knowledge of the properties of optical materials used is essential for a good optical filter design. In Chapter 2 the optical materials are discussed and the effect on filter design is investigated, with an emphasis on the ultraviolet and visible spectral range. The optical properties of commonly used materials are also compared. The refractive index contrast is introduced and used as a criterion to compare the optical materials and designs. The most important conclusion is that the use of air as a 'material' with superior optical properties and, consequently, the airgap as a low-loss and low-index layer results in a significantly higher refractive index contrast, thus a more pronounced optical filter response results for a certain number of layer pairs as compared to an all-dielectric layer design. Silicon-oxide was selected as the high-index layer, which in an airgap optical filter results in a refractive index contrast of 0.27. This index contrast exceeds the highest refractive index provided by the usual all-dielectric filter in the ultraviolet spectrum. Although the optical properties of many materials are well-documented in the literature, the optical properties of thin films are depending on the specific details of the deposition process. Variable angle spectral ellipsometry is introduced as our main tool of investigation of optical properties of the thin films. The Cauchy dispersion model

was implemented for evaluating the optical properties of silicon-oxide (and -nitride) layers that were used for the fabrication.

The residual stress is, almost inevitably, present in most deposited thin films. These forces within the suspended structure can fundamentally affect the shape and operation of the final structure. While a compressive stress in the membranes results in buckling in the structure, a too high value of the tensile stress induces fracture. The residual stress, its sources and its effects on the membrane is discussed in Chapter 3. The deposition method to a large extent determine the stress levels in the deposited films. Therefore, different deposition methods are compared. PECVD method is widely used for optical thin film depositions. Furthermore, changing the deposition parameters in the PECVD provide a high level of control over the residual stress of the deposited layers. Especially, varying the partial pressures of the reactive gases, SiH_4 and N_2O, results in variation in the density of silanol bonds (Si-O-H) within the material. A higher silanol bond density in the layers is associated with a less-compressive residual stress. Two deposition recipes (*Type 1* and *Type 2*) were selected, which are characterized by the different partial pressure of reactive gases, and thus result in different as deposited residual stress level. The density of the silanol bonds can also be affected during the subsequent processes at temperatures higher than the deposition temperature (400 °C). Stress measurement during thermal annealing cycles up to $600\ ^{\circ}C$ was hence performed to study the variations in the residual stress during the fabrication of the layer stack. The results indicate that the thermal annealing decreases the silanol bond density and induces void formation in the films, resulting in a tensile stress layer. Finite-element analysis (FEA) was used to study the von Mises stress distribution due to a constant residual stress in a released structure. The FEA results were used to design a membrane structure considering the assessed ultimate strength of PECVD silicon-oxide layers ($0.75\ MPa\sqrt{m}$).

Preventing stiction of the membrane is the main yield concern in these optical MEMS devices. Therefore, different stiction-free processes and techniques are also introduced and compared in Chapter 3. Supercritical drying using CO_2 as the transfer liquid was found to be the most suitable drying method when considering the dimensions of the airgap-based filter device.

Chapter 4 introduces several fabrication tolerances that can affect the flatness of the released membranes and thus the optical response of the filter. An optical flatness criterion that is based on finesse, which is an essential figure of merit of a Fabry-Perot resonator, is introduced as a measure for quantifying and comparing the effect of the different sources of uncertainty. The effect of roughness, deposition non-uniformity, (finite) etch selectivity, and residual stress gradient are discussed. The effective finesse and thus the acceptable level of tolerances in an optical filter depends on the operating wavelength. The roughness and the deposition non-uniformity in the PECVD silicon-oxide layers limit the maximum achievable finesse to $\mathcal{F} \approx 22.4$. A sufficiently high etch selectivity of the sacrificial layer to the membranes is also required to obtain the required level of finesse. Compared to the alkaline-based etchants such as TMAH, a doped-TMAH etching solution (5% TMAH + silicic acid + ammonium persulfate) results in an order of magnitude improvement in the

etch selectivity ($S \approx 1 - 8 \times 10^4$). This selectivity is sufficient to ensure a thickness variation of less than $1\ nm$ over a lateral length of the sacrificial etch of $10 - 80\ \mu m$ ($\mathcal{F} \approx 100$).

A residual stress gradient in thin films results in the deformation of the released membranes and has a considerable impact on the effective finesse of the structure. Initial estimates of the residual stress profiles of the two PECVD silicon-oxide films (Chapter 4) were used in finite-element analysis to study the deformation of the membrane as a function of various stress gradient profiles. The results indicate that although the stress in *Type 2* PECVD silicon-oxide films is on average more tensile as compared to *Type 1*, the higher stress gradient results in a larger deformation in the membrane. An iterative analysis flow based on a coupled finite-element method and a finite-difference time-domain (FDTD) method has been also introduced to assess the stress gradient profile in an ultra-thin suspended membrane by measuring the variations in the spectral reflection. The FDTD results demonstrated that such a deformation leads to a shift in the spectral response of the airgap structure towards longer wavelengths (a red shift).

Chapter 5 presents the details of the fabrication process and the results. Airgap-based optical filters implementing single and third quarter-wave optical thick (QWOT) layers were designed. A layout design based on unit-cell structure, irrespective of the number and the thickness of the membrane layers, was also presented. Single-QWOT membranes using the two PECVD silicon-oxide deposition recipes were fabricated and analyzed. Obtaining the required flatness over the entire area of the free-standing membranes proved to be challenging. Introducing pre-strained compensating structures using layers with intrinsic stress deposited at the wafer backside was shown to improve the flatness in the membrane. Furthermore, composite silicon-oxide|polysilicon membranes were found to be sufficiently flat. Based on these results, five different Bragg reflector MEMS structures using three-QWOT silicon-oxide layers, silicon-nitride layers, and composite layers were subsequently designed.

Bragg reflectors with one and two periods of 3 QWOT silicon-oxide layers were fabricated. The average spectral reflection at normal incidence over a relatively large area of about $1\ mm^2$ was characterized. Although the spectral response comprised of a combined reflectance of the released membranes, unreleased structures, anchor pins, and access-holes, reflectance curves clearly indicate the effect of the released membranes. Despite the fact that silicon-nitride has a significant spectral absorption in the UV, its excellent mechanical properties (e.g. $E_{SiN} = 200\ GPa$) and high refractive index ($n_{SiN} \approx 2$) gives rise to designs with nitride layers only. Single element Bragg reflectors using 1 QWOT and 3 QWOT layer of PECVD silicon-nitride were also demonstrated. However, the large tensile stress value in silicon-nitride layers ($\sigma \approx 1\ GPa$) limits the feasible dimensions of the membrane area. Finally, composite membranes using 1 QWOT silicon-nitride and 2 QWOT silicon-oxide layers were fabricated. The membranes showed comparatively a higher yield, and an excellent optical response. The results presented in this dissertation demonstrate the feasibility of fabrication of optical MEMS airgap-based optical devices for filtering in the ultraviolet and visible parts of the spectrum.

Samenvatting

Het combineren van de simultane bewerking van groepen van siliciumwafers, zoals gebruikelijk in de micro-elektronica, met de goede mechanische eigenschappen van silicium en de oxides en nitrides in silicium resulteert in goedkope en bedrijfszekere sensoren en actuatoren voor vele toepassingen. Optische MEMS is een variant op de reguliere MEMS, waarbij gebruik wordt gemaakt van de optische eigenschappen van silicium-gebaseerde materialen. In dit proefschrift wordt, geïnspireerd door de fotonische kristalstructuren in de 'Morpho blue' vlinder, het optische ontwerp en het proces voor de fabricage van optische filters over een groot oppervlak en voor toepassing in het en ultraviolet (UV) en zichtbare spectrum onderzocht. De nadruk wordt gelegd op de CMOS-compatibiliteit van het fabricageproces van deze optische filters voor toepassing in ultraviolet microspectrometers voor gasdetectie.

Een luchtspleet-gebaseerd optische filter is een optisch systeem waarin de interferentie van licht dat invalt op de constructie van vrijstaande membranen de beoogde functionaliteit geeft. Het is echter ook een mechanisch systeem, omdat het is samengesteld uit vrijstaande membranen, draagconstructies en gaten welke gedurende de fabricage worden gebruikt voor het vrij-etsen van de structuur door verwijdering van een tussenlaag (opofferingslaag). Bovendien zijn de optische en mechanische eigenschappen verweven. Enerzijds stelt het optische ontwerp beperkingen aan de materialen die kunnen worden gebruikt voor een specifiek spectrum. Anderzijds maakt het mechanische ontwerp het mogelijk om de krachten op de structuren te kunnen dragen, waardoor een stabiele vrijstaande structuur ontstaat welke daadwerkelijk de beoogde optische functie kan uitvoeren. Tenslotte zijn er functionele beperkingen welke in rekening moeten worden genomen, zoals de maximale vulfactor en CMOS-compatibiliteit. Deze problemen beperken de materiaalkeuze en mogelijke werkwijzen voor de productie van dergelijke optische MEMS structuur.

Een gedegen kennis van de eigenschappen van de toegepaste optische materialen is essentieel voor een goed optisch filterontwerp. In Hoofdstuk 2 worden de optische materialen besproken en de invloed op filterontwerpen onderzocht, waarbij de nadruk ligt op het ultraviolette en zichtbare spectrum. Tevens worden de optische eigenschappen van veelgebruikte materialen vergeleken. Het begrip 'brekingsindexcontrast' wordt geïntroduceerd en gebruikt als criterium om de optische materialen en ontwerpen te vergelijken. De belangrijkste conclusie is dat het gebruik van lucht als een 'materiaal' met superieure optische eigenschappen en dus een luchtspleet als een laag met lage verliezen en een lage brekingsindex leidt tot een aanzienlijk hogere brekingsindexcontrast, waardoor bij een zeker aantal gestapelde lagen een filter met een scherpere optische specificatie gerealiseerd kan worden dan bij een ontwerp op basis van uitsluitend diëlektrische lagen. Silicium-oxide werd gekozen als het materiaal met de hoge brekingsindex, welke in

combinatie met de luchtspleet een brekingsindexcontrast van 0,27 mogelijk maakt. Deze brekingsindexcontrast is beter dan de best-mogelijke brekingsindexcontrast die in het ultraviolette spectrum mogelijk zou zijn met de gebruikelijke diëlektrische materiaalcombinaties. Hoewel de optische eigenschappen van verschillende materialen goed zijn gedocumenteerd in de literatuur, zijn de optische eigenschappen van dunne films afhankelijke van de specifieke details van het depositieproces. Spectrale ellipsometrie onder een variabele hoek wordt geïntroduceerd als onze belangrijkste meetmethode bij het onderzoek van de optische eigenschappen van dunne films. Het Cauchy dispersiemodel wordt toegepast voor het evalueren van de optische eigenschappen van silicium-oxide (en -nitride) lagen, welke werden gebruikt voor de fabricage.

Een mechanische restspanning is bijna onvermijdelijk in de meeste gedeponeerde dunne films. Deze krachten in een opgehangen structuur zijn fundamenteel van invloed op de vorm en werking van de uiteindelijke structuur. Terwijl een drukspanning in de membranen leidt tot knikken in de structuur, veroorzaakt een te hoge waarde van de trekspanning scheuring. De oorzaken van restspanningen en het effect op het membraan worden besproken in Hoofdstuk 3. De depositiemethode is grotendeels bepalend voor de spanningsniveaus in de gedeponeerde films. Daarom worden verschillende depositiemethoden vergeleken. PECVD wordt veel gebruikt voor de depositie van optische dunne films. Bovendien geeft de sturing van de depositieparameters in PECVD een hoge mate van beheersing over de restspanning in de gedeponeerde lagen. In het bijzonder leidt de variatie van de partiële druk van het reactieve gas, SiH_4 en N_2O, tot variatie in de dichtheid van silanol (Si-O-H) in het materiaal. Een hogere dichtheid van silanolbindingen in de lagen is geassocieerd met een verminderde residuele drukspanning. Twee recepten zijn geselecteerd voor depositie (*Type 1* en *Type 2*), welke zijn gekenmerkt door een verschillende partiële reactieve gassen, en dus resulteren in verschillende waarden voor de restspanning direct na depositie. De dichtheid van de silanolbindingen kunnen veranderen tijdens de daaropvolgende processen bij temperaturen hoger dan de depositietemperatuur (400 °C). Stressmeting tijdens thermische uitgloeicycli tot maximaal 600 ^{o}C werd derhalve uitgevoerd om de variaties in de restspanning tijdens de fabricage van de gestapelde lagen te bestuderen. De resultaten geven aan dat het thermisch gloeien de silanol bindingsdichtheid verminderd en holtevorming in de films veroorzaakt, waardoor de laag onder een trekspanning kont te staan. Eindige elementen analyse (Finite Element Analysis- FEA) werd gebruikt voor de bestudering van de 'von Mises spanningsverdeling' ten gevolge van een constante restspanning in een vrijstaande structuur. De FEA resultaten werden gebruikt bij het ontwerp van een membraanstructuur, met inachtneming van de als maximaal toelaatbaar geachte treksterkte van PECVD silicium- oxide lagen ($0,75\ MPa\sqrt{m}$).

Het vermijden van verkleving van het membraan met een ander oppervlak (stiction) is de belangrijkste bron van zorg wat betreft de opbrengst in aantallen correct functionerende optische MEMS. Daarom worden verschillende processen en technieken, waarbij stiction in principe vermeden wordt, geïntroduceerd en vergeleken in Hoofdstuk 3. Superkritische droging met CO_2 als de overdrachtvloeistof bleek, bij de afmetingen van de luchtspleet gebaseerde filterinrichting, de meest geschikte

droogmethode zijn.

Hoofdstuk 4 introduceert een aantal bronnen van onzekerheid in de fabricage, welke de vlakheid van de vrijgemaakte membranen en daarmee de optische respons van het filter kunnen beïnvloeden. Een criterium voor optische vlakheid dat is gebaseerd op finesse, welke een essentieel kengetal is van een Fabry-Perot resonator, wordt geïntroduceerd als maat voor het kwantificeren en vergelijken van het effect van de verschillende bronnen van onzekerheid. Het effect van ruwheid, ongelijkmatige depositie, (eindige) etsselectiviteit en gradiënt in de restspanning worden besproken. De effectieve finesse, en daarmee het aanvaardbare toleranties in een optisch filter, is afhankelijk van de keuze van de golflengte waarop het filter wordt gedimensioneerd. De ruwheid en de niet-uniformiteit in de depositie van de PECVD silicium-oxide lagen beperken van de maximaal haalbare finesse tot $\mathcal{F} \approx 22,4$. Een voldoende hoge etsselectiviteit tussen de opofferingslaag en de membranen is ook nodig om het vereiste niveau van finesse verkrijgen. Een gedoteerde TMAH etsoplossing (5% TMAH + kiezelzuur + ammoniumpersulfaat) resulteert in een orde van grootte hogere etsselectiviteit ($S \approx 1 - 8 \times 10^4$) vergeleken met de alkalische etsmiddelen zoals TMAH. Deze selectiviteit is voldoende voor een diktevariatie van minder dan 1 nm over een laterale etslengte van $10 - 80\ \mu m$ ($\mathcal{F} \approx 100$).

De gradiënt in de restspanning in dunne lagen resulteert in de vervorming van de membranen na vrij-etsen en heeft een aanzienlijke invloed op de effectieve finesse van de structuur. Initiële schattingen van de profielen van de restspanning van de twee PECVD silicium-oxide films werden gebruikt in een eindige elementen analyse om de vervorming van het membraan onderzoeken als functie van verschillende spanningsgradiëntprofielen (Hoofdstuk 4). De resultaten geven aan dat, hoewel de gemiddelde trekspanning in *Type 2* PECVD siliciumoxide-films hoger is dan in *type 1*, de hogere spanningsgradiënt toch leidt tot een grotere vervorming in het membraan. Een iteratieve procedure welke is gebaseerd op de koppeling van een eindige-elementenmethode en een eindige-verschillen tijdsdomein (finite-difference time-domain - FDTD) methode werd geïntroduceerd om het profiel van de spanningsgradiënt in een ultradunne vrijstaande membraan te beoordelen, door de meting van de variaties in de spectrale reflectie. De FDTD resultaten toonden aan dat een dergelijke vervorming leidt tot een verschuiving in de spectrale respons van de luchtspleet structuur naar langere golflengten.

Hoofdstuk 5 geeft de details van het fabricageproces en de resultaten. Uitvoeringen van de Luchtspleet-gebaseerde optische filters op basis van de enkelvoudige- en derde kwart-golflengte optische dikke (quarter-wave optical thickness - QWOT) lagen werden ontworpen. Een lay-out ontwerp van de generieke eenheidscel, welke onafhankelijk is van het aantal en de dikte van het membraan lagen, si gepresenteerd. Enkelvoudige-QWOT membranen op basis van de twee PECVD silicium-oxide depositie recepten werden gefabriceerd en geanalyseerd. Het verkrijgen van de vereiste vlakheid over het gehele oppervlak van de vrijstaande membranen bleek uitdagend. De introductie van een compenserende spanning via gedeponeerde lagen onder voorspanning op de achterzijde van de wafer bleek de vlakheid van het membraan te verbeteren. Daarbij bleken samengestelde silicium-oxide | polysilicium membranen voldoende vlak te zijn. Op basis van deze resultaten werden

vervolgens vijf verschillende Bragg reflectors als MEMS structuren met behulp van drie QWOT silicium oxide lagen, silicium nitride lagen en samengestelde lagen ontworpen.

Bragg reflectoren met één en twee perioden van 3 QWOT silicium-oxide lagen werden gefabriceerd. De gemiddelde spectrale reflectie over een relatief goot oppervlak van ongeveer $1\ mm^2$ werd gekarakteriseerd bij loodrechte inval. Hoewel de spectrale respons is samengesteld uit een gecombineerde reflectie van de vrijgemaakte membranen uitgebrachte structuren, ankerpennen en toegang gaten, is duidelijk het effect van de vrijgemaakte membranen zichtbaar in de curven van de reflectie. Ondanks het feit dat silicium-nitride een niet te verwaarlozen absorptie heeft in het UV, geven de uitstekende mechanische eigenschappen (bijvoorbeeld $E_{SiN} = 200\ GPa$) en hoge brekingsindex ($n_{SiN} \approx 2$) aanleiding tot het ontwerp structuren met uitsluitend nitridelagen. Enkel-elements Bragg reflectoren met een 1 QWOT of een 3 QWOT laag van PECVD silicium-nitride werden eveneens getoond. Echter, de hoge waarde van de trekspanning in silicium-nitride lagen ($\sigma \approx 1\ GPa$) beperkt de mogelijke afmetingen van het membraanoppervlak. Tenslotte werden samengestelde membranen met behulp van 1 QWOT silicium-nitride en 2 QWOT silicium-oxide lagen gefabriceerd. De membranen vertoonden een hogere fabricageopbrengst in vergelijking tot de enkelvoudige membranen en een uitstekende optische respons. De in dit proefschrift resultaten demonstreren de haalbaarheid van fabricage van optische MEMS-luchtspleet gebaseerde optische componenten voor filteren in de ultraviolette en zichtbare delen van het spectrum.

1

Introduction

1

1.1. Optical filters for MEMS applications

Optical filters are elements that selectively transmit, absorb, or reflect light. The filters are broadly classified into absorptive and interference (dichroic) filters [1]. In an absorptive filter, light is spectrally absorbed by the atoms which form the filtering layer (glass), and any non-absorbed light is transmitted. Being material-specific (e.g. transition metals or rare earth ions), absorptive filters are challenging to tune. A dichroic filter, on the other hand, is composed of a stack of high- and low-index layers. The interference of the multiple components of the electromagnetic wave results in either spectrally selective transmission or reflection of incident light. As compared to absorptive filters, interference-based filters could provide a much narrower transmission window [1].

In this dissertation, an interference optical filter is the basis of our optical design. Unless otherwise stated, the term *optical filter* and *interference filter* are used interchangeably. Figure 1.1 schematically shows the structure of a typical interference filter, composed of a number of layers with alternating high and low refractive indexes. The thickness of each layer is in the order of the wavelength of interest (i.e. the design wavelength, λ_0). When illuminated, the partial reflections (or transmissions) at the interface between each two adjacent layers interfere, resulting in a well-defined spectral transmission. The relative refractive index contrast ($\Delta = (n_H^2 - n_L^2)/2n_H^2$, where n_H and n_L are the refractive indexes of, respectively, high and low index layers) is a useful measure of the relative difference in the refractive index of the high and low index materials used in the filter. A larger value for the refractive index contrast results in a higher reflectance at each interface and consequently results in a sharper optical response.

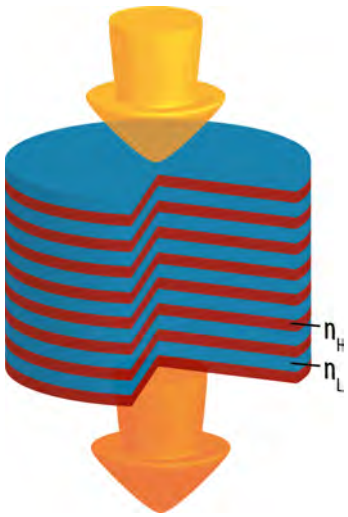

Figure 1.1: Schematic of an optical filter. The filter is composed of an alternating series of high- and low-index layers.

When optical materials are marginally suitable, a low refractive index contrast

may result, which necessitates the use of a large number of layers, and thus introduces fabrication challenges. The refractive index contrast and the number of layers determine the performance of the filter. Although an arbitrarily large peak reflectivity can ideally be achieved using a large number of layers, the bandwidth of the filters cannot be extended (the details of the optical design and constraints are presented in Chapter 2). Furthermore, the choice of optical material is limited by the absorption peaks in the materials. Air, with a refractive index of unity and low absorption in a wide spectrum, offers promising advantages in optical filters. Therefore, the use of air (air-gap) as a low-index material has recently been introduced and studied for very specific optical filter applications.

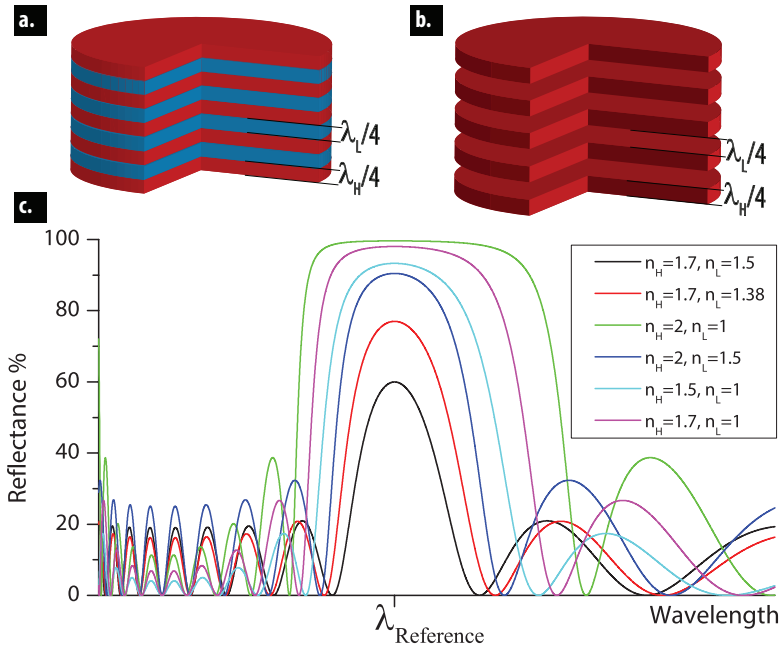

Figure 1.2: a. Schematic of a conventional dielectric-based DBR, b. Schematic of an airgap-based DBR, c. Expected spectral reflectance of several DBRs with nine layers. The transfer matrix method was used to calculate the reflectance. The refractive index of the substrate and the medium is assumed to be unity (air) ($n = 1$).

Distributed Bragg reflectors (DBRs) and Fabry-Perot-based optical filters [2] are the two configurations that are commonly used as the basis for optical filter designs. The underlying optical theory of these filters is discussed in detail in Chapter 2. The high index contrast, which becomes possible when using airgap-based filters, significantly improves the performance of these filters. Figure 1.2 (a.) and (b.) schematically shows the structure of DBRs composed of quarter-wave stacks of high and low index materials. The peak reflectance and bandwidth of DBRs with 4.5 (nine layers: $(H|L)^4H$) periods of different combinations of high and low index layers are shown in Figure 1.2 (c.). The substrate and the low-index medium are assumed to be air ($n = 1$). Therefore, airgap-based designs obtain a significantly

1

higher performance in terms of a higher peak reflectance and longer bandwidth.

A Fabry-Perot interferometer (FPI) based optical filter, as schematically shown in Figure 1.3 (a.) and (b.) is composed of two reflectors (often DBRs) separated by a cavity [2]. Depending on the separation distance of two reflectors (or the cavity length), a specific wavelength is transmitted with a certain full-width at half-maximum (FWHM) through the filter. The spectral resolution and operating range are two important factors in the Fabry-Perot filter. The cavity is for this reason often referred to as the resonator. Figure 1.3 shows the spectral resolution of FPI as a function of its reflectance based on the peak reflectance values presented in Figure 1.2 (c.).

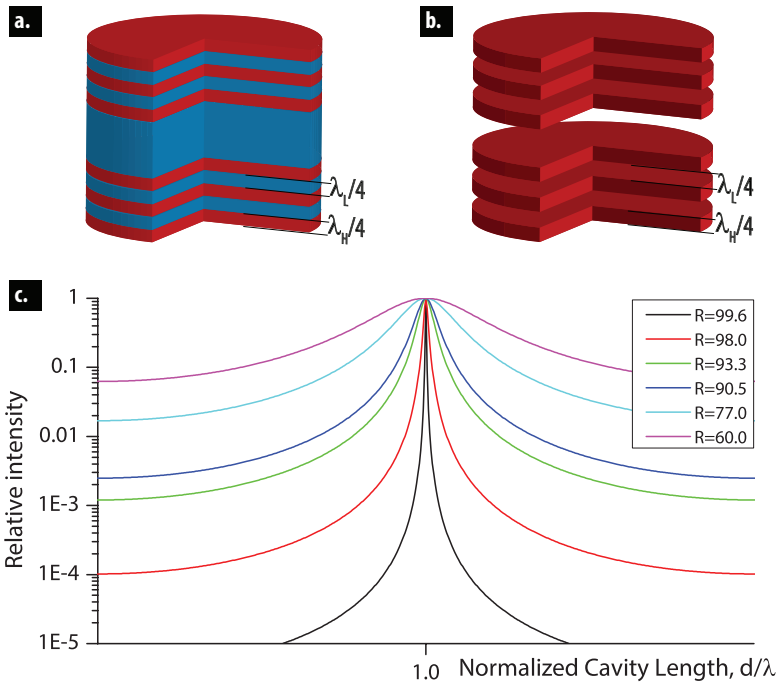

Figure 1.3: a. Schematic of a conventional dielectric-based Fabry-Perot filter, b. Schematic of an airgap-based Fabry-Perot filter, c. Expected spectral transmission of several Fabry-Perot filters with different reflectance. The peak reflectance values were taken from Figure 1.2, and the transmitted peak was calculated using the theoretical analysis.

The quality factor of a Fabry-Perot filter, i.e. its finesse, is a dimensionless measure of how spectrally narrow the peaks are over the available operating range of the filter. Design complexity in terms of the number of layers is reduced when using material systems with a high value for the index contrast. For instance, consider the number of layers required to obtain a Q-factor of better than 25 (i.e. having at least 25 distinct spectral channels over the operating spectral range). A typical all-dielectric layer system composed of ($n_H = 1.7$, $n_L = 1.5$ $Al_2O_3|SiO_2$) with an index contrast of $\Delta = 0.11$ would require $N = 13$ periods per DBR to achieve

a Q-factor of 20. However, using airgap layers, only $N = 4$ periods per DBR of ($n_H = 1.5$, $n_L = 1$ SiO_2|airgap with $\Delta = 0.27$) are required to achieve the same performance.

Fabrication of free-standing membranes is conventionally carried out in micro-electromechanical system (MEMS) processing and many technological procedures are already available [3]. In optical MEMS additional requirements and constraints on the materials are applicable. Some of the materials that would otherwise be highly suitable and are indeed used in conventional optical filters cannot be used in CMOS-based processes, because of this incompatibility. In CMOS-based processes, which are the mainstream fabrication processes of most MEMS devices, the high-temperature depositions adversely affect the functionality of the embedded microelectronics. Furthermore, after the deposition of non-CMOS compatible materials, the wafers cannot be processed in a cleanroom environment, because of the risk of cross-contamination. Compared to conventional MEMS, the number of layers required in an optical filter is larger, while no electrical contact is required.

Table 1.1: All-dielectric and airgap-based optical filters.

	All-dielectric Optical Filters	Airgap-based Optical Filters
Refractive index contrast	Low (UV) to medium (IR)	High (UV-Vis-IR)
CMOS-compatibility	Low	High
Functional size	Large	Limited by structures
Fill factor	High	Limited by supporting structures
Process complexity	Low	High
Residual stress dependency	Low	High: especially for UV-vis

Other factors that are important in MEMS devices are the functional size, fill factor, fabrication process complexity, and dependency on the process parameters such as residual stress. Table 1.1 briefly compares the all-dielectric and airgap-based filters. While a much higher refractive index is available, the functional size (i.e. total area of filters) and the fill factor (i.e. the ratio of the active area by the optically inactive area in the filter) are limited in airgap-based filters. Furthermore, mechanical characteristics of the film (e.g. residual stress) can highly affect the optical performance of the filter. In the following section, the state-of-the-art air-gap based optical filters for optical MEMS applications in infrared to ultraviolet applications are presented.

1

1.1.1. Case study: Morpho rhetenor blue butterfly

Although the recent advances in micro and nanotechnology described in this dissertation have made it possible to fabricate air-dielectric multi-layered filters, the airgap-based structures are not entirely new in nature. Evolution and survival of the fittest forced many species to evolve different tactics and functions to survive of natural selection. The active color change in chameleons using photonic crystals [4] and the sharp blue reflection of wings of *Morpho rhetenor* butterflies (Figure 1.4) [5] are two impressive examples of such an advanced nano-structured optical element in nature.

Figure 1.4: The structural color of a blue Morpho butterfly. The sharp blue/purple color in the wings is not pigment-based. Photographer: Luis Miguel Bugallo Sánchez (reprinted under Gnu license).

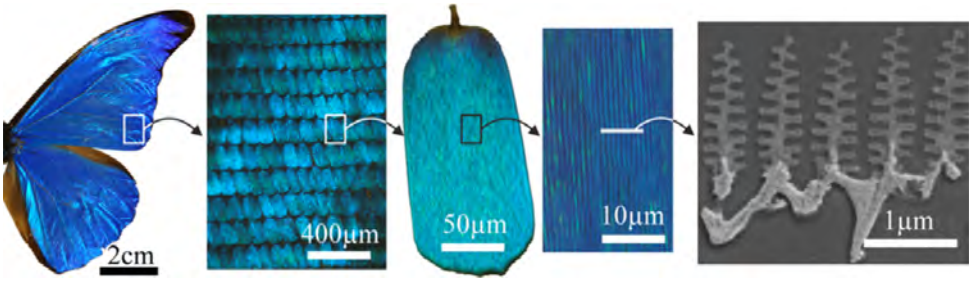

Figure 1.5: Cross-section TEM image of a *Morpho rhetenor* butterfly wing (reprinted from AskNature.org, Author/Photographer/Artist: Radwan [6]).

In the case of the Morpho rhetenor butterfly, the structure is basically composed of arrays of multi-layered ridges of about 10 layers of *chitin*, with a complex refrac-

tive index of $1.56 + 0.06i$ [7] separated by air-gaps, as shown in Figure 1.5. The special arrangement of the 'arrays' in Christmas tree-like ridges distributed over the scales gives additional properties to the wing. This intricate configuration of the multilayer ridges (and their orientation) gives a higher reflection at a wide range of angles of incidence [8]. Fabrication of replicas of the Morpho rhetenor's ridges have been investigated for bio-inspired sensor designs [9, 10].

1.2. State-of-the-art: Airgap-based optical filters

The first demonstration of airgap-based filters in MEMS was reported in late 1990 [11] for infrared applications. Since then, the fabrication of airgap-based optical filters for applications ranging from infrared microspectrometers, telecommunication lines, and ultraviolet-visible LEDs has been investigated. The current state-of-the-art airgap optical components, according to the designed spectrum and process compatibility, can be categorized into four areas of research:

1. III-V-based infrared optical components.
2. III-V-based ultraviolet-visible optical filters.
3. Silicon-based (CMOS compatible) infrared optical filters.
4. Silicon-based (CMOS compatible) ultraviolet-visible optical filters.

The non-CMOS, III-V semiconductors-based, devices have been extensively investigated during the past decade and have reached a high level of sophistication. Therefore, studying and understanding these devices is important for a proper CMOS compatible design. The following section aims to provide a brief overview of the current state-of-the-art in the first three categories. This dissertation aims to investigate the challenges and techniques for the fabrication of optical filters that fall into the fourth category, covering for the first time the technological gap in CMOS compatible, ultraviolet-visible devices.

III-V-based infrared optical components

Spectrally selective, low-cost optical MEMS operation in the near-infrared spectral range (typically $1.5\ \mu m$) have huge potential in communication applications. Devices such as wavelength division multiplexing (WDM) systems, optical switches, and vertical cavity surface emitting lasers (VCSELs) have been used to generate and manipulate optical signals with high wavelength selectivity in a comparatively large bandwidth and have thus revolutionized the telecommunication industry. In these applications, III-V-based direct bandgap semiconductors offer several technological advantages over silicon-based devices [12]. GaAs and InP are two commonly used III-V compound semiconductors, having a bandgap (expressed in equivalent wavelength) of $870\ nm$ and $1550\ nm$, respectively. These semiconductors have consequently provided new design opportunities for telecommunication component fabrication. Furthermore, the epitaxial growth technology provided by MOVPE (Metalorganic Vapour Phase Epitaxy) and MBE (Molecular Beam Epitaxy) offers a sufficiently tight control of the deposition parameters. Thin films of almost arbitrary

1

composition and possessing controlled physical characteristics such as refractive index, etch selectivity, and residual stress can, therefore, be deposited [13].

An ideal optical filter for telecommunication applications must have a wide and continuous tuning range, low tuning power, low insertion loss, high extinction ratio, and no polarization dependence [14]. Tunable Fabry-Perot-based optical filters and distributed Bragg reflectors have been implemented as the basic optical component in these devices. The low refractive contrast of the layers (≈ 0.1), on the other hand, necessitates the use of a large number of layers to achieve an acceptable optical quality. For instance, all-dielectric distributed Bragg reflectors with layers up to 21.5-periods of InGaAs-InAlAs layers with a peak reflectivity of about 98.6%, have been reported for WDM obtaining an FWHM (full width half maximum) of $0.6\ nm$ by Peerling *et al.* [15].

Figure 1.6: SEM views of monolithic tunable Fabry-Perot filters based on InP/air-gap layers. (image reprinted from [12])

Optical filters with non-III-V layer combinations, such as AlGaAs|AlO_x [14, 16] and especially airgap|InP, have been studied making use of the improved optical contrast. Airgap-based optical filters feature the highest refraction index contrast as compared to all-solid state designs, thus yielding simpler or higher-performance filters. The high refractive index contrast of InP-to-air ($n_{InP} = 3.17$), as compared to the conventional all-dielectric or semiconductor based DBRs, provides a high peak reflectivity and a wide bandwidth with only a few layer pairs [17]. Optical filters with multiple air-gaps based on InP membranes have been demonstrated [11, 12, 16–20]. The fabrication of air-gap optical filters has generally been based on an initial deposition of a stack of sacrificial and structural/optical layers. Selective removal of the sacrificial layers results in a stack of free-standing membranes, separated by airgap layers. Figure 1.6 shows a monolithic InP-based tunable Fabry-Perot filter. Optical MEMS switching devices with high spatial and spectral resolution based on InP-air gap DBRs integrated with a photonic crystal structure have also been reported [21].

III-V-based ultraviolet-visible optical filters

Highly efficient III-nitride-based light-emitting diodes (LEDs) have recently enabled the replacement of conventional light sources in even high power applications [22]. The high efficiency of LEDs is attributable to several breakthroughs and developments that have been made in the recent years. A major concern in LEDs is the light extraction efficiency of the device. The light generated in LED material must be transmitted via the interface. The refractive index of most III-nitrides is high

which results in a small critical angle ($24.6°$ for GaN [23]) at the interface with air. Therefore, only the light that is internally transmitted towards the surface at an angle smaller than the critical angle is ultimately emitted. Any initial emission outside this extraction cone is reflected back (i.e. total internal reflection) and is eventually absorbed. The rate at which the emitted light is actually emitted from the semiconductor material into the air is known as the light extraction efficiency.

Various structures have been used to increase the light extraction efficiency of different structures, such as Bragg reflectors, 2D photonic crystals [23] and the use of surface texturing [24] of the LED. Bragg reflectors have been used to reflect the internally reflected light back to the extraction cone, hence the improvement in the light extraction efficiency of the LED. The low refractive index contrast of the available materials, however, fundamentally limits the obtainable reflectivity and band width of the DBRs. Therefore, a very large number of layers (up to 45-pairs [25, 26]) are required to achieve a sufficient reflectance. Growing and depositing such a large number of layers requires high level control over the deposition condition to avoid crack generation in the layer stack [27].

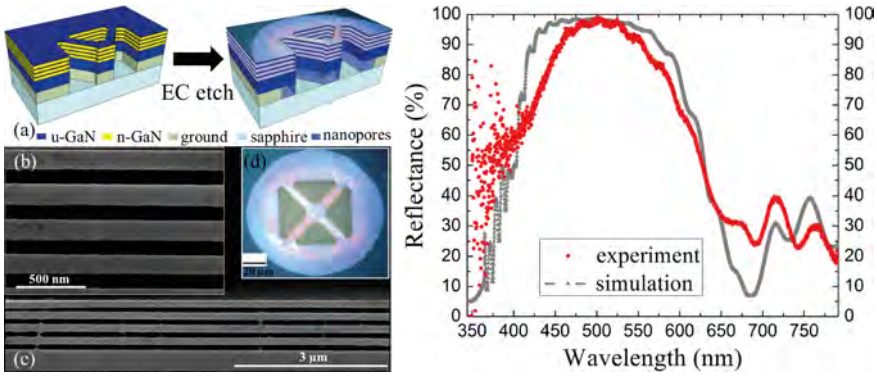

Figure 1.7: SEM images of GaN membrane DBRs. (figure reprinted from [28])

Since the studies of the infrared InP/air-gap, ultraviolet and visible III-nitrides/air-gap DBRs have been investigated by different groups [28–36]. Figure 1.7 shows a GaN/airgap Bragg reflector released via electrochemical etching. The DBRs fabricated up to now (to the author's knowledge) have all been high-order implementations of DBRs ($3 - 5\lambda/4n$ membranes) resulting in sufficient membrane thickness to ensure rigidity and flatness. Moreover, GaN/nanoporous-GaN DBRs have been reported by [37, 38]. Structures with multiple-pair GaN/airgaps have been demonstrated for the visible spectrum resulting in a high peak reflectance ($> 98\%$) achievable with only a few layer pairs.

The achievements in GaN-based LED fabrication have resulted in highly efficient blue LEDs by several research groups [39]. The increased light efficiency is a result of advancements in the deposition of defect-free doped quantum heterostructures. The result has been higher quantum efficiency, as well as the fabrication of DBRs and photonic crystal components which enhance the light extraction efficiency. The

1

Nobel Prize in Physics in 2014 was awarded jointly to Isamu Akasaki, Hiroshi Amano and Shuji Nakamura "for the invention of efficient blue light-emitting diodes which has enabled bright and energy-saving white light sources" [39]. These advances have allowed for the fabrication of highly efficient blue LEDs, which is essential for generating white light in combination with efficient red and green LEDs.

Silicon-based (CMOS compatible) infrared optical filters

Absorption peaks of several interesting gases (such as CO, CO_2, and CH_4) are located in the infrared spectrum. The demand for a low cost, reliable device for measuring the concentration of these gases has motivated the fabrication of silicon-based microspectrometers. Silicon-based technology has many advantages over III-V technology for microspectrometer applications, such as the availability of various processes and the integration capability with microelectronics (e.g. silicon photo detectors).

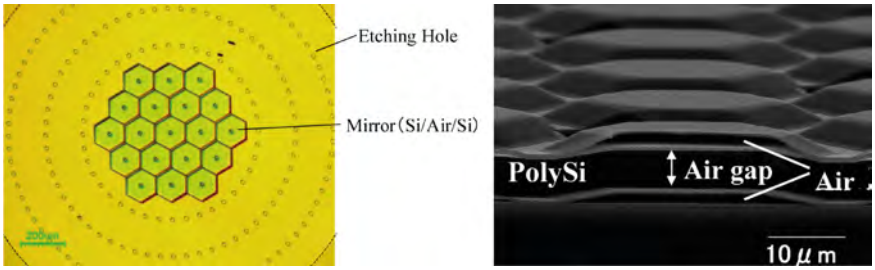

Figure 1.8: SEM and microscope images of freestanding Fabry-Perot optical filters using polysilicon membranes for microspectrometer applications (figure reprinted from [40]).

MEMS infrared emitters and detectors have been the focus of research for years. Many layer combinations with an acceptable refractive index contrast, such as polysilicon and SiO_2 [41] are available in CMOS technologies. However, using air-gap-based optical filters provides an enhanced optical response. A sufficiently high peak reflectance and bandwidth can be obtained, using only two membranes per reflector. Furthermore, the silicon micromachining techniques to achieve flat free-standing membranes is a mature technology. Hydrofluoric (HF) etching of SiO_2 layers also provides almost infinite selectivity. This has led to the fabrication of high resolution, wide band microspectrometers [42].

Different CMOS compatible processes have been investigated for applications in the infrared spectrum. Airgap-based optical filters based on the silicon-nitride/airgap [44] and more extensively (poly)silicon/airgap designed and fabricated by a Japanese research team (see Figure 1.8) [40, 45] and a Finish team at VTT (see Figure 1.9) [42, 43, 46, 47] have been extensively studied.

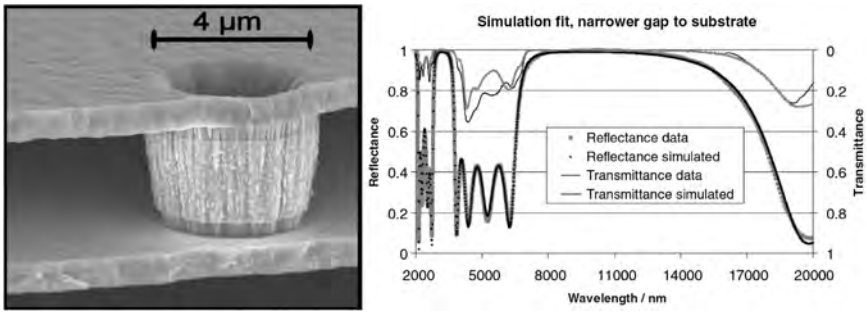

Figure 1.9: SEM image of polysilicon layers separated by QWOT layers. An anchor fixing the membrane is also shown in the figure (figure reprinted from [43]).

1.3. Motivation: MEMS Spectrometers for gas sensing application

The fabrication of low cost, mass-produced microelectromechanical sensor systems (MEMS) by exploiting the advantages of wafer-level fabrication has opened up a vast range of possibilities and applications. MEMS sensors have been hugely successful in airbag deployment systems, but have also been investigated for specific applications such as optical detection, gas sensing, and chemical and biological sensors [48].

Chemical components have unique absorption peaks which are specific to their atomic structure and bonds. These unique chemical-specific absorption spectra are commonly utilized in absorption spectroscopy to detect the presence of specific components and their concentration. An electromagnetic wave traveling through a material (gas, liquid, or solid) are absorbed by the atoms, depending on the energy (or wavelength). These absorption peaks are a sign of transitions taking place between energy states in an atom. When electromagnetic radiation of a particular frequency is absorbed by an atom or chemical compound, in general, the energy of the system rises to a higher energy level (state). According to quantum physics, atomic systems can only be excited to higher energy states by an electromagnetic wave with a certain energy level, and hence the wavelength - $\lambda = hc/E$, where h, c and λ are, respectively, Planck's constant, the speed of the light, and the frequency of the light [49]. Depending on the nature of the energy states, different transitions can be observed, such as: (1) changing the state of the electron, which is mainly in the (deep) ultraviolet($\approx 10 - 400\ nm$) up to the visible ($\approx 400 - 750\ nm$); and (2) rotational and vibrational transitions, (related to the state of the molecules) usually in the infrared ($\approx 750 - 1,000,000\ nm$) and higher wavelengths (see Figure 1.10). Absorption spectroscopy is the analysis of spectral losses in a 'white' light after traveling through the length of a material [50, 51].

Traditionally, gas composition measurements are either performed with expensive industrial gas analyzers such as gas chromatographs [52], non-dispersive infrared (NDIR) sensors and Wobbe index meters, or with low cost pellistors (e.g. [53]), and electrochemical sensors (e.g. [54]). Compared to others, industrial gas

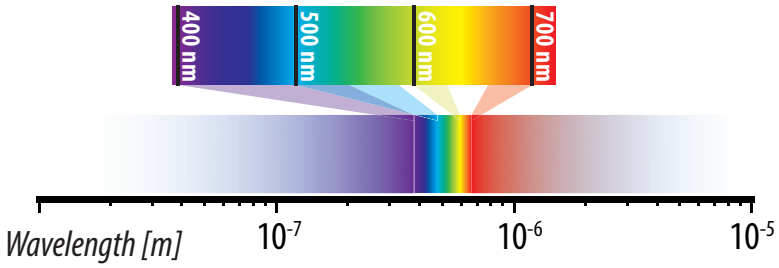

Figure 1.10: Electromagnetic Spectrum. The color representation of the different wavelengths shown in the figure is approximate.

analyzers have a superior detection accuracy and sensitivity. However, these industrial analyzers are bulky, expensive (> 20K Euro), and not suitable for real-time and *in situ* measurements, where as in many consumer applications, a significantly lower spectral performance is typically required [55]. Pellistors, on the other hand, which are small, low cost sensors, suffer from signal drift at low (ppm) gas concentration levels [53]. Electrochemical sensors also suffer from low selectivity and sensor poisoning by certain chemicals [54]. Optical absorption sensing offers attractive features, such as a faster acquisition time, lower signal drift, higher reliability and longer lifetime. Furthermore, optical spectroscopy is non-invasive and self-referenced, and it can be used for *in situ* gas detection [51]. MEMS spectrometers are highly promising in specific low cost applications.

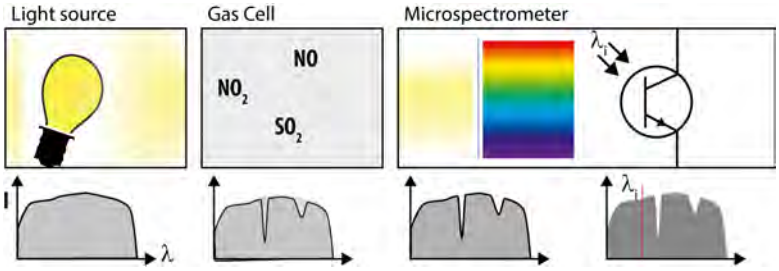

Figure 1.11: Schematics of a gas sensor unit based on absorption spectrometry.

An optical gas sensor is made of four basic elements: a light source, a gas cell, a dispersion unit, and a detection system. Figure 1.11 shows the schematic configuration of a MEMS gas sensor based on absorption spectroscopy. The light source provides wideband electromagnetic radiation that covers the spectrum of interest. When input light enters and passes through the length of the gas cell, the light is spectrally attenuated according to the gas-specific absorption peaks. Subsequently, the transmitted light enters the microspectrometer unit. Measuring the wavelengths in the beam with a significantly reduced amplitude reveals the concentrations of the components present in the gas cell. Therefore, the transmitted light is spectrally filtered and fed into a detector (or a detector array). After the transmission spectrum

analysis, the information used to assess the gas compositions and concentrations is extracted. Furthermore, a spectrum measurement taken without any gas in the chamber is often used as a reference, making this method self-referenced [50].

It must be noted that, while dimension downscaling is generally favorable in MEMS applications, the optical benefits remain disputed [55]. The micro-fabrication of non-planar optical components, such as the lenses and convex or concave mirrors required in an optical system to improve the optical throughput is challenging. The absorption length is directly relevant to the signal that can be measured. Therefore, the optical path length, which is required at a certain wavelength, places a fundamental limit on the smallest dimensions in optical MEMS.

1.3.1. Exhaust emission sensing

The motivation behind the research described here is to analyze, by means of absorption spectroscopy, the combustion products of natural gas, which contain considerable amounts of CO, CO_2, NO_x, and SO_2. Analyzing exhaust gas benefits to the assessment of the combustion process of engines. Moreover, studies show that the death rate in western countries due to pollution-related diseases is almost twice the death rate due to vehicle accidents [56]. Therefore, gas sensing is not restricted to energy efficiency, but has a wide range of applications, from detecting and measuring concentrations of hydrocarbons in natural gas to the diagnosis of diseases by analyzing the breath exhaled and skin emissions of patients [51, 57].

The absorption spectrum of the target gases should be compared to determine the cross-sensitivities and to identify a practical operational range for the spectrometer sensors. Figure 1.12 represents the absorption spectra of some of the exhaust gases in the ultraviolet (UV) visible spectrum. According to the figure, our components of interest have absorption bands over an extended range of the spectrum. It should be noted that a post-processing algorithm, such as the mean square error approach, should be used to deconvolve the spectra and to distinguish between different gas types in the overlapping regions [65, 66].

Although some of these gases (such as CO and CO_2) have absorption peaks in both the infrared and ultraviolet spectra, ultraviolet spectrometry still offers a few advantages. The infrared spectrum is typically crowded with multiple overlapping absorption peaks. Hydrocarbons, which constitute the highest percentage of fuels, and water vapor have a strong absorption spectrum in the infrared. Therefore, an extensive spectral analysis is required in the infrared. On the other hand, the ultraviolet and visible spectra are almost free from the absorption of other components, especially water, thus providing a suitable spectral window for sensing applications. The absorption level of these gases in the ultraviolet is typically smaller than in the infrared. However, the absorption spectra are sparsely distributed in the UV range, thus the distinction between gas components is less challenging. Furthermore, low cost, reliable photo detectors are available in CMOS technology. Therefore, absorption spectroscopy in the UV-visible range offers several potential advantages.

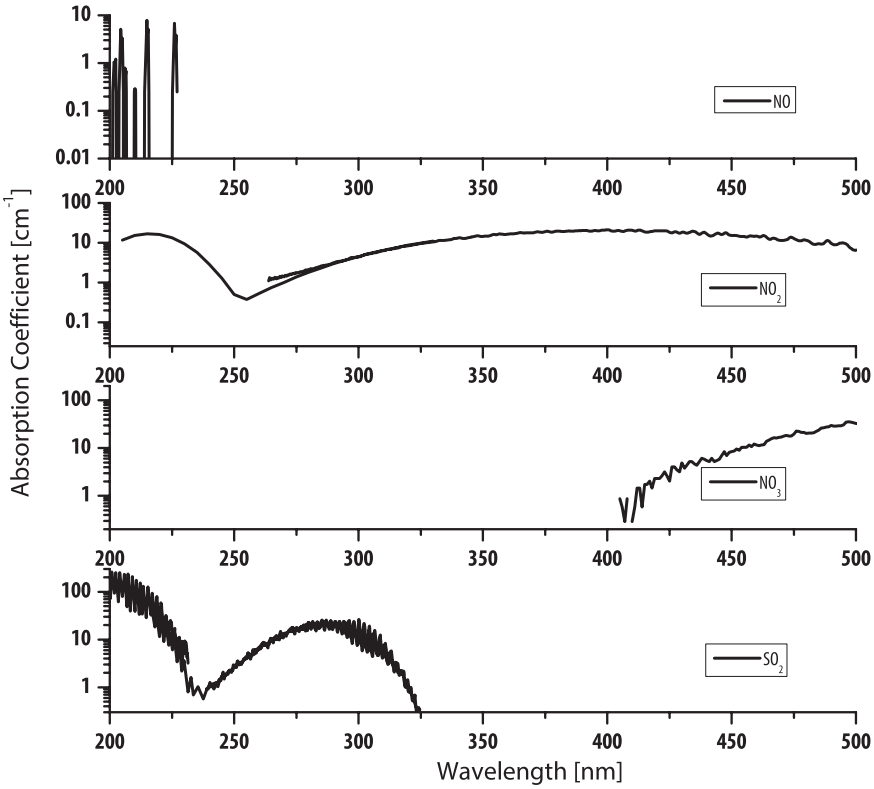

Figure 1.12: Spectral absorptions of exhaust gases. Data obtained from [58–64].

1.4. Microspectrometer configurations

The performance of a microspectrometer mainly depends on the dispersing element, which is implemented in the device to give the wavelength-specific functionality of the device. Microspectrometers based on the dispersion element are classified into diffraction-based (e.g. gratings and prisms) or interference-based (e.g. Fabry-Perot, Michelson, and Mach-Zehnder) systems [55]. Grating-based, interference-based (mostly Fabry-Perot) and Fourier transform-based configurations have been described extensively in the literature [55, 67]. For the first two device types, the spectrometer scans and measures the absorption at each individual wavelength to obtain the absorption spectrum. However, the Fourier transform-based spectrometer measures the absorption of a series of interferograms. The spectral data are subsequently obtained using the Fourier transform algorithm. The following sections briefly present the state-of-the-art MEMS spectrometers based on these configurations.

Fourier-transform infrared (FTIR) microspectrometers

Fourier transform spectroscopy, which is usually a modification of the Michelson interferometer configuration, has also been implemented in MEMS devices. Figure 1.13 shows the schematic operation of a Fourier-transform infrared (FTIR) spectrometer. In the Fourier transform method, a Michelson interferometer is used to produce an *interferogram*. The interferogram passes through the absorbing medium (i.e. the gas sample), and the signal is recorded. By varying the interferogram by sweeping the moving mirror in the Michelson interferometer over a specific length, the change in the recorded energy over time is obtained. The Fourier transform function converts a recorded time spectrum into spectral information. Various MEMS FTIR spectrometer devices have been reported in the literature [68, 69]. While FTIR spectrometers are faster and offer a better signal-to-noise ratio compared to other spectrometer configurations, the resolution of FTIR spectrometers is determined by the scanning length of the moving mirror. Therefore, downscaling the device (and consequently the scanning length) limits the spectral resolution of the FTIR.

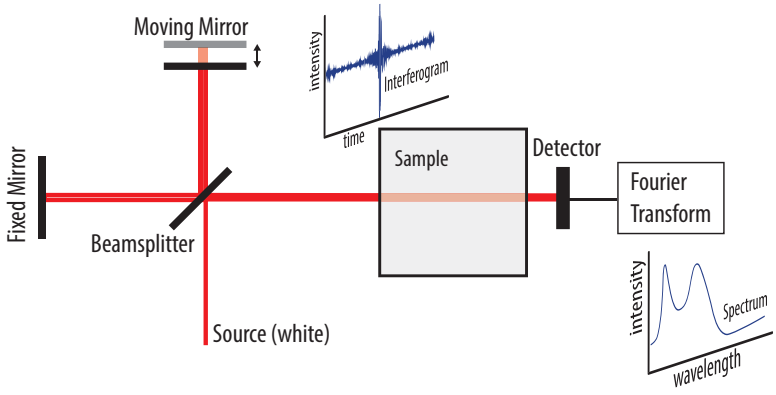

Figure 1.13: Schematics of a FTIR spectrometer.

Grating-based microspectrometers

In grating-based (micro)spectrometers, a grating element spectrally disperses the incident light over an array of detectors or a single moving detector. A spectral resolution in the range of a few nanometers down to sub-nanometers has been achieved using a grating-based visible microspectrometer fabricated in a MEMS fabrication process [70–72]. However, the dispersive elements usually require a long optical path, and optical alignment is a challenge. This poses a challenge in the fabrication of integrated microspectrometers.

Interference-based (optical filter) microspectrometers

Optical filter-based microspectrometers use interference filters to divide a spectrum into a set of transmission peaks. Various optical resonance principles (e.g. Fabry-

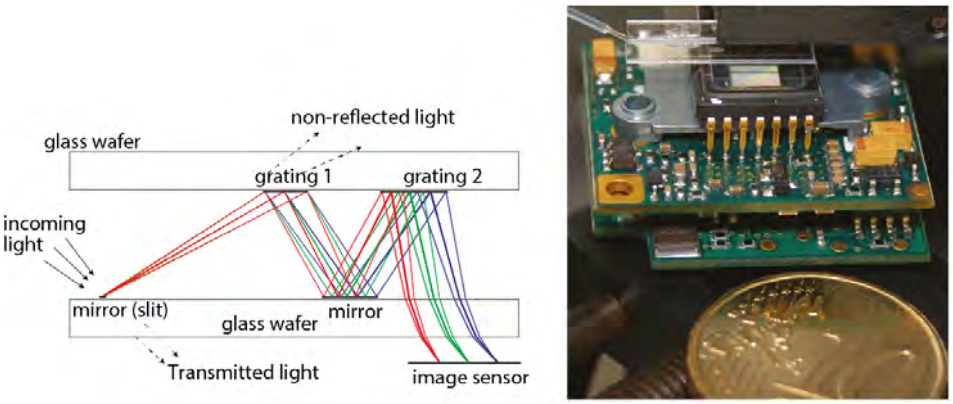

Figure 1.14: Design of the planar microspectrometer. The miniature grating-based spectrometer is shown. Light is fed into the spectrometer from the fiber tip shown in the upper left corner. (Figure reprinted from [71])

Perot, Michelson, and Mach-Zehnder) have been commonly used in the optical filters for (micro)spectrometers [55, 67]. Fabry-Perot interferometers are very common in MEMS spectrometers due to their compact size and simple structures. As discussed before, a Fabry-Perot optical filter is composed of two reflective surfaces that are separated by a non-absorbing medium. Depending on the spacing of the reflectors, a specific wavelength (within a limited spectrum) can be transmitted through the filter. Varying the mirror spacing provides a spectral scan over a specific spectrum.

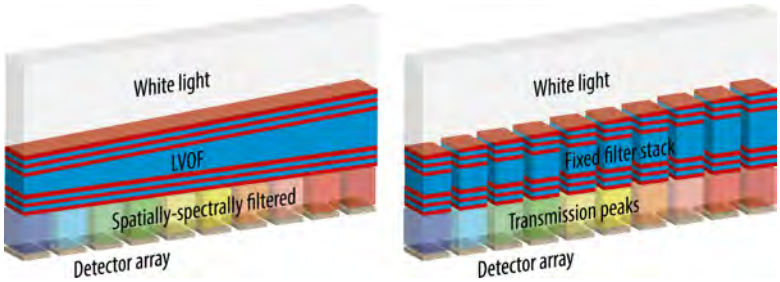

Figure 1.15: a. An array of fixed filters, b. LVOF configuration.

Several fixed and tunable spacing Fabry-Perot based optical filters have been reported in the literature [67, 73, 74]. A high degree of integration and a spectral resolution of a few nanometers (in the visible spectrum) using Fabry-Perot based filters with a fixed setting have been reported [75]. However, to obtain the required spectral power over a wide spectrum, a large number of different fixed filters should be designed, which makes the fabrication technically extremely challenging. Tunable Fabry-Perot filters[74] and linear variable optical filters (LVOFs) [76] are two solutions for this problem.

The LVOF is a Fabry-Perot type filter that consists of two dielectric multi-layered Bragg reflectors, one on each side of a central resonator cavity layer. The thickness of the cavity layer changes linearly along the length of the filter and determines the wavelength of the transmitted light. Therefore, instead of a large number of discrete filters, which is difficult to fabricate, the LVOF operates as a one-dimensional array of Fabry-Perot filters. By passing through the filter, the light is band-pass filtered with a transmission peak wavelength that is set by the width of the resonator at each point and thus by the spatial position along the length of the LVOF [66]. Several techniques are available for fabrication of a lateral taper with a very small taper angle ($\ll 1^o$), such as chemical-mechanical polishing, gray-scale lithography, and reflow. IC-compatible fabrication of a narrow spectral band with high resolution LVOFs based on re-flow, has been developed for the visible/ultraviolet spectral range [77] and the infrared [41] spectrum. A detector array positioned underneath the LVOF records the transmitted light. In this way, each detector element receives a specific wavelength. Hence, the entire structure operates as a micro-spectrometer.

Compared to optical filter-based devices, a grating-type spectrometer offers a wider operating range of a given spectral resolution and a better optical throughput. However, the required optical path length in grating-based devices is a major drawback in device integration and proves to be challenging in the mass production of optical MEMS devices. Optical filter-based microspectrometers, on the other hand, offer an optical performance over the limited bandwidth that is sufficient for a wide range of applications, while also providing a high degree of wafer-level integration.

1.5. Silicon-based (CMOS compatible) ultraviolet-visible optical filters

As discussed in the previous sections, a microspectrometer operating in the ultraviolet-visible spectral range is required for measuring emission gases. The research presented in this thesis investigates the challenges in the fabrication of a microspectrometer for operation in the ultraviolet-visible spectral range for exhaust emission spectroscopy. For a low cost, reliable sensor system, the design and fabrication of each of the main parts of the light source, gas cell, and spectrometer have to be carefully considered.

Traditionally, broadband sources such as halogen lamps, deuterium lamps, or hot-wires, are used as light sources for non-dispersive detection. In MEMS applications, IR-emitting thin film membranes and wires have been fabricated and can be modulated at high frequencies [51]. However, the filament temperature is typically limited to about $500^o\ C$, thus preventing light emission in the UV. The utilization of narrow band LEDs has been reported for visible and infrared spectroscopy [78]. In the ultraviolet spectrum, AlGaN and AlN-based UV-emitting diodes that cover the range of $200 - 400\ nm$ are now becoming available [79, 80]. Mini-spectrometers with UV-LEDs designed for the spectroscopy of SO_2 have been reported [81]. Therefore, LEDs provide a compact light source for MEMS spectrometers. However, these devices are poorly compatible with wafer-level silicon processing.

Silicon-based CMOS photo-detectors are readily available, low cost, and achieve

sufficient sensitivity in the ultraviolet-visible spectral range. The lack of available materials in this spectrum necessitates the implementation of new materials or structures. Implementing a non-CMOS compatible optical filter to the system adds to the cost and process complexity. Therefore, maintaining CMOS-compatibility is essential for achieving the low unit-cost that is paramount in consumer devices and systems. Lack of suitable materials for the ultraviolet-visible spectrum that are also compatible with CMOS processing has motivated the application of air-gap based optical filters.

The optical effect of fabrication tolerances, such as surface quality and structural dimensions, is inversely proportional to wavelength and more critical in ultraviolet optical components as compared to visible and infrared systems. Therefore, the fabrication challenge increases with shorter wavelengths and is significantly higher in the visible/blue part of the optical spectrum as compared to the infrared. The thinner sacrificial layers must be removed with a sufficient selectivity to the membrane material. At the same time, the optical flatness criterion in the thinner membranes becomes more restrictive due to the increased scattering of given surface roughness/waviness with increasing wavelength. This dissertation aims to address several of these challenges for achieving high performance airgap-based optical filters. Therefore, the realization of a reliable, high resolution optical filter in the ultraviolet spectrum is challenging but highly desirable.

Furthermore, many applications require a multi-gas sensing system. Due to the complex absorption peaks and cross-sensitivities, a multi-sensor system comprising different sensors, such as optical, thermal conductivity, and viscosity is needed [82]. While several miniaturized optical gas sensors have been built, these are not entirely CMOS compatible. Hence these are not compatible with the wafer-level production required for the high-volume application of gas distribution. Therefore, a robust, low cost, CMOS compatible and fully integrated MEMS device is needed. The work presented in this dissertation is aimed at utilizing available silicon-based fabrication processes to fabricate high performance, low cost optical gas sensors.

1.6. Organization of this dissertation

Chapter 2 introduces the optical design of optical filters. The optical response enhancement provided by using air-gap-based designs is also discussed. The mechanical design of an ideal multi-layered optical filter is discussed in Chapter 3. The deposition and mechanical properties of different materials are also investigated. The impact of the non-idealities of the fabrication process, such as the presence of gradient residual stress and finite etch selectivity in the optical performance of the filter, is discussed in Chapter 4. Chapter 5 presents the details of the fabrication flow used to realize the air-gap-based filters. Optical characterization results are also presented and are discussed.

References

[1] J. Shelby, *OPTICAL MATERIALS | color filter and absorption glasses,* in *Encyclopedia of Modern Optics*, edited by R. D. Guenther (Elsevier, Oxford, 2005) pp. 440 – 446.

[2] H. A. Macleod, *Thin-film optical filters*, Series in Optics and Optoelectronics (CRC Press, 2010) Chap. Band-Pass Filters, pp. 299–401.

[3] C. J. van Rijn, *Nano and micro engineered membrane technology*, Vol. 10 (Elsevier, 2004).

[4] J. Teyssier, S. V. Saenko, D. van der Marel, and M. C. Milinkovitch, *Photonic crystals cause active colour change in chameleons,* Nat Commun **6** (2015).

[5] S. Niu, B. Li, Z. Mu, M. Yang, J. Zhang, Z. Han, and L. Ren, *Excellent structure-based multifunction of Morpho butterfly wings: A review,* Journal of Bionic Engineering **12**, 170 (2015).

[6] Radwan, *Morpho rhetenor nanostructures,* (2014-04-08).

[7] P. Vukusic, J. R. Sambles, C. R. Lawrence, and R. J. Wootton, *Quantified interference and diffraction in single Morpho butterfly scales,* Proceedings of the Royal Society of London B: Biological Sciences **266**, 1403 (1999), http://rspb.royalsocietypublishing.org/content/266/1427/1403.full.pdf .

[8] W. Wang, W. Zhang, J. Gu, Q. Liu, T. Deng, D. Zhang, and H.-Q. Lin, *Design of a structure with low incident and viewing angle dependence inspired by Morpho butterflies,* Scientific Reports **3**, 3427 EP (2013).

[9] R. A. Potyrailo, H. Ghiradella, A. Vertiatchikh, K. Dovidenko, J. R. Cournoyer, and E. Olson, *Morpho butterfly wing scales demonstrate highly selective vapour response,* Nat Photon **1**, 123 (2007).

[10] R. H. Siddique, R. Hünig, A. Faisal, U. Lemmer, and H. Hölscher, *Fabrication of hierarchical photonic nanostructures inspired by Morpho butterflies utilizing laser interference lithography,* Opt. Mater. Express **5**, 996 (2015).

[11] K. Streubel, S. Rapp, J. Andre, and N. Chitica, *1.26 µm vertical cavity laser with two InP/air-gap reflectors,* Electronics Letters **32**, 1369 (1996).

[12] M. Garrigues, J. Leclercq, and P. Viktorovitch, *III-V semiconductor based MOEMS devices for optical telecommunications,* Microelectronic Engineering **61–62**, 933 (2002), micro- and Nano-Engineering 2001.

[13] N. P. Siwak, X. Z. Fan, and R. Ghodssi, *Fabrication challenges for indium phosphide microsystems,* Journal of Micromechanics and Microengineering **25**, 043001 (2015).

[14] M. Wu, G. Li, W. Yuen, and C. Chang-Hasnain, *Widely tunable 1.5 μm micromechanical optical filter using AlOx/AlGaAs DBR,* Electronics Letters **33**, 1702 (1997).

[15] J. Peerlings, R. Riemenschneider, V. Kumar, M. Strassner, J. Pfeiffer, V. Scheuer, J. Daleiden, K. Mutamba, S. Herbst, H. Hartnagel, and P. Meissner, *Two-chip InGaAs-InP Fabry-Perot p-i-n receiver for WDM systems,* Photonics Technology Letters, IEEE **11**, 260 (1999).

[16] P. Tayebati, P. Wang, D. Vakhshoori, and R. Sacks, *Widely tunable Fabry-Perot filter using Ga(Al)As-AlOx deformable mirrors,* Photonics Technology Letters, IEEE **10**, 394 (1998).

[17] J. Daleiden, V. Rangelov, S. Irmer, F. Romer, M. Strassner, C. Prott, A. Tarraf, and H. Hillmer, *Record tuning range of inp-based multiple air-gap moems filter,* Electronics Letters **38**, 1270 (2002).

[18] N. Chitica, J. Daleiden, J. Bentell, J. André, M. Strassner, S. Greek, D. Pasquariello, M. Karlsson, R. Gupta, and K. Hjort, *Fabrication of tunable InP/air-gap Fabry-Perot cavities by selective etching of InGaAs sacrificial layers,* Physica Scripta **1999**, 131 (1999).

[19] K. Streubel, S. Rapp, J. André, and N. Chitica, *Fabrication of InP/air-gap distributed Bragg reflectors and micro-cavities,* Materials Science and Engineering: B **44**, 364 (1997), 3rd International Workshop on Expert Evaluation and Control of Compound Semiconductor Materials and Technologies.

[20] A. Spisser, R. Ledantec, C. Seassal, J. Leclercq, T. Benyattou, D. Rondi, R. Blondeau, G. Guillot, and P. Viktorovitch, *Highly selective and widely tunable 1.55 μm InP/air-gap micromachined Fabry-Perot filter for optical communications,* Photonics Technology Letters, IEEE **10**, 1259 (1998).

[21] J. L. Leclercq, P. Rojo-Romeo, C. Seassal, J. Mouette, X. Letartre, and P. Viktorovitch, *3D structuring of multilayer suspended membranes including 2D photonic crystal structures,* Journal of Vacuum Science & Technology B **21**, 2903 (2003).

[22] N. Holonyak, *Is the light emitting diode (LED) an ultimate lamp?* American Journal of Physics **68**, 864 (2000).

[23] J. J. Wierer, A. David, and M. M. Megens, *III-nitride photonic-crystal light-emitting diodes with high extraction efficiency,* Nature Photonics **3**, 163 (2009).

[24] H. Guo, X. Zhang, H. Chen, P. Zhang, H. Liu, H. Chang, W. Zhao, Q. Liao, and Y. Cui, *High performance GaN-based LEDs on patterned sapphire substrate with patterned composite SiO2/Al2O3 passivation layers and TiO2/Al2O3 DBR backside reflector,* Opt. Express **21**, 21456 (2013).

[25] M. Arita, M. Nishioka, and Y. Arakawa, *InGaN vertical microcavity LEDs with a Si-doped AlGaN/GaN distributed Bragg reflector,* physica status solidi (a) **194**, 403 (2002).

[26] C. Berger, A. Dadgar, J. Blüsing, and A. Krost, *In-situ growth monitoring of AlInN/AlGaN distributed Bragg reflectors for the UV-spectral range,* Journal of Crystal Growth **370**, 87 (2013), 16th International Conference on Metalorganic Vapor Phase Epitaxy.

[27] T. Moudakir, S. Gautier, S. Suresh, M. Abid, Y. E. Gmili, G. Patriarche, K. Pantzas, D. Troadec, J. Jacquet, F. Genty, P. Voss, and A. Ougazzaden, *Suppression of crack generation in AlGaN/GaN distributed Bragg reflectors grown by MOVPE,* Journal of Crystal Growth **370**, 12 (2013), 16th International Conference on Metalorganic Vapor Phase Epitaxy.

[28] D. Chen and J. Han, *High reflectance membrane-based distributed Bragg reflectors for GaN photonics,* Applied Physics Letters **101**, 221104 (2012), http://dx.doi.org/10.1063/1.4768806.

[29] A. Altoukhov, J. Levrat, E. Feltin, J.-F. Carlin, A. Castiglia, R. Butté, and N. Grandjean, *High reflectivity airgap distributed Bragg reflectors realized by wet etching of AlInN sacrificial layers,* Applied Physics Letters **95**, 191102 (2009), http://dx.doi.org/10.1063/1.3259720.

[30] J. H. Ryu, H. Y. Kim, H. K. Kim, Y. S. Katharria, N. Han, J. H. Kang, Y. J. Park, M. Han, B. D. Ryu, K. B. Ko, E.-K. Suh, and C.-H. Hong, *High performance of InGaN light-emitting diodes by air-gap/GaN distributed Bragg reflectors,* Opt. Express **20**, 9999 (2012).

[31] R. Sharma, Y.-S. Choi, C.-F. Wang, A. David, C. Weisbuch, S. Nakamura, and E. L. Hu, *Gallium-nitride-based microcavity light-emitting diodes with air-gap distributed Bragg reflectors,* Applied Physics Letters **91**, 211108 (2007), http://dx.doi.org/10.1063/1.2805028.

[32] R. Sharma, E. D. Haberer, C. Meier, E. L. Hu, and S. Nakamura, *Vertically oriented GaN-based air-gap distributed Bragg reflector structure fabricated using band-gap-selective photoelectrochemical etching,* Applied Physics Letters **87**, 051107 (2005), http://dx.doi.org/10.1063/1.2008380.

[33] A. C. Tamboli, M. C. Schmidt, A. Hirai, S. P. DenBaars, and E. L. Hu, *Photoelectrochemical undercut etching of m-plane GaN for microdisk applications,* Journal of The Electrochemical Society **156**, H767 (2009), http://jes.ecsdl.org/content/156/10/H767.full.pdf+html .

[34] C. Xiong, P. R. Edwards, G. Christmann, E. Gu, M. D. Dawson, J. J. Baumberg, R. W. Martin, and I. M. Watson, *High-reflectivity GaN/air vertical distributed Bragg reflectors fabricated by wet etching of sacrificial AlInN layers,* Semiconductor Science and Technology **25**, 032001 (2010).

[35] R. Tao, M. Arita, S. Kako, and Y. Arakawa, *Fabrication and optical properties of non-polar III-nitride air-gap distributed Bragg reflector microcavities,* Applied Physics Letters **103**, 201118 (2013), http://dx.doi.org/10.1063/1.4832069.

[36] T. Mitsunari, T. Tanikawa, Y. Honda, M. Yamaguchi, and H. Amano, *AlN/air distributed Bragg reflector by GaN sublimation from microcracks of AlN,* Journal of Crystal Growth **370**, 16 (2013), 16th International Conference on Metalorganic Vapor Phase Epitaxy.

[37] J. Park, J.-H. Kang, and S.-W. Ryu, *High diffuse reflectivity of nanoporous GaN distributed Bragg reflector formed by electrochemical etching,* Applied Physics Express **6**, 072201 (2013).

[38] B.-C. Shieh, Y.-C. Jhang, K.-P. Huang, W.-C. Huang, J.-J. Dai, C.-F. Lai, and C.-F. Lin, *InGaN light-emitting diodes with embedded nanoporous GaN distributed Bragg reflectors,* Applied Physics Express **8**, 082101 (2015).

[39] Nobelprize.org, *The nobel prize in physics 2014,* (28 Jan 2016), nobel Media AB 2014. Web.

[40] T. Enomoto, M. Suzuki, T. Iwaki, H. Wado, and Y. Takeuchi, *Infrared absorption sensor for multiple gas sensing. Development of a Fabry–Perot spectrometer with ultrawide wavelength range,* Electronics and Communications in Japan **96**, 50 (2013).

[41] M. Ghaderi, N. P. Ayerden, A. Emadi, P. Enoksson, J. H. Correia, G. d. Graaf, and R. F. Wolffenbuttel, *Design, fabrication and characterization of infrared LVOFs for measuring gas composition,* Journal of Micromechanics and Microengineering **24**, 084001 (2014).

[42] M. Tuohiniemi, A. Näsilä, A. Akujärvi, and M. Blomberg, *MOEMS Fabry–Perot interferometer with point-anchored Si-air mirrors for middle infrared,* Journal of Micromechanics and Microengineering **24**, 095019 (2014).

[43] M. Tuohiniemi and M. Blomberg, *Surface-micromachined silicon air-gap Bragg reflector for thermal infrared,* Journal of Micromechanics and Microengineering **21**, 075014 (2011).

[44] S. Irmer, K. Alex, J. Daleiden, I. Kommallein, M. Oliveira, F. Römer, A. Tarraf, and H. Hillmer, *Surface micromachined optical low-cost all-air-gap filters based on stress-optimized Si3N4 layers,* Journal of Micromechanics and Microengineering **15**, 867 (2005).

[45] M. Suzuki, H. Wado, and T. Yoshida, *Optical multilayer mirror and Fabry-Perot interferometer having the same,* (2010), uS Patent 7,733,495.

[46] M. Tuohiniemi, A. Näsilä, and J. Mäkynen, *Characterization of the tuning performance of a micro-machined Fabry–Perot interferometer for thermal infrared,* Journal of Micromechanics and Microengineering **23**, 075011 (2013).

[47] M. Tuohiniemi, M. Blomberg, A. Akujärvi, J. Antila, and H. Saari, *Optical transmission performance of a surface-micromachined Fabry–Perot interferometer for thermal infrared,* Journal of Micromechanics and Microengineering **22**, 115004 (2012).

[48] S. Xia, D. Chen, Z. Qi, X. He, C. Peng, X. Chen, C. Bian, L. Qu, and J. Sun, *Microsystems and Nanotechnology*, edited by Z. Zhou, Z. Wang, and L. Lin (Springer Berlin Heidelberg, Berlin, Heidelberg, 2012) Chap. Microelectromechanical Sensors, pp. 207–260.

[49] M. Born, E. Wolf, and A. Bhatia, *Principles of Optics: Electromagnetic Theory of Propagation, Interference and Diffraction of Light* (Cambridge University Press, 1999).

[50] N. Tkachenko, *Optical Spectroscopy: Methods and Instrumentations* (Elsevier Science, 2006).

[51] J. Hodgkinson and R. P. Tatam, *Optical gas sensing: a review,* Measurement Science and Technology **24**, 012004 (2013).

[52] A. S. Brown, M. J. Milton, C. J. Cowper, G. D. Squire, W. Bremser, and R. W. Branch, *Analysis of natural gas by gas chromatography: Reduction of correlated uncertainties by normalisation,* Journal of Chromatography A **1040**, 215 (2004).

[53] H. Debeda, L. Dulau, P. Dondon, F. Menil, C. Lucat, and P. Massok, *Development of a reliable methane detector,* Sensors and Actuators B: Chemical **44**, 248 (1997).

[54] G. Korotcenkov, S. D. Han, and J. R. Stetter, *Review of electrochemical hydrogen sensors,* Chemical Reviews **109**, 1402 (2009), pMID: 19222198, http://dx.doi.org/10.1021/cr800339k .

[55] R. F. Wolffenbuttel, *MEMS-based optical mini- and microspectrometers for the visible and infrared spectral range,* Journal of Micromechanics and Microengineering **15**, S145 (2005).

[56] G. Dooly, C. Fitzpatrick, and E. Lewis, *Optical sensing of hazardous exhaust emissions using a UV based extrinsic sensor,* Energy **33**, 657 (2008).

[57] S.-I. Ohira and K. Toda, *Micro gas analyzers for environmental and medical applications,* Analytica Chimica Acta **619**, 143 (2008).

[58] H. Keller-Rudek, G. K. Moortgat, R. Sander, and R. Sörensen, *The MPI-Mainz UV/VIS spectral atlas of gaseous molecules of atmospheric interest,* Earth System Science Data **5**, 365 (2013).

[59] B. A. Thompson, P. Harteck, and R. R. Reeves, *Ultraviolet absorption coefficients of CO_2, CO, O_2, H_2O, N_2O, NH_3, NO, SO_2, and CH_4 between 1850 and 4000 a,* Journal of Geophysical Research **68**, 6431 (1963).

[60] J. A. Davidson, C. A. Cantrell, A. H. McDaniel, R. E. Shetter, S. Madronich, and J. G. Calvert, *Visible-ultraviolet absorption cross sections for NO_2 as a function of temperature,* Journal of Geophysical Research: Atmospheres **93**, 7105 (1988).

[61] R. Atkinson, D. L. Baulch, R. A. Cox, J. N. Crowley, R. F. Hampson, R. G. Hynes, M. E. Jenkin, M. J. Rossi, and J. Troe, *Evaluated kinetic and photochemical data for atmospheric chemistry: Volume i - gas phase reactions of O_x, HO_x, NO_x and SO_x species,* Atmospheric Chemistry and Physics **4**, 1461 (2004).

[62] J. Mellqvist and A. Rosén, *DOAS for flue gas monitoring—II. Deviations from the Beer-Lambert law for the U.V./visible absorption spectra of NO, NO_2, SO_2 and NH_3,* Journal of Quantitative Spectroscopy and Radiative Transfer **56**, 209 (1996).

[63] S. Ahmed and V. Kumar, *Quantitative photoabsorption and flourescence spectroscopy of SO_2 at 188–231 and 278.7–320 nm,* Journal of Quantitative Spectroscopy and Radiative Transfer **47**, 359 (1992).

[64] K. Bogumil, J. Orphal, T. Homann, S. Voigt, P. Spietz, O. Fleischmann, A. Vogel, M. Hartmann, H. Kromminga, H. Bovensmann, J. Frerick, and J. Burrows, *Measurements of molecular absorption spectra with the SCIAMACHY pre-flight model: instrument characterization and reference data for atmospheric remote-sensing in the 230–2380 nm region,* Journal of Photochemistry and Photobiology A: Chemistry **157**, 167 (2003), atmospheric Photochemistry.

[65] R. Rubio, J. Santander, J. Fonollosa, L. Fonseca, I. Grácia, C. Cané, M. Moreno, and S. Marco, *Exploration of the metrological performance of a gas detector based on an array of unspecific infrared filters,* Sensors and Actuators B: Chemical **116**, 183 (2006).

[66] A. Emadi, H. Wu, G. de Graaf, and R. Wolffenbuttel, *Design and implementation of a sub-nm resolution microspectrometer based on a linear-variable optical filter,* Opt. Express **20**, 489 (2012).

[67] R. Wolffenbuttel, *State-of-the-art in integrated optical microspectrometers,* Instrumentation and Measurement, IEEE Transactions on **53**, 197 (2004).

[68] N. P. Ayerden, U. Aygun, S. T. S. Holmstrom, S. Olcer, B. Can, J.-L. Stehle, and H. Urey, *High-speed broadband FTIR system using MEMS,* Appl. Opt. **53**, 7267 (2014).

[69] H. Kumar, N. Nisam, A. Kulkarni, V. Dhingra, and K. K. Singh, *Lamellar grating interferometer ftir spectroscopy and its applications: A review,* in *2015 IEEE 15th International Conference on Nanotechnology* (2015) pp. 1107–1110.

[70] S. Grabarnik, R. Wolffenbuttel, A. Emadi, M. Loktev, E. Sokolova, and G. Vdovin, *Planar double-grating microspectrometer,* Opt. Express **15**, 3581 (2007).

[71] S. Grabarnik, A. Emadi, E. Sokolova, G. Vdovin, and R. F. Wolffenbuttel, *Optimal implementation of a microspectrometer based on a single flat diffraction grating,* Appl. Opt. **47**, 2082 (2008).

[72] S. Grabarnik, A. Emadi, H. Wu, G. de Graaf, and R. F. Wolffenbuttel, *High-resolution microspectrometer with an aberration-correcting planar grating,* Appl. Opt. **47**, 6442 (2008).

[73] K. Aratani, P. French, P. Sarro, D. Poenar, R. Wolffenbuttel, and S. Middelhoek, *Surface micromachined tuneable interferometer array,* Sensors and Actuators A: Physical **43**, 17 (1994).

[74] J. Correia, M. Bartek, and R. Wolffenbuttel, *Bulk-micromachined tunable Fabry–Perot microinterferometer for the visible spectral range,* Sensors and Actuators A: Physical **76**, 191 (1999).

[75] J. Correia, G. de Graaf, S. Kong, M. Bartek, and R. Wolffenbuttel, *Single-chip CMOS optical microspectrometer,* Sensors and Actuators A: Physical **82**, 191 (2000).

[76] A. Emadi, *Linear-variable optical filters for microspectrometer application*, Ph.D. thesis, Delft University of Technology, (TU Delft), Delft, The Netherlands (2010).

[77] A. Emadi, H. Wu, S. Grabarnik, G. de Graaf, and R. F. Wolffenbuttel, *Vertically tapered layers for optical applications fabricated using resist reflow,* Journal of Micromechanics and Microengineering **19**, 074014 (2009).

[78] S. Alexandrov, G. A. Gavrilov, A. Kapralov, S. A. Karandashev, B. A. Matveev, G. Y. Sotnikova, and N. M. Stus, *Portable optoelectronic gas sensors operating in the mid-ir spectral range (λ=3 5 μm),* in *Second International Conference on Lasers for Measurement and Information Transfer* (International Society for Optics and Photonics, 2002) pp. 188–194.

[79] H. Hirayama, S. Fujikawa, N. Noguchi, J. Norimatsu, T. Takano, K. Tsubaki, and N. Kamata, *222–282 nm AlGaN and InAlGaN-based deep-UV LEDs fabricated on high-quality AlN on sapphire,* physica status solidi (a) **206**, 1176 (2009).

[80] Y. Taniyasu and M. Kasu, *Aluminum nitride deep-ultraviolet light-emitting p–n junction diodes,* Diamond and Related Materials **17**, 1273 (2008), proceedings of Diamond 2007, the 18th European Conference on Diamond, Diamond-Like Materials, Carbon Nanotubes, Nitrides and Silicon CarbideDiamond 2006.

[81] T. Fukuchi and T. Shiina, *Development of multireflection absorption spectroscopy device using ultraviolet LEDs,* Electronics and Communications in Japan **95**, 62 (2012).

[82] G. de Graaf, F. Bakker, and R. Wolffenbuttel, *Sensor platform for gas composition measurement,* Procedia Engineering **25**, 1157 (2011), eurosensorsXXV.

2

Optical Design

2

2.1. Introduction: Thin-film Optical Filters

Optical filters are implemented in a wide range of optical MEMS devices [1]. Micro-spectrometers, in particular, use optical filters to *'disperse'* a (semi) white spectrum of light into a sequence of wavelengths [2]. Interference-based optical filters (dichroic filters) are the main filter type to be commonly used in optical MEMS [3]. The interference-based filters are wavelength sensitive elements that transmit, reflect, or block the incident light based on its wavelength or frequency. The design of such interference-based filters is discussed in this chapter.

Interference-based optical filters are generally multilayers of dielectric thin-films, where the complex interference pattern between the interfaces characterizes the spectral response of the structure. Analysis of the interference-based optical filters requires an understanding of the electromagnetic (EM) wave theory. This chapter briefly introduces the relevant basics of the EM theory in dielectric mediums. The optical properties of the materials is an important parameter for a proper optical design. Therefore, in spectral ellipsometry method is introduced as a technique for measuring the optical properties of materials. Afterwards, a few common filter designs, namely anti-reflectance filters, Bragg reflectors, and Fabry-Perot filters are introduced. The equations governing the reflectance and transmittance of these structures are presented. In the subsequent sections, the necessity of an airgap design for the ultra-violet and visible designs in terms of optical performance are discussed. Finally, a generic approach to the optical design of airgap filters intended for the ultra-violet to visible spectrum is presented.

2.2. Electromagnetic wave propagation in dielectrics medium

For studying the interference-based optical filters, the light should be considered as a harmonic wave (i.e. waves with a definite temporal frequency). The geometrical (ray) optics, which is often used to study the propagation of light *rays* in optical devices such as lens systems, cannot properly describe the wave nature of the light. Therefore, electromagnetic wave theory (physical optics) has to be applied to study the propagation of light in different dielectrics and interfaces.

The electromagnetic wave theory treats the light as an electromagnetic wave governed by a set of four equations that is known as the *Maxwell equations* [4]. Solving the Maxwell equations, considering the boundary conditions, provides a solution to the interaction of light with the medium. The interference-based filters are in general piecewise-homogeneous dielectric mediums, which means that the optical properties are constant and homogeneous (but different) in each of the layers. Dielectrics are in general isotropic, non-conductive, and non-magnetic ($\mu = \mu_0$) materials. As an electric field $\mathbf{E}$[1] propagate through a dielectric material, composed of nuclei and their bounded electrons, a dipole moment $\mathbf{P}$ proportional to the electric field is induced ($\mathbf{P} = (\epsilon - \epsilon_0)\mathbf{E}$) [5–7], where ϵ is the permittivity of the medium, and ϵ_0 is the vacuum permittivity.

[1] In this thesis the boldface notation is used to represent vectors

Solving the Maxwell equations for a homogeneous medium results in an electric wave function in the form of Helmholtz equation

$$\nabla^2\mathbf{E} - \epsilon\mu\frac{\partial^2\mathbf{E}}{\partial t^2} = 0. \tag{2.1}$$

Here we consider a harmonic plane wave propagating along the z-axis as a typical solution to the Helmholtz equation.

$$\mathbf{E}_{\mathbf{r},t} = \mathbf{E}_0 e^{i(kz-\omega t+\phi)} \tag{2.2}$$

In this wave equation (2.2), ω is the temporal frequency (or *angular frequency*) and k is the spatial frequency (or *wavenumber*) of the electromagnetic wave. ϕ is the initial phase of the wave at the reference point ($\mathbf{r} = \mathbf{0}$ and $t = 0$). Substitution of the plane wave equation into the Helmholtz equation yields the relation between the angular frequency and the spatial frequency of the wave.

$$-k^2\mathbf{E}_0 e^{i(kz-\omega t+\phi)} + \epsilon\mu\omega^2\mathbf{E}_0 e^{i(kz-\omega t+\phi)} = 0 \tag{2.3a}$$

$$k = \omega\sqrt{\epsilon\mu_0} \tag{2.3b}$$

$$= \frac{2\pi c}{\lambda}\sqrt{\epsilon\mu_0} \tag{2.3c}$$

$$= \frac{2\pi}{\lambda}\tilde{n} \tag{2.3d}$$

Here $\tilde{n} \equiv \sqrt{\epsilon_r}$ is defined as the *refractive index* of the medium which characterizes the response of the material to the interaction of light with the material (the polarization of the atoms). As it will be shown in this chapter, an interference-based optical filter can be comprehensively described by specifying only the values of refractive indexes (together with the thicknesses) of the layers comprising the filter. The refractive index in its general form is a complex quantity that can be represented by its real and imaginary parts:

$$\tilde{n} = n + i\kappa, \tag{2.4}$$

where n is the (real) refractive index and the imaginary part, κ, is the extinction coefficient of the material. By substitution of the expression for the complex refractive index (Equation 2.4) into the wave equation (2.2) results in an electric field with an exponentially decaying component.

$$\begin{aligned}\mathbf{E}_{\mathbf{r},t} &= \mathbf{E}_0\, e^{i\left(kz-\omega t+\phi\right)} \\ &= \mathbf{E}_0\, e^{i\left(2\pi(n+i\kappa)z/\lambda-\omega t+\phi\right)} \quad = \mathbf{E}_0\, e^{-2\pi\kappa z/\lambda} e^{i\left(2\pi nz/\lambda-\omega t+\phi\right)}.\end{aligned} \tag{2.5}$$

The energy of an electromagnetic wave, or its *irradiance*, I $[W/m^2]$ is the time average of the square of the wave amplitude.

$$I = \epsilon c \langle \mathbf{E} \cdot \mathbf{E} \rangle \tag{2.6}$$

Consequently, the propagating electromagnetic wave exponentially loses energy in the medium with a decay constant of α.

$$I = \epsilon c \; e^{-4\pi\kappa z/\lambda} \; |\mathbf{E}_0|^2 = \epsilon c \; e^{-\alpha z} \; |\mathbf{E}_0|^2$$
$$\text{where } \alpha = \frac{2\kappa\omega}{c} = \frac{4\pi\kappa}{\lambda} \tag{2.7}$$

2.3. Transmission and reflection at an interface

The wave equation represented in the previous section describes the propagation of a planar electromagnetic wave in a homogeneous dielectric medium. In most cases, however, the light propagates through dielectrics of different refractive indexes. The interaction of the light with the dielectric medium at the interface results in partial reflection and transmission of the incident wave.

Consider the case, shown in Figure 2.1, in which a beam of light (electromagnetic wave) propagating in a medium of refractive index of n_1 and a wavenumber of k_i radiated on a dielectric interface of a medium of n_2 , and at an angle of θ_i respect to the interface normal. The solution to the Maxwell equations at the n_1, n_2 boundary results in a set of equations known as *Fresnel Equations* [4]. Fresnel equations describe the reflected and transmitted energy of a light impinging on a dielectric boundary. The seemingly simple but profound results of the Fresnel equations are as follows:

- The frequency of the reflected and transmitted wave at a boundary remains constant. $\omega_i = \omega_t = \omega_r$
- The reflected beam travels with the same angle respect to the normal. **Law of reflection (Snell's law):** $\theta_r = \theta_i$
- The ratio of the $\sin$-s of the incident light to the transmitted light angles is proportional to the ratio of the refractive indexes of the two mediums. **Law of refraction:** $n_1 \sin\theta_r = n_2 \sin\theta_t$

TE and TM waves

The reflection and transmission coefficient of the incident wave are defined as the ratio of the reflected or transmitted electric field to the incident electric field, and, in general, depends on the *polarization* (or the direction of the electric field) of the wave. The *Transverse electric* (TE) and *Transverse magnetic* (TM) polarization states are commonly defined and used in planar waves. TE (or S-polarization) waves are the electromagnetic waves that have electric fields that are perpendicular to the plane of incidence and parallel to the boundary (interface) plane. TM (or P-polarization) waves have their electric fields parallels to the plane of incidence. The reflection coefficients can be derived from the Fresnel's equations:

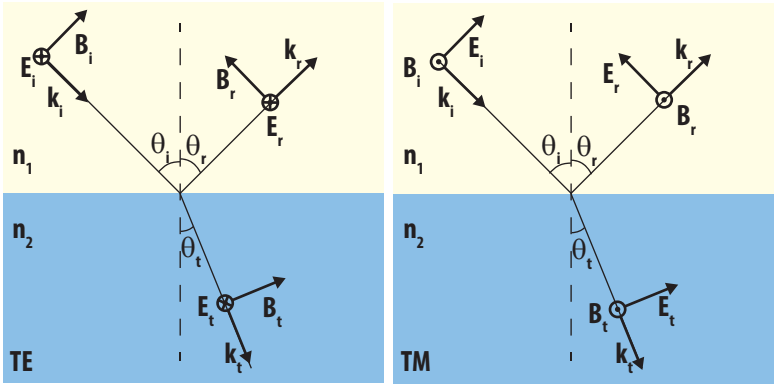

Figure 2.1: The reflection and refraction of TE and TM polarizations at an interface.

$$r \equiv \frac{E_r}{E} \quad \text{and} \quad t \equiv \frac{E_t}{E} \tag{2.8}$$

$$r_{TE} = \frac{\cos\theta_i - \sqrt{(n_2/n_1)^2 - \sin^2\theta_i}}{\cos\theta_i + \sqrt{(n_2/n_1)^2 - \sin^2\theta_i}} \tag{2.9a}$$

$$r_{TM} = \frac{-(n_2/n_1)^2\cos\theta_i + \sqrt{(n_2/n_1)^2 - \sin^2\theta_i}}{(n_2/n_1)^2\cos\theta_i + \sqrt{(n_2/n_1)^2 - \sin^2\theta_i}} \tag{2.9b}$$

The fraction of the energy that is reflected or transmitted at the interface (reflectance and transmittance) is equal to the ratio of the squares of the electric field amplitudes. Furthermore, if the absorption is negligible, the sum of the reflectance and transmittance is unity $R + T = 1$.

$$R = |r|^2 \quad \text{and} \quad T = 1 - |r|^2 \tag{2.10}$$

2.4. Interference-based optical filters

When two electromagnetic waves of $\mathbf{E}_1$ and $\mathbf{E}_2$ of the same frequency collide, the waves *interfere* [4]. The energy of the wave becomes a function of the phase difference between the two waves:

$$\begin{aligned} \mathbf{E}_t &= \mathbf{E}_1 + \mathbf{E}_2 \\ I &= \epsilon c\langle \mathbf{E}_t \cdot \mathbf{E}_t \rangle \\ I &= I_1 + I_2 + I_{12} = \epsilon c\langle \mathbf{E}_1 \cdot \mathbf{E}_1 + \mathbf{E}_2 \cdot \mathbf{E}_2 + 2\,\mathbf{E}_1 \cdot \mathbf{E}_2 \rangle \end{aligned} \tag{2.11}$$

$$I_{12} = \epsilon c \langle 2\ \mathbf{E}_1 \cdot \mathbf{E}_2 \rangle \tag{2.12}$$

The first two terms in the Equation 2.11 correspond to the irradiance of each wave. The third term, however, depends on the interaction (or *interference*) of the two waves (Equation 2.12) and represents the wave nature of light. As the electric fields are complex quantities, the interference term depends on the phase difference between the two waves. The time average of the fast time-oscillating functions ($e^{-2i\omega t}$) cancels out and the spatial term remains. Therefore, for a planar wave of Equation 2.2 the interference term becomes:

$$\begin{aligned} I_{12} &= 2\epsilon c \mathbf{E}_1 \cdot \mathbf{E}_2 \langle \cos\delta \rangle \\ \delta &= (\mathbf{k}_1 \cdot \mathbf{r}_1 + \phi_1) - (\mathbf{k}_2 \cdot \mathbf{r}_2 + \phi_2) \end{aligned} \tag{2.13}$$

The phase difference is a function of the optical path length difference of the waves interacting with each other. For two waves of equal intensities, if $\cos\delta = +1$ the fields constructively interfere and add up, and when $\cos\delta = -1$ the fields destructively interfere.

In the case of multiple dielectric layers, the incident light undergoes a series of partial reflections and transmission at each boundary. If the thicknesses of the dielectric layers are in the order of the wavelength, the cascading rays of reflected lights at each boundary strongly interfere. The interference of the waves (as shown in Equation 2.13 for two waves) depends on the path-length difference and hence the layer thicknesses, refractive index, and wavelength of the wave. Therefore, the intensity of the reflected or transmitted light become a function of the wavelength of the incident light. This strong spectral dependence on the dimension and optical properties of the structure is the basis of the thin-film interference-based (dichroic) optical filters. Some important cases are introduced in this section, and their spectral response is studied. As these structures are the building blocks of most elaborate optical filters used in many MEMS devices, a detailed study of these optical elements is required.

2.4.1. Single thin film layer: Quarter-wave optical layer

The simplest optical filter can be made of a thin dielectric layer deposited on a substrate. The schematic of such a filter is shown in Figure 2.2. The phase difference between the multiple reflected waves in this configuration is proportional the thickness of the film and cos of the incident angle respect to the surface normal. This structure resembles the rainbow-like patterns appearing in a thin oil layer on the surface of the polluted water.

A phase difference due to a single passing through a thin film of thickness t and refractive index of n_f is equal to:

$$\delta_t = \frac{2\pi}{\lambda_0} n_f t_f \cos\theta_t.$$

The total phase difference of light after reflection from the lower interface and reappearance at the upper interface is equal to $\delta = 2\delta_t + \delta_r$ in which the δ_r is the

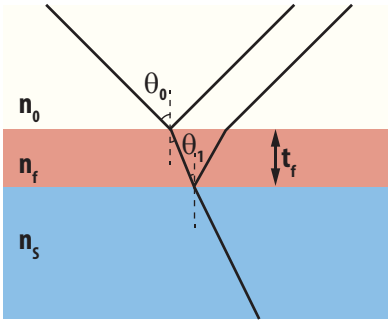

Figure 2.2: Reflections from a single layer thin-film.

phase change in the wave due to the reflection at an interface between two media (n_f to n_s). At normal incidence ($\theta_0 = 0$) the phase difference at single travel is $\delta_t = 2\pi n_f t/\lambda_0$. Furthermore, it can be shown that at normal incidence $\delta_r = \pi$ for $n_f < n_s$, and $\delta_r = 0$ for $n_f > n_s$. Figure 2.3 shows the typical reflection at normal incidence angle as a function of the layer thickness, t_f (or normalized optical thickness, $n_f t_f/\lambda_0$), and for different refractive index combinations.

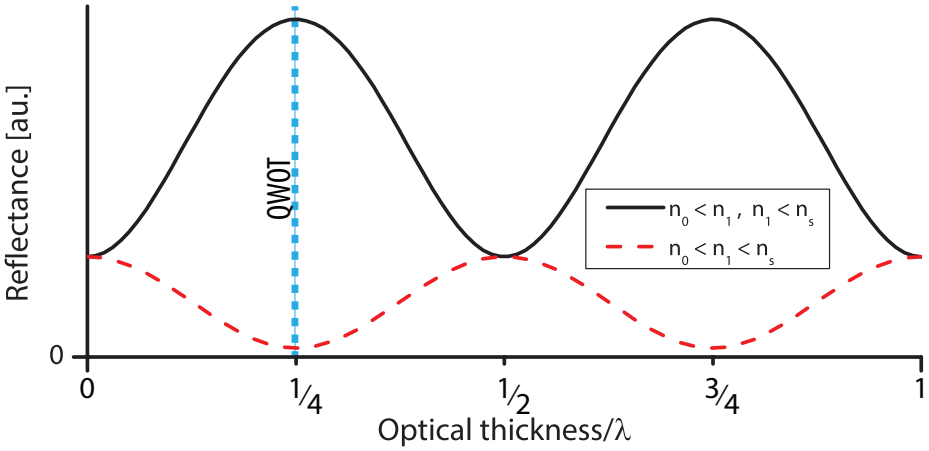

Figure 2.3: Variation of the reflectance of a thin-film as a function of normalized optical thickness.

The especially important case is when the thickness of the film is equal to a quarter of the wavelength in the medium ($t_f = \lambda/4n$, as marked by a dashed line in Figure 2.3). The phase difference at a single passage through this layer, which is commonly known as a quarter-wave optical-thick (QWOT) layer, at normal incidence ($\theta_t = 0$) is $\delta_t = \pi/2$. Therefore, if the $n_0 < n_f < n_s$ then the phase difference between the waves reflected from the top interface and the bottom interface is:

$$\delta = \delta_{r1} - \delta_{r2} = (2\delta_t + \pi) - (\pi) = \pi$$

Therefore, the two waves cancel out (destructive interference) and the thin-film

behaves as an anti-reflectance filter (at λ_0). It is interesting to note that for the particular case of $n_1 = \sqrt{n_0 n_s}$ the QWOT layer becomes a perfectly anti-reflecting layer (at λ_0). On the other hand, if $n_0 < n_1$ and $n_1 > n_s$ the phase difference between the reflected waves vanishes, resulting in a constructive interference in the partially reflected waves.

$$\delta = \delta_{r1} - \delta_{r2} = 2\delta_t - \pi = 0$$

2.4.2. Fabry-Perot optical resonator

Fabry-Perot interferometers are the basis of the most high-resolution filters used in the optical MEMS devices. In the general configuration, a Fabry-Perot interferometer (FPI) consists of two parallel partial reflectors that are separated by a cavity, as shown in Figure 2.4.

An incident wave propagating through the FPI undergoes multiple partial reflections at each mirror. The interference between the multiple reflected and transmitted waves results in a strong correlation between the length of the cavity and the wavelength (or frequency) of the wave transmitted through the filter. The electric field of the wave transmitted through the interferometer can be calculated as a function of the mirror reflection and transmission coefficients ($r,\ t$), and also the distance between the mirrors [4].

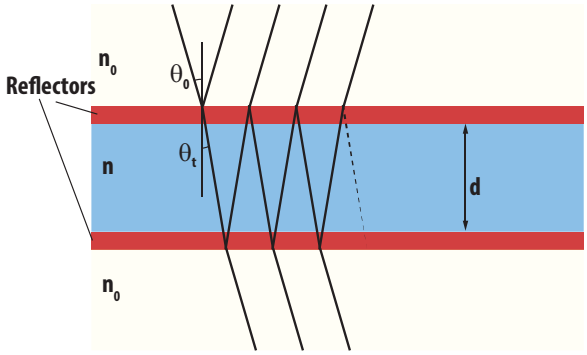

Figure 2.4: Schematics of a Fabry-Perot interferometer.

$$E_T = \frac{t^2 e^{-i\delta/2}}{1 - r^2 e^{-i\delta}} E_I \tag{2.14}$$

$$\delta = 2kd = 4\pi nd/\lambda \tag{2.15}$$

Here $\delta =$ is the phase difference due to a round-trip between the reflectors. Therefore, the transmittance through the FPI becomes in the form of an Airy function (Equation 2.16).

$$T = \frac{I_T}{I_I} = \left|\frac{E_T}{E_I}\right|^2 = \frac{T^2}{(1-R)^2}\left[1 + F\sin^2(\delta/2)\right]^{-1} \tag{2.16}$$

where $R + T + A = 1$. Furthermore, in general case of a negligible absorption loss in the FPI the equation becomes

$$T = \left[1 + F \sin^2(\delta/2)\right]^{-1} \tag{2.17}$$

F in this equation (Equation 2.17) is called the *coefficient of finesse* and highly depends on the reflectance of the mirrors.

$$F \equiv \frac{4r^2}{\left(1 - r^2\right)^2} = \frac{4R}{(1-R)^2} \tag{2.18}$$

According to the Equation 2.17, for a $\delta = 2m\pi$ (in which m is an integer) the transmission is $T = 1$ (without considering the absorption losses). In terms of Equation 2.15 a maximum transmission condition can be obtained.

$$\delta = 2kd = \frac{4\pi nd}{\lambda} = 2m\pi \tag{2.19}$$

Hence, the transmitted wavelength is depending on the length of the cavity and the transmission order, m. Therefore, the Fabry-Perot structure becomes transparent for a sequence of equally-spaced frequencies.

$$\lambda_m = \frac{2nd}{m}, \text{ and } \nu_m = \frac{cm}{2nd} \tag{2.20}$$

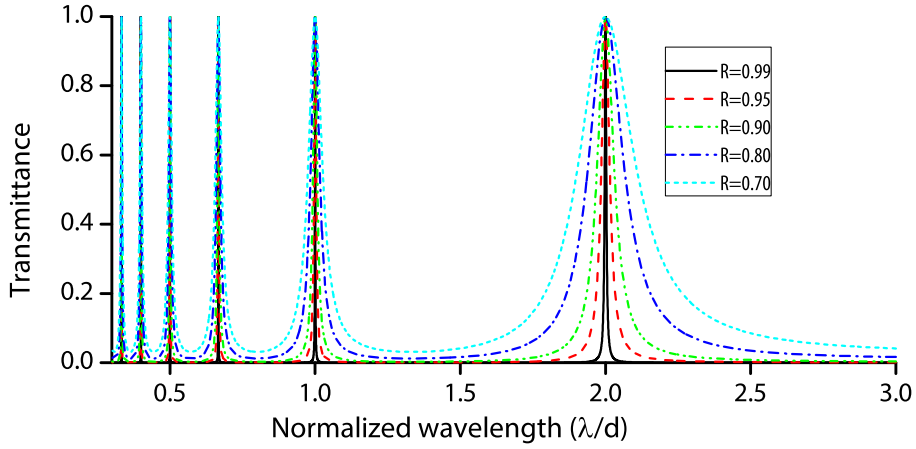

Figure 2.5: Transmittance of a typical Fabry-Perot resonator for different mirror reflectance and over different wavelengths.

Figure 2.5 shows the typical transmittance of a Fabry-Perot interferometer. Two important parameters of a Fabry-Perot filter are FWHM and free spectral range

(FSR). FWHM represents the spectral full-width of a transmitted peak at its half-maximum intensity. The phase difference for which the transmitted intensity drops to its half maximum is called half-width half-maximum δ_{HM}. The transmittance of a wave with a phase difference of δ_{HM} away from the peak transmission at order m can be obtained (using $\sin(\delta_m \pm \delta_{HM}) = \pm\sin(\delta_{HM})$).

$$\delta_{FWHM} = 2\delta_{HM} = 4\arcsin\frac{1}{\sqrt{F}}. \tag{2.21}$$

Furthermore, the phase difference between two adjacent transmission peaks or the *Free spectral range (FSR)* is also $\delta_{FSR} = \delta_{m+1} - \delta_m = 2\pi$. The ratio between the FSR and FWHM phase differences is called the *Finesse* ($\mathcal{F}$) (not to be confused with the coefficient of finesse (F)):

$$\mathcal{F} = \frac{\delta_{FSR}}{\delta_{FWHM}} = \frac{\pi}{2\arcsin\left(1/\sqrt{F}\right)} \tag{2.22}$$

The spectral distance between the adjacent transmission peaks in terms of wavelength λ_{FSR} can be calculated using Equation 2.19. It is interesting to note that the λ_{FSR} is not equal for the peaks at low- and high-wavelength sides of the interested peak. The minimum FSR is the distance between the peak and its lower wavelength neighboring peak and is equal to

$$\lambda_{FSR} = \lambda_m - \lambda_{m+1} = \frac{2nd}{m(m+1)} = \frac{\lambda_m}{m+1}. \tag{2.23}$$

The FWHM of the m-th order is inversely proportional to the finesse of the Fabry-Perot.

$$\lambda_{FWHM} \approx \frac{m+1}{m}\frac{\lambda_{FSR}}{\mathcal{F}} = \frac{\lambda_m}{m\mathcal{F}} \tag{2.24}$$

The finesse is, therefore, an important figure of merit in Fabry-Perot-based optical filters. Even though, the finesse of an FPI system can ideally reach very high values by increasing the reflection coefficient (r), in practice various non-idealities in the system strongly reduce the effective finesse. A detailed investigation of these effects is presented in Chapter 4.

2.4.3. Distributed Bragg reflectors (DBR)

Consider a structure composed of N alternating layers of high and low refractive index ($n_H - n_L$) each of a QWOT thickness. This structure represents a highly practical configuration composed of a substrate with a layer stack deposited which is referred to as **substrate/(L-H)^N/medium** (shown in Figure 2.6a.). The series of the QWOT double-layers is basically a series of QWOT layers with $n_0 < n_1$, $n_1 > n_s$ (see Section 2.4). Therefore, each double-layer increases the reflectance due to the constructive interference between the layers. This structure is known as a *distributed Bragg reflector*, as it closely resembles the Bragg's law in crystals, which was first proposed by William Lawrence Bragg and William Henry Bragg in

1913 [5]. However, it is interesting to note that even though the Bragg condition is only satisfied at a single wavelength (λ), the reflectance is high over an extended spectral band around the Bragg frequencies, due to the interference of multiple reflections of the input wave between the interfaces.

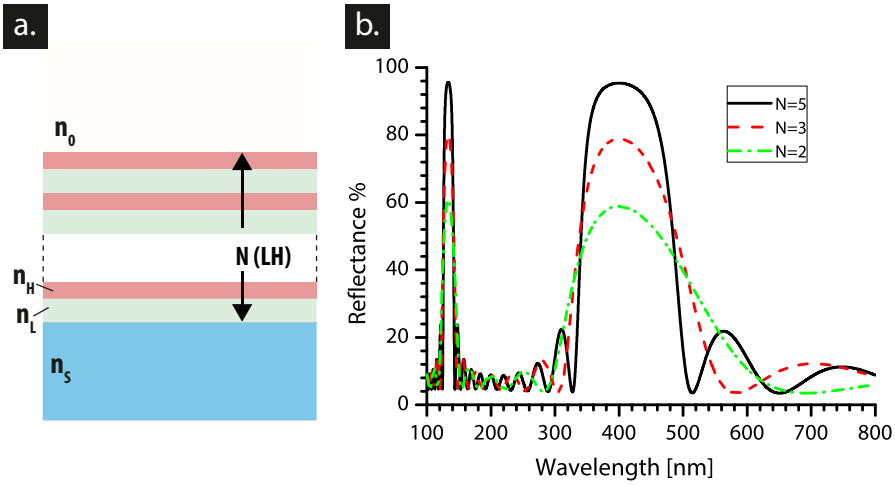

Figure 2.6: a. Schematics of a distributed Bragg reflector. b. Spectral reflectance of a high-low stack for a different number of double-layers (N). Here $n_s = 1.47(\text{Fused silica at } 400\ nm)$, $n_L = 1$, and, $n_H = 1.5$.

The reflectance of a DBR structure can be analytically calculated [8]. At normal incidence the reflection coefficient and bandwidth is given by the Equations 2.25 [9]. The reflectance of DBRs with a different number of double-layers are shown in Figure 2.6b. Furthermore, since the sum of the reflectance and transmittance in non-absorbing layers is unity ($T = 1 - R$), Bragg reflectors can be designed as high- or low-pass filters.

$$r = \frac{n_0\, n_H^{2N} - n_s\, n_L^{2N}}{n_0\, n_H^{2N} + n_s\, n_L^{2N}} \tag{2.25a}$$

$$\frac{\Delta\lambda}{\lambda_0} = \frac{4}{\pi} \arcsin\left(\frac{n_H - n_L}{n_H - n_S}\right) \tag{2.25b}$$

2.4.4. Thin-film dielectric single-cavity filters

A dielectric single cavity filter is schematically shown in Figure 2.7. This structure is basically a Fabry-Perot filter with two DBRs as its reflectors. Equation 2.17 for the transmission of the filter is still applicable. However, the reflectance, R, is the equal to the reflectance of the DBRs and is evaluated by Equation 2.25.

Several different configurations with the high or low-index cavity, and having a different number of high and low-index layers in each DBR can be used. Although

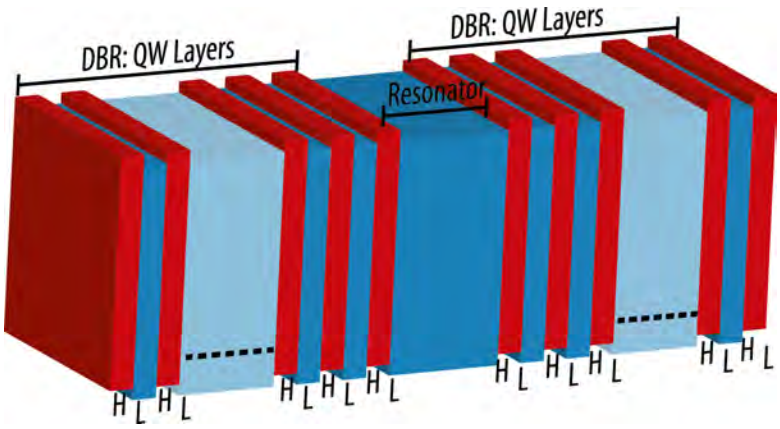

Figure 2.7: Schematic of a single-cavity optical filter. The filter is composed of two DBRs each with N quarter wave (QW) layers separated by half wave (HW) layer cavity.

the response of such filter in simple cases can be analytically evaluated, an accurate analysis, in general, is rather unwieldy. However, methods such as transfer matrix can be used. In this dissertation, the transfer matrix method using a commercially available optical thin film software (TFCalc) has been applied for the analysis and optimization of the filters. Since the dielectric DBRs have a limited bandwidth, transmission sidebands appear at the sides of the main peak. This sideband transmission in most cases can be suppressed by adding an absorptive filter or a pass-band (long or short) filter [10].

2.5. Ellipsometry

Measuring the refractive index of the deposited layers is highly important for a proper optical design. Methods such as reflectometry and ellipsometry are commonly used to measure the optical properties of optical thin films. Ellipsometry is a sensitive technique based on the measuring the change in the polarization state of the light as reflected from the sample surface. The two important parameter in the ellipsometry are defined based on the ratio between the p-polarized and s-polarized reflection coefficient (see section 2.3)

$$\rho = \frac{r_p}{r_s} = \tan(\Psi)e^{i\Delta} \tag{2.26}$$

As the ratio of the reflection coefficients is complex, ellipsometry measures both the change in the intensity of the reflected polarization (Ψ) and the phase change information (Δ). Furthermore, as ellipsometry is measuring the relative phase change in the polarized light, it does not depend on the absolute intensity of the beam. Therefore, ellipsometry provides a higher sensitivity as compared to the methods such as reflectometry that mainly rely on the intensity measurement. In general, ellipsometry can be applied to measure parameters such as the optical constant,

thickness, doping concentration, crystal orientation, and the surface and interfacial roughness of the samples.

2.5.1. Variable angle spectroscopic ellipsometry

Performing the ellipsometry over a spectrum and at multiple angles (known as variable angle spectroscopic ellipsometry-VASE) is capable of measuring the optical properties and thickness with high accuracy. Furthermore, ellipsometry measurement over a spectrum provides the possibility of modeling the material based on the available dispersion models. For a single layer, the complex refractive index of the layer can be related to the ellipsometry parameters and the angle (θ) in which the measurement is performed.

$$\tilde{n}^2 = (n + i\kappa)^2 = \sin^2\theta\left[1 + \tan^2\theta\left(\frac{1-\rho}{1+\rho}\right)^2\right] \tag{2.27}$$

However, measurements of structures with higher complexity (e.g. thin film multilayers) the analytical solution is not usually available. A regressive analysis as shown in Figure 2.8 is performed to obtain various parameters. Initially, measuring the sample provides series of ellipsometry parameters (Ψ and Δ) for each wavelength. An optical model based on the 'expected' layer thicknesses and refractive index dispersion in the films is defined. A set of ellipsometry variables are then generated based on the model (Ψ_{Gen} and Δ_{Gen}) and compared with the measured values. An optimization algorithm is then used to fine-tune different parameters of the model while minimizing an error function (mean square error -MSE). The model can be subsequently changed until a small enough error is obtained.

In this thesis, ellipsometry (M2000, JA Woollam Co.- Figure 2.9) has been widely applied to measure the optical properties of different deposited materials. The resulted refractive index data were used in the optical simulation software for designing the optical filters. Ellipsometry was also used for measuring the thickness of the deposited layers and calibrating the deposition rates. Furthermore, the VASE measurement technique provides the possibility of mapping the thickness over the surface of the wafer. Thickness mapping analysis was routinely done for measuring deposition uniformity. VASE measurements are typically very precise that is if a unique model is used, the resulted fit of different parameters is precisely repeatable. The accuracy of the measurement is difficult to determine as the variable must be measured and compared in a more accurate and precise method.

2.5.2. Dispersion models

The refractive index of materials typically varies by the wavelength. This variation is called *dispersion*. Furthermore, according to the Kramers-Kroning relations [5], the absorption coefficient and refractive index in absorbing materials are coupled. Various dispersion models are used in VASE analysis to model the optical properties of the layers. Depending on the material types, different models can be used. The Cauchy and oscillator models are widely used for, respectively, dielectrics and absorbing layers such as semi-conductors. These models are hence repeatedly

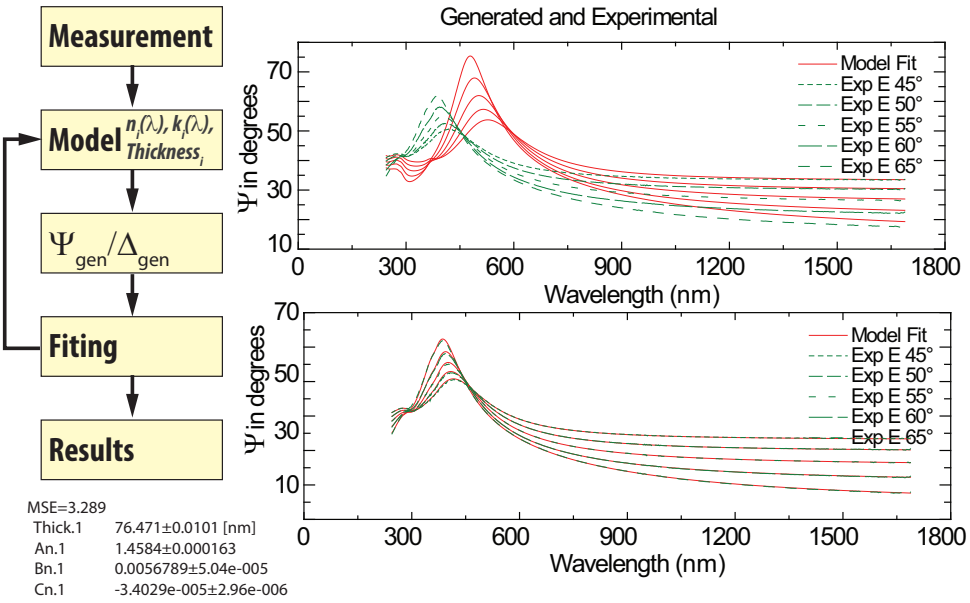

Figure 2.8: The basic procedure used in ellipsometry measurement to determine material properties.

used in this thesis for measuring the optical properties and the thickness of the deposited layers.

Cauchy model

The Cauchy dispersion model is typically used to describe dielectrics (and semiconductors for energy levels much smaller than their bandgap) at *normal* dispersion (the refractive index decreasing with the wavelength) [11].

$$n(\lambda) = A_n + \frac{B_n}{\lambda^2} + \frac{C_n}{\lambda^4} + \cdots \tag{2.28}$$

The Cauchy model is only used for the non-absorbing materials. To model absorbing materials, an Urbach absorption function [12] is usually used. The Urbach absorption function represents the absorption tail of a material with a band edge of γ bellow its band gap.

$$k(\lambda) = \alpha \exp\big(\beta(E - \gamma)\big) \tag{2.29}$$

the Cauchy model has been used for modeling the refractive index in the dielectric layers used in this research (SiO_2 and SiN).

Oscillator models

Oscillator models have been developed to model absorbing materials. The oscillator models generally describe the material as a cloud of (charged) particles oscillating at the interaction with light. Based on the oscillator models, the refractive index

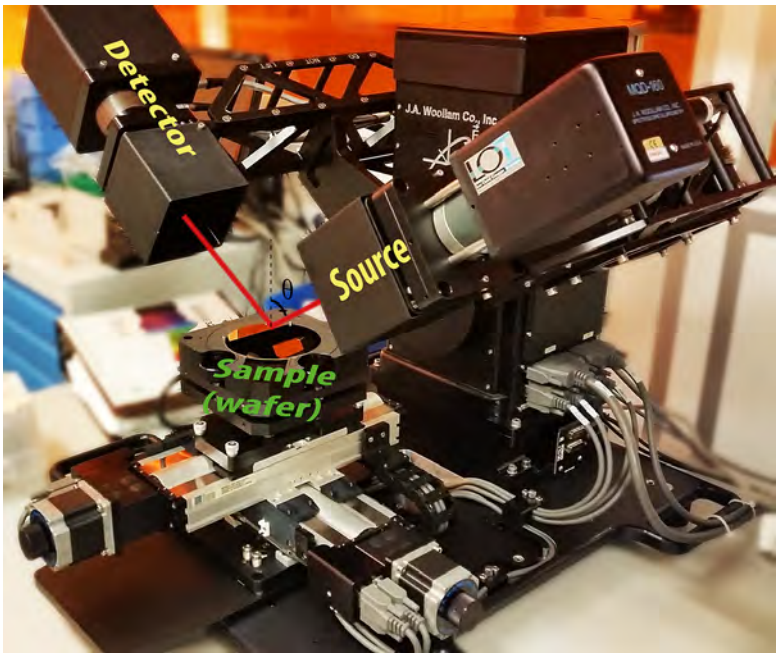

Figure 2.9: A variable angle ellipsometer (M2000, JA Woollam Co.). The light reflected by the sample surface at each measurement angle is analyzed to obtain the optical information of the sample.

and the absorption coefficient are inter-related. Hence, both of the imaginary and real parts of the refractive index can be calculated using the equations known as *Kramers-Kronig* equations [7]. Oscillator models are used for many absorbing materials, such as semiconductors (above their fundamental bandgap), metals, and conductive oxides (which cannot be appropriately modeled using the Cauchy model). Despite that the optical filters intended for the ultraviolet and visible spectrum are composed of dielectrics, due to the fabrication requirements, other layers such as polysilicon (as the sacrificial layers) layers are also used. Therefore, measuring the thickness and uniformity of these layers is highly important. An oscillator model was applied to analyze the deposited polysilicon layers.

2.6. Optical Filters for the UV-visible spectrum

As discussed in Chapter 1, DBRs and Fabry-Perot filters are widely used in optical MEMS devices, such as MEMS spectrometers and wavelength division multiplexing (WDM) systems. In particular, a Fabry-Perot interference-based (FPI-based) filter with dielectric DBRs as the reflectors, which are separated by a cavity (dielectric or air), provide a reliable optical filter. Highly reflective DBR structures can be designed in the parts of the spectrum in which the dielectrics are loss-less and have a high refractive index contrast. Tuning the cavity length provides the possibility of selecting the wavelength passing through the filter. Various configurations of the

Fabry-Perot optical filters, such as fixed-cavity, tunable cavity, and linearly variable optical filters [13, 14] have been widely investigated.

The ambition of the research presented here is to explore novel optical filter structures for use in the UV-Visible spectrum. As will be discussed in this section, the optical properties of the dielectrics play an important role in the design and performance of the filter. The following section investigates the requirements (and limitations) imposed by the specification of an optical design on the optical properties of the materials. The choice of a suitable material for the dielectric optical structure is of paramount importance. As discussed before, the (complex) refractive indexes of the dielectrics (together with the thicknesses) comprise all of the required (optical) information to predict the spectral response of any conventional optical filter. According to Equation 2.7, the optical power in the wave is reduced during propagation in a dielectric layer with non-zero extinction coefficient, κ. Furthermore, the response of a typical DBR depends on the refractive index of the high and low-index layers (Equation 2.25). Therefore, the spectral response of the resulting (FPI-based) optical filter strongly depends on the choice of the refractive indexes (Equation 2.18) and consequently on the choice of materials.

2.6.1. Refractive index contrast

Consider a DBR composed of N double-QWOT layers of a high- and low-index materials (substrate/(L-H)^N/medium). As shown in the previous section, the peak reflectance is a function of the number of pairs (N) and the refractive indexes of the materials used (n_H, n_L). Here we define *refractive index contrast*, Δ, of the high and low-index materials comprising the double layer as

$$\Delta = \frac{n_H^2 - n_L^2}{2n_H^2}. \tag{2.30}$$

In this definition, for different refractive indexes of the material in a double-layer, the refractive index contrast varies from $\Delta = 0$ (for $n_H = n_L$) up to $\Delta = 0.5$ (for $n_H >> n_L$). By replacing the refractive indexes in Equation 2.25.a with Δ the reflectance of Bragg reflectors can be expressed as:

$$\begin{aligned} r &= 1 - \frac{2\gamma(1-2\Delta)^N}{1+\gamma(1-2\Delta)^N} \\ &\approx 1 - 2\gamma(1-2\Delta)^N + 2\gamma^N(1-2\Delta)^{2N} + \cdots \quad \text{as } \Delta \to 0.5 \end{aligned} \tag{2.31}$$

Here $\gamma = n_s/n_o$ is the ratio of the refractive indexes of substrate and incident medium. Similarly, the bandwidth of the DBR (Equation 2.25) can be expressed as:

$$\frac{\Delta\lambda}{\lambda} = \frac{4}{\pi}\arcsin\frac{1-\sqrt{1-2\Delta}}{1+\sqrt{1-2\Delta}} \tag{2.32}$$

It is interesting to note that both peak reflectance (R) and bandwidth ($\Delta\lambda/\lambda$) do not depend on absolute values of refractive indexes but only on their relative contrast

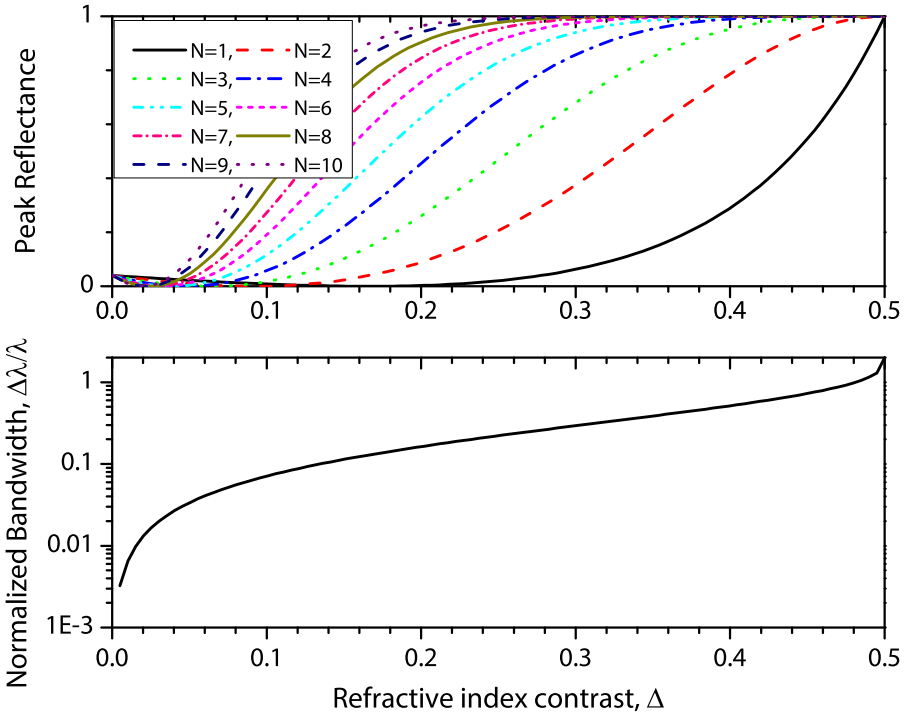

Figure 2.10: Peak reflectance and bandwidth of a distributed Bragg reflector as a function of the refractive index contrast of the high and low-index materials. ($\gamma = 1.5$)

(Δ). For small refractive index contrasts, the DBR has a bandwidth of

$$\Delta\lambda/\lambda \approx 2\Delta/\pi + 2\Delta^2/\pi + \cdots (\text{for } \Delta \ll 0.5).$$

On the other hand, when refractive index contrast approaches to 0.5, the $\arcsin$-term approaches to $\pi/2$, resulting in a (maximum) bandwidth equal to the double of the wavelength ($\Delta\lambda = 2\lambda$). However, Equation 2.32 is an approximation hence do not provide the correct result at very high refractive contrast values. Therefore, both equations (2.31 and 2.32) show that irrespective of the design, a higher refractive index contrast results in a higher peak reflectance and a wider bandwidth.

Figure 2.10 shows the variation of the peak reflectance and bandwidth of a DBR with a different number of periods (N). In this figure the substrate and the medium are considered to be SiO_2 and air, respectively, hence $\gamma = 1.5$. The structure is represented as Glass/$(L\text{-}H)^N$/air. According to the figure, the peak reflectance of a typical DBR increases significantly with refractive index contrast. The bandwidth, on the other hand, is independent of the number of periods (N) and increases slowly (almost linearly) with the refractive index contrast.

Equations 2.31 2.32 only characterize an approximation of the peak reflectance

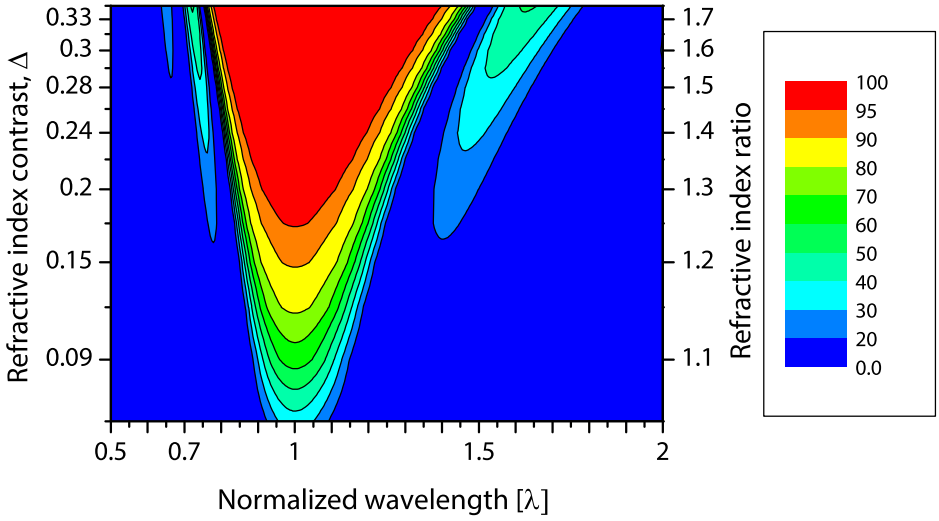

Figure 2.11: Reflectance contour plots of a 5-pair distributed Bragg reflector.

value over the specified bandwidth. Furthermore, in many applications, such as tunable Fabry-Perot filters, the spectral distribution of the reflectance is important. In this research, the exact spectral reflectance of the DBR structures is evaluated using transfer matrix method (TFCalc, Software Spectra, Inc.). Figure 2.11 shows the spectral reflection contour plot of a $N = 5$ DBR at different refractive index contrast values obtained by TFCalc. According to Figure 2.11, the reflectance peak is distributed around the center wavelength, while the distribution is higher toward the longer wavelengths. Furthermore, reflection ripples form at both sides of the central peak. The intensity of these ripples also increases with refractive index contrast. In practice, various fitting methods are used in filter designs to suppress the parasitic peaks by varying the layer thicknesses[10].

2.6.2. Absorption losses in optical filters

Another important performance-limiting factor in the optical filters is the spectral absorbance of the materials. According to Equation 2.7, when the imaginary part of the complex refractive index increases, the irradiance of the incident wave drops exponentially. Many dielectrics are absorbing in the UV or infrared and cannot be used for the optical applications. Therefore, in the design of an optical filter, the materials must be chosen such a way that they give a high refractive index contrast while minimizing the absorption. Figure 2.12 shows the refractive index and extinction coefficient of some of the commonly used dielectrics. As can be seen from Figure, most of the materials with high refractive index, have an absorption peak in the UV-blue range of the spectrum. This limits the available refractive index contrast to less than $\Delta < 0.3$. Therefore, the choice of suitable materials for use in

the UV-visible spectrum is limited.

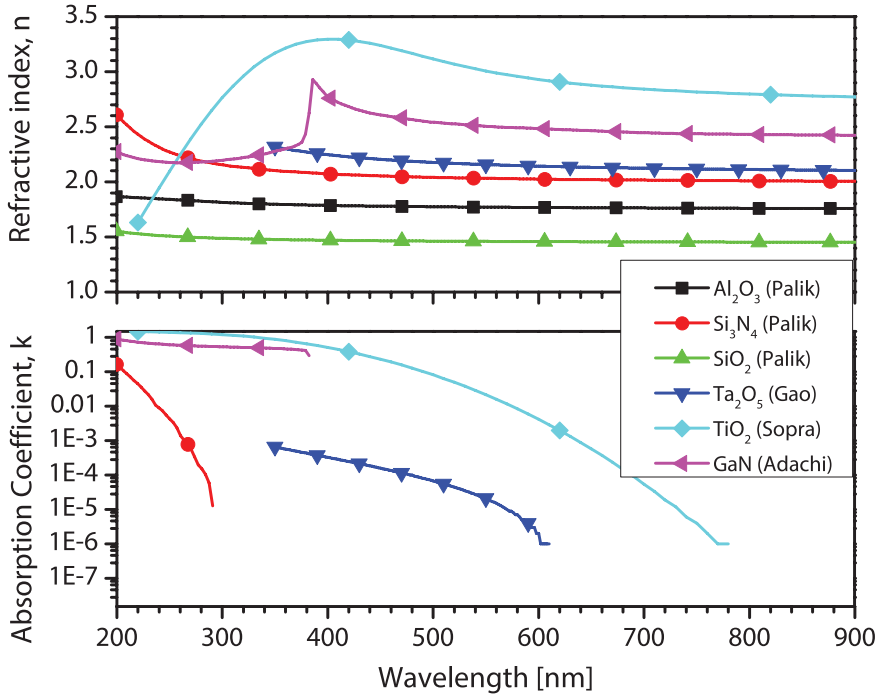

Figure 2.12: Refractive index and absorption coefficient of typical materials used for optical filters [15–19].

2.6.3. Air as an optical layer

The optical properties of the air are highly interesting from the optical design point of view. Air with a refractive index of unity ($n_{air} = 1.0002828$ at $400\ nm$ [20]) provides a very high refractive index contrast. The refractive index contrast of some typical layer combinations is shown in Figure 2.13. These refractive index contrast curves are derived using the data shown in Figure 2.12 It can be seen that the refractive contrasts of higher than $\Delta = 0.3$ can be obtained using air-dielectric double-layers. Furthermore, the negligible absorption coefficient of the air over a wide spectrum ($\kappa \approx 0$ from about $200\ nm$ and higher) satisfy the conditions of a perfect low-index material [21, 22]. Therefore, using air together with one high-index dielectric results in a superior optical performance as compared with the all-dielectric filters. The state-of-the-art of the airgap based filters was presented in the Introduction chapter (Chapter 1). Here the aim is to design an airgap-based optical filter using CMOS-compatible materials and techniques for UV-visible spectrum.

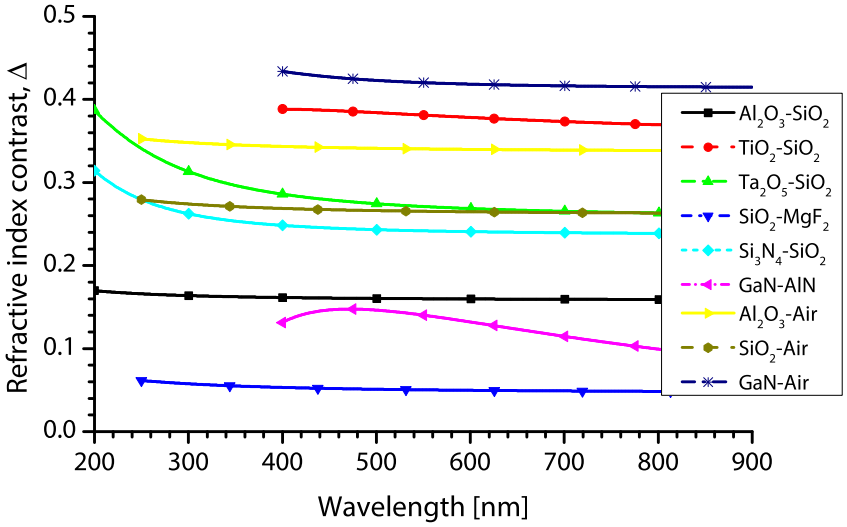

Figure 2.13: Refractive index contrast of common dielectrics. The refractive index data presented in Figure 2.12 were used to evaluate the refractive index contrast.

2.7. Airgap-based optical filter design

This section presents the design of FPI-based optical filters centered at $400\ nm$ using different layer combinations. Three material systems are investigated here: Al_2O_3, SiO_2, and air. Al_2O_3 and SiO_2 are both CMOS-compatible, have negligible absorption in the ultraviolet range and are commonly used as the material in many optical filter designs. The refractive index contrast curves of three possible combinations using these materials are shown in Figure 2.13. According to the figure, the refractive index contrast for the Al_2O_3 | SiO_2 layer system is about 0.16, while the airgap-based designs have a higher contrast of 0.27 and 0.34 (respectively for SiO_2|air and Al_2O_3|air).

To compare these layer systems, three Fabry-Perot-based filter designs with similar complexity (layer number) are designed. The filters are Fabry-Perot-based and are composed of two distributed Bragg reflectors separated by a cavity layer. An optical thin-film coating software package based on transfer matrix (TFCalc, Software Spectra, Inc.) has been used to obtain the spectral response of the multi-layered thin-film structures. The refractive index of the layers (as presented in Figure 2.12) were used for the analysis. Furthermore, the refractive index data for the ultraviolet grade Fused silica wafers (JGS1) were used as the substrate (thickness= $0.5\ mm$).

Although, a high number of layers (> 10 layers) is common in optical filter designs [10], such a layer system is not favorable for many CMOS-compatible processes. Therefore, a total number of 11 layers was considered to be a lower limit for such a filter and used for this study. It must be noted that the maximum accept-

Table 2.1: List of layer thicknesses of an 11-layer Fabry-Perot filter centered at $400\ nm$. The thickness of each layer is 1 QWOT, $T_{SiO_2} = 68\ nm$, $T_{Al_2O_3} = 56\ nm$, and $T_{air} = 100\ nm$.

	$Al_2O_3 \mid SiO_2$	$SiO_2 \mid Air$	$Al_2O_3 \mid Air$	
0	Fused silica	Fused silica	Fused silica	Substrate
1	Al_2O_3	-	Al_2O_3	DBR 1 (γ=1.5)
2	SiO_2	Air	Air	
3	Al_2O_3	SiO_2	Al_2O_3	
4	SiO_2	Air	Air	
5	Al_2O_3	SiO_2	Al_2O_3	
6	SiO_2	Air	Air	Resonator
7	Al_2O_3	SiO_2	Al_2O_3	DBR 2 (γ=1.0)
8	SiO_2	Air	Air	
9	Al_2O_3	SiO_2	Al_2O_3	
10	SiO_2	Air	Air	
11	Al_2O_3	SiO_2	Al_2O_3	

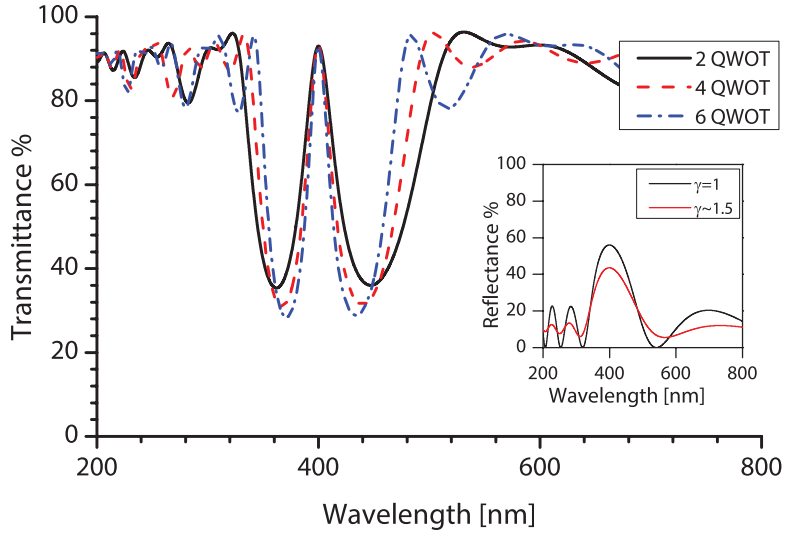

Figure 2.14: Spectral transmittance of an $AL_2O_3|SiO_2$-based optical filter as listed in Table 2.1. Multiple resonator layer thicknesses were plotted. The figure in the insert shows the reflectance of the top ($\gamma = 1$) and the bottom ($\gamma = 1.5$) DBRs.

able layer number in a CMOS process depends on many factors such as deposition temperature and residual stress. Therefore, this layer number (11) is chosen rather

arbitrarily and merely to compare the performance of these three material systems. Table 2.1 lists the three filter designs. These optical designs are based on single QWOT layers. Moreover, no optimization on the thicknesses was performed.

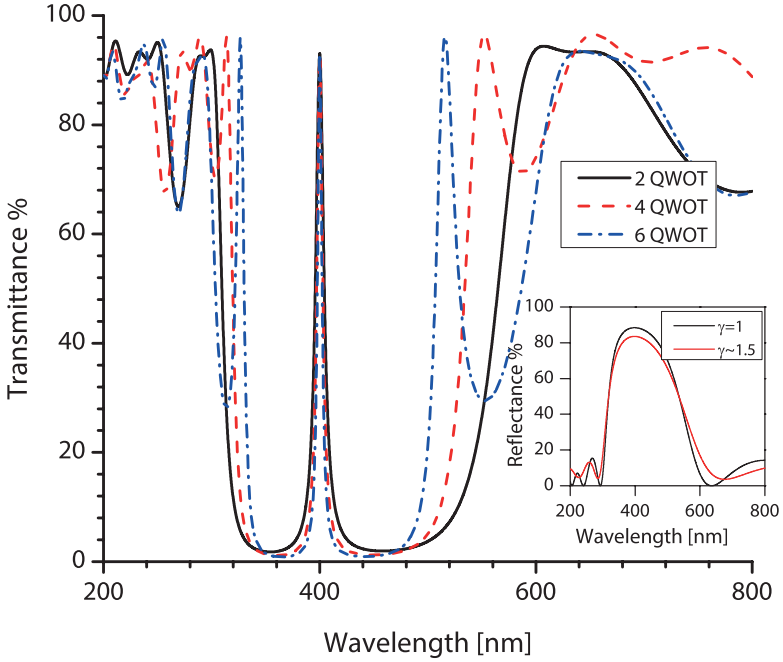

Figure 2.15: Spectral transmittance of an AL_2O_3|airgap-based optical filter as listed in Table 2.1. Multiple resonator layer thicknesses were plotted. The Figure in the insert shows the reflectance of the top ($\gamma = 1$) and the bottom ($\gamma = 1.5$) DBRs.

It should be noted that the designed filter is not symmetric. This asymmetry stems from the fact that the layers are deposited on a wafer (substrate), while the top side of the filters is exposed to free space (air). In these filter designs, the bottom DBR is placed on a fused silica wafer. Therefore, DBRs would have γ values of 1.0 and about 1.5 for top and bottom DBRs respectively (see Equation 2.31). Furthermore, a high-index layer is used to improve the index matching between the filter layers and fused silica substrate. The first layer in SiO_2|air design is omitted due to the similar refractive indexes of SiO_2 and fused silica.

Figure 2.14 shows the spectral transmittance of the all-dielectric design based on AL_2O_3|SiO_2 layer system designed at $400\ nm$ (Table 2.1). The reflectance of the DBRs is also plotted in the insert of the figure. Figure 2.15, on the other hand, shows the transmission peak of the AL_2O_3|air design. The comparatively higher refractive index contrast of the layers gives a rather sharp transmission over a much wider bandwidth.

Although Al_2O_3|air would in principle result in a higher contrast (Figure 2.13, the SiO_2 as the high-index material (together with air as the low-index layer) have a few benefits for a CMOS-compatible optical design. The refractive index contrast

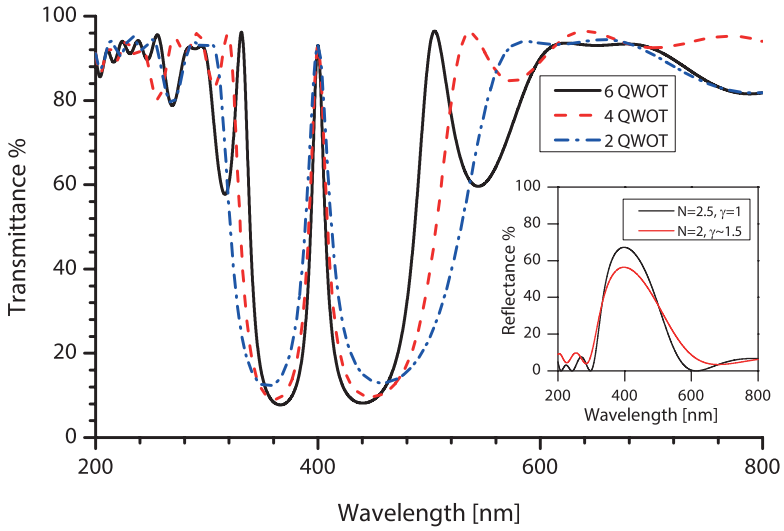

Figure 2.16: The spectral transmittance of a SiO_2|airgap-based optical filter as listed in Table 2.1 and for different cavity length. The figure in the insert shows the reflectance of the top ($\gamma = 1$) and the bottom ($\gamma = 1.5$) DBRs.

of SiO_2 and air is quite high, while its absorption at low-wavelengths is negligible. Furthermore, several processes are available for the deposition and patterning of SiO_2 thin-films. Therefore, in this research, SiO_2 layers is chosen as the main material for optical filter fabrication.

Figure 2.16 shows the expected spectral reflectance of the DBRs according to the layer listing presented in Table 2.1. A peak reflectance of about 60% for $\gamma = 1.5$ and 70% for a $\gamma = 1.0$ is obtainable using SiO_2|air structures. The spectral transmittance of the resulting Fabry-Perot filter is also presented in Figure 2.16.

Table 2.2: The peak transmittance and FWHM of the filter design according to layer listing in Table 2.1.

Cavity length	FWHM transmission peak at 400 nm [nm]		
	Al_2O_3 | SiO_2	SiO_2 | Air	Al_2O_3 | Air
2 QWOT	29.4	22.4	8.9
4 QWOT	23.9	16.6	6.2
6 QWOT	20.0	13.1	4.7

As discussed in Section 2.4.2, by increasing the length of the cavity, the FPI operates at higher transmission orders. Table 2.2 lists the FWHM and peak transmittance obtainable with these optical designs at different FPI orders. Compared to the all-dielectric design, the SiO_2|air provides an about 35% sharper peak at the third transmission order (6 QWOT).

References

[1] S. Xia, D. Chen, Z. Qi, X. He, C. Peng, X. Chen, C. Bian, L. Qu, and J. Sun, *Microsystems and Nanotechnology*, edited by Z. Zhou, Z. Wang, and L. Lin (Springer Berlin Heidelberg, Berlin, Heidelberg, 2012) Chap. Microelectromechanical Sensors, pp. 207–260.

[2] N. Tkachenko, *Optical Spectroscopy: Methods and Instrumentations* (Elsevier Science, 2006).

[3] J. Hodgkinson and R. P. Tatam, *Optical gas sensing: a review,* Measurement Science and Technology **24**, 012004 (2013).

[4] E. Hecht, *Optics* (Addison-Wesley, 2002).

[5] M. Born, E. Wolf, and A. Bhatia, *Principles of Optics: Electromagnetic Theory of Propagation, Interference and Diffraction of Light* (Cambridge University Press, 1999).

[6] F. Pedrotti, L. Pedrotti, and L. Pedrotti, *Introduction to Optics* (Pearson Prentice Hall, 2007).

[7] A. Fox, *Optical Properties of Solids*, Oxford master series in condensed matter physics (Oxford University Press, 2001).

[8] H. MacLeod and H. Macleod, *Thin-Film Optical Filters, Fourth Edition*, Series in Optics and Optoelectronics (CRC Press, 2010) Chap. Multilayer high-reflectance coatings.

[9] C. J. R. Sheppard, *Approximate calculation of the reflection coefficient from a stratified medium,* Pure and Applied Optics: Journal of the European Optical Society Part A **4**, 665 (1995).

[10] H. A. Macleod, *Thin-film optical filters*, Series in Optics and Optoelectronics (CRC Press, 2010) Chap. Band-Pass Filters, pp. 299–401.

[11] H. Fujiwara, *Spectroscopic Ellipsometry: Principles and Applications* (Wiley, 2007).

[12] F. Urbach, *The long-wavelength edge of photographic sensitivity and of the electronic absorption of solids,* Phys. Rev. **92**, 1324 (1953).

[13] R. F. Wolffenbuttel, *MEMS-based optical mini- and microspectrometers for the visible and infrared spectral range,* Journal of Micromechanics and Microengineering **15**, S145 (2005).

[14] A. Emadi, H. Wu, G. de Graaf, and R. Wolffenbuttel, *Design and implementation of a sub-nm resolution microspectrometer based on a linear-variable optical filter,* Opt. Express **20**, 489 (2012).

[15] S. Adachi, *Optical constants of crystalline and amorphous semiconductors: Numerical data and graphical information,* (Springer US, Boston, MA, 1999) Chap. Cubic Gallium Nitride (β-GaN), pp. 188–197.

[16] F. Gervais, *Aluminum oxide (Al_2O_3),* in *Handbook of Optical Constants of Solids*, edited by E. D. Palik (Academic Press, Burlington, 1997) pp. 761 – 775.

[17] H. Philipp, *Silicon dioxide (Sio_2), type α (crystalline),* in *Handbook of Optical Constants of Solids*, edited by E. D. Palik (Academic Press, Burlington, 1997) pp. 719 – 747.

[18] H. Philipp, *Silicon nitride (Si_3N_4) (noncrystalline),* in *Handbook of Optical Constants of Solids*, edited by E. D. Palik (Academic Press, Burlington, 1997) pp. 771 – 774.

[19] L. Gao, F. Lemarchand, and M. Lequime, *Exploitation of multiple incidences spectrometric measurements for thin film reverse engineering,* Opt. Express **20**, 15734 (2012).

[20] P. E. Ciddor, *Refractive index of air: new equations for the visible and near infrared,* Appl. Opt. **35**, 1566 (1996).

[21] M. Ghaderi, N. P. Ayerden, G. de Graaf, and R. F. Wolffenbuttel, *Surface-micromachined Bragg reflectors based on multiple airgap/SiO_2 layers for CMOS-compatible Fabry-Perot filters in the UV-visible spectral range,* Procedia Engineering **87**, 1533 (2014).

[22] M. Ghaderi, N. P. Ayerden, G. de Graaf, and R. F. Wolffenbuttel, *Optical characterization of mems-based multiple air-dielectric blue-spectrum distributed bragg reflectors,* in *SPIE Microtechnologies*, Vol. 9517 (International Society for Optics and Photonics, 2015) pp. 95171M–95171M–6.

3

Mechanical design of MEMS optical filters

3.1. Residual stress in optical MEMS

The typical large-area optical MEMS devices presented here are, like many other MEMS structures, composed of free-standing suspended plates or membranes. In these optical devices, not only the optical design and tolerances play a significant role, but also the mechanical design of the structure have to be considered. Various effects such as fracture, buckling, delamination can significantly influence the device operation and fabrication yield. The sources and effects of these failure modes in the airgap-based MEMS structures have to be studied for a successful device fabrication.

Airgap-based optical filters are composed of a stack of sub-wavelength thick membranes separated by sub-wavelength (air)gaps. While electrical contacting is essential in traditional MEMS and limits the number of movable layers to be stacked, the optical characteristics of the layers are much more important in optical MEMS. Furthermore, the optical application does not necessarily require electrical contacting to each layer and allows stacking of a relatively large number of layers to form an optical filter. Since the layer thicknesses decrease with the targeted wavelength range, the intended operating spectrum has a major implication on the layer thicknesses and acceptable tolerances in the fabrication process in such systems. The membrane structure must be carefully designed to achieve the required performance, while both the optical and the mechanical properties must be considered.

Even though the typical optical devices do not have any moving mechanical part, the multi-membrane design is a mechanically complex structure. The residual stress is dominant in thin films and could significantly affect the flatness and rigidity of the membrane after the release. Controlling the residual stress in membrane systems is of great importance. An important part of this optical-MEMS design includes the study of the mechanical structure and predicting the post-release behavior of such a structure. Two main effects are considered. The presence of any deformation in the membrane (i.e. buckling of the membrane) is one of the important limiting factors in the optical performance of the resonance-based optical filters. It is widely known that, as compressive layer results in a buckled structure, tensile stress is required in membranes to obtain a flat membrane. Furthermore, the membranes must have enough rigidity to withstand the forces that are mainly applied by the residual stress within the layers. A high tensile stress induces fractures in the membrane. In this sense, the effect of the stress level on the fracture and failure-prone sites have to be studied. Therefore, there is an important trade-off between the flatness requirement and rigidity of the structure that has to be studied.

Designing an airgap-optical filter must be done at two levels. At the material level, the appropriate properties, such as residual stress, uniformity, and step coverage is characterized. Secondly, the effect of various geometrical features, such as membrane size, anchor shape, and perforations considering the impact of mechanical properties of the material on the structure as a complete system are investigated. The modeling of the mechanical systems and layers in MEMS has been extensively presented in the literature. This chapter aims to study the various mechanical constraints, and systematically optimize the fabrication of appropriate membranes having a sufficient yielding strength for optical applications. To do so,

various measurement techniques, theoretical and numerical modeling, and simulation tools have been applied.

In this chapter, the following challenges are addressed. The nature of the residual stress in the thin-films is introduced. Different deposition methods are compared, and an appropriate method is selected. Different techniques for the stress engineering in the layers are investigated. Finally, various stiction-free drying methods are presented.

3.2. Origin of residual stress in thin-films

It is known that the residual stress is a dominant force in the thin-film structures. Hence, a detailed understanding of the nature of the stress acting on or within the thin-films is crucial for enabling the implementation of approaches to avoid or compensate for the residual stresses in a design [1] Residual stress is defined as the internal force distribution on a unit area of the material after or during the fabrication. This stress distribution can generate a deformation in the structure. The deformation energy in the structure, G_ϵ, is proportional to the square of the residual stress and inversely proportional to the bi-axial modulus of the material:

$$G_\epsilon = \frac{\sigma^2}{2\bar{E}} \tag{3.1}$$

where $\bar{E}$ is the biaxial modulus that is defined in terms of E Young's modulus and ν the Poisson's ratio of the material.

$$\bar{E} = \frac{E}{1-\nu} \tag{3.2}$$

The presence of any residual stress in thin-films is almost inevitable. Stress build up in the thin-film layers is typically due to the deposition characteristics and internal material composition, or a hysteresis effect of the process history. The process history includes effects such as depositions at higher temperatures or thermal annealing after the layer deposition. In MEMS structures, residual stress often results in different effects such as buckling, wrapping, fracturing, and delamination in the structure. Based on the source, residual stresses are often classified as intrinsic and extrinsic (mostly thermal) stresses. The overall stress in a thin-film is the combined effect of these two distinct components:

$$\sigma_t = \sigma_{intrinsic} + \sigma_{Thermal}. \tag{3.3}$$

3.2.1. Intrinsic Stresses

In most thin-films deposited (or grown) on a substrate, typically the lattice mismatch and spacing between the crystal grains, micro/nano-voids within the layer, impurities, and doping levels, and phase transitions [1–4] often results in a film under a residual stress. The overall effect of these forces results in a tension in the film. The residual stresses originating from the micro or nanostructural composition of the layer are known as intrinsic stress. The nature of the intrinsic stress varies

with the deposition conditions, such as temperature, gas composition and chamber pressure. Furthermore, as many of these effects depends on the layer thickness, the intrinsic stress also often depends on the material thickness. The effects of both deposition parameters and layer thickness on the intrinsic stress in the layer will be discussed in detail in the next sections.

3.2.2. Thermal Stress

In many MEMS processes, the film deposition occurs at elevated temperatures. The thermal stress is the stress applied to the film by the substrate due to a mismatch in the coefficient of thermal expansion (CTE) of the substrate and the deposited layer [4]. After cooling to the room temperature, the wafer and the added layer shrink to a slightly different lengths. This mismatch strain (i.e. relative displacement, $\Delta L/L$) at low temperatures result in an unbalanced force acting on the wafer that bends the wafer. In an isotropic film, the thermal stress measured at temperature T_0 can be defined in terms of the difference between the expansion coefficients of the film and wafer (α_f and α_w) and the deposition temperature T:

$$\sigma_{Thermal} = \frac{E}{1-\nu}(\alpha_w - \alpha_f)\Delta T \tag{3.4}$$

where $\Delta T = T - T_0$ and the E is the Young's modulus and ν the Poisson's ratio of the film. Accordingly a thin-film with an expansion coefficient lower than that of the wafer deposited at temperatures above the room temperature would exhibit a compressive stress. Similarly, a higher expansion coefficient in the thin-film results in tensile stress. Note that according to this polarity convention; the compressive stress corresponds to negative, and the tensile stress corresponds to positive residual stress values. At high-temperature deposition processes (i.e. large ΔT), thermal stress is usually the dominating factor.

Table 3.1: Thermal stress in different dielectrics deposited on a $< 100 >$ Silicon wafer [5–7].

Layer	ΔT [K]	α_f [ppm/K]	$\sigma_{Thermal}$ [MPa]
Thermal SiO_2	800–1000	0.5 [5]	-170 – -220
PECVD SiO_2	250	2.7 [6]	~0
PECVD SiO_2 -annealed	300	2.1 [6]	-20
PECVD SiO_2 -annealed	400	1.5 [6]	-50
PECVD SiN	280	2.48 [7]	-5

The thermal expansion coefficients of some typical dielectrics are listed in Table 3.1. The thermal stresses of such layers on a silicon wafer at room temperature (25 °C) have also been calculated. It should be noted that the thermal expansion coefficient of silicon increases with temperature; from $\alpha_w = 2.69 \times 10^{-6}$ 1/K at about room temperatures up to 4.44×10^{-6}1/K at about 1000 °C [8].

3.3. Materials and deposition methods

The fabrication of airgap optical filters is based on surface micromachining. The essential feature of surface micromachining is the subsequential and alternating build-up of two types of layers; i.e. layers that are to stay (structural layers) and layers that are to be removed at a later stage in the processing (sacrificial) in such a way that free-standing structures result [9]. The structure is built by addition (deposition) or removal (etching) of layers on the surface of a substrate. The choice of appropriate materials for airgap filter structures is complicated by several constraints. Optical and mechanical requirements, as well as the fabrication challenges, impose these limitations. The optical requirements, in terms of the refractive index and absorption coefficient, were explained in Chapter 2. This chapter studies the optical device as a mechanical structure. The design of such a structure depends on the residual stress in the membrane materials.

As discussed before, the residual stress in thin-films is influenced by several deposition parameters. The versatility of the mechanical structure, specifically the rigidity of the membranes, is strongly affected by the methods used to deposit the thin-films. It can be noted that, while the choice of the material is made by the optical requirements (see Chapter 2), the mechanical design imposes constraints on the deposition methods.

As discussed in Chapter 2, dielectrics, mainly oxides and nitrides, satisfy the optical requirements of the UV-visible optical filters. Furthermore, many dielectrics are widely used in microelectronic and MEMS devices and the availability of multiple deposition methods provides the possibility of tuning the material properties to comply with the mechanical (and optical) requirements. Various deposition methods based on the physical vapor deposition (PVD) methods, such as sputtering and evaporation, the chemical vapor deposition (CVD), and thermal oxidation are used for the deposition of a wide range of CMOS-compatible materials. The following section lists some of the deposition techniques and briefly discusses the general characteristics of the deposited layers.

Thermal oxidation

Thermal oxidation of silicon is a well-known technique for growing uniform high (optical) quality oxide layers. Thermally grown silicon-oxides are present in almost all CMOS device as the passivation, masking, and sacrificial layers. Bare surface of a silicon substrate or layer can react with the oxygen and form an oxide layer. The silicon oxide layer can form even at room temperatures. However, the low diffusivity of the oxygen atoms into the silicon. Therefore, the oxide provides a barrier and the oxidation automatically stops. This so-called *native oxide* layer is typically of $1-2/nm$ thickness (for crystalline silicon) [10]. At elevated temperatures ($800 - 1000$°C), the diffusivity of the reactive gasses (oxygen or water) increase and hence thicker layers can be deposited [9]. In **dry oxidation** method, oxide is grown by introducing oxygen to the high-temperature furnace resulting in the following chemical reaction:

$$Si + O_2 \longrightarrow SiO_2.$$

Similarly in **wet oxidation**, the water vapor is used as the reacting agent:

$$Si + 2\,H_2O \longrightarrow SiO_2 + 2\,H_2.$$

Due to a higher diffusivity of the H_2O molecules, the oxide can be grown at higher rates and at relatively lower temperatures. The layer quality, on the other hand, is typically lower than the dry oxidation. The thermal budget (i.e. the temperature profile) in dry oxidation process is significantly higher than that of wet oxidation. This is especially important if there are already integrated CMOS devices on the wafer. Therefore, unless a very thin oxide layer (typically bellow about $100\ nm$) is required, the wet oxidation method is preferred.

In thermal oxidation, Silicon atoms are partially consumed to form the added layer. Due to the Si to O_2 ratio in SiO_2 the oxidation consumes about 0.46 *unit* of Si to result in 1 *unit* of SiO_2. This means that the Si crystal lattice now has to expand by about 54% to 'fit' the O_2 atoms. Therefore, the oxidation of silicon results in an intrinsically compressive stress layer [11]. The residual stress in the thermal oxide layers is reported to be about 300 MPa compressive [12]. This compressive stress in the oxide membrane usually results in buckling of the membrane after the release.

Atomic Layer Deposition (ALD)

In atomic layer deposition (ALD) is the target layer is deposited by repetitive deposition cycles of single-atom layers (also known as monolayers) on the surface of the substrate. Each precursor gas is introduced individually to the chamber forming a monolayer on the surface. The chamber is then purged with an inert gas and the second precursor is introduced which reacts with the previously deposited monolayer forming a single layer of the desired material [13]. Various oxides, nitrides, and pure elements can be deposited using ALD. The ALD is typically performed at temperatures up to 400^oC. While the deposition rate of ALD is typically low, extremely conformal and high-quality films can be deposited [14].

Low-Pressure Chemical Vapor Deposition (LPCVD)

Chemical vapor deposition (CVD) is the deposition of a solid layer as a result of a chemical reaction in the chamber. In CVD, the precursors are vaporized and injected into the chamber. The high temperature (substrate temperatures ranging from $400^o\ C$ to $1000^o\ C$) of furnace provides the required energy for the chemical reaction to happen [15–17]. Therefore, the high deposition temperatures usually result in a significant thermal stress. The CVD is usually performed at low-pressure conditions and hence referred to as LPCVD. The low-pressure deposition condition results in faster deposition rates and better deposition uniformity and step coverage in the deposited layer. Many dielectrics, such as oxides and nitrides, and pure elements, such as polysilicon, can be deposited using LPCVD.

Plasma Enhanced CVD (PECVD)

Plasma enhanced CVD (PECVD) is a particular type of the CVD in which the deposition is assisted by a plasma condition [17]. The presence of the plasma (usually RF) reduces the required energy for the reaction of the precursors. Therefore, the reaction happens at comparatively lower temperatures as compared to the CVD. Depositions at temperatures up to 400 °C are possible using PECVD [14, 15]. In

many optical and microelectronic applications, plasma enhanced chemical vapor deposition (PECVD) is used for deposition of dielectrics. Especially, the low deposition temperatures (up to $400^o\ C$) in PECVD offer a CMOS-compatibility advantage, because the post-CMOS high-temperature deposition methods cannot be applied. The deposition rate of the typical PECVD is also higher and provides the possibility of depositing rather thick layers. In terms of the residual stress, PECVD films that are deposited at lower temperatures usually show a lower thermal stress level. Furthermore, varying deposition parameters such as the precursor flow, chamber pressure, and excitation power also changes the composition of the film, thus providing the possibility of tuning the mechanical (and optical) properties of the film [18].

Table 3.2: Various deposition methods of SiO_2 films.

Layer	Deposition rate	Uniformity	Tunability of optical and mechanical characteristics
PECVD	High	Good	High
LPCVD	Low	Good	Low
Thermal oxidation	Low	High	Low
ALD	Low	High	Low
Sputtering	High	Low	High

3.4. Residual stress measurement

For local (and overall) stress calculations and optimization the residual stress of the individual layers in a multilayer stack have to be measured. The residual stress in the thin-films can only be measured by analyzing its effects on a mechanical structure. In most of these methods the stress is evaluated by measuring the deformation due to the stress. Fitting the deformation with the appropriate model enables the calculation of the residual stress. Therefore, the accuracy of stress measurement not only depends on the measurement resolution but also affected by the analytical model used for the stress evaluation.

Various methods are available in thin-films and MEMS fabrication to measure the residual stress. Non-destructive imaging techniques XRD (X-ray diffraction) [19, 20], Raman spectroscopy [21], and neutron deflection [22] have been applied to evaluate the stress levels and sources by measuring the lattice spacing in crystalline and polycrystalline materials. Even though these methods provide an accurate local stress measurement, they are costly and usually not available in CMOS cleanrooms.

Special MEMS structures have been developed to measure the residual stress in thin films. The measurement principle in these MEMS structures is generally based on buckling or rotational techniques. Measuring the deformation (expansion or contraction) due to the presence of the stress in a freestanding structure is

the basic principle of the buckling technique. Bridges and ring structures have been studied for measuring compressive and tensile stress, respectively, in thin films. However, the accuracy of the measurement is limited by the step size of the structure array [23]. In the rotational MEMS structures the compressive or tensile stress is converted to a rotation of the asymmetric structure. The rotation of the structure is measured using structures such as micro-verniers. By measuring the rotation angle, the stress can be measured. Furthermore, a single structure is capable of measuring both tensile and compressive stresses [23].

The wafer curvature measurement technique [4, 24] has been used to assess the residual stress in the deposited thin-films. This technique is based on the measurement of wafer curvature prior to the layer deposition and thereafter. The relative change in the wafer curvature is caused by the added mechanical stress to the system and hence can be used to assess the residual stress in a thin-film. In the case of the layer deposition, the total residual stress in the thin-film changes the curvature of the wafer (Figure 3.1). As mentioned earlier, the convention is that a positive relative curvature value R corresponds to a tensile stress in the added layer, while a negative curvature change represents a compressive layer. The Stoney equation [25], which stated as:

$$\sigma_f = \frac{E_w t_w^2}{6Rt_f(1-\nu_w)} \tag{3.5a}$$

$$R^{-1} = R_f^{-1} - R_i^{-1}. \tag{3.5b}$$

associates the residual stress of a thin-film with the curvature change in the wafer (R) and thickness of the film (t_f). Here t_w is the wafer thickness, and E_w and ν_w are the Young's modulus and Poisson's ratio of the wafer.

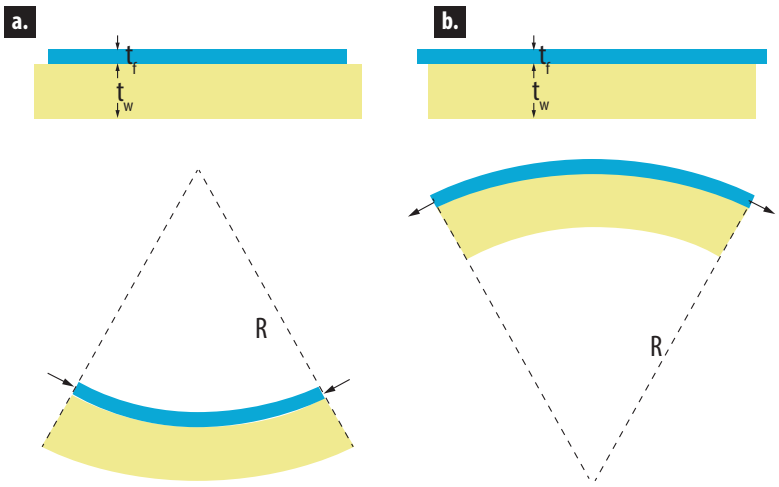

Figure 3.1: Schematic of change in wafer curvature due to the residual stress, a. Tensile stress, and b. Compressive stress

The limitations and assumptions of the Stoney model have to be considered before it can be used for the interpretation of measurements [26]. First of all, the thickness of the film must be much thinner than that of the wafer. Secondly, the thin-film must be homogeneous and isotropically cover the wafer surface. Thirdly, the radius of curvature must be equal along every in-plane direction on the wafer. Therefore, the curvature measurement method assumes a uniform distribution of stress within the layer and stress gradients and local (in-plane) variations of stress is averaged over the entire wafer.

Throughout this work, the wafer curvatures due to the residual stress of the thin-films (on 10 cm diameter silicon wafers) were measured using a KLA-Tencor Flexus 2900 system (Milpitas, CA. USA). Unless otherwise indicated, all measurements have been done at room temperature.

3.5. PECVD Silicon-oxide as the optomechanical material

As discussed in section 3.3, both PECVD and ALD offer many advantages over other methods for the membrane material deposition (see Table 3.2). Due to the inherently lower CTE of oxide films as compared to that of silicon, the thermal stress is always compressive. The lower deposition temperatures in ALD and PECVD provides the possibility to deposit films with a lower thermal stress. Furthermore, the tuning possibility available in these methods offer can be used to deposit films with desired properties.

In this research, PECVD silicon-oxides were selected as the optical/mechanical material. This choice over the ALD was mainly due to the higher deposition rates and availability of the process in the cleanroom. Although the PECVD deposited oxides usually feature an as-deposited compressive stress, the additional advantage is the possibility of tuning the stress by several deposition parameters. This tunability provides the possibility of achieving oxide layers with the required tensile stress level which is sufficient for stretching a membrane without rupturing. Tarraf *et al.* [18] investigated the effects of the deposition temperature and duty cycle of the dual-frequency excitation plasma on the residual stress in the silicon-oxide and silicon-nitride layers deposited in PECVD method for optical MEMS. Their results indicate that the stress of silicon-oxide layers depends only on the deposition temperature and not affected by the frequency variations (frequency interlacing time). However, silicon-nitride layers are affected by both deposition temperature and duty cycle. Flat, concave, and convex freestanding membranes were reportedly fabricated [18].

The residual stress in the PECVD thin-film strongly depends on the film composition. In low-temperature depositions, such as PECVD (or sputtering), several competing parameters affect the residual stress level in the films. First of all despite that the deposition occurs at a low temperature, the thermal stress contribution cannot be neglected [27]. Furthermore, in these methods the wafer surface is usually bombarded by ions (atoms) (i.e. sputtering effect at a high bias). The energy of the particles determines how tight the atoms are arranged during the deposition.

Since the temperature is low, the atoms cannot freely move on the surface toward their zero-energy position. At high ion energies (with a DC bias for instance) the deposited atoms are closely packed results in an intrinsically compressive film [17, 27]. On the other hand, in low bombardment ion energies, micro/nano-voids can usually form resulting in a tensile layer. Furthermore, impurities, especially the hydrogen-bonds, are affecting the mechanical properties of the film [28]. As many of these effects are varying in time during the deposition process, there are stress gradients along the layer thickness, the intrinsic stress also often depends on the layer thickness. Therefore, varying the deposition parameters usually can be used to change the composition of the film [28], and the stress level in the film to meet the functional requirements of the design.

Two deposition recipes were used to deposit the films with different as-deposited mechanical properties. Both recipes were based on the Silane (SiH_4) chemistry and carried out at 400 °C in a multi-station PECVD system. The deposition recipes are listed in Table 3.3. The higher total gas flow and a slightly higher N_2O-to-SiH_4 ratio in the *type 2* recipe result in a higher deposition rate and a higher concentration of the incorporated impurities and voids. Therefore, *type 2* results in a less-compressive layer. Table 3.4 lists the as-deposited residual stress values of the layers measured on <100> bare silicon wafers.

Table 3.3: PECVD deposition of SiO_2 films

Parameter	Type 1	Type 2
Temperature	400 °C	400 °C
SiH_4 flow rate	210 sccm	300 sccm
N_2O flow rate	6000 sccm	9500 sccm
N_2 flow rate	3150 sccm	1500 sccm
Deposition rate	8.5 nm/sec	9.5 nm/sec

3.6. Thermal annealing of PECVD thin-films

Full characterization of the mechanical (and optical) properties of the thin films is essential for a successful structural design of the airgap optical filter. Furthermore, tuning the residual stress by thermal annealing can be used to achieve a preferable stress level in the film. The preferred stress is tensile, with a stress level that is sufficient for stretching a membrane without rupturing. Furthermore, during the fabrication process, the wafers are typically subjected to high temperatures (i.e. subsequent layer depositions). Understanding the residual stress level and changes during the subsequent layer depositions that add to the thermal budget is crucial for predicting the device performance and yield.

Thermal annealing of the PECVD films can change the chemical bonds between atoms in the layer. The effects of the thermal annealing and aging (i.e. shelf

life) on the mechanical characteristics (e.g. residual stress and thermal expansion coefficient) of PECVD deposited films have been widely investigated [29, 30]. Specifically, the hydrogen concentration in the PECVD deposited films decreases after annealing [3]. The shrinkage of the film, however, is significant only for temperatures more than about 700 °C and is associated with a significant change in the stress at such elevated temperatures [31]. Haque *et al.* [29] studied the correlation between the residual stress in the PECVD films with atomic bonds in the structure of the layer. Their study indicates that a high concentration of hydrogen (Si-H) and silanol (Si-OH) bonds occur in the low-temperature depositions. These atomic bonds contribute to the stress in the thin film. The subsequent reversible and irreversible changes by annealing and aging varies the stress in the deposited film. Similarly, thermal annealing in PECVD silicon-nitride films shows similar variations in the stress level in the films [18, 32]. Therefore, thermal annealing has been widely applied in many MEMS processes to change and control the residual stress in the low-temperature-deposited films [32].

In this study, two types of PECVD oxides were deposited on silicon wafers at 400 °C. Then the wafers were subjected to the annealing cycles up to 600 °C. The relevant characteristics before, during, and after thermal annealing steps were measured. The change in the refractive indices of the layers due to the annealing was also studied.

3.6.1. Stress variation in thermal annealing

To study the effects of the annealing on the residual stress in the deposited films following process flow were carried out. PECVD oxide films of both types and with a thickness of 500 nm were deposited on 100 mm diameter, $525\ \mu m$ thick <100> Silicon wafers.

The thickness of the layers was chosen to be higher than typically used for the filters in terms of optical thicknesses (about 70 nm [see Chapter 2]), to ensure the accurate measurement of the relative curvature change at lower residual stress values. Furthermore, this is in the range of the oxide layers required for anchoring of the membranes.

The residual stress in the films was derived from wafer curvature measurement data that was acquired prior to and subsequent to the film deposition (KLA-Tencor, Flexus 2900). Table 3.4 shows and compares the uniformity and residual stress of the deposited films.

Residual stress in low-temperature deposited oxide films is often composed of both thermal and intrinsic stress components. The low-temperature PECVD oxide deposition (typically at 400 °C) result in a microscopically non-uniform and porous layer [30]. Moreover, the reactive deposition methods result in the incorporation of the residual gasses in the resulting layer. Both these effects contribute to an intrinsic residual stress in the deposited film. Any subsequent high-temperature process (higher than the deposition temperature) will induce specific structural changes in the film. The changes can be divided into two main domains. At temperatures up to about 700 °C, the annealing induces micro-structural changes in the film that results in an irreversible change in the stress behavior of the film. The silane-based PECVD

Table 3.4: Uniformity and residual stress measurement of dielectric thin-film layers. Thermally oxidized poly-silicon and ALD alumina were also included for the sake of comparison. The uniformity values were measured using ellipsometry analysis of 21-points over the area of a 10 cm silicon wafer.

Layer	Deposition Temperature [°C]	Uniformity	As-deposited residual stress [MPa]
Thermal poly-oxide	800 - 1000	1 - 2.5%	~ -300
PECVD oxide: Type 1	400	~1%	-100
PECVD oxide: Type 2	400	~1%	0
ALD Alumina	400	very high	300

oxide contains a certain amount of hydrogen atoms, which is released during the annealing [18]. The void formation and the subsequent shrinkage results in a shift in residual stress toward the tensile stresses [30]. At a relatively high-temperature anneal (higher than about 700 °C), however, atoms can move through the layer in a reflow process. The re-arrangement of the atoms typically results in a stress-free layer at that specific temperature. As a next step in the annealing cycle, the wafer is cooled down. In this step, the thermal stresses become dominant in the film, due to the mismatch in the coefficient of thermal expansion (CTE) of the thin-film and the wafer. The oxides typically have a CTE of lower than silicon ($\alpha_{Si} \approx 3\ ppm/K$ [8] and $\alpha_{SiO_2} = 1.5 - 2.1\ ppm/K$ [6]), and become highly compressive after cooling down [30].

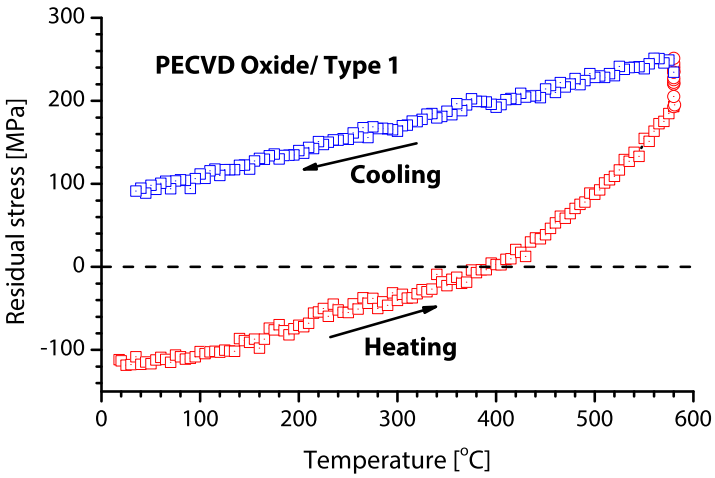

Figure 3.2: $\sigma - T$ curve of thermal annealing stress measurements: Type-1 PECVD oxide: the relaxation time at peak temperature is 15 minutes.

In-situ stress measurement was performed during thermal annealing using the

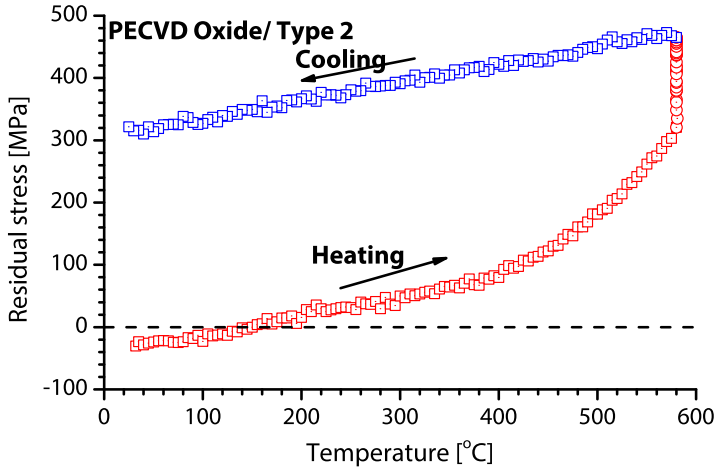

Figure 3.3: $\sigma - T$ curve of thermal annealing stress measurements: Type-2 PECVD oxide: the relaxation time at peak temperature is 30 minutes.

wafer curvature measurement method (KLA-Tencor, Flexus 2900). A maximum annealing temperature of 580 °C was selected. This temperature is the deposition temperature of LPCVD polysilicon that is chosen as the sacrificial material in the airgap filter (see Chapter 5). First the wafers were heated up with 10 °C/min rate to 580 °C and remained at this temperature for a defined relaxation time. The wafers then were cooled down to the room temperature with a similar rate. Figure 3.2 shows the *in situ* measurement of the residual stress during an annealing cycle of a *Type 1* PECVD oxide layer with 15 minutes of retention at 580 °C. Similarly, the Type 2 oxide was annealed up to 580 °C and with the retention time of 30 minutes. Figure 3.3 shows the *in situ* measurement of the residual stress in a $500\ nm$ layer of *Type 2* during an annealing cycle. The figures clearly indicate the irreversible change in the PECVD oxide layer after annealing at temperatures higher than the deposition temperature. Figure 3.4 shows the relative stress variations during the retention time at the peak annealing temperature in Type 1 and 2. The variations are toward a positive stress (tensile) in both layers. It can be noted that after about 25 minutes the residual stress in the film is saturated and is not changing.

It is interesting to note that Type 2 oxide, which was intended as an (as-deposited) low-stress oxide, results in a higher tensile stress after annealing (or any high-temperature process such as LPCVD polysilicon deposition) as compared to Type 1. Therefore, these tests confirm the significance of annealing on the stress level and, consequently, also on the prediction of the mechanical rigidity of the resulting structure.

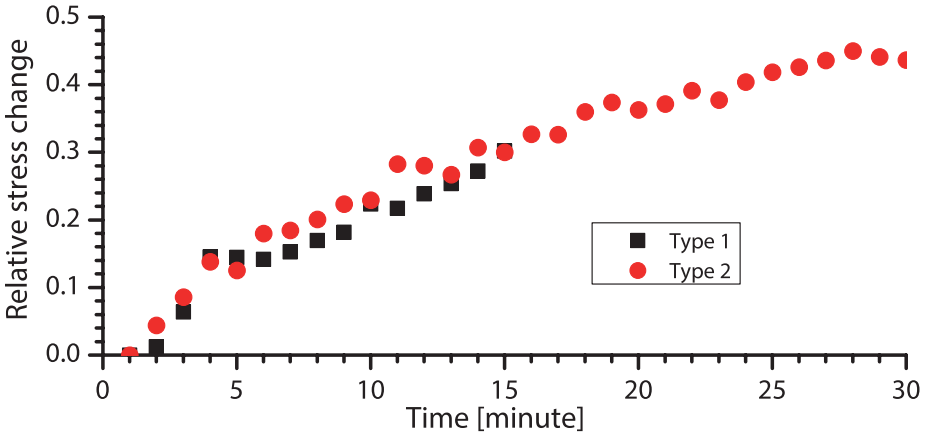

Figure 3.4: The relative variations in the residual stress during the retention at the peak temperature as a function of the annealing time.

3.6.2. Thermal stress analysis: Coefficient of thermal expansion

As discussed before, the thermal stress depends on the mismatch between the coefficients of thermal expansion (CTE) in the film and the substrate. The stress-temperature ($\sigma - T$) plots (Figures 3.2 and 3.3) can be divided into three specific parts. First, during the annealing from room temperature up to the deposition temperature at 400 °C, the change in residual stress with temperature is linear. At the deposition temperature, the thermal component of the residual stress vanishes. At the second part, annealing at higher temperatures induces a non-linear change in the residual stress that indicates an irreversible structural change in the layer. Finally, during the cooling down (and subsequent annealing cycles), the response becomes linear again. This behavior is explained considering the fact that the total stress is the summation of an intrinsic part and a thermal component. Even though the temperature dependency of the intrinsic component is complex, the thermal stress is linearly proportional to the temperature. Therefore, the 'non-linear' region in the thermal cycling indicates the change in the intrinsic stress, while the obvious 'linear' changes in the cooling down stage of the annealing cycles correspond to the thermal stress in the film [6]. The coefficient of thermal expansion (CTE) of the layer, therefore, can be calculated using the annealing cycles.

$$\frac{d\sigma}{dT} = \frac{d(\sigma_{thermal} + \sigma_{intrinsic})}{dT} \tag{3.6}$$

During the heating and cooling stages and at the temperatures below the deposition temperature (or the anneal temperature after the first cycle), the variation of the intrinsic stress is negligible [6]. Therefore, the derivative of the characterizes the variation in thermal stress of the deposited film.

$$\frac{d\sigma}{dT} = \frac{d(\sigma_{thermal})}{dT} = \frac{E_f}{1-\nu_f}(\alpha_f - \alpha_w) \tag{3.7}$$

The CTE mismatch ($\Delta CTE = \alpha_f - \alpha_w$) can be calculated using the Young's modulus and Poisson ratio of PECVD oxide reported in the literature [6] ($E_f = 81.5\ GPa$ and $\nu_f = 0.17$). Although the CTE of the silicon wafer is temperature dependent, an average value has been considered in this research (typically $\alpha_{si} = 2.69\ ppm/K$ at the low temperatures [8]). Furthermore, the temperature dependency of Young's modulus and Poisson ratio of PECVD layers were disregarded. Therefore, the stress-temperature hysteresis plots can be used to specify the total stress in its thermal and intrinsic components. Linear regression analysis using the least-square methods has been applied to obtain the slope of the stress-temperature curves. From the data in Figures 3.2 and 3.3, the CTE for Type 1 oxide is calculated to be $0.32 \pm 0.03\ ppm/K$ while CTE for type 2 is $0.25 \pm 0.03\ ppm/K$. Figures 3.5 and 3.6 shows the stress components of the two different oxides. The figure indicates that the Type 1 oxide has almost no as-deposited intrinsic stress, while the Type 2 oxide is initially tensile. The annealing increases the intrinsic stress for both oxide recipes.

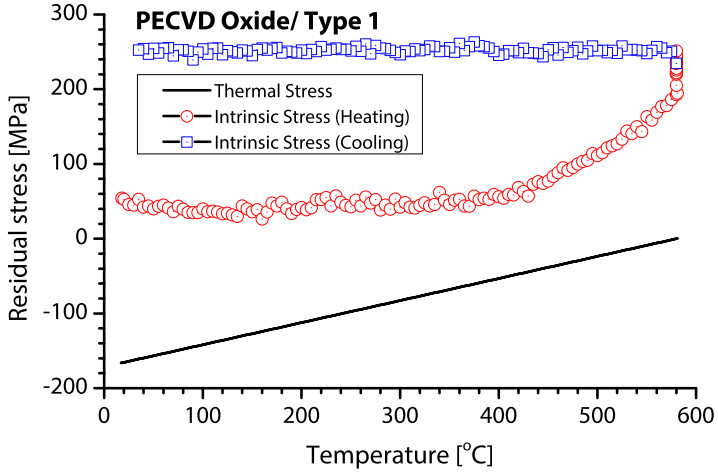

Figure 3.5: $\sigma - T$ curve of thermal annealing stress measurements as derived from the data in Figure 3.2:Type-1 PECVD oxide: the relaxation time at peak temperature is 15 minutes.

3.7. Thermal annealing of ultra-thin membranes

As was discussed in section 3.2.1, the microstructure of the deposited layers could vary with thickness, partially because of the thermal loading of early deposited part by the subsequent part [33]. The effect can be modeled as a monotonous increase

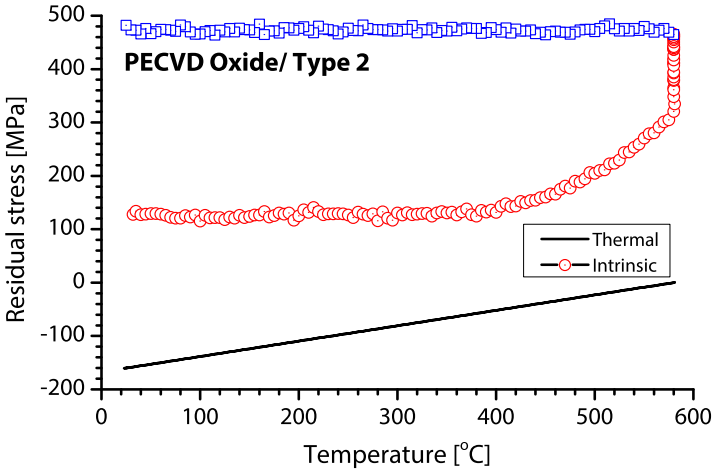

Figure 3.6: $\sigma - T$ curve of thermal annealing stress measurements as derived from the data in Figure 3.3:Type-2 PECVD oxide: the relaxation time at peak temperature is 30 minutes.

of the residual stress until a material-specific saturation reached. While the stress gradient along the thickness (i.e. the vertical direction) can be neglected for thick layers, the stress gradient is significant for thin layers. The results in the previous section were intentionally derived from rather thick layers, in order to not compromise the accuracy of the measurement technique (see Equation 3.5). For a more precise description of the stress in the optical thicknesses for ultraviolet and visible applications (tens of nanometre thickness), the stress-temperature hysteresis must be studied in films of the actual thickness. PECVD oxide layers (of both types) of 70 nm were deposited on several bare <100> silicon wafers. The residual stress was subsequently evaluated using the same technique, as discussed in the previous section by measuring the curvature of the wafer (KLA-Tencor Flexus 2900). The wafers were annealed up to the maximum annealing temperature at 580 °C, remained at that temperature for 1 h and were subsequently cooled down to the room temperature. The wafer curvature was measured at every 5 °C step. The residual stress was measured for both types of oxide in situ, and the results are shown in Figures 3.7 and 3.8. Due to its thinner thickness, the curvature change is relatively small and hence the error, is higher as compared to the thick layer measurements.

For a breakdown of the residual stress into its intrinsic and thermal components, the CTE were evaluated from the slope of $\sigma - T$ curves during the cooling by linear fitting and were found to be equal to $\alpha_f = 0.88 \pm 0.27\ ppm/K$ for Type 1 and $\alpha_f = 1.6 \pm 0.26\ ppm/K$ for the Type 2 PECVD oxide. Compared to the thick layers, the CTE of the thin layers is found to be significantly higher. These results are indicators of a rather reversible change in the residual stress of the layer by annealing. As represented in Figures 3.9 and 3.10, subtracting the calculated thermal stress from

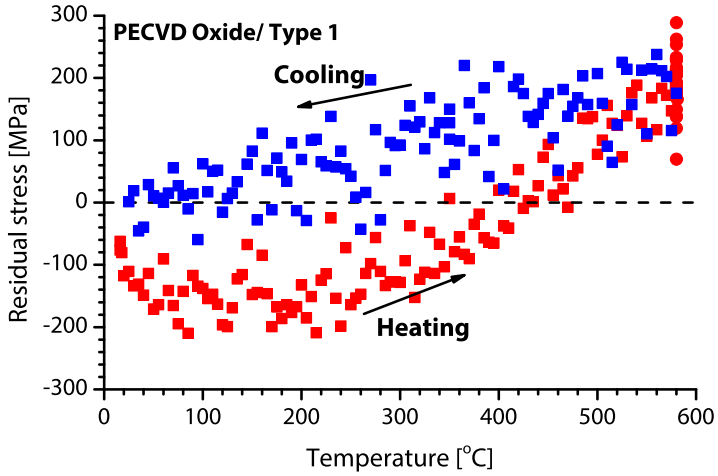

Figure 3.7: $\sigma - T$ curve of thermal annealing stress measurements in thin oxide films of Type 1.

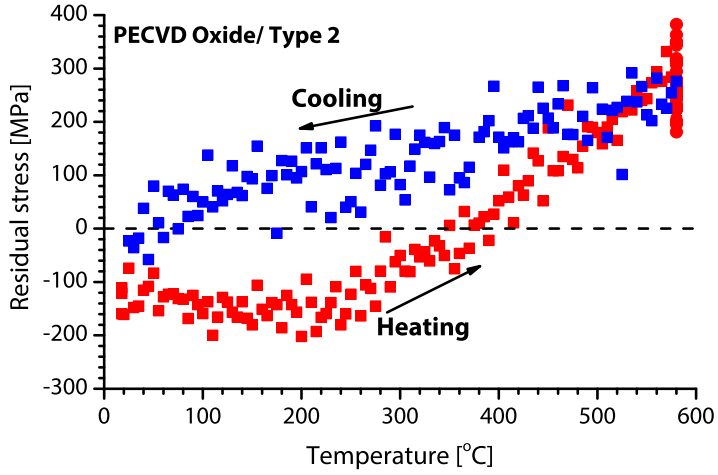

Figure 3.8: $\sigma - T$ curve of thermal annealing stress measurements in thin oxide films of Type 2.

the total stress shows a slight shift in the intrinsic stress during the annealing. According to the results, the intrinsic stress becomes more tensile at the annealing temperature. Furthermore, the variations in the intrinsic stress both oxide types during the peak temperature were statistically analyzed using ANOVA (analysis of variance) and show a p-value of higher than the significance level of $\alpha = 0.05$. This indicates that the residual stress does not significantly change after reaching the maximum annealing temperature.

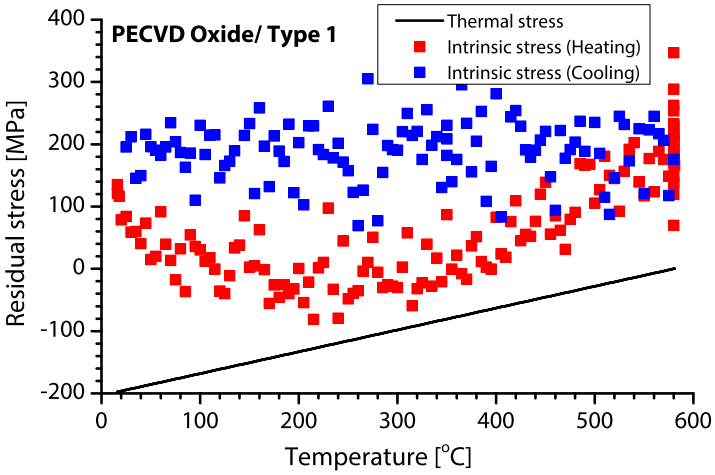

Figure 3.9: Thermal and intrinsic stress components in the thin oxide films of *Type 1.*

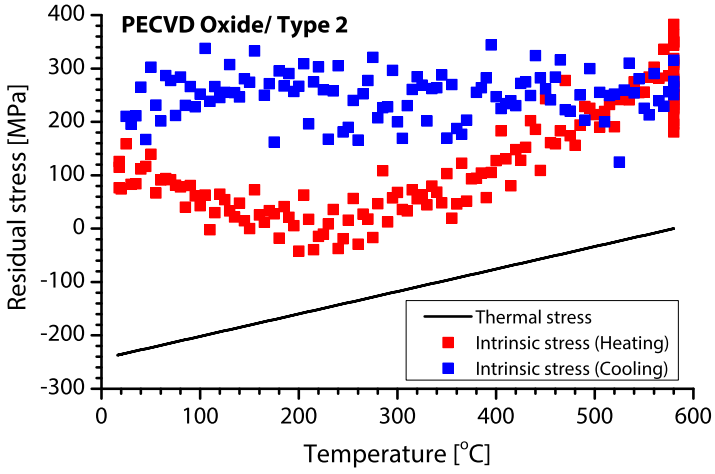

Figure 3.10: Thermal and intrinsic stress components in the thin oxide films of *Type 2.*

Compared to the thick layers, the CTE of the thin layers are found to be significantly higher. Figure 3.11 show the variation of CTE in PECVD oxide layers measured at different thickness values.

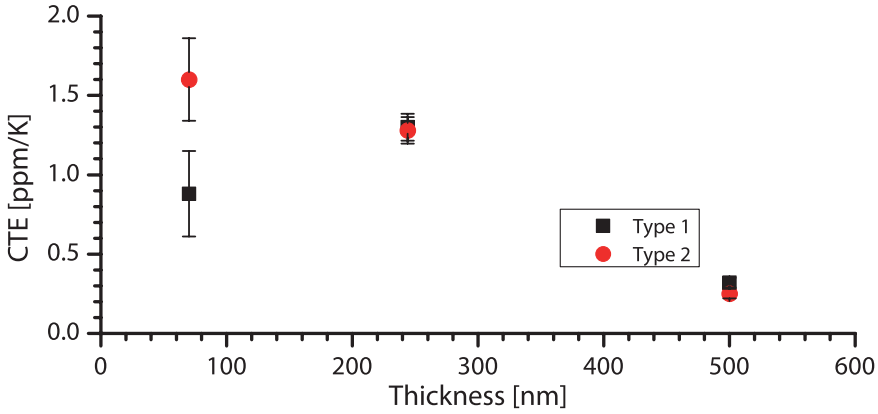

Figure 3.11: The CTE in thick and thin PECVD oxide layers.

3.7.1. Optical effects

Methods such as infrared spectroscopy have been widely applied to study the material variations [29, 34]. Infrared spectroscopy is based on the spectral absorption of the film in the infrared range, specifically at about $4.4\ \mu m$ and $11.4\ \mu m$, due to the absorption in Si-H groups [29]. Studying the variations of these absorption peaks provide a better understanding of the bonding characteristics and impurity content of the layers. In this work, the thickness of the layers is about 10 times lower than the wavelength range. Since the absorption exponentially decreases with the thickness, analyzing such a thin film results in insufficient spectral absorption for ensuring a reliable measurement. Therefore, these methods for analyzing thin films is not very suitable for this research. Variable angle spectroscopic ellipsometry (VASE) is a robust and reliable method to investigate the optical properties of the optical properties of the film from ultraviolet up to infrared, by measuring the ratio of the reflection of different polarization of the incident wave. The sensitivity of the VASE analysis is hence significantly higher than infrared spectroscopy. Furthermore, the refractive index of the material is directly relevant for the optical applications considered in this work. Thus, refractive index of the layers prior to and after the annealing step is measured.

For the optical filter applications, the optical design (layer thicknesses) is decisive which depends both on the physical thickness and on the (complex) refractive index information of the deposited film. In the multilayer airgap filter structures, the membrane is the high-index layer, and a high refractive index value is desirable. The extinction coefficient of the film is usually due to the contaminants that are incorporated in the film and must be minimized to achieve a high optical transmission. Furthermore, the changes in optical index provide an insight into the internal changes in the material after the annealing. In this study, the refractive index of the layers was analyzed using *VASE* (variable angle spectroscopic ellipsometry) method (J.A. Woollam Co, M2000) before and after the annealing cycles. The acquired data was then fitted using a Cauchy layer model to obtain the refractive index of the film

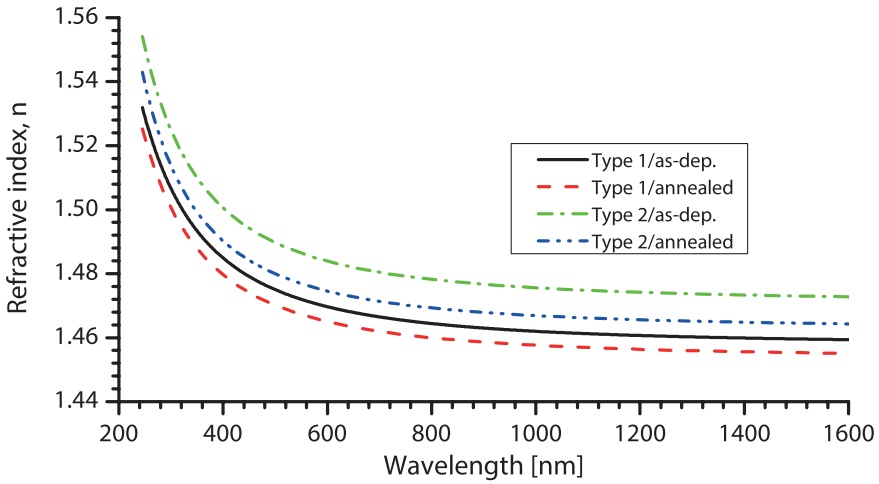

Figure 3.12: The refractive index of the PECVD oxides prior and after the annealing, measured by VASE.

[35] (see Chapter 2). The absorption coefficient was also fitted for each wavelength to obtain the residual absorbance of the films.

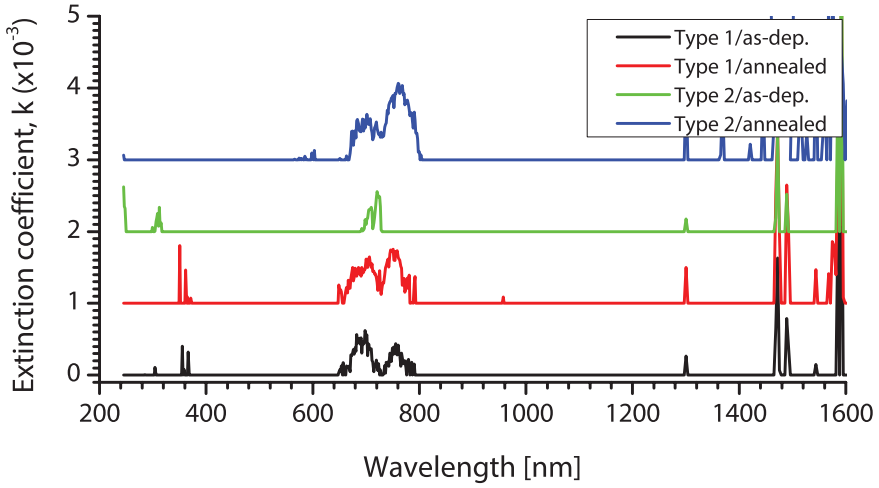

Figure 3.13: The stacked absorption coefficient plots of the PECVD oxides prior and after the annealing, measured by VASE. (The curves are shifted by 1×10^{-3}.)

Figure 3.12 shows the measured refractive index of the layers, before and after the annealing. It is interesting to note that the refractive index of Type 2 films is higher than Type 1. This difference is due to a higher N_2O-to-SiH_4 flow ratio during the deposition of Type 2 films. Therefore, the films are of a slightly different composition. Specifically, Type 2 has a higher N_2O-to-SiH_4 ratio (31.7 and 28.6 for Type 2 and Type 1, respectively) which means that the oxide is less stoichiometric (or

silicon rich). After annealing the refractive indexes of both PECVD film types were reduced. However, the reduction in the refractive index for the Type 2 is found to be higher (0.7% reduction, as compared to 0.4% for the Type 1, both at $400\ nm$). At the same time, the physical layer thicknesses do not change significantly after annealing (less than 1% for both oxide types). Thermal annealing effectively depletes the layer from the residual gasses. Decomposition of the Si-H bonds creates more voids [30] that result in a reduced effective refractive index. Therefore, the decrease in the refractive index indicates that the density of the Si-H bonds in the layer is reduced by the annealing. This reduction in Si-H bonds is higher in Type 2 which has a higher initial density of Si-H bonds. Therefore, the observation is in agreement with the suggested structural changes in terms of void formation mentioned already.

In terms of the optical design, the decrease in the refractive index is not desirable. The refractive-index-contrast defined as $\Delta = (n_H^2 - n_L^2)/2n_H^2$, is the commonly used criteria representing the optical performance of the filter. The relative change in the optical contrast at $400\ nm$ wavelength is calculated as 0.006 for type 1 and 0.011 for type 2 oxides. Therefore, even though the change in the refractive index is measurable in terms of the refractive index contrast, the variations in terms of the refractive index contrast are insignificant. It should also be noted that the reduction of the intensity of the transmitted light through an optical filter depends on the extinction coefficient k (which defines the absorption coefficient, α) of the film:

$$\begin{aligned} \alpha &= \frac{4\pi}{\lambda} k \\ \frac{I}{I_o} &= e^{-\alpha d} \end{aligned} \tag{3.8}$$

where I_o is the intensity of the incident light, λ is the light wavelength, and d is the depth that the light has traveled in the layer. Figure 3.13 shows the absorption coefficient of oxide thin-films before and after the annealing as measured by VASE method. The absorption coefficient for both oxide types was measured to be below 10^{-3} for the ultraviolet-visible spectrum. This extinction coefficient corresponds to about 5% reduction in the transmittance in a 10-period airgap filter.

3.8. Fabrication process-flow

Historically, manufacturing MEMS structures can be considered as an extension of integrated circuit (IC) fabrication. The micro-electro-mechanical-systems use the structural properties of available materials in the IC processing to bring actuation or sensing capabilities to the device. MEMS devices integrate multiple functionalities into a system, bridging the gap between the microelectronics and the physical realm. MEMS fabrication methods combine the batch fabrication capabilities of microelectronics with the new functionalities such as mechanical, optical, and chemical providing low-cost mass-fabricated systems. Several established processes in IC industry such as layer depositions, lithographic patterning, and etching are applied to manufacture MEMS devices. Special MEMS processes, such as deep reactive

ion etching (DRIE), have also been developed to enable the fabrication of different devices.

In this study, a CMOS-compatible surface micromachining fabrication process was designed for the fabrication of the airgap filters. The details of the fabrication will be discussed in Chapter 5. However, an understanding of the process is essential for the process design. The surface micromachining is an additive fabrication method in which layers are added to a substrate (deposition). Lithographic patterning and etching steps are then used to define the MEMS structure. This is in contrast to the bulk micromachining that the structures are etched into the substrate.

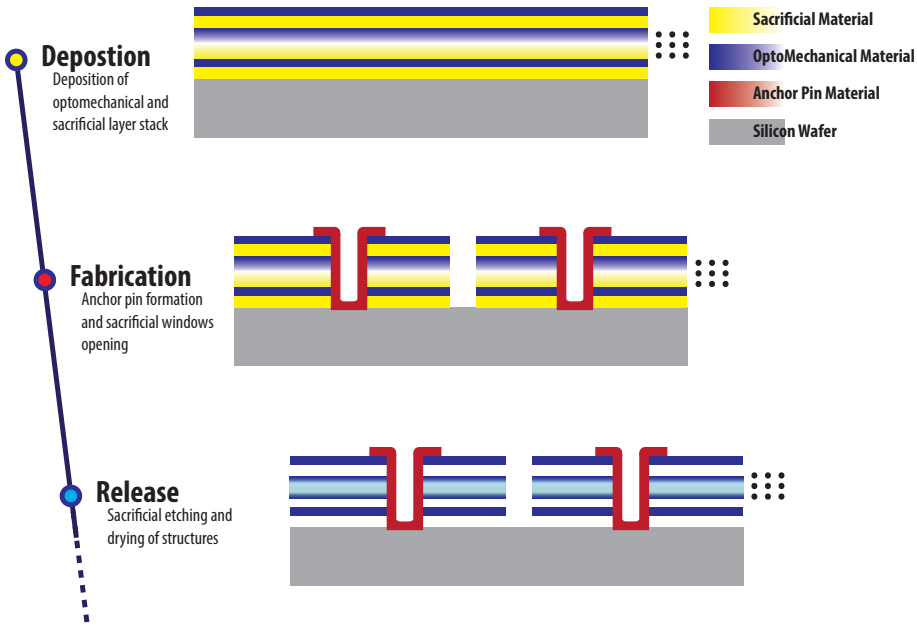

Figure 3.14: Schematics of the fabrication process flow steps. **Deposition:** Repetitive deposition of sacrificial and mechanical layer system; **Fabrication:** Fabrication of the pin-shaped anchors and sacrificial etching openings; and **Release:** sacrificial etching and stiction-free drying.

The simplified fabrication process flow of airgap filters is shown in Figure 3.14. The fabrication can be divided into three main stages. Initially sacrificial and optomechanical layers were deposited alternatingly. The number and thickness of the deposited layers are chosen according to the optical design. The thickness of the sacrificial layers is also equal to the airgap layers in the optical design. In the second stage, the mechanical structure is fabricated in several steps. A set of openings is patterned and etched through the layers. An anchor layer is then deposited and was used for covering the access holes and forming a pin-shape anchoring. The sacrificial openings are then patterned and etched through the structure. In the release stage, the sacrificial layers are isotropically removed, while the anchors hold the structure. Finally, the structures undergo a stiction-free drying process (for the

case of the liquid phase drying).

3.9. Effects of stress in thin-film membranes

The airgap optical filters do not comprise any moving parts, and the residual stress is typically the dominating force acting on the structure. The dielectrics thin-films are also classified as brittle materials, as these are not ductile under stress, and plastic deformation does not occur. Therefore, after reaching the ultimate strength, the material would fracture [36]. The typical stress-strain curves of a brittle and a ductile material are shown in Figure 3.15.

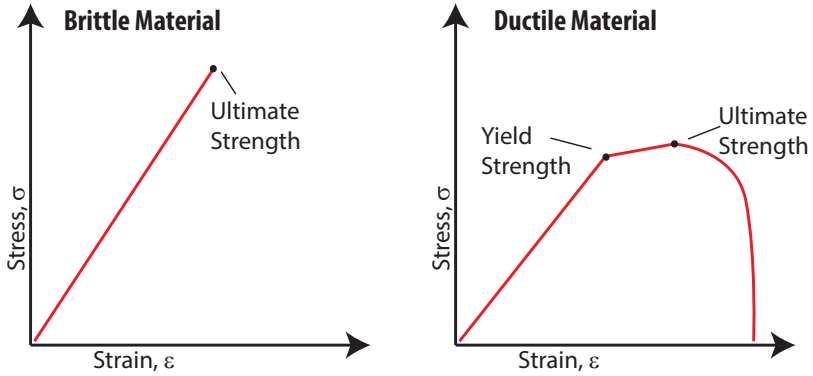

Figure 3.15: A typical stress-Strain curve for brittle and ductile materials [36].

In brittle materials, a high stress energy in the films can result in a transition from elastic deformation into fracture initiation and propagation. Compressive films tend to expand, and tend to cause delamination at the interface and buckling. In tensile films, the tendency is to shrink, and beyond its ultimate strength micro-cracking occurs [37]. Various material and geometry factors affect the stress distribution within the membrane. The overall effects must be characterized and studied for a successful design of an airgap optical filter.

3.9.1. Fracture

Hutchinson and Sou have comprehensively studied the crack propagation in pre-tensioned (tensile) films [37]. According to the model proposed, a critical thickness at which the film starts to crack due to its tensile stress can be defined as

$$h_c = \frac{\Gamma \tilde{E}_f}{Z\sigma^2} \tag{3.9}$$

in which $\tilde{E} = E/1 - \nu$ is the biaxial modulus and Γ is the *work of fracture* of the film. Z is a dimensionless driving force factor and depends on the type of the crack. As stated by [38] in the case of a surface crack, i.e. fracture starting from the surface propagating toward the interface, the Z is equal to 3.951, and for the channeling cracks, propagating parallel the film, the Z factor is 1.976. Rewriting

the equation 3.9 provides an estimation of the maximum applicable tensile stress exerted on the membrane for a given membrane thickness.

$$\sigma_c = \sqrt{\frac{\Gamma \tilde{E}_f}{Zh}} \tag{3.10}$$

Fracture toughness K is a criterion for resistance to propagation of a crack in the material. In terms of fracture toughness of mode-I cracks (tensile opening), K_{IC}, the relation would become:

$$\Gamma = \frac{K_{IC}^2}{E} \tag{3.11a}$$

$$\sigma_c = \frac{K_{IC}}{\sqrt{Zh(1-\nu)}} \tag{3.11b}$$

Table 3.5: Ultimate strength (critical stress) for common dielectrics available in MEMS fabrication processes. The ultimate strength is calculated for a $60\ nm$ thick layer.

Material	K_{IC} [MPa $\sqrt{m}$]	Critical Stress [GPa]
PECVD SiO_2	0.77 [39]	1.83
LPCVD low stress SiN	1.8 [38]	4.26
Si_3N_4 (Stoichiometric)	14 [39]	33.20
Alumina (Al_2O_3)	2.34 [40]	5.5
PECVD SiO_2: Type 2 (this work)	0.75	1.83

An indirect measurement method can be applied to estimate the fracture toughness of the deposited layer. Several samples were coated with a tensile layer of different values of thickness and visually analyzed to estimate the critical thickness (h_c). The micro cracks are visible if the thickness of the oxide layer exceeds the critical thickness. The fracture toughness is proportional to the square root of the critical thickness ($K_{IC} \propto \sqrt{h_c}$), hence, the error in fracture toughness in this method is $\Delta K_{IC}/K_{IC} = \Delta h_c/2h_c$. This method was used to estimate the fracture toughness of type-2 oxide after annealing at 600 °C. Figure 3.16 and 3.17 show the fracture propagation in tensile stress PECVD oxide layers (type 2) above the critical thickness. The fracture toughness of the oxide used here was measured to be at least $0.75 \pm 0.05\ MPa\sqrt{m}$. Table 3.5 lists the fracture toughness of some common dielectrics and their respective critical stress (stress at ultimate strength). It should be noted that the fracture toughness in thin-films depends strongly on the structural defects within or on the surface of the film. Therefore, the deposition conditions, as well as the material properties, play a significant role in the resistance to fracture. Even though the typical average residual stress is well below the ultimate strength, the stress can build up in the sharp corners and exceed the ultimate strength.

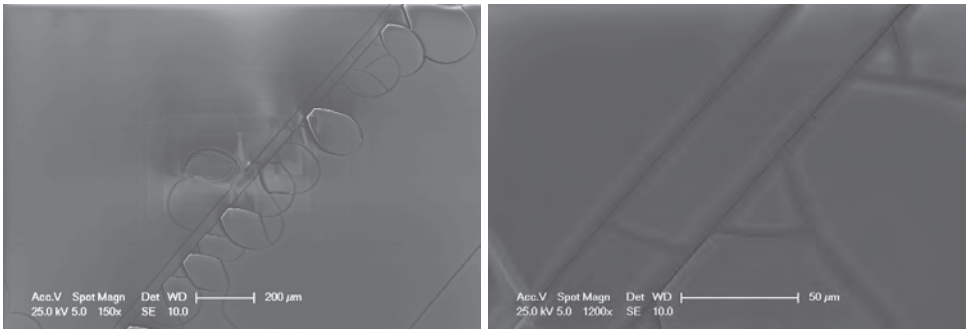

Figure 3.16: SEM micrographs of fracture propagation in $5\mu m$ thick tensile PECVD oxide layers.

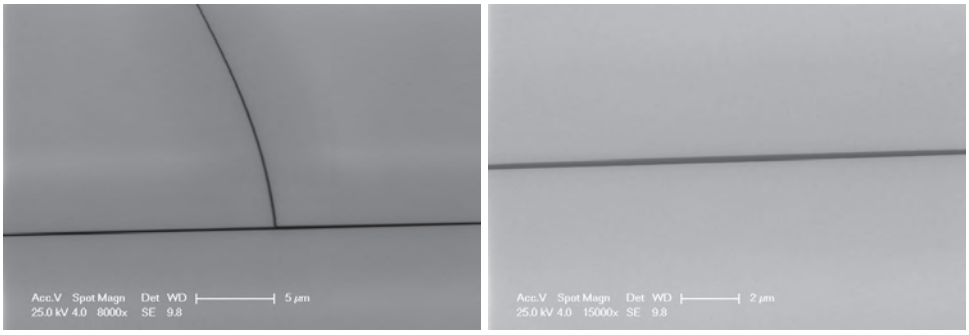

Figure 3.17: SEM micrographs of fracture propagation in $3\mu m$ thick tensile PECVD oxide layers.

3.9.2. Effect of Perforation on the membrane strength

The sacrificial release is the final step in the fabrication. Several access windows must be opened in the membrane to enable the etching of the underlying sacrificial layers. The openings introduce stress-critical points in the membrane, thus making the membrane susceptible to fracture. The perforation usually results in weakening of the membrane and lowering the ultimate strength (see Figure 3.15). In first approximation suggested by [39, 40] the reduction in the Young's modulus (E) and hence the ultimate strength (σ_{max}) is proportional to the perforation factor, i.e. the area of the perforated holes to the total area of the membrane:

$$E_p = (1 - P)E \tag{3.12a}$$

$$\sigma_{max_p} = (1 - P)\sigma_{max} \tag{3.12b}$$

where the Ep is the Young's modulus of the perforated membrane and $P = (\text{Perforated area})/(\text{Total area})$ is the perforation factor. In some applications such as micro-sieves, the perforation factor is typically high (up to 0.5) and hence the strength of the membrane is significantly reduced. Compared to the sieving applications, the needed perforation in the optical membranes considered here is typically

much lower ($P \sim 0.005$) which results in an almost 0.5% decrease in the Young's modulus. Therefore, the perforation does not significantly affect the stiffness of the membrane. In terms of the fracture, however, the perforation locally increases the stress concentrations in the membrane [41] and provides the fracture initiation sites. Therefore, despite that the effect of the perforation on the rigidity of the membrane is marginal, it can locally affect the membrane structure and flatness.

3.9.3. Finite Element Analysis

The *von Mises* yield criterion is commonly used in the context of mechanical structures (including MEMS) to evaluate the local concentration of stress in a structure. In distortion energy theory [42], von Mises stress is defined as a scalar projection of the stress tensor elements. Accordingly the von Mises stress is stated as a function of the principal stress components:

$$\sigma_{von\ Mises} = \sqrt{\frac{1}{2}[(\sigma_1 - \sigma_2)^2 + (\sigma_2 - \sigma_3)^2 + (\sigma_3 - \sigma_1)^2]}. \tag{3.13}$$

When the $\sigma_{von\ Mises}$ reaches the yield strength, the material would change from elastic deformation to irreversible plastic deformation. As discussed in this section, for brittle material exceeding the ultimate strength would result in fracturing of the device. Therefore, in the context of this thesis the distinction between the ultimate strength and fracture failure stress is avoided. Von Mises stress provides a criterion to ensure that the membrane will survive a certain level of tensile stress. In this approach the maximum von Mises stress, while considering the safety factor (of 10), must be lower than the yield strength of the membrane material.

Finite element analysis (FEA) were carried out using a commercially available software package (COMSOL Multiphysics) to evaluate the von Mises stress in the membrane structure. The residual stress of each layer was measured (Table 3.4) and used for the finite element modeling. Comparing the resulting von Mises stress distribution with the critical stress obtained from the theory of fractures (section 3.9.1) would identify the fracture-prone areas in the structure. An understanding of the FEM is essential for ensuring the reliability of the results. The finite element method uses advanced numerical algorithms to solve the partial differential equations (PDE) that are governing the physical system. The basis of the method relies on the division (discretization) of the geometry into a set of *elements* or *mesh*. PDEs are subsequently estimated and solved for each element based on the conditions set on the boundaries of the domain.

While the discretization provides solutions to the complex geometries in which an analytical solution is impossible, it is important to understand (and to try and avoid) the drawbacks of any FEA. First, the FEA at its best provides an approximated solution to the appropriate PDE set. The accuracy of result mainly depends on the element size. Therefore, the mesh generation must be carefully studied. The elements have to be sufficiently small (locally) to enable the analysis of the minimum physical dimensions of the model to account properly for the changes occurring in the structure. Smaller elements (and thus more elements to cover the

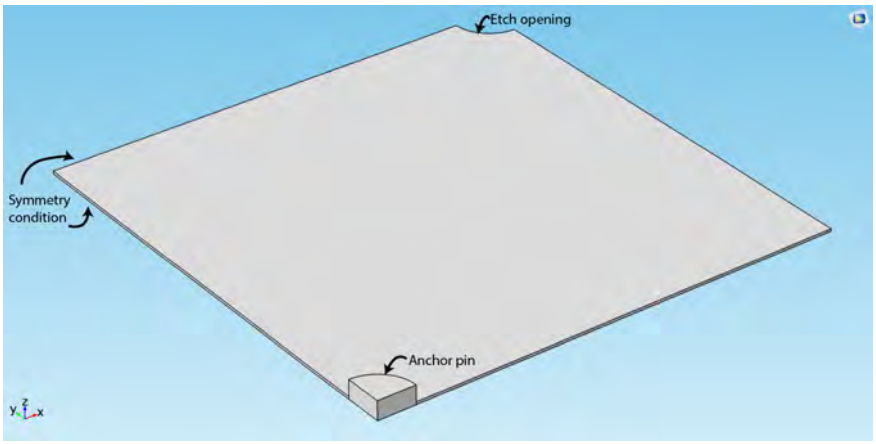

Figure 3.18: 3D model of the membrane, COMSOL Multiphysics

relevant dimensions of the structure) result in a more accurate solution. However, the larger the number of elements requires a higher computation power (and time). This trade-off between the elements size and computation power usually limits the accuracy of the solutions. Finally, the proper boundary conditions must be applied[1].

Steady-state (stationary) FEA was applied to study the effect of the residual stress in a clamped semi-rectangular membrane. The structure consists of a semi-infinite flat membrane, anchored with a set of periodically repeating cylindrical pins. A set of circular openings (as is required for the sacrificial etching) is also cut through the membrane to account for the stress distribution effects of the openings. A unit cell structure, considering the symmetries of the design, was designed in such as way that it is possible to take the stress concentration effects at the openings into account. Figure 3.18 shows the 3D model of a unit cell of the membrane array designed in COMSOL Multiphysics. The dimensions are listed in Table 3.6.

Table 3.6: Dimensions of the membrane used for FEM analysis of airgap

Material	Dimension [µm]
Membrane thickness	70
Anchor periodicity length	25
Access-hole periodicity	25
Anchor diameter	2
Access-hole diameter	2

The so-called **Roller** boundary condition was applied to the side walls. This

[1]This is not specific to FEA and applies also to any set of integral equations.

boundary condition ensures that the displacement vector ($\mathbf{u}$) along the surface normal ($\mathbf{n}$) is zero ($\mathbf{u}.\mathbf{n} = 0$). The structure can move freely in the normal plane. This boundary condition is hence used to imply a periodicity of the structure. The anchors were defined as the fixed constraints $\vec{u} = 0$. In the mesh generation, the minimum element size was chosen to be $1/5\ th$ of the membrane thickness. Furthermore, extra mesh refinement made at the corners would result in an average mesh quality of better than 0.5 and minimum mesh quality of better than 0.1 over the entire volume of the membrane (Figure 3.19). This is in accordance with the mesh quality requirement of higher than 0.1 for a reliable discretization of the geometry [43]. Mesh quality is a dimensionless quantity between 0 and 1 representing the regularity of the mesh element's shape. The subtle variations in the mesh quality arise from the random nature of the mesh generation and do not have an implication on the simulation results.

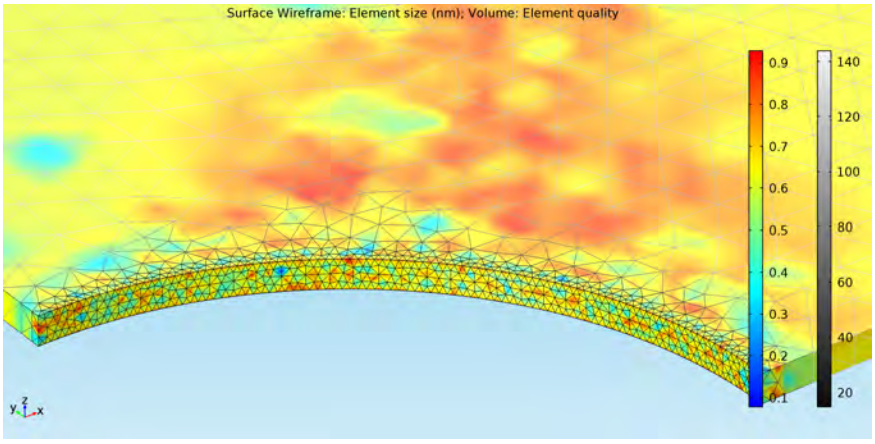

Figure 3.19: Customized mesh generation at the anchoring points and openings ensures an accurate result; The grayscale wireframe represents the element size (in nm), and the rainbow distribution shows the element quality of the generated mesh.

The stationary solver (default settings) was used to study the effects of an initial isotropic stress of $300MPa$ on the membrane. Figures 3.20 and 3.21 shows the von Mises stress distribution and thin-film deformation of the membrane due to the residual stress in the film. The results indicate that for a residual stress of $300MPa$ the von Mises stress around the opening is about $400MPa$ and increases to $550MPa$ at the anchors. As these values are obtained for an ideal case (i.e. no material defect), usually a safety factor of 2 is considered for proper structural design. When these local stresses exceed the yielding strength, a fracture occurs in the membrane structure.

Furthermore, as this model only considers an isotropic stress in the film, the model (and the PDEs) is symmetric over the thickness and only in-plane displacement occurs.

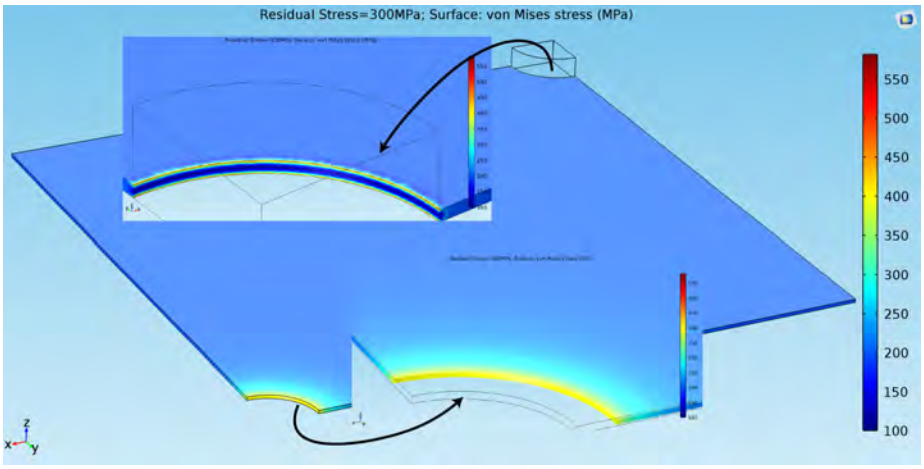

Figure 3.20: Von Mises stress distribution over a membrane unit cell with an isotropic residual stress: Isotropic residual stress of 300 MPa (Tensile).

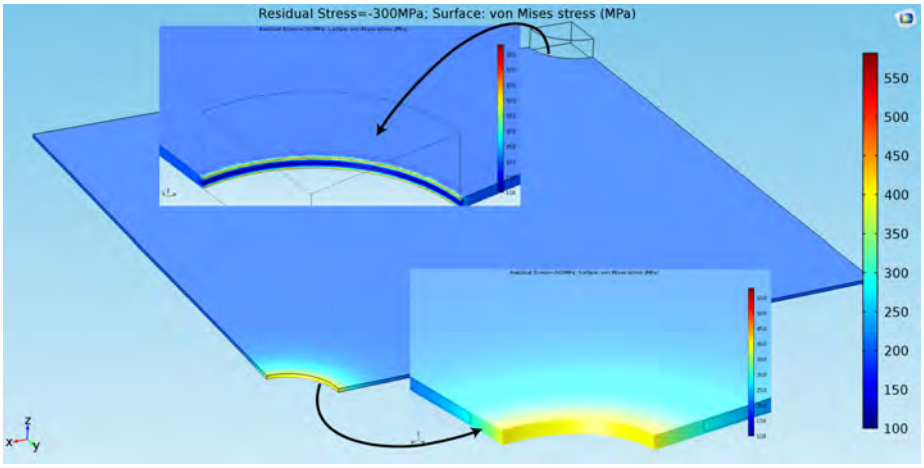

Figure 3.21: Von Mises stress distribution over a membrane unit cell with an isotropic residual stress: Isotropic residual stress of −300 MPa (Compressive).

3.10. Stiction in surface-micromachined airgap-based optical filters

Stiction is the unwanted adhesion of two adjacent surfaces during the fabrication or operation of the MEMS devices. Preventing stiction is one of the main yield concerns in MEMS devices. Since the optical airgap structures do not have any moving parts the stiction during the operation is not concerned here. At the final stage of the fabrication, however, due to the large aspect ratio of the structures and low roughness, the effect of the stiction is prominent. The sacrificial release of the

membranes is the very last step in the fabrication of the device. During this step, a sacrificial layer is removed in an isotropic etching step via the openings on the front side. To avoid stiction, special measures must be taken during the transition from the liquid environment of the etchant to the air (or vacuum).

In order to avoid stiction in optical membranes, it is important to understand affecting forces and estimate their effects in the fabrication of such devices. Generally, the adhesion between two surfaces can be due to the capillary forces, hydrogen bridging, Electrostatic forces and Van der Waals forces acting on the surfaces. Tas *et al.* [44] comprehensively studied the effects of the various forces on the stiction in the MEMS fabrication. Comparing the forces involved, the capillary force is dominant stiction inducing factor during the fabrication. A thin layer of liquid under a suspended area would attract the suspended surface due to the pressure drop inside the liquid. The attractive capillary force acting on the suspended area can be defined as:

$$F = -\frac{2A\gamma_{la}cos\theta_c}{g}, \tag{3.14}$$

where g is the gap, θ_c is the contact angle between the liquid and solid, A is the wet area, and γ_{la} is the surface tension of liquid-air interface. In equilibrium an equally but positive force acts on the membrane (typically by the mechanical stiffness of the structure) thus keeping the area separated. During the drying, the two forces compete and define the outcome. The total energy in such a system is the sum of the stored elastic energy and the surface energy due to the stiction, while the system tends to get to the minimum energy state. The adhesion force is proportional to both the wetted area (A) and the gap size (A). At the onset of the contact, other short-distance forces such as hydrogen bridging and Van der Waals forces become effective and the structure permanently adheres to the surface. The average adhesion energies for stiction forces are listed in Table 3.7.

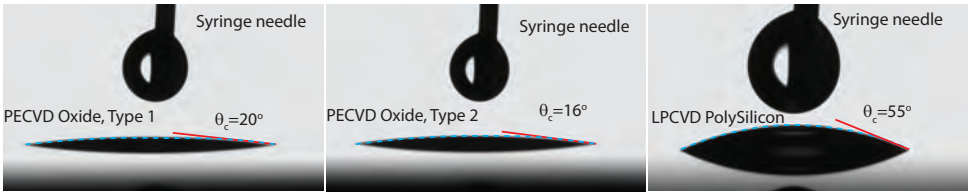

Figure 3.22: Contact angle of a water droplet on PECVD oxide layers. The low contact angle in oxide layers is a measure of hydrophilicity of the layers. The contact angle of LPCVD Polysilicon (with $2nm$ native oxide layer) is reported for the sake of comparison.

In the UV-visible optical membrane filters, the thickness of each membrane is in the range of sub-$100nm$, while the membranes are span over a range of several microns to minimize the scattering effects of the holes and anchors. This requires of drying structures with a thickness to length ratio of more than $1:250$. Furthermore, the oxide layers are typically hydrophilic surfaces and hence the contact angle of aqueous solution on (and between) the membranes is almost zero (Figure 3.22).

The roughness of the oxide layers is also low (in the order of few nm). These effects result in strong contact forces due to the hydrogen bridging and Van der Waals force. The combination of the dimensional and material characteristics available in optical airgap filters provide a very challenging case.

Table 3.7: Typical stiction forces in MEMS structures[44]

Stiction force	Active range	Surface energy [mJ/m^2]
Hydrogen bridging	contact	100
Van der Waals	< 20 nm	12 - 140
Capillary force	~1/d	146 (water at 20 °C)

The stiction depends on the rigidity of the structure as well as on the capillary forces involved. For a cantilever beam, for instance, the maximum length of the cantilever that can be fabricated (with evaporation drying methods) can be analytically calculated as [44]:

$$l_{critical} = \sqrt[4]{\frac{3Et^3g^2}{16\gamma_{la}cos\theta_c}}. \tag{3.15}$$

It is shown that for double-clamped beams and circular membranes the same relation still holds except the constant. Considering the order of magnitudes in the airgap-based optical filters ($t \sim g \sim 100\ nm,\ l \sim 10\ \mu m$) drying requires a maximum adhesion energies in the order of $0.1\ mJ/m^2$, which is two orders of magnitude lower than that of typical solvents 3.8.

Table 3.8: Surface tension of typical transfer liquids at 20 °C [45].

Liquid	Surface tension [mJ/m^2]
Water	72.8
Acetone	25.2
n-hexane	18.4

For complex structures (such as the pin anchored airgap), finding the analytical solution is cumbersome or is not possible. FEA proves to be an efficient tool to study various effects in complex structures and hence was used for the analysis of the stiction in the membrane. The stiction force can be added as a boundary load that is proportional to the gap size. Since this study is nonlinear, numerical techniques such as the load ramping are used to improve the convergence of the Newton-Raphson iterative (stationary) solver [43]. In this method, the maximum acceptable adhesion energy (in terms of surface tension) to avoid the stiction can be obtained.

To demonstrate the feasibility of the FEA, the critical length in a cantilever beam was studied and the result was in accordance with the values reported by [44].

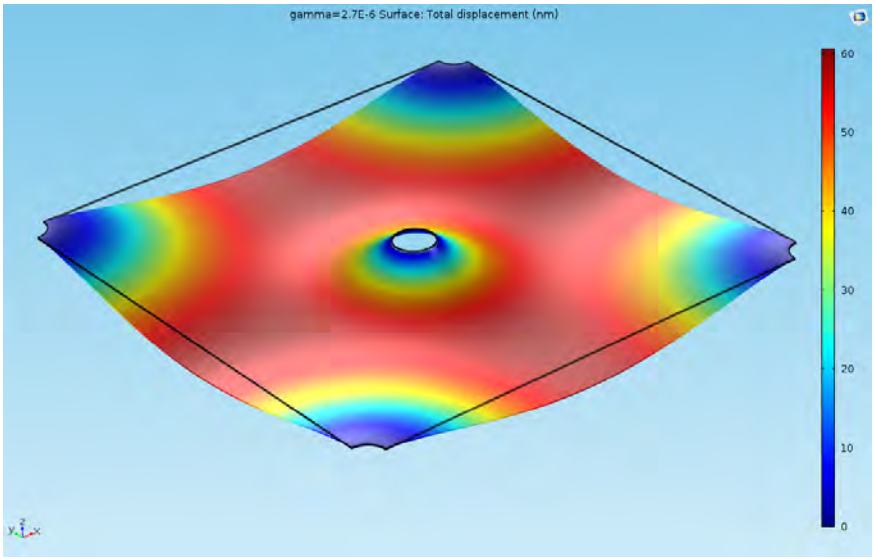

Figure 3.23: FEA of the stiction in an airgap-based optical filter structure. A capillary force due to the stiction energy of $2.7\mu J/m^2$ is applied to the membrane

Accordingly a $100\ \mu m$ long, $5\mu m$ thick cantilever with a $1\mu m$ gap size touches the substrate if a surface energy of about $50mJ/m^2$ is applied during the drying. This is roughly in agreement with the analytical result that for such a cantilever, a surface energy of about $70mJ/m^2$ results in permanent stiction of the beam.

A similar analysis was applied to the optical membranes. Figure3.23 shows the membrane displacement due to the stiction energy of $2.7\mu J/m^2$. Based on the FEA, a transfer liquid with a surface tension of less than about $3\ \mu J/m^2$ is required to avoid any stiction to the substrate. This is well below the surface tension of most liquids [see Table 3.8]. Consequently, special measures must be taken to avoid stiction in the membranes.

3.10.1. Drying methods

Several methods have been studied and used in the MEMS fabrication to avoid stiction. This section studies the various methods and compares their characteristics for successful drying of Airgap filters.

Low surface tension liquids

Lowering the surface tension of the liquid environment by transferring the samples to a low-surface tension liquid or and/or increasing the contact angle of the liquid by changing the substrate material is a quite well-known technique. However, according to the FEM analysis, a very low surface tension is necessary to avoid any stiction, while material (and hence the contact angle) cannot be chosen freely.

Freeze-sublimation drying

Freeze drying method avoids the stiction due to the capillary forces of the liquids by freezing the carrier liquid and subsequent sublimation of the solid phase to the vapor phase. The sublimation is typically performed at atmospheric pressure and under nitrogen flow until all the solid has evaporated. Figure 3.24 shows the typical schematic of a pressure-temperature phase diagram of carrier liquids used for sublimation drying.

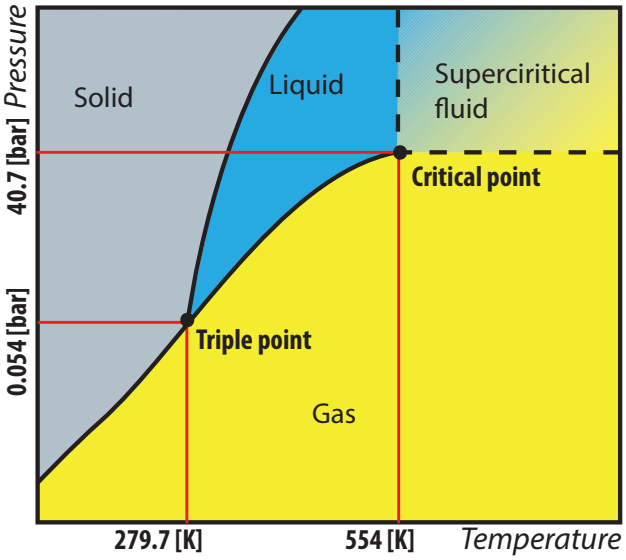

Figure 3.24: Schematic representation of pressure-temperature phase diagram of Cyclohexane. Triple and critical point data were adapted from NIST Chemistry WebBook [46].

The schematic of the freeze-sublimation drying process is depicted in Figure 3.25. After etching, the sample is transferred to H_2O bath to dilute the etchant and stop the etching. Subsequently, the samples go trough Acetone bath, Isopropanol bath and finally to a Cyclohexane bath. Cyclohexane has a high vapor pressure and low latent heat during the sublimation (as compared to water) and widely used as the freeze-drying carrier liquid. Finally, the samples are transferred to the cooling unit, which is set at a temperature below the triple point (6.6 °C). The frozen cyclohexane then gradually sublimated in an N_2 flow. The samples are then heated up to room temperature to avoid the water condensation on the samples. Since the drying step skips the liquid phase, the stiction is avoided. The vapor has to escape from the sacrificial openings. Therefore, the sublimation rates for long sacrificial distances is rather low.

Supercritical drying

Supercritical drying prevents the stiction due to the capillary forces via phase transition of the carrier liquid to a supercritical phase. Generally, the variation of temperature and pressure in pure component results in a phase transition between solid,

Figure 3.25: Schematic diagram of the sequence of freeze sublimation drying process.

liquid, and vapor (gas). At the critical point, the distinction between liquid and vapor phase vanishes. This new phase is called supercritical fluid, and the physical properties of the liquid change dramatically. Since no liquid-gas interface exists, there is no surface tension in the supercritical fluid. Therefore, the capillary forces do not act on the structures. CO_2 has a low critical temperature and pressure and hence is widely used for the supercritical drying. The pressure-temperature phase diagram and variation of the surface tension [47] of CO_2 is shown in Figure 3.26.

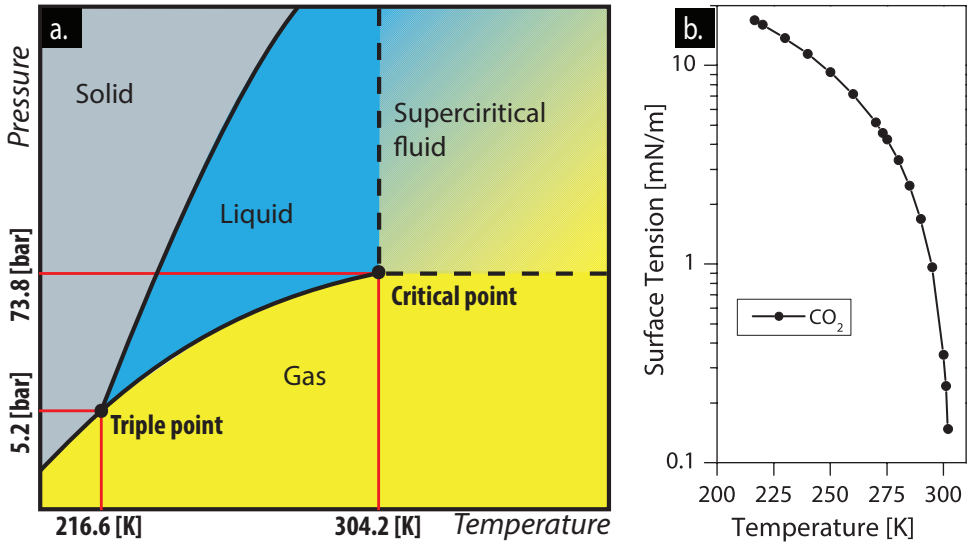

Figure 3.26: (a) Schematic representation of pressure-temperature phase diagram of CO_2. Triple and critical point data were adapted from NIST Chemistry WebBook [46]. (b) variation of surface tension in CO_2 near the critical point obtained from [47].

The schematic of the drying process is shown in figure 3.27. After the etching, the samples go through H_2O, Acetone, and Isopropanol, and high purity Isopropanol baths to replace the H_2O in the gaps with Isopropanol alcohol. Samples are subsequently transferred to the CPD Module, which is filled with pure Isopropanol. The CPD module replaces the Isopropanol with liquid CO_2, and the pressure and temperature are subsequently brought to those associated with the critical state (Figure 3.26.a). Venting the chamber gradually removes the CO_2 from

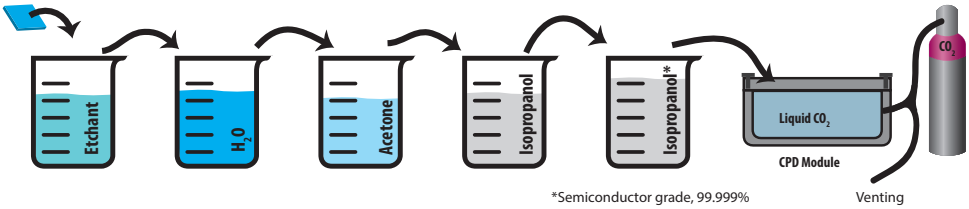

Figure 3.27: Schematic of the sequence of operations in critical point drying

the gaps, and the structure will be released. Due to the reliability and repeatability of the results, the CPD technique has been used in this research for the drying purpose.

Other methods

Other methods such as adding temporary supports to strengthen the structure and dry (plasma or vapor phase) sacrificial etching to avoid the use of liquids [44] are also presented in the literature.

References

[1] J. Laconte, D. Flandre, and J. Raskin, *Micromachined Thin-Film Sensors for SOI-CMOS Co-Integration* (Springer US, 2006) Book section 3, pp. 47–103.

[2] W. Buckel, *Internal stresses,* Journal of Vacuum Science & Technology **6**, 606 (1969).

[3] X. Zhang, K. S. Chen, R. Ghodssi, A. A. Ayón, and S. M. Spearing, *Residual stress and fracture in thick tetraethylorthosilicate (teos) and silane-based pecvd oxide films,* Sensors and Actuators A: Physical **91**, 373 (2001).

[4] L. B. Freund and S. Suresh, *Thin Film Materials* (Cambridge University Press, 2004) cambridge Books Online.

[5] G. Lucovsky, M. J. Mantini, J. K. Srivastava, and E. A. Irene, *Low-temperature growth of silicon dioxide films: A study of chemical bonding by ellipsometry and infrared spectroscopy,* Journal of Vacuum Science & Technology B **5**, 530 (1987).

[6] J. Thurn and R. F. Cook, *Stress hysteresis during thermal cycling of plasma-enhanced chemical vapor deposited silicon oxide films,* Journal of Applied Physics **91**, 1988 (2002).

[7] A. K. Sinha, H. J. Levinstein, and T. E. Smith, *Thermal stresses and cracking resistance of dielectric films (SiN, Si_3N_4, and SiO_2) on Si substrates,* Journal of Applied Physics **49**, 2423 (1978).

[8] Y. Okada and Y. Tokumaru, *Precise determination of lattice parameter and thermal expansion coefficient of silicon between 300 and 1500 k,* Journal of Applied Physics **56**, 314 (1984).

[9] T. M. Adams and R. A. Layton, *Introductory MEMS: fabrication and applications*, Vol. 70 (Springer Science & Business Media, 2009).

[10] M. Morita, T. Ohmi, E. Hasegawa, M. Kawakami, and M. Ohwada, *Growth of native oxide on a silicon surface,* Journal of Applied Physics **68**, 1272 (1990).

[11] A. Szekeres and P. Danesh, *Mechanical stress in SiO_2/Si structures formed by thermal oxidation of amorphous and crystalline silicon,* Semiconductor Science and Technology **11**, 1225 (1996).

[12] E. Kobeda and E. A. Irene, *A measurement of intrinsic SiO_2 film stress resulting from low temperature thermal oxidation of Si,* Journal of Vacuum Science & Technology B **4**, 720 (1986).

[13] R. W. Johnson, A. Hultqvist, and S. F. Bent, *A brief review of atomic layer deposition: from fundamentals to applications,* Materials Today **17**, 236 (2014).

[14] S. Roy and C. K. Sarkar, *MEMS and Nanotechnology for Gas Sensors* (CRC Press, 2015) Chap. Deposition, pp. 31–48, 0.

[15] L. A. Chow, *6 - equipment and manufacturability issues in CVD processes,* in *Handbook of Thin Film Deposition (Third Edition)*, edited by K. Seshan (William Andrew Publishing, Oxford, 2012) third edition ed., pp. 127 – 178.

[16] B. Bhushan, ed., *Encyclopedia of Nanotechnology* (Springer Netherlands, Dordrecht, 2012) Chap. Low-Pressure Chemical Vapor Deposition (LPCVD), pp. 1233–1233.

[17] H. Frey, *Handbook of Thin-Film Technology*, edited by H. Frey and H. R. Khan (Springer Berlin Heidelberg, Berlin, Heidelberg, 2015) Chap. Chemical Vapor Deposition (CVD), pp. 225–252.

[18] A. Tarraf, J. Daleiden, S. Irmer, D. Prasai, and H. Hillmer, *Stress investigation of PECVD dielectric layers for advanced optical MEMS,* Journal of Micromechanics and Microengineering **14**, 317 (2004).

[19] P. S. Prevey, *X-ray diffraction residual stress techniques,* ASM International, ASM Handbook. **10**, 380 (1986).

[20] C.-H. Ma, J.-H. Huang, and H. Chen, *Residual stress measurement in textured thin film by grazing-incidence x-ray diffraction,* Thin Solid Films **418**, 73 (2002).

[21] J. W. Ager and M. D. Drory, *Quantitative measurement of residual biaxial stress by raman spectroscopy in diamond grown on a ti alloy by chemical vapor deposition,* Phys. Rev. B **48**, 2601 (1993).

[22] M. T. Hutchings, P. J. Withers, T. M. Holden, and T. Lorentzen, *Introduction to the characterization of residual stress by neutron diffraction* (CRC Press, 2005) Chap. Introduction, pp. 1–23, 0.

[23] B. P. van Drieënhuizen, J. F. L. Goosen, P. J. French, and R. F. Wolffenbuttel, *Comparison of techniques for measuring both compressive and tensile stress in thin films,* Sensors and Actuators A: Physical **37–38**, 756 (1993).

[24] K.-S. Chen and K.-S. Ou, *Chapter eighteen - MEMS residual stress characterization: Methodology and perspective,* in *Handbook of Silicon Based MEMS Materials and Technologies*, Micro and Nano Technologies, edited by V. Lindroos, M. Tilli, A. Lehto, and T. Motooka (William Andrew Publishing, Boston, 2010) pp. 305 – 316.

[25] G. G. Stoney, *The tension of metallic films deposited by electrolysis,* Proceedings of the Royal Society of London A: Mathematical, Physical and Engineering Sciences **82**, 172 (1909), http://rspa.royalsocietypublishing.org/content/82/553/172.full.pdf .

[26] K.-S. Chen and K.-S. Ou, *Modification of curvature-based thin-film residual stress measurement for MEMS applications,* Journal of Micromechanics and Microengineering **12**, 917 (2002).

[27] H. Frey and T. Helmut, *Handbook of Thin-Film Technology*, edited by H. Frey and H. R. Khan (Springer Berlin Heidelberg, Berlin, Heidelberg, 2015) Chap. Measurements of Thin Layers After the Coating Process, pp. 301–355.

[28] E. Bustarret, M. Bensouda, M. C. Habrard, J. C. Bruyère, S. Poulin, and S. C. Gujrathi, *Configurational statistics in a-$Si_xN_yH_z$ alloys: A quantitative bonding analysis,* Phys. Rev. B **38**, 8171 (1988).

[29] M. S. Haque, H. A. Naseem, and W. D. Brown, *Correlation of stress behavior with hydrogen-related impurities in plasma-enhanced chemical vapor deposited silicon dioxide films,* Journal of Applied Physics **82**, 2922 (1997).

[30] K.-S. Chen, X. Zhang, and S.-Y. Lin, *Intrinsic stress generation and relaxation of plasma-enhanced chemical vapor deposited oxide during deposition and subsequent thermal cycling,* Thin Solid Films **434**, 190 (2003).

[31] S. Bigl, W. Heinz, M. Kahn, H. Schoenherr, and M. Cordill, *High-temperature characterization of silicon dioxide films with wafer curvature,* JOM **67**, 2902 (2015).

[32] A. Bagolini, A. S. Savoia, A. Picciotto, M. Boscardin, P. Bellutti, N. Lamberti, and G. Caliano, *Pecvd low stress silicon nitride analysis and optimization for the fabrication of cmut devices,* Journal of Micromechanics and Microengineering **25**, 015012 (2015).

[33] T. Van der Donck, J. Proost, C. Rusu, K. Baert, C. Van Hoof, J.-P. Celis, and A. Witvrouw, *Effect of deposition parameters on the stress gradient of CVD and PECVD poly-SiGe for MEMS applications,* (2004) pp. 8–18.

[34] J.-H. Zhao, T. Ryan, P. S. Ho, A. J. McKerrow, and W.-Y. Shih, *Measurement of elastic modulus, poisson ratio, and coefficient of thermal expansion of on-wafer submicron films,* Journal of Applied Physics **85**, 6421 (1999).

[35] J. Gerald E. Jellison, *Chapter 3 - data analysis for spectroscopic ellipsometry,* in *Handbook of Ellipsometry*, edited by H. G. T. A. Irene (William Andrew Publishing, Norwich, NY, 2005) pp. 237 – 296.

[36] A. L. Hartzell, M. G. Silva, and H. R. Shea, *MEMS Reliability* (Springer US, Boston, MA, 2011) Chap. In-Use Failures, pp. 85–177.

[37] J. W. Hutchinson and Z. Suo, *Advances in Applied Mechanics*, Vol. Volume 29 (Elsevier, 1991) Chap. Mixed Mode Cracking in Layered Materials, pp. 63–191.

[38] C. A. Zorman, R. C. Roberts, and L. Chen, *MEMS Materials and Processes Handbook*, edited by R. Ghodssi and P. Lin (Springer US, Boston, MA, 2011) Chap. Additive Processes for Semiconductors and Dielectric Materials, pp. 37–136.

[39] W. S. Yang, S. M. Cho, H. Ryu, S. H. Cheon, B. G. Yu, and C. A. Choi, *Deformation reduction of a mems sensor by stress balancing of multilayer,* in *Sensor Technologies and Applications, 2008. SENSORCOMM '08. Second International Conference on* (2008) pp. 391–395.

[40] C. Van Rijn, M. van der Wekken, W. Nijdam, and M. Elwenspoek, *Deflection and maximum load of microfiltration membrane sieves made with silicon micromachining,* Microelectromechanical Systems, Journal of **6**, 48 (1997).

[41] I. Chasiotis and W. G. Knauss, *The mechanical strength of polysilicon films: Part 2. size effects associated with elliptical and circular perforations,* Journal of the Mechanics and Physics of Solids **51**, 1551 (2003).

[42] R. Solecki and R. J. Conant, *Advanced Mechanics of Materials* (Oxford University Press, 2003).

[43] C. Multiphysics, *Comsol multiphysics reference manual (version 5.1),* COMSOL (2015).

[44] N. Tas, T. Sonnenberg, H. Jansen, R. Legtenberg, and M. Elwenspoek, *Stiction in surface micromachining,* Journal of Micromechanics and Microengineering **6**, 385 (1996).

[45] *Surface tension values of some common test liquids for surface energy analysis,* (Last updated: 24 Nov 2006), http://www.surface-tension.de/ -Data obtained on November 2015.

[46] P. J. Linstrom and W. Mallard, *NIST chemistry webbook* (National Institute of Standards and Technology Gaithersburg, MD, 2001) (retrieved November 15, 2015).

[47] *Dortmund data bank: Surface tension of carbon dioxide,* (2015).

4

Tolerances in airgap-based optical filters

4.1. Introduction

Although airgap-based optical filters are generally one-dimensional optical components, these are also three-dimensional mechanical structures. This means that only the position of a flat surface in one direction is relevant. An important exception is the LVOF [1], where the surface is also sloped in one direction. Maintaining a well-defined, predictable, and uniform optical response over the entire structure is a major challenge in the fabrication of airgap-based optical filters, which is composed of a stack of membranes with the optical interference in the layers determining the spectral response (both in the reflectance or transmittance mode) of the structure. Fabrication tolerances and mechanical properties must be considered in the design of such large-area airgap-based optical filters. Various parameters such as the optical thickness uniformity, roughness, and flatness of the membrane affect the optical response of the filter. These parameters are either dependent on the material characteristics (roughness and optical thickness uniformity) or affected by the fabrication process characteristics (flatness and thickness uniformity).

The fabrication of the airgap filters is an additive process based on MEMS surface micromachining. In this process layers are added (*deposited*), patterned, and selectively removed (*etched*) from the wafer surface. The deposited layers generally have a roughness of up to $10\ nm$ rms. Furthermore, during the etching step the surfaces in contact with the etchant environment (dry or wet) can typically become rough. This roughness of the deposited layers usually contributes to the scattering losses in the optical filters. Maintaining thickness and refractive index uniformity in the deposited (and etched) layers over the entire MEMS structure is essential for the optical filter applications. The optical thicknesses involved in the interference filters is typically in the order of a quarter of the wavelength. Therefore, the uniformity tolerances are typically getting higher at shorter design wavelengths.

An airgap optical filter is a complex structure of parallel perforated membranes that are structurally connected by a number of mechanical supports. As was discussed in Chapter 3, the residual stress is almost inevitable in the deposited thin films. In the free-standing structures, the residual stress in the layers is the dominant force acting on the structure. The residual stress in the deposited materials is typically in the order of several tens of MPa. Therefore, the deformation induced by the residual stress can greatly contribute to the optical losses in the structure.

This chapter aims to study the effects of the various process parameters on the optical response of the airgap-based optical filters. The deposition uniformity, roughness, and etch selectivity is discussed and their related optical losses are compared. The post-release deformation of the membranes due to the residual stress is also studied. The residual stress in the films is typically non-uniform. Therefore, the stress profile in the PECVD deposited layers and their effects on the membrane deformation is also studied using finite element analysis (FEA). A finite-difference time-domain (FDTD) analysis has been applied on the FEA generated deformed structures, and the optical response was analyzed. Finally, several single membrane structures were fabricated. The patterns of deformation of the membrane are compared and methods to avoid or minimize the membrane deformation are presented.

4.2. Optical flatness criterion

In the optical device, the surface roughness and flatness should satisfy the optical flatness criteria, which requires a maximum acceptable uncertainty of layer thickness in the direction of the wave propagated, in terms of the root-mean-square (RMS) thickness of less than the design wavelength/20. In a Bragg reflector centered at 400 nm, for instance, with the structure is composed of $sub - 100\ nm$ dielectric layers that are separated by 100 nm wide airgaps. This criterion hence requires an RMS roughness of better than 20 nm over the active area of the device. Furthermore, the RMS deformation of the membranes must also remain below $\lambda/20$ over an area of several λ^2 . Maintaining this strict criterion is challenging in ultra-thin membranes.

For a better understanding of the effects of the fabrication tolerances and for comparing the different sources of layer thickness variations, a rigorous analysis of the effects of the optical criterion is needed. The formulation in terms of Finesse (of a Fabry-Perot-based filter) is useful in order to quantify various effects of the optical characteristics on the airgap filter performance. The finesse $\mathcal{F}$, as defined in Chapter 2, is a figure of merit in the Fabry-Perot filters and is the ratio between the free spectral range of the cavity and the FWHM of the transmitted peaks [2]. Ideally, the finesse of a Fabry-Perot filter is only a function of the reflectance of mirrors comprising the filter. However, the finesse is reduced by various tolerance parameters such as the non-parallelism, roughness, waviness of the mirrors [3]. Therefore, the effective finesse ($\mathcal{F}_{eff}$) of a non-ideal system considering different factors can be expressed as:

$$\frac{1}{\mathcal{F}_{eff}^2} = \frac{1}{\mathcal{F}_o^2} + \frac{1}{\mathcal{F}_{non-parallel}^2} + \frac{1}{\mathcal{F}_{waviness}^2} + \frac{1}{\mathcal{F}_{roughness}^2}. \tag{4.1}$$

In this formulation (Equation 4.1) $\mathcal{F}_o$ is the finesse of an ideal Fabry-Perot resonator. In the presence of the non-idealities, however, the finesse is reduced for a value that is denoted as the effective finesse.

The non-parallelism is defined as a relative tilt of one of the mirrors of the Fabry-Perot filter and is described as:

$$\mathcal{F}_{non-parallel} = \frac{\lambda}{2\Delta t}$$

in which Δt is the end-to-end cavity length change due to the tilt in the mirrors.

Generally, the *surface finish or texture*, depending on the spatial frequency of the height variations is classified as roughness and waviness. The roughness is determined by the high-frequency variations and typically depends on the deposition (and etching) characteristics. The effect of an RMS roughness of R_a (assuming a Gaussian distribution) in the effective finesse is also defined as:

$$\mathcal{F}_{roughness} = \frac{\lambda}{\sqrt{22}R_a}.$$

The waviness, on the other hand, is the curvature-like low-frequency variations in the layer profile. Therefore, stress-induced deformations can be considered as

an effective waviness in the membranes. The effect of a spherical waviness with a center-to-edge height difference of Δw is described as

$$\mathcal{F}_{waviness} = \frac{\lambda}{2\Delta w}.$$

It should be noted that the finesse terms related to the non-idealities are all proportional to the wavelength (λ). Therefore, the intended spectrum is directly relevant to the acceptable tolerances involved in a filter design.

4.3. PECVD oxide and polysilicon layer system

As discussed in Section 4.2, the fabrication tolerances play a significant role in the optical response of the filter. This section studies the effect of the optical tolerances in a fabrication process based on a polysilicon and oxide layer system. The PECVD deposited oxides (see Chapter 3) were used for the membrane material, while LPCVD deposited polysilicon was selected as the sacrificial layer. The material and process characteristics must be studied to predict and understand the optical behavior of the filter. The objective is to identify approaches for obtaining the required flatness and optical thickness uniformity over the active area of the optical filter intended for the UV-Visible spectrum.

4.3.1. Roughness

It is safe to say that some degree of roughness is unavoidable in any deposited (or grown) layer. Therefore, roughness always affects and limits the response of any optical filter. The PECVD deposited layers normally have a high surface roughness due to the grain formation during the deposition. Furthermore, the grain size increases with the substrate temperature and causes higher surface roughness. It has been reported that PECVD films deposited on silicon wafers typically have an average roughness of $Ra = 3.8 - 5.0\ nm$ [4]. For a filter designed centered at a $400\ nm$ wavelength range, this roughness corresponds to a finesse contribution of $\mathcal{F}_{roughness} = \lambda/\sqrt{22}Ra < 22.4 - 17.06$. Therefore, any filter design based on PECVD films at its best (regardless of the layer number) would tend to a finesse of about $\mathcal{F}_{eff} \approx 22.4$. This value is equivalent to a finesse of an ideal Fabry-Perot filter with a mirror reflectivity of $r \approx 0.86$.

4.3.2. Deposition uniformity

The uniformity of the deposition rate highly depends on the process used for the deposition of the thin-films. The layer thickness uniformity, therefore, depends on deposition technique. Moreover, it significantly depends on the setting of the process (e.g. high deposition rate for thick layers typically results in effectively high non-uniformity). ALD and oxidation are typically considered as methods that result in a high thickness uniformity in the layer. In the PECVD deposition, the uniformity is directly related to plasma ion energy distribution in the chamber. Furthermore, as the deposition rates of the PECVD is typically high, the effects such as the ignition time (i.e. the time needed for the plasma to ignite and stabilize) becomes more

important. Therefore, the thickness control becomes increasingly difficult for the deposition of ultra-thin layers.

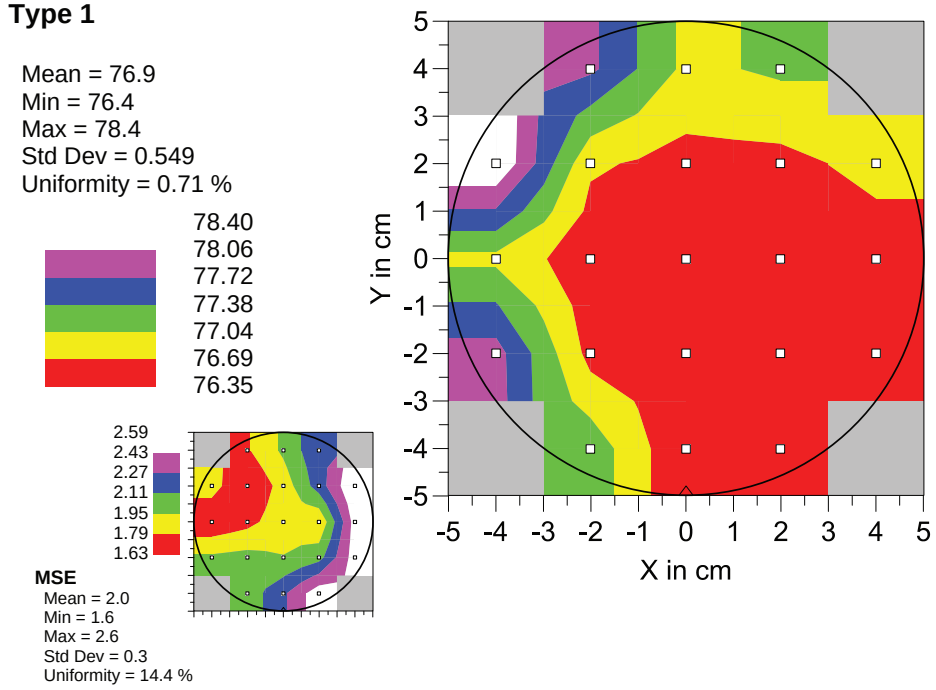

Figure 4.1: Thickness uniformity mapping of *Type 1* PECVD deposited oxides measured by VASE (variable angle spectroscopic ellipsometry). The MSE distribution of the optical model used for the analysis is also shown. (The values shown in the insert are all in nanometer.)

In this research, the layers were deposited using a commercially available PECVD module (Novellus Concept One). Although this system is equipped with a seven-stage deposition module (i.e. seven depositions of each $1/7$th of the target thickness), we used only one-stage to deposit the very thin layers required for this application. In Chapter 3, two different deposition recipes were introduced and labeled as *Type 1* and *2*. The deposition uniformity for *Type 1* and *2* oxides films was measured by VASE mapping on 21 points distributed over the 10 cm diameter area. Figure 4.1 and 4.2 shows the deposition uniformity for the two PECVD oxide recipes. The deposition time was chosen according to the previous deposition rate calibration (see Chapter 3) and to obtain a target thickness of $77\ nm$. The deposition (non-)uniformity over the wafer area was measured to be below 1% for the both oxide recipes. Considering that the devices would be fabricated in the center of the wafer, the non-uniformity in the thickness is even lower. For the optical filter application, the non-uniformity within a single filter element (with few millimeters lateral dimensions) is in the order of sub-nm. Therefore, the effect of thickness non-uniformity on the effective finesse is typically insignificant and can

be disregarded.

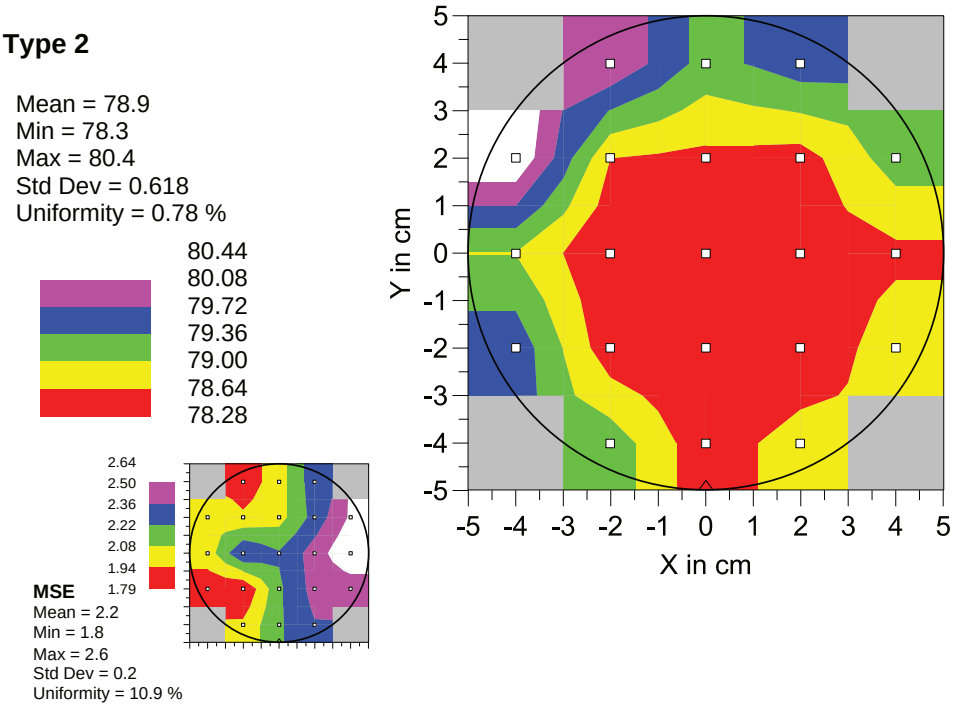

Figure 4.2: Thickness uniformity mapping of *Type 2* PECVD deposited oxides measured by VASE (variable angle spectroscopic ellipsometry). The MSE distribution of the optical model used for the analysis is also shown. (The values shown in the insert are all in nanometer.)

Moreover, the thickness uncertainty was measured to be less than $\pm 2\ nm$ ($77 \pm 2\ nm$). It should be noted that the higher deposition rate of Type 2 recipe results in a shorter deposition time and a slightly higher non-uniformity and larger thickness uncertainty in the deposited layer. The effect of this thickness uncertainty results in a finesse factor of $\mathcal{F}_{non-uniformity} = \lambda/2\Delta t \approx 100$ for the ultraviolet and visible applications. Compared to the contribution of the roughness to the finesse, the effect of the thickness uncertainty is marginal.

4.3.3. Etch selectivity

The fabrication of air-gap optical filters is based on the initial deposition of a stack of sacrificial layers and structural layers to be used as membranes. The etching of the sacrificial layers is the last step in the fabrication of the airgap-based filters. During this step, the sacrificial layer is removed in an isotropic process. Ideally, the etching should selectively remove the sacrificial material while the membrane material should be sufficiently resistant to the etching. The etch selectivity is a unit-less criterion and is defined as the ratio between the etch rate of the sacrificial

material and that of the membrane material:

$$S = \frac{ER_{Sacrificial}}{ER_{Membrane}} \tag{4.2}$$

When etching over a sacrificial length L, in a method with etch selectivity S, a thickness of δt (see Equation 4.3) would also be removed from each side of the membrane. Figure 4.3 shows the effect of a finite selectivity.

$$\delta t = L \; / \; S \tag{4.3}$$

Therefore, the uniformity of the thickness of the membranes not only relies on the deposition homogeneity but also the etching selectivity during the sacrificial release is directly relevant. For instance, etching over a length of equal to $10\ \mu m$, while requiring that the thickness loss should be limited to $\delta t = 1\ nm$ implies a minimum selectivity in the order of 10^4. According to the Equation 4.1, this selectivity would result in a finesse component of about $\mathcal{F} \approx 100$.

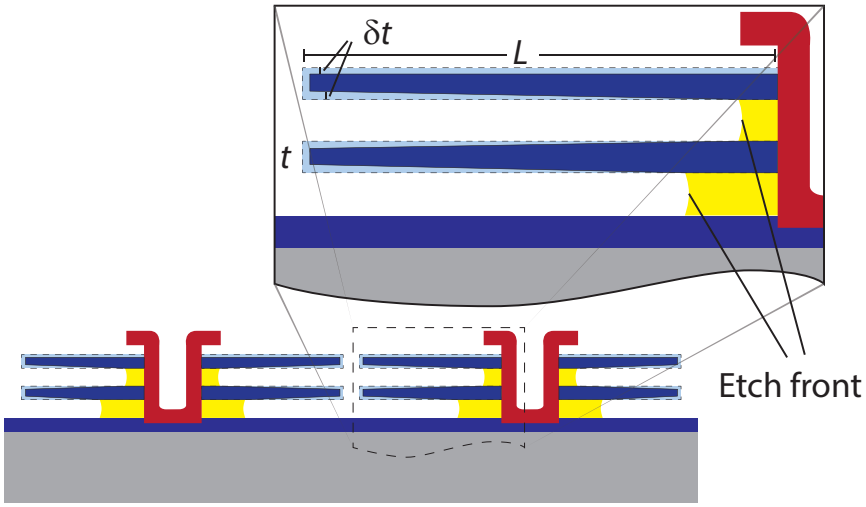

Figure 4.3: Schematic Effect of the etch selectivity on the thickness uniformity.

In most III-V-based MEMS devices such as WDM and VCSEL intended for infrared spectrum, InP is used as the membrane material. In the fabrication of these devices, layers containing impurities (e.g. aluminum and germanium) are used as the sacrificial material. Furthermore, the etch rate of the sacrificial layers, hence its selectivity can be tuned by varying the concentration of these impurities. Various wet etching techniques have been developed for etching the sacrificial layers such as FeCl3-based etching of GaInAs layers [5–10], HF-based etching of aluminum-rich layers [11], HCL-based etching of InAlAs [12], and H2O2-based etching of InAlAs or InGaAs layers [12]. Since the effect of the tolerances decreases with thicker layers which are used in the optical devices intended for infrared spectrum, these methods have sufficient selectivity.

Similarly in the III-V-based ultraviolet LEDs, a wide range of different etching methods such as electrochemical etching of AlInN [13, 14], doped GaN [15], and of AlN [16], photo-electrochemical etching of AlGaN [17–19], and nitride-acid etching [20] have been reported in the literature. Other methods, such as focused ion beam (FIB) milling [21] and decomposition and sublimation of GaN at high temperatures (AlN/air-gap DBRs) [22, 23], have also been investigated.

In conventional CMOS-compatible MEMS fabrication, typically membranes of silicon or silicon-nitride are fabricated. In these processes, silicon-oxide layers are commonly used as the sacrificial layers. The wet and vapor phase etching of the SiO_2 is a well-known method for the release of such a membrane with sufficient selectivity required for most CMOS-compatible mechanical devices [24]. However, in the UV-visible airgap filters, unlike most MEMS processes, the membranes are based on silicon-oxide layers. A suitable sacrificial material and etching technique have to be designed to achieve the required selectivity. Silicon and polySilicon have been reportedly used as the sacrificial material combined with silicon-oxide structural layers [25]. The oxide membranes can be released in a wet etching step, using alkaline-based etchants such as KOH or TMAH, or in a dry (or vapor-phase) etching step such as using vaporized XeF_2.

XeF_2 is a white solid material at room temperature and has a low sublimation pressure. In its vapor phase, XeF_2 has a high silicon etch rate without the need for any external energy source (e.g. a plasma). Therefore, the physical etching (i.e. etching by bombardment with high energy ions) does not occur [26]. Therefore, XeF_2 is highly selective to silicon dioxide as well as photoresists, silicon nitride, silicon carbide, and metals such as aluminum, and titanium [26]. Furthermore, the vapor-phase etching eliminates the stiction forces that are involved in the processes based on liquid phase etching [27, 28]. However, XeF_2 in the contact with water forms HF that etches the SiO_2 membranes and the etch must be carried out in a controlled environment. Furthermore, it generates a safety issue in the cleanroom processes.

Table 4.1: Etch rates and selectivity for SiO_2 and Si in KOH and TMAH, and doped−TMAH [29].

Etching Solution	Condition	Si <100> Etch rate [μm/h]	SiO_2 Etch rate [nm/h]	Etch selectivity (Si/SiO_2)
KOH	22% - 50 °C	25	25	$1000=10^3$
KOH	22% - 80 °C	90	250	$360 \approx 4 \times 10^2$
TMAH	3% - 50 °C	7	50	$140 \approx 10^2$
TMAH	3% - 80 °C	60	180	$333 \approx 3 \times 10^2$
doped-TMAH	5% - 60 °C	85	8	$\approx 10^4$
doped-TMAH	5% - 80 °C	57	6	$\approx 9 \times 10^4$

Alkaline-based etchants, such as KOH and TMAH (Tetra Methyl Ammonium Hydroxide), are quite well-known in MEMS fabrication. Wet etching using TMAH is

commonly used in CMOS-compatible fabrication due to the absence of metal ions. However, unlike the XeF_2 etching, the etch selectivity of alkaline-based etchants to oxides is comparatively low. Silicon doping or the addition of silicic acid ($Si(OH)_4$) has been reportedly used to improve the selectivity of the TMAH to the aluminum [30–32]. Furthermore, the addition of an oxidizer such as ammonium persulfate ($(NH_4)_2S_2O_8$) in the dual-doped TMAH suppresses the formation of the hillocks and results in an improved surface quality as compared to the undoped etchants [29, 31, 33]. Moreover, the dual-doped TMAH solution has an improved selectivity to the silicon-oxide layers. The etch rate of silicon and SiO_2 in the dual-doped TMAH has been studied by [29, 33]. Table 4.1 summarizes some of their results and also presents the calculated selectivity. The etch rates presented in the table corresponds to the etch rate of <100> silicon wafers and thermally grown SiO_2. It can be concluded that only doped-TMAH offers a etch selectivity sufficient for airgap optical filter applications.

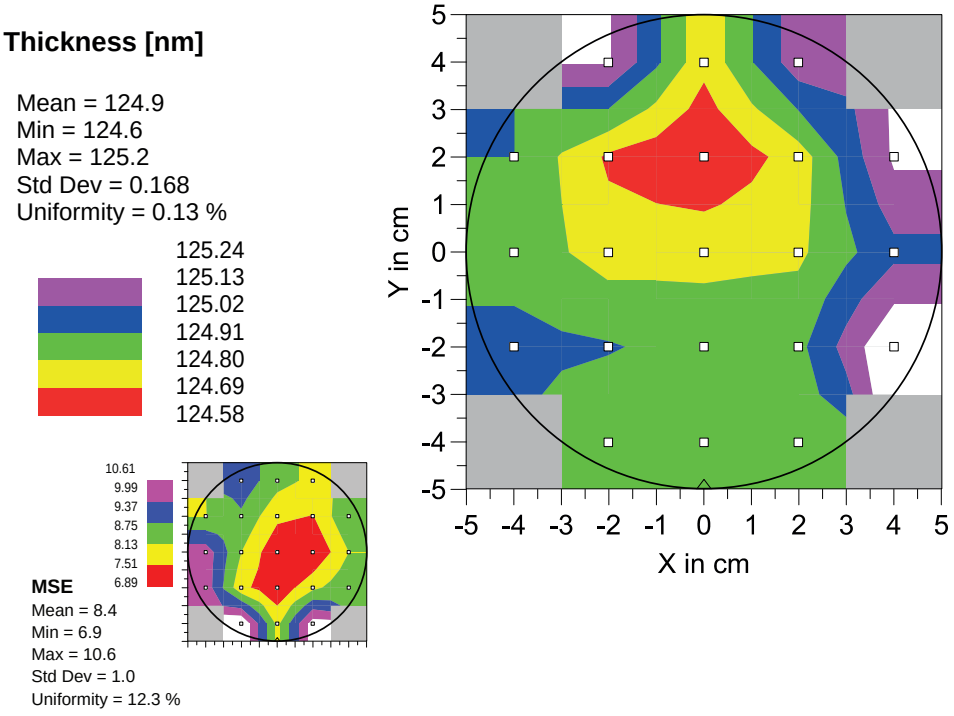

Figure 4.4: Thickness uniformity mapping of the LPCVD deposited polysilicon layers measured by VASE

In this research LPCVD deposited Polysilicon has been selected as the sacrificial material combined with the PECVD oxide as the structural layer material. LPCVD polysilicon layers have been deposited using Silane chemistry at 580 °C. As previously discussed in Chapter 3, polysilicon deposition also acts as the thermal annealing step for the stress tuning in the thin-films. The uniformity of the LPCVD

polysilicon, which is equal to the uniformity of the airgap layer thickness (disregarding the eventual buckling) was also measured to be about 0.1% (see Figure 4.4). A 5% dual-doped TMAH solution has been produced by mixing $38\ gr/l$ of silicic acid and $7\ gr/l$ of AP into 5% TMAH-water solution. The etch rate of polysilicon has been measured and plotted in Figure 4.5. Furthermore, no measurable oxide etch rate was observed (within the measurement accuracy), thus confirming a high selectivity. Therefore, the selectivity is expected to be in the order of 10^4 which is sufficient for the UV-visible airgap filter application.

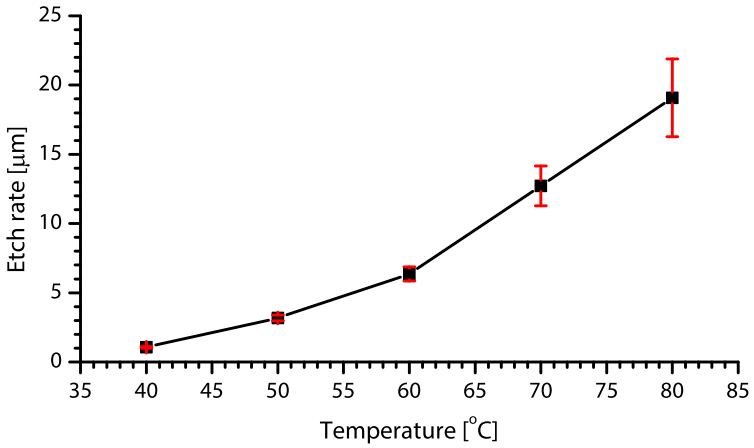

Figure 4.5: Etch rate of polySilicon in 5% dual doped TMAH solution.

4.3.4. Stress gradient in the membranes

The effect of a uniform residual stress in the released membrane was discussed in Chapter 2. However, the residual stress is usually also associated with a stress gradient along the thickness of the deposited film. Unlike the case of uniform stress, a gradient stress in the thin film leads to a deformation of the released structure. The intrinsic stress is usually responsible for the stress gradient in the film [34]. A stress gradient can occur in silicon microstructures due to the nonuniform doping, oxygen diffusion at thermal oxidation [35] and grain formation in the CVD and PECVD layers [34]. In thermal oxidation the stress becomes less compressive toward the top side of the layer. In the CVD or PECVD deposited films, the stress gradient is usually related to the growth of the grains of irregular shapes.

The stress gradient in the film greatly affects the deformation of the free-standing membranes and cantilevers. Dedicated methods have been developed to measure the stress gradient profile in the film. A commonly used method is measuring the deflection in thin-film cantilever beams. Figure 4.6 shows a schematic of a cantilever that is anchored at one end and free-standing at the other end (i.e. single-end clamped). Before the release the cantilever is attached to the sacrificial layer, thus constrained to stay flat. After the release, however, the cantilever beam

can freely move. If the stress is uniformly distributed along the thickness of the layer, the cantilever will stay flat. On the other hand in the presence of a stress gradient, the structure tends to strain in such a way to release the stress energy stored. Therefore, the cantilever would bend toward the more tensile side. The direction and magnitude of the deflection of the cantilever can be used to assess the stress gradient in the film.

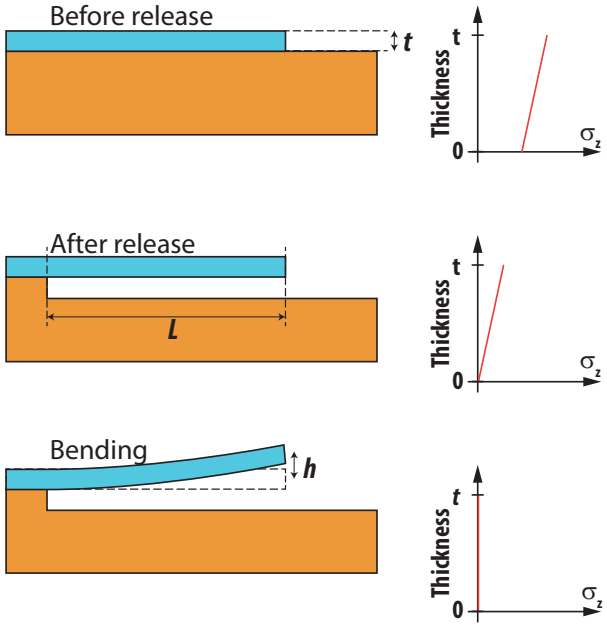

Figure 4.6: Stress gradient in a free-standing cantilever. (Adapted and reproduced from [34].)

Similar to the wafer curvature-based calculation of the stress using the Stoney equation, a stress difference of $\Delta\sigma$ between the top and bottom of the film would result in a deflection equal to h [34]. The relation between the deflection and the stress difference can be analytically expressed as:

$$\begin{aligned} \Delta\sigma &= \sigma(t) - \sigma(0) \\ h &= \frac{L^2}{2E}\frac{\Delta\sigma}{t}, \end{aligned} \tag{4.4}$$

where E is the Young's modulus of the film, and t and L is the thickness and length of the cantilever beam. According to the sign convention in Figure 4.6, an effective positive stress gradient would buckle the cantilever upward. This method is widely used to assess the stress gradient of the thin films in MEMS devices. It should be noted that a linear stress gradient profile along the thickness of the layer is assumed. However, the stress profile in the layers is often non-linear. Progressive layer thinning is often used to estimate this non-linear stress profile. In this method, the stress gradient is measured at different thicknesses of the beam and for each

a linear profile is assumed. The overall (non-linear) stress gradient profile can be constructed by combining the profiles [36]. For the ultra-thin layers, the non-linear stress gradient profile and its effect on the deformation of the membrane is particularly important [37]. The progressive thinning method, however, becomes increasingly inaccurate for very thin layers. Therefore, we resorted to wafer bowing measurements at using FEA for interpretation of the results.

Finite Element Analysis

The PECVD deposited thin-films are known to exhibit a stress gradient along the thickness of the layer, which is due to the grain size variation along the thickness [36]. Furthermore, for the UV-visible applications the free-standing membranes are much thinner than those typically used in MEMS devices and the variation of the stress along the thickness is also expected to be more significant. The effect of the deformation due to the stress gradient must be taken into account for a successful optical filter design. Therefore, the stress variation along the thickness must be studied to understand its effects on the flatness of the membranes. FEA has been applied to study the effects of different stress gradient profile on the thin-film deformation.

The stress gradient is commonly defined as a general polynomial function varying along the thickness of the layer and centered at middle of the film [37]:

$$\sigma_t(z) = \sum_{n=0}^{\infty} \sigma_n \left(\frac{z}{t/2}\right)^n. \tag{4.5}$$

In a first order approximation, only a linear variation is considered. Therefore, Equation 4.5 consists of a uniform residual component of σ_0 and a linearly varying component of σ_1. Figure 4.7 represents a typical stress profile along the thickness of a silicon-oxide membrane with a thickness of $70\ nm$, in the case where $\sigma_0 = 200\ MPa$, for different values of σ_1 along the thickness.

$$\sigma_t(z) \approx \sigma_0 + \sigma_1\left(\frac{z}{t/2}\right) = \sigma_0 + 2\sigma_1\left(\frac{z}{t}\right). \tag{4.6}$$

Finite element analysis provides an efficient and accurate tool to study the effect of the stress gradient in the layer. A model (similar to the model used in Chapter 2) was defined in COMSOL Multiphysics to study the membrane deformation due to the stress gradient. A stress gradient function associated with the stress profiles was defined as shown in Figure 4.7. The deformation of the membrane that results from the particular a stress gradient ($\sigma_0 = 200\ MPa$ and $\sigma_1 = 50\ MPa$) is shown in Figure 4.8. The most striking observation from this figure is that the membrane undergoes a very high deformation around the openings that are included for the sacrificial etching.

Figure 4.9 shows the stress-induced deformation (waviness) along a diagonal line from the anchor point to the access-hole (in the center) for various values of $2\sigma_1$ as already derived and plotted in Figure 4.7. It can be seen that a stress gradient

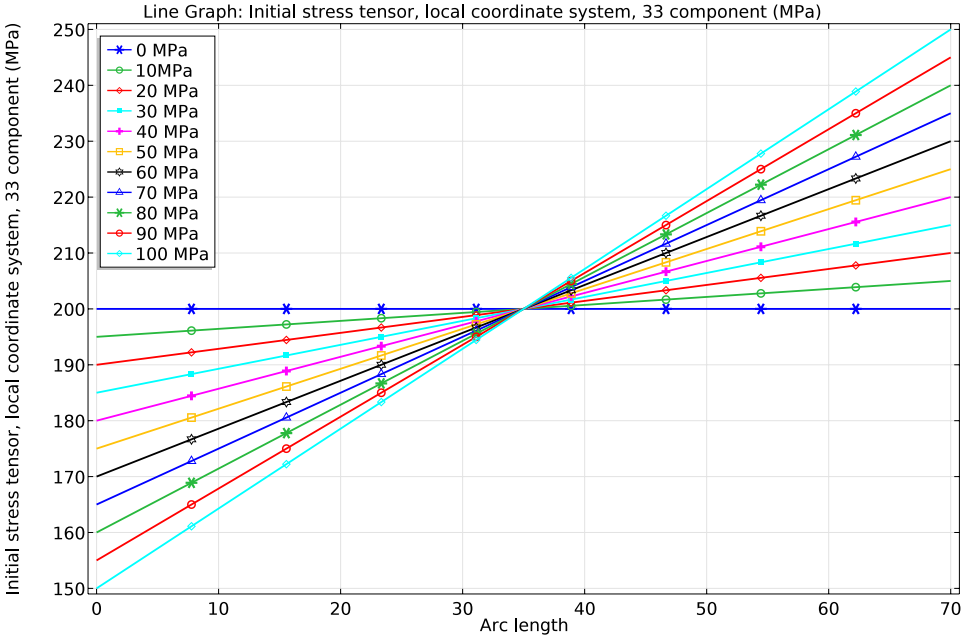

Figure 4.7: Linear stress gradient profile along the thickness of a $70\ nm$ membrane. The uniform residual stress was assumed to be $\sigma_0 = 200\ MPa$. The stress gradient is assumed toward more tensile values at the top. The numbers in the legend show the $2\sigma_1$ values.

of $\sigma_1 = 15\ MPa$ in the film would result in a center-to-edge height difference of $10\ nm$. This deformation corresponds to a finesse contribution of $\mathcal{F}_{waviness} \approx 20$.

The stress profile in ultra-thin membranes typically changes abruptly along the thickness. The interface boundaries of the layer typically have a less tensile stress [36].The residual stress then rapidly increases with the thicknesses. This rapid change in the stress is usually in the range of a few nanometers and is usually neglected for micron thick layers [36]. In the UV-visible airgap-based filters, the layer thickness is typically in the order of sub-100nanometers. Therefore, the effect of the abrupt change in the residual stress is significant.

The stress profile can be approximated as an abrupt change in the stress near the interface, whereas at a larger thickness asymptotically reaches the linear approximation. At the other extreme, the thick films, the stress typically converges to a saturation level. This convergent or generally asymptotic behavior of the stress cannot be easily approximated by the polynomial Function 4.5. In this case we propose a new term to the Equation 4.5 that can effectively account for this non-linear stress profile 4.10. In this case, the modified version of the stress profile equation becomes:

$$\sigma_t(z) = \int_{n=0}^{1} \sigma_n \left(\frac{z}{t}\right)^n \quad \text{where} \quad n \in \mathbb{R}. \tag{4.7}$$

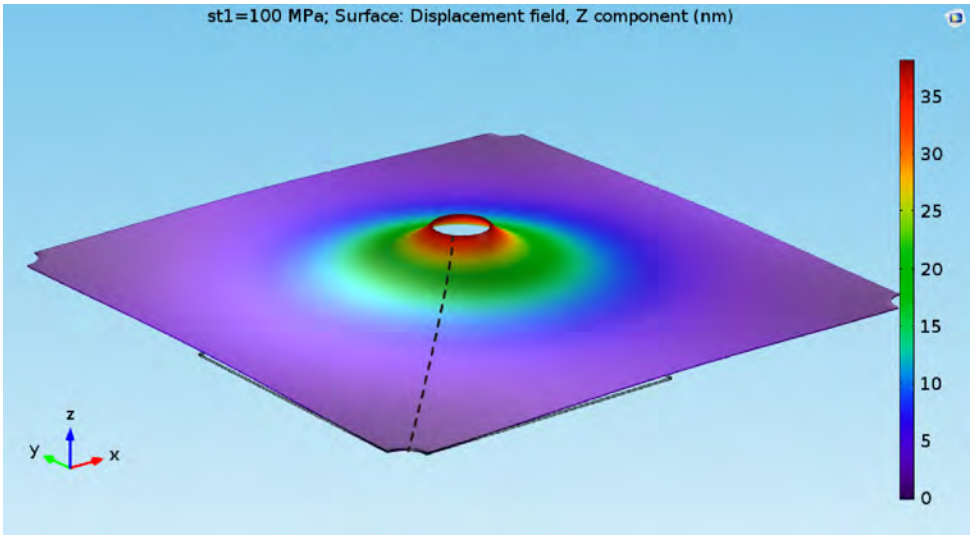

Figure 4.8: Membrane deformation for a linear stress gradient profile along the thickness of the membrane. The uniform residual stress was assumed to be $\sigma_0 = 200\ MPa$ and $\sigma_1 = 50\ MPa$. The stress gradient is assumed toward more tensile values at the top.

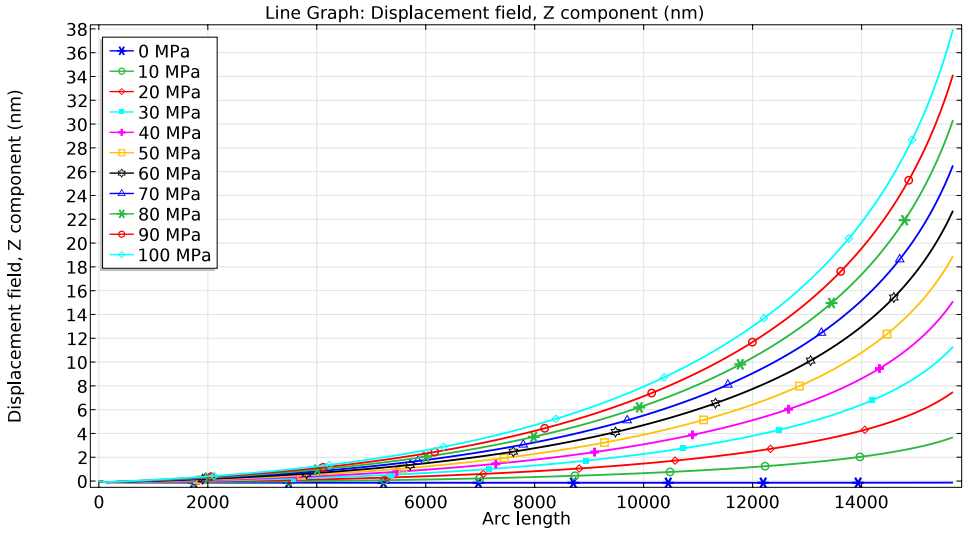

Figure 4.9: The deformation of the membrane along a diagonal line from the edge to the center (shown in Figure 4.8) as a result of the stress profiles shown in Figure 4.7

In this function, n is a real number between 0 and 1. For $n = 0$ a uniform stress distribution is assumed and $n = 1$ denotes a linear stress gradient. This function is non-linear at small thicknesses and is almost linear at higher thicknesses. Here we considered a particular case of a single term in terms of the $\sigma_t(z) \approx \sigma_0 + \sigma_n(z/t)^n$,

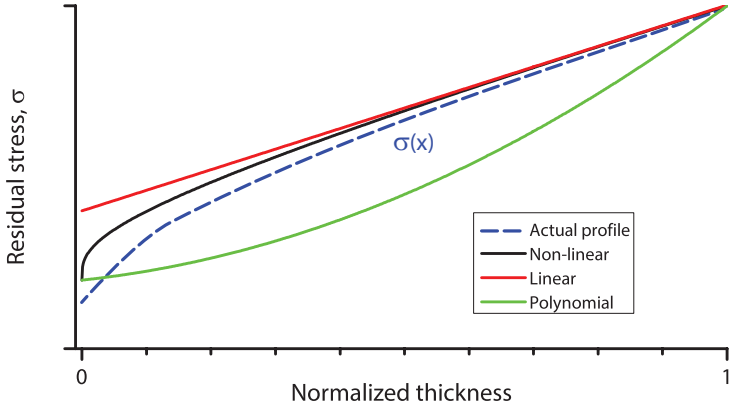

Figure 4.10: Gradient of residual stress in thin-films: the actual stress profile and various analytical fit functions are presented.

where σ_0 is assumed to be the stress at the interface side (bottom side) of the layer. To compare the effect of such behavior with the linear case, a single term in the stress profile (Equation 4.7) for $n = 0,\ 0.1,\ ...,\ 1$ was applied to the finite element model of a $70\ nm$ SiO_2 membrane-cell. Here we consider a stress of $\sigma_0 = 200\ MPa$ and a constant $\sigma_n = 100\ MPa$ for every n-value. The stress profile of such a stress variation is plotted in Figure 4.12. Note that the mesh size has to be chosen properly in order to account for the abrupt stress variation in the thin film. As a rule of thumb, the mesh size (at least in a specific direction) has to be as small as the shortest spatial variation (e.g. stress profile). Therefore, a 3D sweep mesh with smallest element size at the bottom side (the bottom interface edge) was generated. The mesh size was systematically increased along the thickness to avoid generating a huge number of mesh elements (and consequently a long computational time). A mesh with an average mesh quality (as defined in Chapter 3) of 0.02 over the large area and a minimum mesh quality of better than 0.1 at the edges was generated (See Figure 4.11). It should be noted that Figure 4.12 shows the actual stress applied to the FEA simulation while the effect of the mesh size variations is included.

The resulting membrane deformation along a line from an anchor point to an access hole due to the applied stress profile with different power (n) is shown in Figure 4.13. The results, show that the non-linear stress profile results in a suppressed deformation as compared to the linear variation. However, this is due to the choice we made that the stress difference between (and at) the both sides of the layer is kept at a fixed value. The residual stress on the bottom and top interface for all these stress profiles (except for the $n = 0$) is the same. The non-linear stress profile, as opposed to the linear profile, hence resulted in a fast change in the first few nanometers (less than $10\ nm$) and then with a less-steep change until reaching the stress value at the top surface.

The flexibility of the non-linear stress profile of Equation 4.7 provides an effective and more accurate tool to study the stress variations in the thin-films. A general

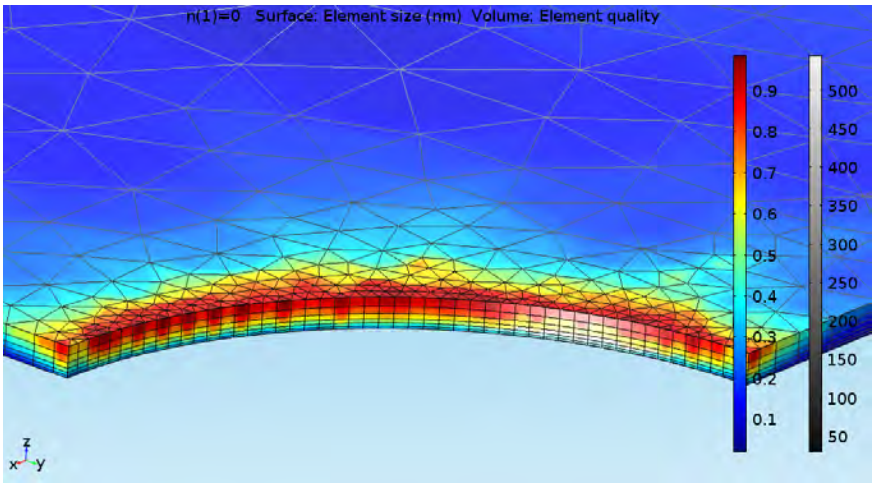

Figure 4.11: Generated mesh for the stress gradient study based on a triangular-sweep mesh algorithm. The mesh size is in the order of a few nanometers at the interface (bottom) and increases with an arithmetic distribution toward the topside.

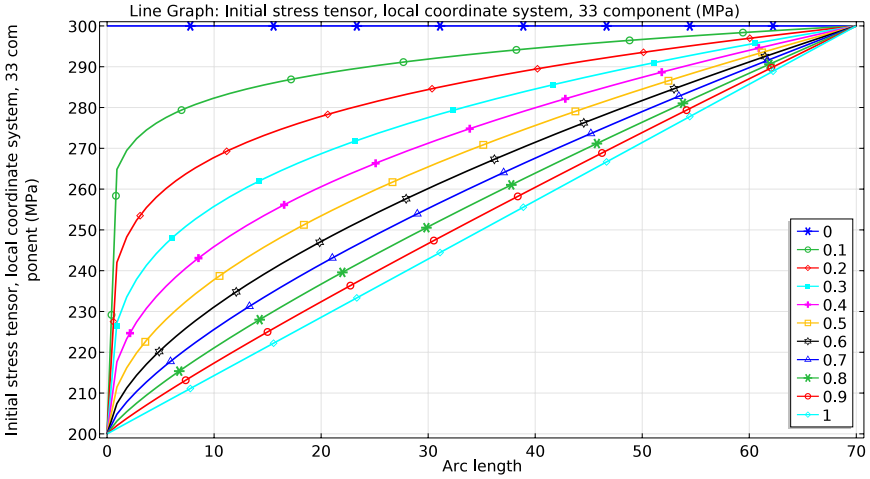

Figure 4.12: Non-linear stress gradient profile along the thickness of the membrane. The uniform residual stress was assumed to be $\sigma_0 = 300\ MPa$. The stress gradient is assumed toward more tensile values at the top.

function consisting of a uniform stress ($n = 0$), linear variation ($n = 1$), and non-linear variation ($0 < n < 1$) can be used to approximate the stress profile the ultra-thin films.

$$\sigma_t(z) \approx \sigma_0 + \sigma_1(z/t) + \sigma_n(z/t)^n \tag{4.8}$$

In Equation 4.8 the spatial terms are normalized, so that the σ_i terms correspond

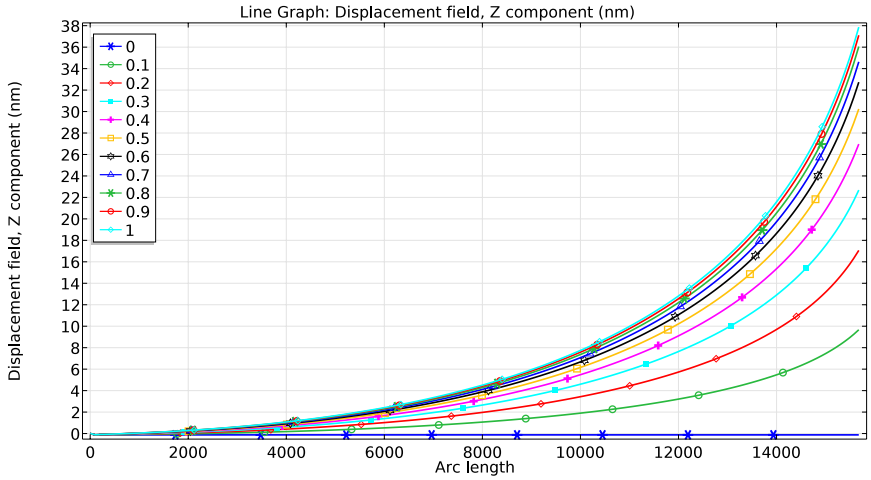

Figure 4.13: The deformation of the membrane along a diagonal line from the edge to the center (shown in Figure 4.8) as a result of a Non-linear stress gradient profile along the thickness of the membrane (based on the stress profiles shown in Figure 4.7)

to the uniform stress (σ_0), linear stress (σ_1) and a single n^{th} powered stress contribution (σ_n).

Case study: PECVD oxide thin films

As discussed in Chapter 3, two PECVD oxide recipes were used to deposit the membrane materials. Although a silane-based chemistry was used for the deposition of both oxides, a slightly different SiH_4-to-N_2O ratio (about 29 and 33 respectively for Type 1 and Type 2) results in a different stress profile in the deposited layers. The layers were then annealed at $580^o\ C$ to obtain a tensile residual stress. Figure 4.14 shows the stress at different thickness of the layers.

The stress gradient function of Equation 4.6 is fitted to the measured data points. For the sake of comparison, a hypothetical function based on Equation 4.8 was also considered, with an arbitrary power of $n = 0.3$ applied, and was fitted. Obviously, due to the limited number of data points, the non-linear fit is only presented to show the effects of a non-linear stress gradient in the thin films as compared to the linear profile. Figure 4.14 shows the result of the curve fitting for the both oxide recipes. A numerical analysis software package (OriginPro) was used to fit the function to the data. The fitted variables are shown in Table 4.2 and are based on Equation 4.8.

The fitted curves were used as the input data for an FEA in COMSOL Multiphysics. Similar to the previous sections, a silicon oxide membrane with a thickness of $70\ nm$ and considering the symmetries and proper boundary conditions was used for the analysis. The stress gradient was applied, and the deformation of the membrane was studied. Figures 4.15 and 4.16 show and compare the effect of the modified stress gradient (non-linear stress gradient) as compared to the linearly varying stress gradient in *Type 1* and *Type 2* annealed PECVD oxides. Accordingly,

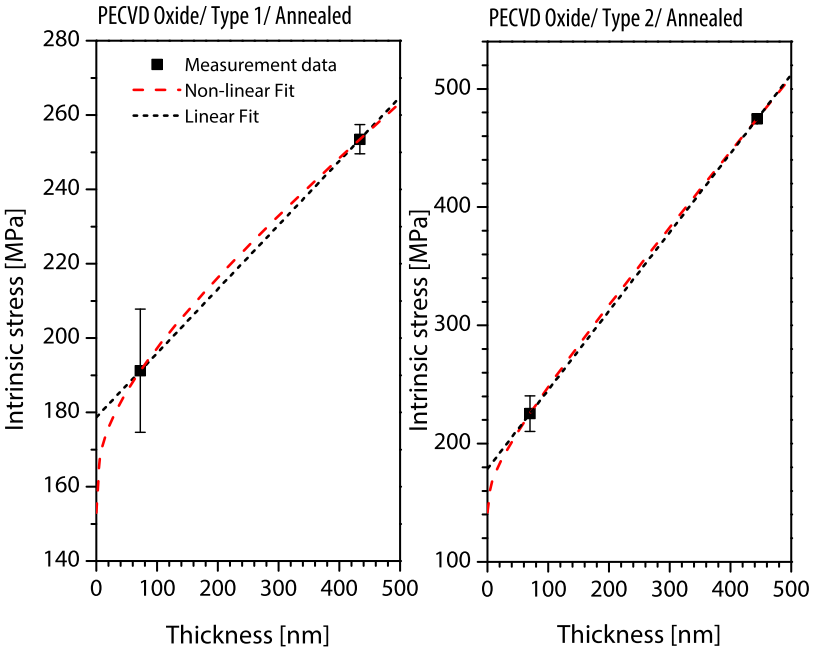

Figure 4.14: The fitted curves for the stress gradient in *Type 1* (left-side) and *Type 2* (right-side) PECVD oxide thin films.

Table 4.2: The curve fitting data obtained for Type 1 and 2 PECVD oxides annealed at $580\ ^{o}C$. The fitted parameters for the linear fit and non-linear fit (test function) are listed.

Fit parameter	PECVD Oxide: Type 1		PECVD Oxide: Type 2	
	Linear	Non-linear	Linear	Non-linear
σ_0 [MPa]	178.7	153	178.7	142
σ_1/t [MPa nm^{-1}]	0.17	0.12	0.67	0.58
σ_n [MPa], n=0.3		29		43

a modified stress gradient profile gives 111% (more than two-fold) increase in the deformation of *Type 1* oxide and an about 39% increase for *Type 2*. It is interesting to note that even though Type 2 oxide is more tensile and expected to result in a better flatness, the high amount of stress gradient in the oxide results in a higher degree of deformation as compared to Type 1.

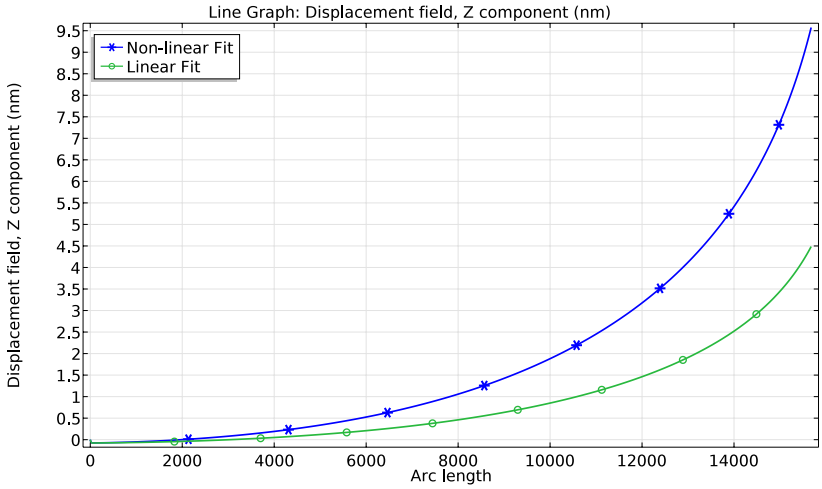

Figure 4.15: FEA analysis of the residual stress-induced deformation in $580\ ^{o}C$ annealed PECVD oxide of *Type 1* along a diagonal from anchor to the access hole (as shown in Figure 4.8).

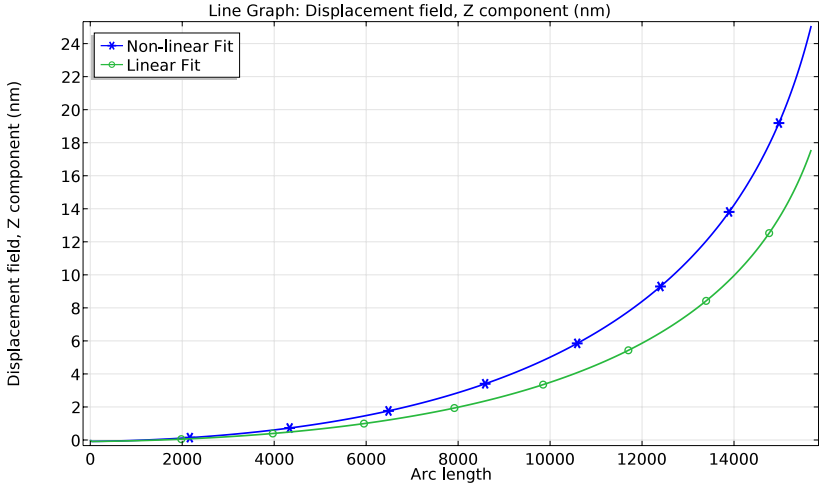

Figure 4.16: FEA analysis of the residual stress-induced deformation for the $580\ ^{o}C$ annealed PECVD oxide of *Type 2* along a diagonal from anchor to the access hole (as shown in Figure 4.8).

4.4. In-plane Stress variations in thin PECVD oxide membranes

The impact of a stress gradient in thin-film membranes was discussed in the previous section. However, the residual stress can vary over the area due to different factors such as the local grain orientation. This stress variation is expected to be an order of magnitude less than the stress variation along the thickness. This section

studies the effects of such variations on the deformation pattern of the membrane.

FEA of in-plane stress distribution

A finite element analysis (using COMSOL Multiphysics software package) was carried out to estimate the stress variation that can lead to such a random deformation pattern. In this simulation, a structure composed of four unit cells was modeled with the proper boundary conditions (i.e. symmetry planes and fixed points). The multi-cell model was chosen so the variations at different direction could be investigated. A two-dimensional in-plane (x, y-plane) weight function was multiplied by the stress gradient function (z-axis) in the membrane. The stress in the membrane, therefore, is a function of two stress components: a stress gradient along the thickness and a slight variation over the area of the membrane. This definition makes it possible to investigate the stress non-uniformity in the membrane, while considering the stress gradient. In this study, a two-dimensional Gaussian distribution function centered at $(x_0,\ y_0)$ was defined. Modifying the standard deviation (Σ -not to be confused with the residual stress-) along the *x* and *y*-axis was used to generate practically any stress variation of interest (Equation 4.10). α is a unit-less weight parameter and used to vary the stress the stress profile in the membrane.

$$G(x) = \frac{1}{\Sigma\sqrt{2\pi}} e^{-\frac{x-x_0}{2\Sigma^2}} \tag{4.9}$$

$$\sigma_T(x,y,z) = \sigma(x,y)\sigma(z) = \left[1 + \alpha\ G(x)\ G(y)\right]\ \sigma(z) \tag{4.10}$$

Here a negative α-value was used, which implies that the stress becomes less tensile at the specific areas. This stress profile function was used for the FEA, and the induced deformation was studied. Several stress profiles were *'randomly'* generated, and the deformation of the membrane was compared. A 10% in-plane stress peak variation ($\alpha = -0.1$) was found to have a significant effect on the deformation of the membrane. Figures 4.17 and 4.18 show some of the generated in-plane stress profiles including a -10% variation in residual stress (x,y-plane) and the related deformation generated in *Type 1* and *2* PECVD oxide membranes and considering a non-linear stress gradient (z-axis) as defined in Section 4.3.4.

According to the figures, the in-plane variation in residual stress results in an asymmetric deformation pattern in the membranes. While the shape of the deformation pattern is similar for both PECVD oxide types, the deformation is higher for *Type 2*. Therefore, the residual stress gradient (along the thickness) directly affects the magnitude of deformation due to the in-plane stress variation.

4.4.1. FDTD analysis of optical effects

The deformation of the membranes has a significant impact on the response of the optical filter. Any analytical solution to describe the optical effects of the deformed geometry is rather unwieldy. Therefore, a numerical method has to be used. Furthermore, the dimensions involved in such a simulation are in the order of $10\ \mu m \approx 25\lambda$ in length and $100\ nm \approx 0.25\lambda$ in the thickness. Typically for an FEM analysis, a mesh size of at least $\lambda/4$ is required to account properly for the optical

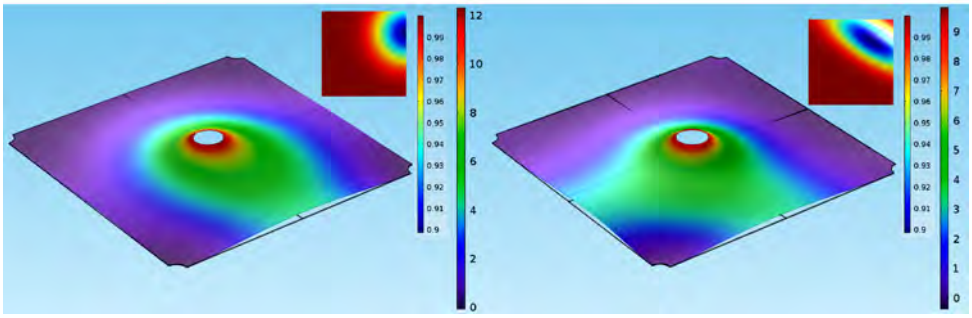

Figure 4.17: Stress-induced deformations generated by a 3D stress profiles in *Type 1* PECVD oxide. The 2D stress in-plane profile of ($\alpha = -0.1$) is shown in the insert. A non-linear stress gradient along the thickness (according to Table 4.2) was also applied.

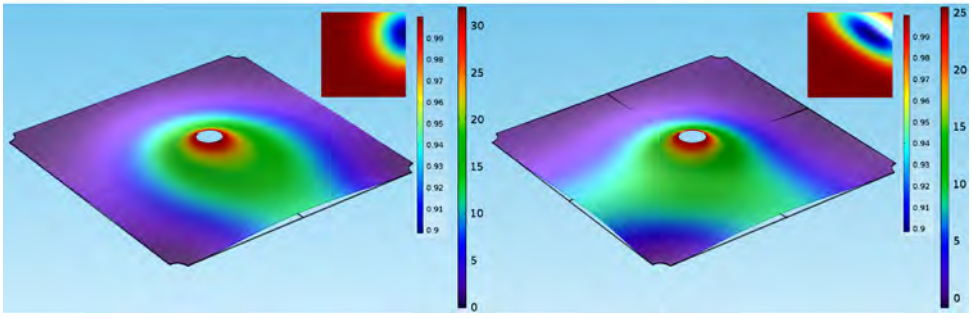

Figure 4.18: Stress-induced deformations generated by a 3D stress profiles in *Type 2* PECVD oxide. The 2D stress in-plane profile of ($\alpha = -0.1$) is shown in the insert. A non-linear stress gradient along the thickness (according to Table 4.2) was also applied. Note that even though the deformation pattern is similar to the deformation in 4.17, the deformation is higher in *Type 2* oxide (see the legend).

layer. However, a much smaller mesh size is required to study the subtle variations in the flatness. Therefore, FEM analysis of the optical response of the structures require an excessive computational power and, therefore, was not pursued.

A finite-difference time-domain (FDTD) analysis was used in this research to study the optical response of the deformed membranes. The FDTD method uses finite differences to approximate spatial and temporal derivatives in the Maxwell equations [38]. The membrane deformation generated, using finite element modeling of a 2-period DBR, was exported to use as the deformed geometry for the FDTD analysis. The FDTD analysis was carried out using a commercially available software package (CST microwave studio).

In the FDTD analysis, the transient solver is suitable for high-frequency applications and was used in these simulations. A TEM boundary condition is assumed for the structure. At this boundary condition, perfect electric conductor (PEC) and perfect magnetic conductor (PMC) with waveguide port are used. A perfectly matched layer (PML) absorbing boundary condition are used in place of the waveguide ports on the both sides of the structure. In this case, the polarization of the incident

electromagnetic wave is confined in such a way that the electric field should be polarized along the PEC boundary, hence imposing a TEM electromagnetic field. Furthermore, To minimize the solution power, the silicon wafer under the membranes is disregarded in this study.

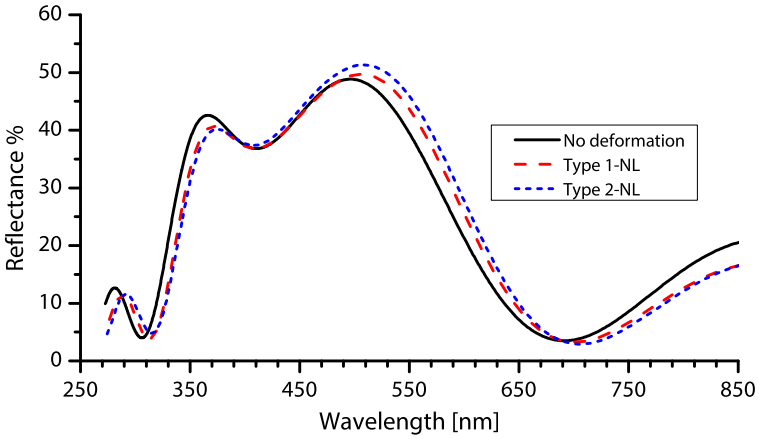

Figure 4.19: Expected optical response of the deformed membranes due to a non-linear stress gradient profile as shown in Figure 4.14 induced deformations in the membranes.

The output of the simulation is obtained in terms of the scattering parameters of S_{11} and S_{21} for the reflection and transmission coefficients, respectively. Figure 4.19 shows the effect of the stress gradient in the oxide membranes due to the stress gradient. The obtained results show a peak widening and a spectral shift toward the longer wavelengths for the low-waviness regime. The peak height at wavelength range below $400\ nm$ range also decreases for both oxide types. Furthermore, the shift is higher for Type-2 oxide layer. This was expected, based on the FEM results where Type 2 showed a higher membrane deformation as compared to Type 1.

The results presented here can be used as a technique for measuring the residual stress profile based on reflection measurements. Subsequent to the fabrication of the airgap filters, the reflection of the structure can be measured. Comparing the measurement results with the FDTD analysis of various hypothetical gradient stress profiles, enables a better assessment of the residual stress.

References

[1] A. Emadi, H. Wu, S. Grabarnik, G. de Graaf, and R. F. Wolffenbuttel, *Vertically tapered layers for optical applications fabricated using resist reflow,* Journal of Micromechanics and Microengineering **19**, 074014 (2009).

[2] F. Pedrotti, L. Pedrotti, and L. Pedrotti, *Introduction to Optics* (Pearson Prentice Hall, 2007).

[3] M. Born, E. Wolf, and A. Bhatia, *Principles of Optics: Electromagnetic Theory of Propagation, Interference and Diffraction of Light* (Cambridge University Press, 1999).

[4] M. R. Amirzada, A. Tatzel, V. Viereck, and H. Hillmer, *Surface roughness analysis of SiO_2 for PECVD, PVD and IBD on different substrates,* Applied Nanoscience **6**, 215 (2016).

[5] K. Streubel, S. Rapp, J. Andre, and N. Chitica, *1.26 μm vertical cavity laser with two InP/air-gap reflectors,* Electronics Letters **32**, 1369 (1996).

[6] N. Chitica, J. Daleiden, J. Bentell, J. André, M. Strassner, S. Greek, D. Pasquariello, M. Karlsson, R. Gupta, and K. Hjort, *Fabrication of tunable InP/air-gap Fabry-Perot cavities by selective etching of InGaAs sacrificial layers,* Physica Scripta **1999**, 131 (1999).

[7] T. Kusserow, R. Zamora, J. Sonksen, N. Dharmarasu, H. Hillmer, T. Nakamura, T. Hayakawa, and B. Vengatesan, *Monolithic integration of a tunable photodetector based on InP/air-gap Fabry-Perot filters,* in *Optical MEMS and Nanophotonics, 2008 IEEE/LEOS Internationall Conference on* (2008) pp. 134–135.

[8] C. J. Tay, C. Quan, H. Liu, M. Gopal, and R. Akkipeddi, *Stress gradient of a micro-optoelectromechanical systems Fabry–Perot cavity based on InP,* Journal of Micro/Nanolithography, MEMS, and MOEMS **9**, 023010 (2010).

[9] C. Prott, F. Romer, E. Ataro, J. Daleiden, S. Irmer, A. Tarraf, and H. Hillmer, *Modeling of ultrawidely tunable vertical cavity air-gap filters and VCSELs,* Selected Topics in Quantum Electronics, IEEE Journal of **9**, 918 (2003).

[10] M. Strassner, J. C. Esnault, L. Leroy, J. L. Leclercq, M. Garrigues, and I. Sagnes, *Fabrication of ultrathin and highly flexible InP-based membranes for microoptoelectromechanical systems at 1.55 μm,* IEEE Photonics Technology Letters **17**, 804 (2005).

[11] P. Tayebati, *Electrically tunable optical filter utilizing a deformable multi-layer mirror,* (1998), uS Patent 5,739,945.

[12] C. Seassal, J. L. Leclercq, and P. Viktorovitch, *Fabrication of InP-based free-standing microstructures by selective surface micromachining,* Journal of Micromechanics and Microengineering **6**, 261 (1996).

[13] A. Altoukhov, J. Levrat, E. Feltin, J.-F. Carlin, A. Castiglia, R. Butté, and N. Grandjean, *High reflectivity airgap distributed Bragg reflectors realized by wet etching of AlInN sacrificial layers,* Applied Physics Letters **95**, 191102 (2009), http://dx.doi.org/10.1063/1.3259720.

[14] J. H. Ryu, H. Y. Kim, H. K. Kim, Y. S. Katharria, N. Han, J. H. Kang, Y. J. Park, M. Han, B. D. Ryu, K. B. Ko, E.-K. Suh, and C.-H. Hong, *High performance of InGaN light-emitting diodes by air-gap/GaN distributed Bragg reflectors,* Opt. Express **20**, 9999 (2012).

[15] D. Chen and J. Han, *High reflectance membrane-based distributed Bragg reflectors for GaN photonics,* Applied Physics Letters **101**, 221104 (2012), http://dx.doi.org/10.1063/1.4768806.

[16] E. Cho, D. Pavlidis, and E. Sillero, *GaN/air gap based micro-opto-electro-mechanical (MOEM) Fabry-Perot filters,* physica status solidi (c) **4**, 2764 (2007).

[17] R. Sharma, Y.-S. Choi, C.-F. Wang, A. David, C. Weisbuch, S. Nakamura, and E. L. Hu, *Gallium-nitride-based microcavity light-emitting diodes with air-gap distributed Bragg reflectors,* Applied Physics Letters **91**, 211108 (2007), http://dx.doi.org/10.1063/1.2805028.

[18] R. Sharma, E. D. Haberer, C. Meier, E. L. Hu, and S. Nakamura, *Vertically oriented GaN-based air-gap distributed Bragg reflector structure fabricated using band-gap-selective photoelectrochemical etching,* Applied Physics Letters **87**, 051107 (2005), http://dx.doi.org/10.1063/1.2008380.

[19] A. C. Tamboli, M. C. Schmidt, A. Hirai, S. P. DenBaars, and E. L. Hu, *Photoelectrochemical undercut etching of m-plane GaN for microdisk applications,* Journal of The Electrochemical Society **156**, H767 (2009), http://jes.ecsdl.org/content/156/10/H767.full.pdf+html .

[20] C. Xiong, P. R. Edwards, G. Christmann, E. Gu, M. D. Dawson, J. J. Baumberg, R. W. Martin, and I. M. Watson, *High-reflectivity GaN/air vertical distributed Bragg reflectors fabricated by wet etching of sacrificial AlInN layers,* Semiconductor Science and Technology **25**, 032001 (2010).

[21] B. Zhang, Z. Zhang, J. Xu, Q. Ren, C. Jin, Z. Yang, Q. Wang, W. Chen, X. Hu, T. Yu, Z. Qin, G. Zhang, D. Yu, and B. Zhang, *Effects of the artificial Ga-nitride/air periodic nanostructures on current injected GaN-based light emitters,* physica status solidi (c) **2**, 2858 (2005).

[22] R. Tao, M. Arita, S. Kako, and Y. Arakawa, *Fabrication and optical properties of non-polar III-nitride air-gap distributed Bragg reflector microcavities,* Applied Physics Letters **103**, 201118 (2013), http://dx.doi.org/10.1063/1.4832069.

[23] T. Mitsunari, T. Tanikawa, Y. Honda, M. Yamaguchi, and H. Amano, *AlN/air distributed Bragg reflector by GaN sublimation from microcracks of AlN,* Journal

of Crystal Growth **370**, 16 (2013), 16th International Conference on Metalorganic Vapor Phase Epitaxy.

[24] M. Tuohiniemi, M. Blomberg, A. Akujärvi, J. Antila, and H. Saari, *Optical transmission performance of a surface-micromachined Fabry–Perot interferometer for thermal infrared,* Journal of Micromechanics and Microengineering **22**, 115004 (2012).

[25] C. A. Zorman, R. C. Roberts, and L. Chen, *MEMS Materials and Processes Handbook*, edited by R. Ghodssi and P. Lin (Springer US, Boston, MA, 2011) Chap. Additive Processes for Semiconductors and Dielectric Materials, pp. 37–136.

[26] P. Chu, J. Chen, R. Yeh, G. Lin, J. Huang, B. Warneke, and K. Pister, *Controlled pulse-etching with xenon difluoride,* in *Solid State Sensors and Actuators, 1997. TRANSDUCERS '97 Chicago., 1997 International Conference on*, Vol. 1 (1997) pp. 665–668 vol.1.

[27] E. Hoffman, B. Warneke, E. Kruglick, J. Weigold, and K. Pister, *3d structures with piezoresistive sensors in standard cmos,* in *Micro Electro Mechanical Systems, 1995, MEMS '95, Proceedings. IEEE* (1995) pp. 288–.

[28] G. Lin and R. A. Lawton, *3d MEMS in standard processes: Fabrication, quality assurance, and novel measurement microstructures,* JPL Report, http://parts.jpl. nasa. gov/docs/Lin2. pdf (2001).

[29] K. Biswas and S. Kal, *Etch characteristics of KOH, TMAH and dual doped TMAH for bulk micromachining of silicon,* Microelectronics Journal **37**, 519 (2006).

[30] O. Tabata, *pH-controlled TMAH etchants for silicon micromachining,* Sensors and Actuators A: Physical **53**, 335 (1996), proceedings of The 8th International Conference on Solid-State Sensors and Actuators.

[31] S. Brida, A. Faes, V. Guarnieri, F. Giacomozzi, B. Margesin, M. Paranjape, G. Pignatel, and M. Zen, *Microstructures etched in doped TMAH solutions,* Microelectronic Engineering **53**, 547 (2000).

[32] P. Sarro, S. Brida, C. Ashruf, W. Vlist, and H. Zeijl, *Anisotropic etching of silicon in saturated tmahw solutions for ic-compatible micromachining,* Sensors and Materials **10**, 201 (1998), cited By 11.

[33] K. Biswas, S. Das, D. Maurya, S. Kal, and S. Lahiri, *Bulk micromachining of silicon in TMAH-based etchants for aluminum passivation and smooth surface,* Microelectronics Journal **37**, 321 (2006).

[34] J. Laconte, D. Flandre, and J. Raskin, *Micromachined Thin-Film Sensors for SOI-CMOS Co-Integration* (Springer US, 2006) Book section 3, pp. 47–103.

[35] S. C. H. Lin and I. Pugacz-Muraszkiewicz, *Local stress measurement in thin thermal SiO_2 films on si substrates,* Journal of Applied Physics **43**, 119 (1972).

[36] T. Van der Donck, J. Proost, C. Rusu, K. Baert, C. Van Hoof, J.-P. Celis, and A. Witvrouw, *Effect of deposition parameters on the stress gradient of CVD and PECVD poly-SiGe for MEMS applications,* (2004) pp. 8–18.

[37] W. Fang and J. A. Wickert, *Determining mean and gradient residual stresses in thin films using micromachined cantilevers,* Journal of Micromechanics and Microengineering **6**, 301 (1996).

[38] J.-M. Jin, *Theory and Computation of Electromagnetic Fields* (John Wiley & Sons, Inc., 2010) pp. 295–341.

5

Fabrication of airgap Optical Filters based on PolySilicon-SiO_2

5.1. Introduction

The fabrication process presented in this chapter is based on the polysilicon-SiO_2 layer combination, which was developed and characterized in Chapters 3 and 4. Fabrication of CMOS-compatible air-gap optical filters according to a design for the ultraviolet and visible spectrum is more challenging as compared to a design for the infrared. The challenges in the fabrication of a UV/visible air-gap-based optical filter are fourfold:

1. Firstly, a quarter-wave optical thickness (QWOT) design in this particular part of the spectrum typically implies a sub-100 nm thickness of both the dielectric layer and the air-gap. The exceptionally high etch selectivity between the polysilicon and the SiO_2 layers in a doped TMAH solution, that was described in Chapter 4, is required for an accurate and constant thickness of these layers over the filter area. The access windows that are vertically etched to allow the sacrificial release by underetching of the SiO_2 layers results in a loss of effective filter area (i.e. a reduction of the fill factor of the filter; the part of the coated chip area that can actually be operated as the intended filter).

2. Secondly, a demanding filter design typically requires a large number of layer-air-gap pairs, which need to be anchored to the substrate. However, proper anchoring of the multi-membrane in such an optical filter should be achieved without resulting in a large surface area taken by these anchoring pillars, which would further reduce the fill factor.

3. Thirdly, the effect of the poor residual stress control in such very thin SiO_2 films complicates the realization of large-area membranes. The effect of the stress gradient on deformation of a membrane and optical response were studied in Chapter 4.

4. Fourthly, the membrane surfaces need to be optically flat. As will be described in Section 5.7, straining techniques can be used to reduce surface waviness. However, rupturing of the membranes has to be avoided, which is more difficult to ensure in thinner membranes. Basically, the process window for achieving flat membranes without rupturing becomes more narrow with thinner membranes. Moreover, a shorter pitch between anchoring poles has to be selected, thus further reducing the fill factor.

Any fabrication flow should in principle be independent of the specifics of the designed components or devices to be realised. However, these four process-related complications need to be taken into consideration in the filter design. This is basically similar to the set of design rules that are typically specified in terms of minimum dimensions and spacing for any microelectronic process for ensuring proper operation of the integrated micro-electronic components. In the design of an optical filter, three main design rules result.

1. The first design rule is related to the design of a filter that incorporates a series quarter-wave optical-thick (QWOT) layers. The complications of sub-100

nm layers in such a filter may be a reason for an interference-based optical filter design with the operation of each membrane at a higher order (i.e. 3QWOT or 5QWOT). The thicker optical layers imply membranes of higher rigidity. However, this would typically result in more sub-peaks in the transmission function and thus is at the expense of the optical response of the structure. This trade-off between the structural rigidity and optical response is an essential design choice in visible/UV airgap-based filter design.

2. The second design rule is the maximum unit filter area, as defined by the pitch between etch windows and/or anchoring poles. This unit filter area is set by the stress in the membranes and reduces with membrane thickness. This dimension depends on the design wavelength and the use of QWOT, 3QWOT and/or 5QWOT structures in the design.

3. The third design rule results from the area needed for the anchoring pole and the access windows used for the sacrificial release. Although the higher index of refraction contrast of the airgap-based filter design, as compared to all-dielectric designs is helpful in reducing filter complexity, a demanding filter design would nevertheless require a significant number of layer-airgap pairs. In principle, the effectiveness of the anchoring using the pillar has to be independent of the number and thickness of the layers (membranes), which sets the minimum value of the cross-sectional area of the anchoring pole. In addition, the pitch between anchoring poles in set by the straining technique used and the membrane thickness. Therefore, these dimensions are depending on the design wavelength and the use of QWOT, 3QWOT and/or 5QWOT structures in the design. It should be noted that the anchors and access-holes transmit and reflect unfiltered light. This stray light would significantly affect the overall optical transmission through the filter area. Therefore, reflectors or absorbers should be used and aligned with the position of the anchors and etching widows to avoid the transmission or reflection respectively of light through these parts of the filter structure.

This introduction indicates the significant interdependence between the fabrication and the design. For this reason this chapter introduces the optical design roadmap for fabrication of CMOS-compatible air-gap filters. The optical response of high-order designs is discussed. A layout design based on the FEM simulations of Chapter 4 is introduced. This design is based on unit-cell structures to yield a high fill factor (up to $\approx 98\%$) over a large area. Subsequently, the fabrication process is discussed in detail. A straining method is introduced to further straighten the membranes. The fabrication results are presented and are optically characterized.

5.2. Optical design roadmap

The optical design of interference-based optical filters has been studied in Chapter 2. The distributed Bragg reflectors (DBRs), which are the basis of many complex optical filters, are composed of several 1-QWOT layers of high and low index layers. Moreover, DBRs with higher *odd* multiples (i.e. 3, 5, ...) of QWOT (Quarter-wave

Optical-thickness) layers also satisfy the interference condition, resulting in a reflection at a specific center wavelength. Similarly, Fabry-Perot optical filters can have a cavity of *even* multiples of QWOT layers (i.e. 2, 4, 6,...).

In air-gap-based optical filters, higher order designs have a few advantages and consequences. In optical filters designed to operate at a certain wavelength, the thickness of the layers (membranes and sacrificial layers) decrease linearly with the wavelength. For filters designed for shorter wavelengths (e.g. ultraviolet spectrum) the membranes become thinner. Consequently, the thickness control during the deposition becomes more difficult. A better thickness control can be achieved using higher order designs. Using higher order designs, a better thickness control can be achieved. Furthermore, the stiffness of a membrane (i.e. its resistance to deformation) increases by t^3 [1]. A 3-QWOT membrane, for instance, is 27 times stiffer than a 1-QWOT membrane. Therefore, a high order design provides a reliable thickness control and a more robust structural design.

Using odd multiples of QWOT membranes has already been used in many state-of-the-art airgap devices in infrared and ultraviolet. The stress gradient in InP-based membranes often results in a deformation of the membrane and departure from the optical design. The stress gradient in InP membranes is often related to the variation of arsenic (As) concentration [2]. This stress concentration is typically in the order of $10\ Mpa/\mu m$ [2]. Maintaining an optimal membrane flatness has hence limited the use of thin $\lambda/4n$ (known as QWOT- Quarter wave optical thickness) layers, which is ideal for a DBR structure. Therefore, earlier works were focused on fabrication of membranes of $3-5\lambda/4n$ (odd-multiples) thick layers [3, 4]. Even though the stress gradient are probably unavoidable, a proper mechanical design (usually through finite element modeling) can result in a negligible deformation of the membrane [2]. Single QWOT free-standing layers have been released using stress-controlled deposition methods and proper mechanical designs [1, 2]. In ultraviolet and visible, GaN-based optical filters fabricated up to now (to the author's knowledge) are composed of 3 or higher order membranes (for instance see [5–8]).

On the other hand, the transition to high order designs comes at the expense of limited bandwidth and higher-order ripples in the out-of-band spectrum. Figure 5.1 shows the expected reflectance of DBRs of a different optical order and designed for a $400\ nm$ center wavelength, as calculated in TFCalc using transfer matrix method [9]. The curves show the reflectance of various 2-period ($N=2$) DBRs with $n_L=1$ (air) and $n_H \approx 1.5$ (SiO_2) designed for a peak reflectance at $400\ nm$ (see Chapter 1). Moreover, the data for SiO_2 used here is based on the VASE best-fit data, as shown in Chapter 3. The top curve labeled $1Q1Q$ shows the reflectance of a first-order DBR (i.e. the 1 QWOT layers of air-gap and membranes). Curves labeled as $1Q3Q$, and $1Q5Q$ show the reflectance of a DBR of respectively 3 and 5 QWOT membranes, separated by 1 QWOT air-gaps. The curve labeled $Q3Q3$ is the reflectance of a DBR with 3 QWOT membranes and air-gap layers.

The bandwidth and peak reflectivity of the main reflection band is evaluated and listed in Table 5.1. Accordingly, the reflection bandwidth decreases with increasing the DBR order. This decrease is about 35% for $1Q3Q$ and about 50% for $1Q5Q$ and $3Q3Q$ designs (as compared to the standard $1Q1Q$ design). On the other

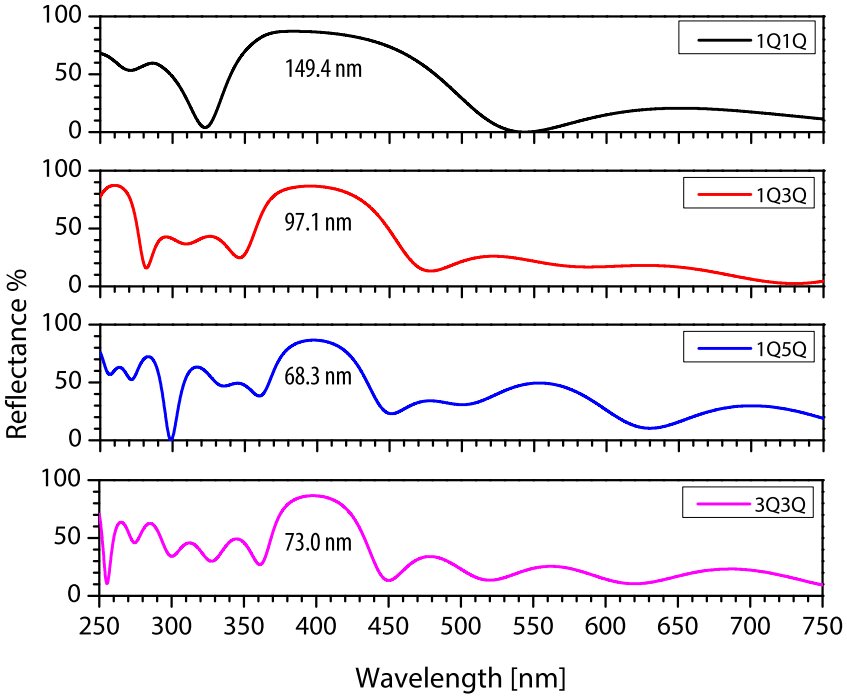

Figure 5.1: Expected reflectance of DBRs with $N = 2$ of air and SiO_2 at higher odd orders.

Table 5.1: Bandwidth and peak reflectivity variations in high-order optical DBR designs.

LH-Layers	Bandwidth [nm]	Peak reflectivity %
1Q1Q	149.4	87.1
1Q3Q	97.1	86.7
1Q5Q	73.0	86.4
3Q3Q	68.3	86.6

hand, the peak reflectivity at the center wavelength does not change as much. Furthermore, ripples in the reflection curve appear in high-order designs. The out-of-band reflection level generally increases for thicker membranes (high-refractive-index layers), while the wider air-gap layers (low-refractive-index layers) add to the number of ripples in the out-of-band region. According to these results, a fabrication roadmap is devised. A $1Q1Q$ design gives the best performance, but the fabrication of such a thin layers is challenging. The $1Q3Q$ design was found to be the most appropriate design.

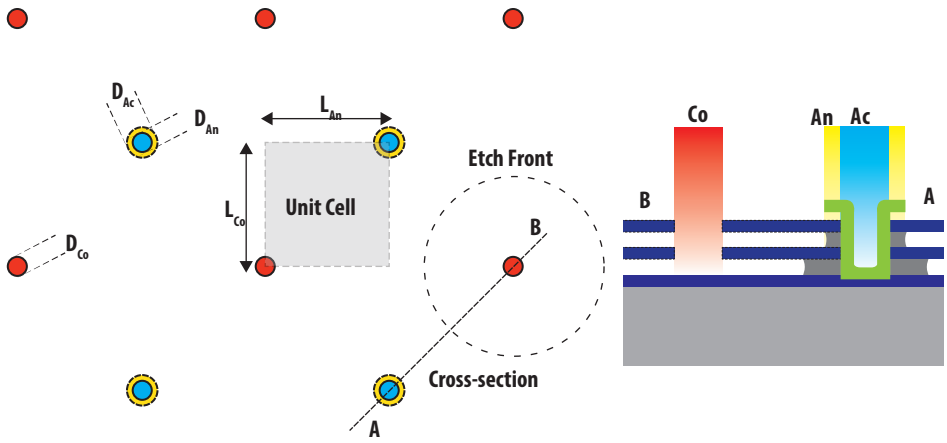

Figure 5.2: Layout design

5

5.3. layout Design

The layout design of an optical (air-gap) filter structure depends on several factors and specifications. A proper structural design must consider material-based factors, such as etch selectivity between the structural and sacrificial layers, and the state of the residual stress of the structural layers. The specifications, such as fill factor and the required active area, imposed by optical applications is also decisive.

In the III-V-based optical devices (LEDs and WDMs), a small active area, typically up to $100\ \mu m$ diameter are interested [1, 5, 8, 10, 11]. However, in absorption spectroscopy applications a larger optically active area would translate into a larger optical signal (intensity). Furthermore, the practical operation of structures such as LVOF would require a large optical area.

The necessary number of optical membranes required for any application, to some extent, can influence the layout design. Due to the high refractive contrast between air and membrane in the infrared spectrum, (e.g. $n_{Si}/n_{air} \approx 3$), only a few number of layers are necessary to obtain the specifications of the required optical response in most applications [12, 13]. On the other hand, the refractive index contrast available in the CMOS-compatible systems is limited. Therefore, a higher number of periods ($N = 2$ or higher) is necessary to achieve the intended spectral response.

The fabrication process is based on a three-masked process: anchoring mask (**An**), anchor cover (**Ac**), and contact opening for the sacrificial etching (**Co**). A unit-cell-based design with anchor pins and access-holes was developed. The main design of the masks was based on a rectangular array of circular sacrificial access-holes and anchor pins. Figure 5.2 shows the generic design of the masks. As shown in the figure, the **An** and **Co** patterns define the area that has to be etched through the already deposited layer stack. As the thickness of the membrane layers required for ultraviolet range filters is low, an auxiliary anchoring layer is deposited

after the opening of the anchor-holes. It must be noted that this layer must have a high etch selectivity to the sacrificial etching. This layer is usually the same as the membrane material is deposited to obtain a high adhesion to the membrane material. Furthermore, the deposition process must have a high step coverage. This auxiliary anchoring layer is then patterned using the **An** mask. This mask covers the already deposited anchors using a photoresist layer. This layer keeps the anchors from etching while removing the excessive area of the anchoring layer. This will result in pin-shape structures that can anchor any number of membranes. A schematic cross-section of a fabricated structure based on this mask (line A to B) is shown in the insert of Figure 5.2.

Table 5.2: Typical mask dimensions

Parameter	Dimensions [µm]	Description
L_{AN}	12.5	Anchor half-distance to the nearest anchor
L_{CO}	12.5	Contact-hole half-distance to the nearest
D_{AN}	2	Diameter of the anchor holes
D_{CO}	2	Diameter of the contact openings
D_{AC}	3	Diameter of the anchor coverings

As discussed before, the dimensions of the access hole and anchor pin and also the pitch between adjacent ones affect the optical throughput of the filters. While a locally dense pattern would consume the active area of the optical filter, a sparse design would result in a weak membrane structure. The diameter of the etching access-holes used for sacrificial etching and the anchor-pins were chosen equal to $2\ \mu m$. This is the minimum possible diameter of features that can be reliably fabricated when using the lithography equipment available. Furthermore, the diameter of the anchor overlaps the discs in the **An** mask. The anchor pins and access holes in the membrane would significantly affect the overall optical response of the filter. Therefore, the size and periodicity of the anchor pins and access holes were chosen to achieve a high active area. The periodicity of the access holes ($2L_{Co}$) also determines the etching distance (hence etching time). As was shown in Chapter 4, the etch selectivity between oxide and polySilicon is about $1-8\times10^4$ for a doped-TMAH solution (at $60^o - 80^o\ C$). Therefore, an etch length of $12.5\ \mu m$ (from one access hole to the center) has been selected to limit the etching of the membrane to values below $1\ nm$ at the wide range of etching temperatures. Furthermore, according to the etch rate of doped-TMAH solution, an etching duration from 40 minutes up to 120 minutes (corresponding to a solution temperature of $80^o\ C$ down to $60^o\ C$). This also results in a marginal loss of active area ($\approx 0.5\%$). Based on the results obtained in Chapter 4, a typical length of $25\ \mu m$ between each anchor point can be used while keeping the deformation bellow $10\ nm$. Table 5.2 lists the various dimensions used for the mask design. Other structures, such as anchored hexagon-shaped structures with different patterns were also designed and were

included in the mask fabrication.

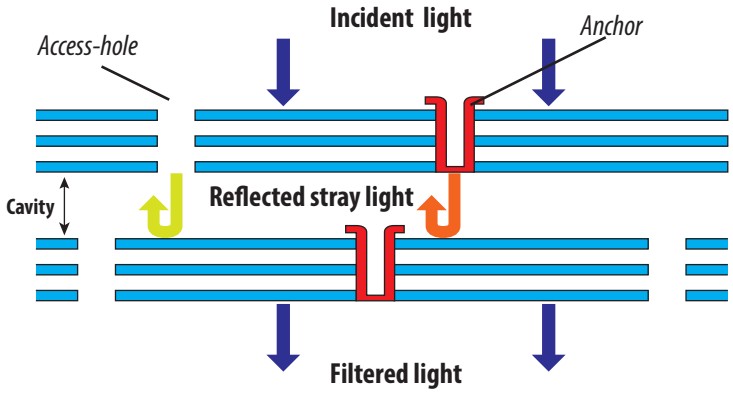

Figure 5.3: Schematic of a shifted layout (cross-section) design for rejection of the stray light.

A tunable transmission filter is a key component in a microspectrometer application. The presence of areas within the filter area with non-defined transmission would deteriorate the performance of such an instrument. This is especially the case for parasitic transmission at low optical signal levels. A possible solution, in this case, is shifting the position of access holes and anchoring in the top and bottom reflectors. In this configuration (shown in Figure 5.3) a reflector always covers the anchors and access holes. Therefore, the interference condition is not satisfied, and the stray light will be reflected back.

5.4. Fabrication of air-gap based Optical filters

The CMOS-compatible fabrication of free-standing membrane structures is presented in this section. The fabrication process is based on the simplified process flow was already schematically presented in Chapter 3. The schematic of the fabrication process of the membrane is shown in Figure 5.4. The fabrication was carried out on 10 cm diameter, <100> silicon wafers. SiO_2 thin film layers were deposited using PECVD method and used as the structural material. Moreover, polysilicon layers deposited using LPCVD was used as the sacrificial material. Furthermore, a PECVD oxide layer was also used as the anchoring layer. The fabrication is divided into three steps, **deposition**, **structuring**, and **sacrificial release**.

5.4.1. Layer deposition

In the **deposition** step, a stack of layers of PECVD oxide and polysilicon were deposited according to the optical design. As discussed in Chapter 3 and 4 polysilicon and PECVD oxide layers were used as the sacrificial and membrane materials respectively. The sacrificial polysilicon layers were deposited in LPCVD chamber at $570^o\ C$. The deposition of the oxide layers was performed in a 7-station deposition chamber (Novellus Concept One). Multi-station deposition systems are typically

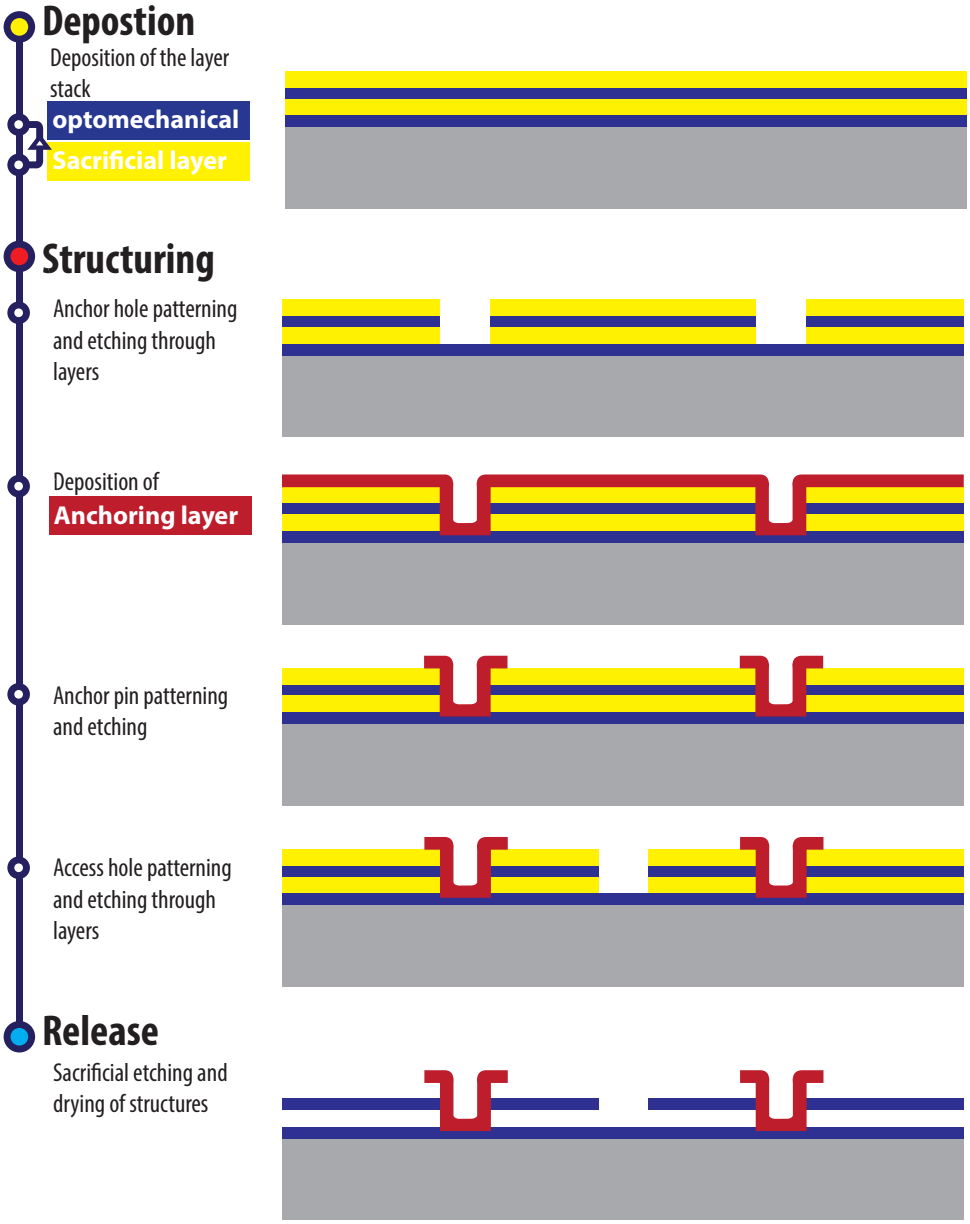

Figure 5.4: Schematic of the fabrication process: a. Deposition of sacrificial and membrane layers, b. Etching access-holes for anchor pins, c. Deposition of an anchor layer, d. Selective etching of the anchor layer, e. access-hole opening, and f. sacrificial release of the membrane.

used to obtain a high deposition throughput (wafers per hour) in industrial fabrication. The wafer would receive a partial deposition (i.e. $1/7^{th}$) at each deposition

station. However, deposition of very thin layers using this system require a very short deposition time (e.g. about 1 second). To ensure a stable deposition, when considering effects such as the uncertainty in the ignition time of the plasma for such a short deposition time, the deposition of the thin membranes was carried out at a single station. The thickness and uniformity of the deposited layers were measured using variable angle spectroscopic ellipsometry (VASE) (M2000, J.A. Woollam Co.) to calibrate the deposition time. Furthermore, the refractive index of the deposited PECVD oxide layers was evaluated using ellipsometry (as shown in Chapter 3) and used for the optical design.

The order of the layer deposition (starting with 1 directly on top of the silicon substrate) of an N-period Bragg reflector is listed in Table 5.3. Since the fabrication is based on the sacrificial etching of silicon, the silicon wafer must be protected. An oxide layer (first layer) protects the silicon wafer during the sacrificial etching of the polysilicon. Therefore, this passivation oxide layer must also be included in the optical design. Due to the relatively high step in refractive index between the oxide layer and silicon wafer, an oxide layer is used for the passivation of the wafer.

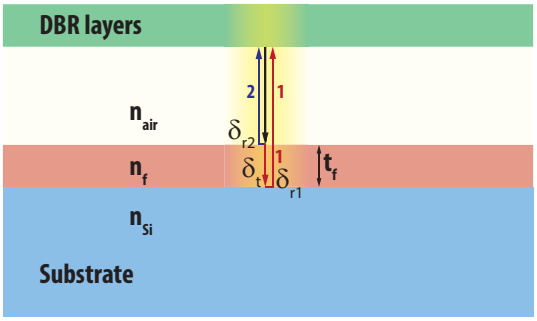

Figure 5.5: Light interference at the passivation layer.

The thickness of the passivation oxide layer must be selected to maintain a high reflectance of the filter. Figure 5.5 shows an incident wave at the passivation layer. In an airgap filter, the passivation layer has two interfaces, one with silicon wafer on one side, and with air on the other side. Irrespective of the number of membrane layers, the three-medium system is similar to the case studied in Chapter 2 (Section 2.4.1). The phase difference between two waves reflected at the two interfaces of Silicon|SiO_2 and SiO_2|air (i.e. ray 1 and ray 2 in Figure 5.5) is:

$$\begin{aligned} \delta &= \delta_2 - \delta_1 \\ \delta_2 &= 2\delta_t + \delta_{r_2}, \\ \delta_1 &= \delta_{r_1}. \end{aligned} \tag{5.1}$$

Because $n_{Si} > n_{SiO_2} > n_{air}$, at both interfaces, the wave is reflected by a medium with a higher index of refraction. Thus, considering a normal incidence angle $\delta_{r_1} = \delta_{r_2} = \pi$. The phase difference between the waves hence becomes $\delta = 2\delta_t$, where $\delta_t = 2\pi n_f t_f / \lambda_0$. Therefore, to obtain a high reflectance the t_f has to be selected in

such that a constructive interference occur between the reflected waves ($\delta = 2m\pi$). A 2-QWOT layer results in $\delta = 2\delta_t = 2\pi$, and hence was used as the passivation layer.

The fabrication flow follows with the deposition of the sacrificial and membrane layers according to the optical design. Although optical filters are in principle based on layer optical thicknesses of an integer multiple of the quarter wave layers, the dispersion of the refractive index of the dielectrics usually calls for a refinement of the design. Therefore, the thickness of all layers is optimized using the transfer matrix method in TFCalc [9]. A polysilicon layer is deposited subsequent to the deposition of the last oxide layer to protect the membrane during the structuring. This polysilicon layer is used as the etch-stop layer for patterning the anchor layer.

Table 5.3: Layer thicknesses used for the fabrication of an N-period optical filter.

Deposition order	Layer	Thickness	Function
1	PECVD oxide	2 QWOT	Passivation
2	LPCVD polysilicon	1, 3 QWOT	Sacrifical layer
3	PECVD oxide	1, 3 QWOT	Membrane
...	...	...	...
2N+1	PECVD oxide	1, 3 QWOT	Membrane
2N+2	LPCVD polysilicon	≈ 100 – 200 nm	Passivation
2N+3	PECVD oxide	≈ 500 – 1000 nm	Anchoring layer (after patterning)

Variable angle spectroscopic ellipsometry (VASE) can be used to characterize the layer thickness and layer interfaces after the deposition of the layer stack (and subsequent annealing steps). This is especially important to study the interdiffusion of layers and interface changes in thin layer stacks [14, 15]. Ellipsometry results ensure that the layers are optically according to the design.

Bragg reflectors with one and two periods centered at $400\ nm$ based on 1-QWOT layers of polysilicon and SiO_2 ($1Q1Q$ design) have been designed. Subsequent to the deposition of the layers, the layer stacks were measured by VASE. A corresponding model based on already characterized polysilicon and SiO_2 was built and fitted over the thickness. Figure 5.6 shows the measurement and the fitted curve based on an appropriate model for a one-period DBR ($N = 1$). The fitted model, to a great extent, follows the Ψ and Δ measured after the deposition. The fitted model (as shown in Figure 5.6) completely follows the measured ellipsometry data in the wavelength range between $600\ nm$ and higher. However, the fit is not as good in the shorter wavelengths (from $250/nm$ up to about $600\ nm$). This is mainly due to the fact that the polysilicon is highly absorbing in that range, and the previously-fitted model for polysilicon has a limited accuracy. Therefore, the data below $600\ nm$ were disregarded in the analysis.Table 5.4 lists the expected and the thickness of the layers as measured by VASE. According to the results, the

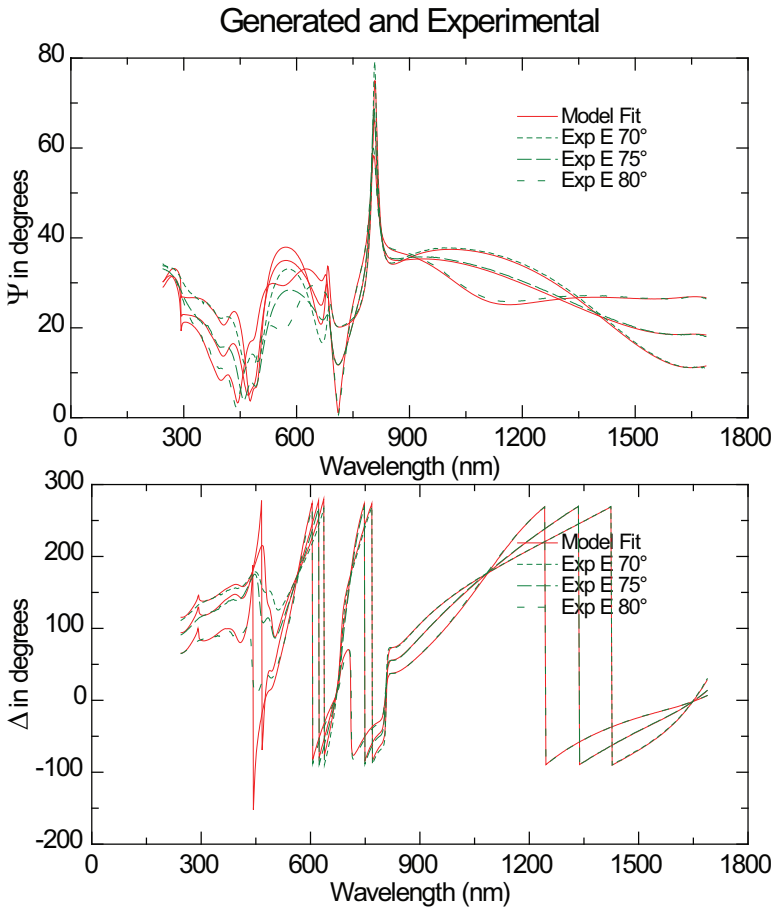

Figure 5.6: VASE analysis of a layer stack of a $N = 1$ 1Q1Q DBR before release. The red curve shows the best fit model.

thickness of the layers in the stack are found to be within the expected $\pm 7\ nm$. Furthermore, no interdiffusion of the layers was observed.

Table 5.4: Single Period DBR thickness of 1Q1Q thick layers

Order	Layer	Expected thickness [nm]	Measured thickness [nm]
1	Oxide	135.5	127.8
2	PolySilicon	100	106.1
3	Oxide	67	65.3
4	PolySilicon	100	106.2

Similarly, Figure 5.7 shows the measured and fitted curves of ellipsometry variables (Ψ and Δ) for a two-period DBR. Table 5.5 lists the expected and measured thicknesses of the layers.

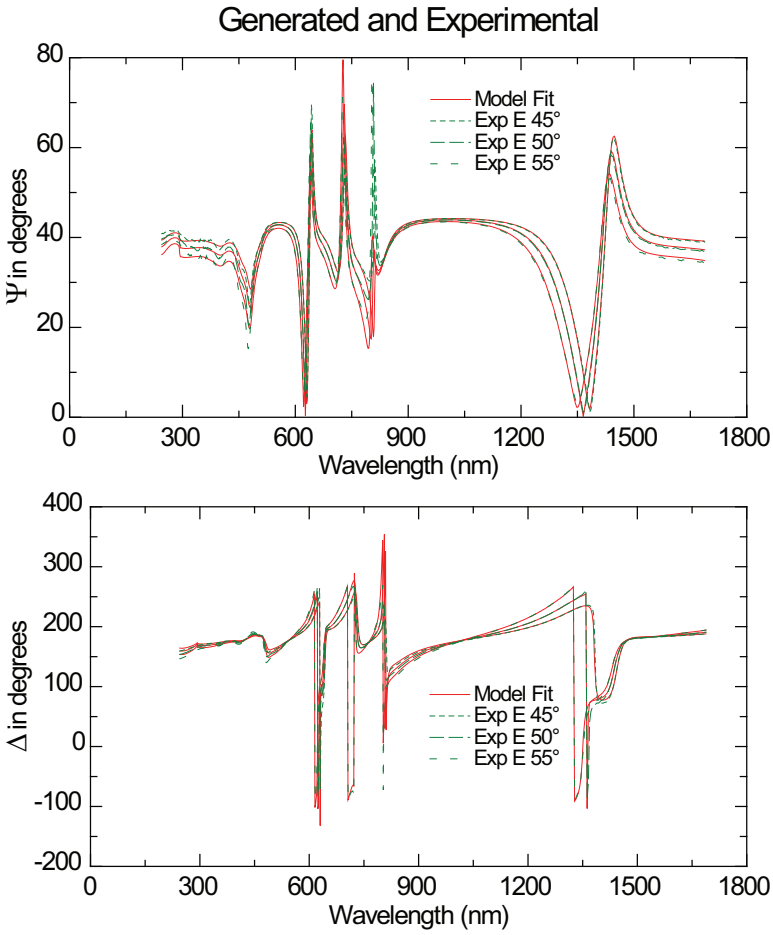

Figure 5.7: VASE analysis of a layer stack of a $N = 2$ 1Q1Q DBR before release. The red curve shows the best fit model.

Table 5.5: Double Period DBR thickness of 1Q1Q layers

Order	Layer	Expected thickness [nm]	Measured thickness [nm]
1	Oxide	135.5	126.7
2	PolySilicon	100	107.4
3	Oxide	67	66.5
4	PolySilicon	100	99.9
5	Oxide	67	66.3
6	PolySilicon	100	99.8

5.4.2. Structuring

The aim of the **structuring** step is to define the structure of the membranes by forming the anchoring structures supporting the membrane and also etching a set of access holes for enabling the sacrificial release. The anchors were designed as pin-shaped structures that can support any number of membranes. A set of opening patterns for the anchors were patterned on the wafers. As discussed before, the openings within the membrane area are $2\ \mu m$ diameter circles to maximize the effective area (i.e. fill factor) and are distributed evenly over the membrane area. The distance between each neighboring opening was kept equal to $25\ \mu m$. The pattern was then etched through the top layers (see Figure 5.4) in alternating plasma etching steps for polysilicon and oxide layers. The PECVD deposition offers an acceptable step coverage required for filling of the anchor holes hence was used as the anchoring layer. Figure 5.8 shows the 45 degree tilted SEM image of a cross-section of the area of some of the anchors in a cleaved sample. A subsequent $300\ nm$ PECVD oxide layer was deposited as the anchoring layer. Since both the membrane and the anchor are composed of PECVD oxide, the adhesion of the membranes to the anchors is expected to be high.

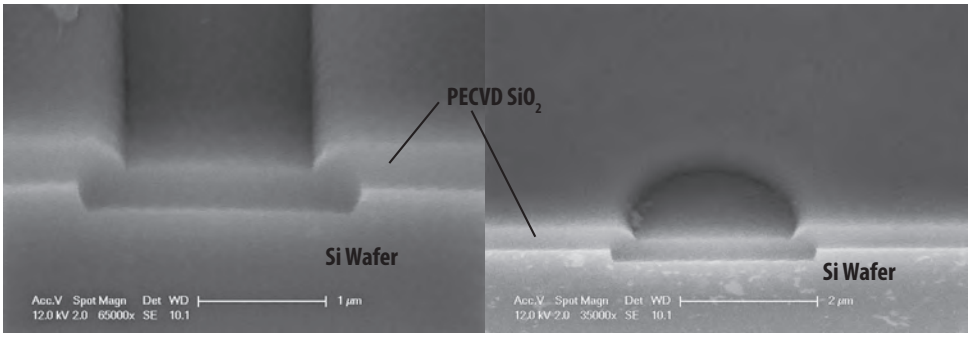

Figure 5.8: Step coverage of PECVD oxide layers in the anchor holes.

As the next step, the anchors were covered by a photoresist layer and patterned

using another (anchor covering-AC) mask. The remaining area of the anchor material was subsequently removed in a plasma etch. A pattern of access holes was realized on the membranes and etched through the sacrificial and structural layers. These openings provide access to the polysilicon layer for the sacrificial release.

5.4.3. Sacrificial release

In the last step, **Sacrificial release**, the polysilicon layers were etched in a 5% dual-doped TMAH solution at $75\ ^{o}C$. As discussed in Chapter 5, this solution gives an etch rate of about $16\ \mu m/hr$. Therefore, the samples were etched for 60 minutes (an etch time of about 45 minutes plus 15 minutes of overetch). A stiction-free drying process based on the critical point drying (see Chapter 3) was also used to dry the samples while avoiding the stiction.

5.5. Optical setup used for experimental validation

A reflection measurement setup shown in Figure 5.9 was used to characterize the fabricated samples. A deuterium-halogen light source (DH2000, Ocean Optics) serves as a wideband light source, covering the ultraviolet ($200\ nm$) and the visible range (up to $900\ nm$) for the spectral analysis. A seven-fiber bundle reflection probe was used (UV/Vis reflection probe, Avantes) to measure the spectral reflection at a specific area.

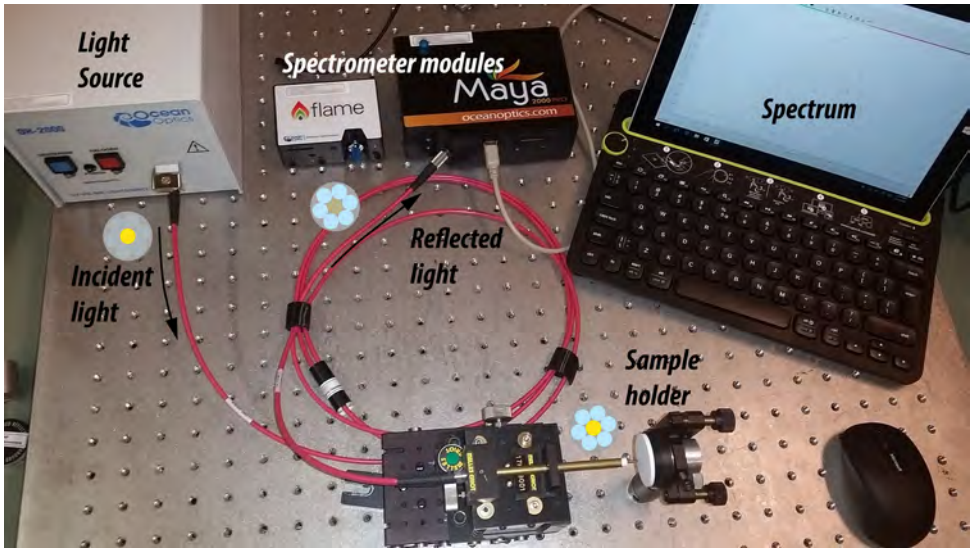

Figure 5.9: Reflection measurement setup.

Six illumination fibers within the bundle, each with $200\mu m$ core diameter and a numerical aperture of $N.A. = 0.22$ are connected to the light source. The probe-tip is placed in front of the sample and illuminates the surface. The reflected light is then collected by a read fiber ($200\mu m$ core diameter, $N.A. = 0.22$) in the center of

the probe. The viewing angle of the read-out fiber results as:

$$\theta = \arcsin(N.A./n) = \arcsin 0.22 = 12.7^{o}. \tag{5.2}$$

Therefore, while the minimum measurable diameter is about $200\ \mu m$ diameter (at the touch of fiber tip with the sample). As the position of the sample moves further away from the probe, a larger area is exposed and can be characterized. The read fiber is then connected to the spectrometer modules depending on the intended spectrum. A dedicated high-resolution spectrometer for UV with the typical resolution of about $0.3\ nm$ (Maya2000 Pro, Ocean Optics) and visible spectrum with the typical resolution of about $1\ nm$ (Flame, Ocean Optics). The recorded spectral analysis is then recorded. It should be noted that an initial measurement is performed using a diffuse reflectance standard (WS-1, Ocean Optics) to normalize the spectral output of the light source.

5.6. Results and discussion

N=1

Several samples were fabricated in two separate batches based on the process and layout discussed above. The batches were treated identically except for the PECVD deposition recipe used for fabrication of the membranes. The polysilicon etch rate was consistent with the etch rates measured before (see Figure 4.5 in Chapter 4). Figure 5.10 shows the microscope images of an area of free-standing membranes. The microscope images of the single membrane reflectors clearly show the waviness (or deformation) distribution over the membrane. An interference rainbow patterns can be seen in the microscope images, which is due to the changing interference of the white light between the wafer surface and the membrane caused by the surface topology (this effect is similar to fringes).

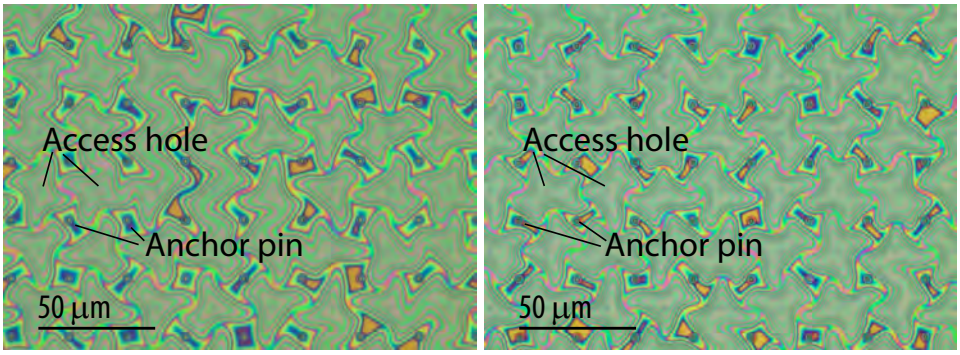

(a) PECVD oxide Type 1 (b) PECVD oxide Type 2

Figure 5.10: Microscope image of the released membranes of PECVD oxide membranes. The rainbow pattern shows the waviness in the released membranes.

It should be noted that the direct measurement of the very thin membrane deformation would be extremely difficult. A stylus measurement would itself affect

the membranes or would break the very thin membranes, while confocal microscopy is affected by the complex fringe formation due to the membranes and gives an incorrect result at the standard setting of the instrument. The deformation of the membranes qualitatively complies with the FEM analysis, as presented in Chapter 4, and confirms the gradual deformation toward the access holes.

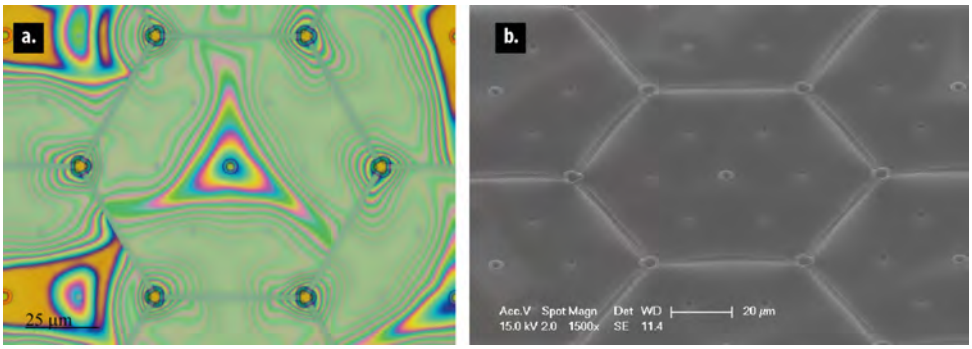

Figure 5.11: a. Microscope image of the single membrane (N=1) of *Type 1*. The interference fringes indicate a stress induced deformation in the membrane. b. 45-degree tilted SEM image of the same membrane.

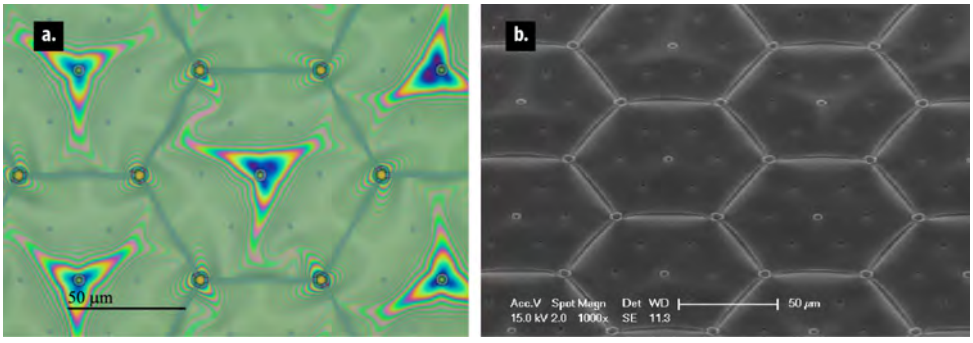

Figure 5.12: a. Microscope image of the single membrane (N=1) of *Type 2*. The interference fringes indicate a stress induced deformation in the membrane. b. 45-degree tilted SEM image of the same membrane.

Figure 5.11 shows a microscope image and SEM graph of hexagon-shape *Type 1* membrane. The deformation of the membrane is rather low as can be seen in the SEM image. However, interference fringes can be seen in the microscope images in Figure 5.11. The interference fringes indicate that the deformation of the membrane is higher than the flatness required by the optical design. Similarly, Figure 5.12 shows the microscope and SEM images of similar structure with *Type 2* PECVD membrane. The distribution of the rainbow patterns in the samples shows lower deformation in the samples with *Type 1* oxide membrane as compared to the samples of *Type 2* oxide membrane. This observation also confirms the results

of the stress gradient study (see Figures 4.15 and 4.16 in Chapter 4). Scanning electron microscope images of some other released structures are shown in Figures 5.13 and 5.14.

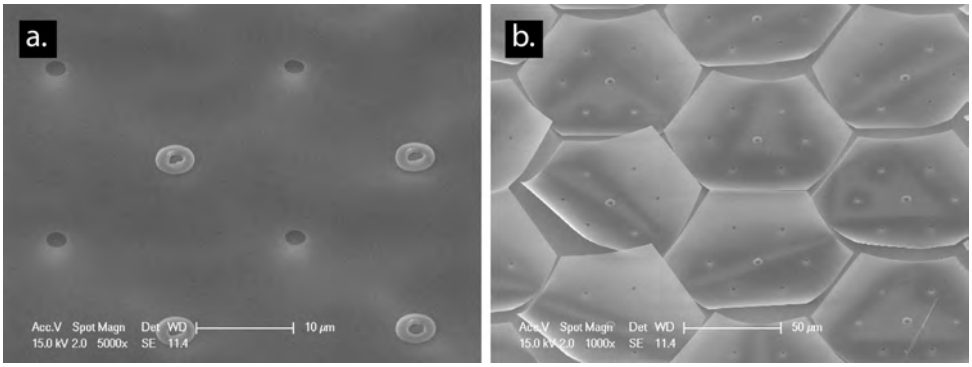

Figure 5.13: Various thin membranes of Type 1 oxide.

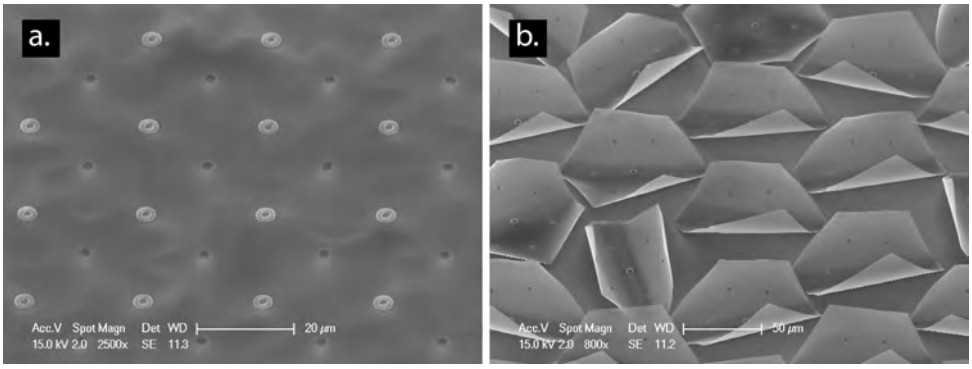

Figure 5.14: Various thin membranes of Type 2 oxide.

N=2

Several structure with two periods (of *Type 1* PECVD oxide) were also fabricated in the process described above. Figure 5.15 shows the microscope images the released structures. Similar to the single membrane structure the membranes are slightly deformed. This deformation is also similar for both membranes, and the membranes are separated. Figures 5.16 and 5.17 show the SEM and microscope images of various structures with two membranes. These structures also show that the membranes are separated.

These results show a higher membrane deformation as compared to the FEM and FDTD simulations presented in Chapter 4. Therefore, other effects must be considered. The strong deformation pattern seen in the released structures may result from various causes, such as plastic deformation of the membrane during the

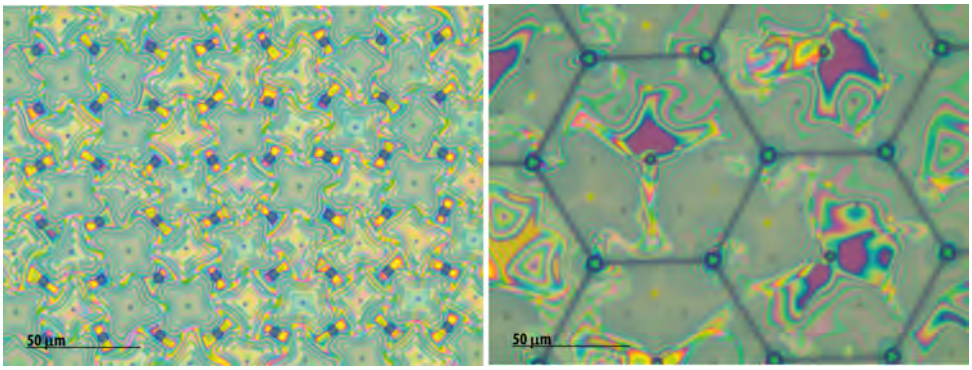

Figure 5.15: PECVD oxide membranes N=2.

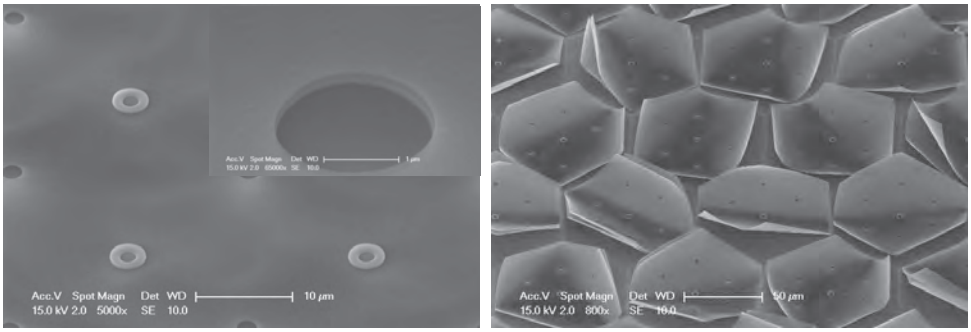

Figure 5.16: PECVD oxide membranes N=2.

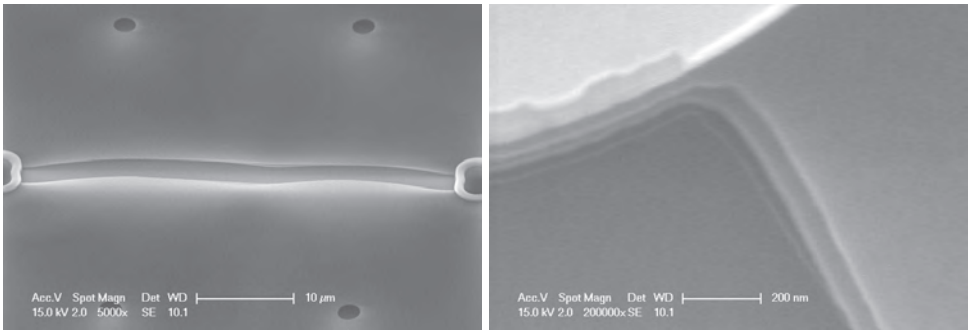

Figure 5.17: PECVD oxide membranes N=2.

deposition of compressive polysilicon layers. Plastic deformation of thin films has been reported in the literature. It has been shown by Maseeh and Senturia [16] that a temporary highly compressive layer on a tensile layer can develop high-stress values at the interface, which could result in plastic deformation of the strained

layer, even after the removal of the compressive layer. A similar mechanism may be responsible for the deformation of the membranes. It must be noted that the results obtained in Chapter 4 are based on the stress level in a SiO_2 layer without considering the stress of polysilicon that is used as the sacrificial layer. The sacrificial polysilicon layers are in a state of compressive stress. Therefore, plastic deformation could take place at the interface with the oxide membranes. Moreover, as shown in Chapter 4, the state of stress at the interfaces (hence the stress gradient) can dramatically intensify the deformation of the membrane.

Furthermore, this high-stress at the interface can be caused by other fabrication related issues. For instance, during the wet sacrificial etching of polysilicon, gas bubbles can be accumulated under the membrane before they can escape through the access-holes. An air bubble passing under the membrane may imposes a stress to the membrane that can displace or possibly deform the membrane. Therefore, using methods to minimize the bubbling effect by lowering the surface tension of the etching solution (typically done by adding alcohols) is being investigated.

5.7. Straining Methods

As was demonstrated in the previous section, achieving flatness in ultra-thin membranes is challenging. Varying the deposition parameters to obtain adequate tensile stress have been widely applied in literature to avoid buckling. However, as was discussed in previous sections, this becomes more challenging when reducing the layer thickness. Moreover, the stress gradient along the membranes thickness in very thin PECVD membranes is significant, which can result in a deformed membrane. To achieve the optical flatness criteria, *external* straining techniques to flatten the membrane seem to have potential. The Stoney equation implies that a layer with a tensile (or compressive) stress on the wafer's backside is equivalent to an identical, but compressive (or tensile), layer on the wafer's front-side. Many MEMS devices use a symmetric structure on both sides of the wafers to keep the wafer curvature in a unstressed condition during the entire process (for instance see [17, 18]).

In this research, a simple straining method using the stress of a layer on the wafer backside was investigated. Residual stress of a layer on the backside of the wafer changes the curvature of the wafer. Depending on the polarity of the residual stress of the backside layer, this wafer buckling can effectively stretch the front side layers (in which the membranes are realized). The thickness of the backside layer can be used as a parameter to obtain an effective tension of the membrane on the front side.

The schematic of the straining method is shown in Figure 5.18. The residual stress of the layer on the backside of the wafer bends the wafer. The radius of curvature of the wafer R depends on the residual stress σ and thickness of the layer d_f.

$$R = \frac{E d_s^2}{6 d_f \sigma} \tag{5.3}$$

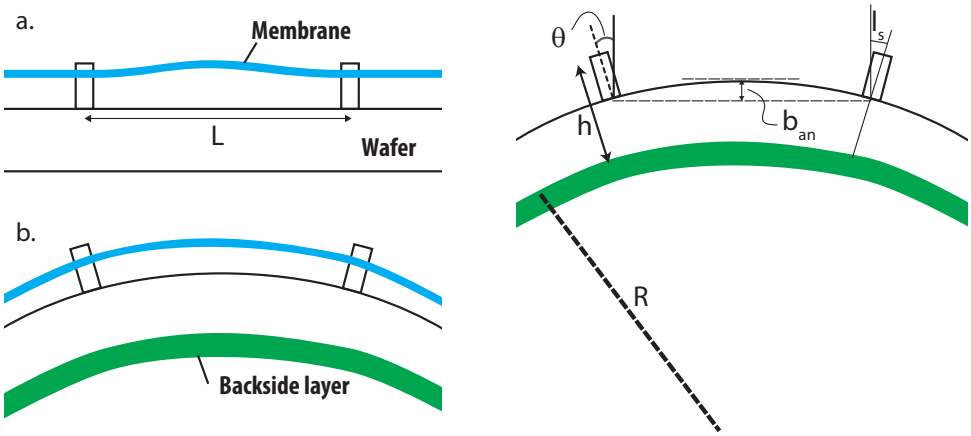

Figure 5.18: Schematic of a backside straining. a) un-strained wafer with buckled membrane. b) strained wafer (not to scale) resulting in an unbuckled membrane.

The wafer bow over a length of L, between two consecutive anchors, can be estimated as:

$$b_{an} \approx \frac{L^2}{8R} \tag{5.4}$$

The effective elongation of the distance between the anchors can hence be approximated by $2l_s$.

$$\tan\theta = \frac{2b_{an}}{L_{an}} \tag{5.5}$$

$$l_s = h\tan\theta \tag{5.6}$$

There are two effects when using the straining method. Firstly, a sufficiently high stress level is required to obtain enough straining on the membrane to actually remove the waviness. However, this stress level at the anchor points can easily exceed the yield strength of the material (see Section 3.9.3 in Chapter 4). Secondly, the straining of the membrane and the thickness (or the residual stress) of the backside layer are linearly related. Therefore, a thick tensile layer on the backside is required to obtain enough straining. However, the associated stress may be beyond the fracture initiation threshold of the layer (see Section 3.9.1 in Chapter 3). For PECVD SiO_2 layers of *Type 2* after annealing a fracture initiation thickness of about $2\ \mu m$ is expected (see chapter 3). The initiation of fracture in the backside layer relieve the stress, hence limits the maximum straining of the membrane. Therefore, this limits the applicable straining available for the structures.

5.7.1. Results and discussion

The strained membranes where fabricated using thick tensile stress *Type 2* PECVD oxide layers. During the fabrication and subsequent to the **deposition** and **structuring** steps, a $1500\ nm$ thick *Type 2* PECVD oxide Layer was deposited on the wafer backside. The wafer was subsequently annealed for 60 minutes at $600^o\ C$ to obtain a tensile stress. The residual stress in this layer was measured to be about $300\ MPa$. According to Equation 5.6, the membrane extends by about 0.5 to $0.7\ nm$ (for different structures) between the anchors when using this backside straining layer. The remaining part of the process (the sacrificial release step) was completed as for the original process.

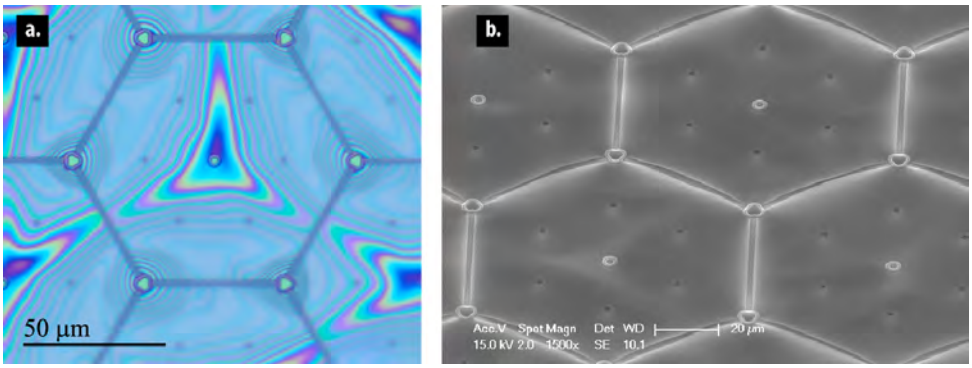

Figure 5.19: a. Microscope image of compound SiO_2-polysilicon membranes fabricated with a $1.5\ \mu m$ backside layer. b. 45-degree tilted SEM image of the same membrane.

Figure 5.19 shows microscope and SEM images of the released PECVD oxide membranes (*Type 1*) with a backside layer. A careful inspection of the interference fringes qualitatively indicates a lower deformation of the membrane as compared to the non-strained samples (See Figure 5.11). However, the straining was insufficient for obtaining an optically flat membrane. Although most samples fabricated via the straining method display a similar behavior, a few of them were optically flat. Figure 5.20 shows microscope images of one those samples. SEM images of the structures also illustrated in Figure 5.21. Optical investigation of the membranes, however, revealed that that a $77\ nm$ thick polysilicon layer has remained on the membrane layers. Although that the result seem counter-intuitive, as the polysilicon is the sacrificial material, closer investigation of the membranes reveal a very thin (less than $10\ nm$) SiO_2 layer on top of the polysilicon passivation layer.

The reflectance of the area shown in Figure 5.21 was measured and shown in Figure 5.22 (red curve). Based on the results, the reflectance is not according to the optical design. Optical design software (TFCalc) was used to reproduce the measured optical response. Several designs were analyzed and compared with the measured reflectance. The best-fit curve is also shown in the bottom half of Figure 5.21. Design 1 in Table 5.6 lists the optical design that corresponds to this measurement.

As an additional test, the area was intentionally damaged resulting in snapped

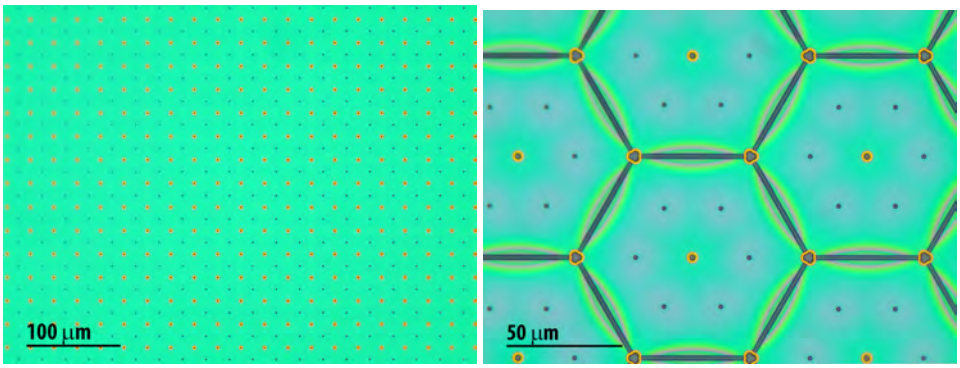

Figure 5.20: Microscope image of the released membranes of PECVD oxide membranes.

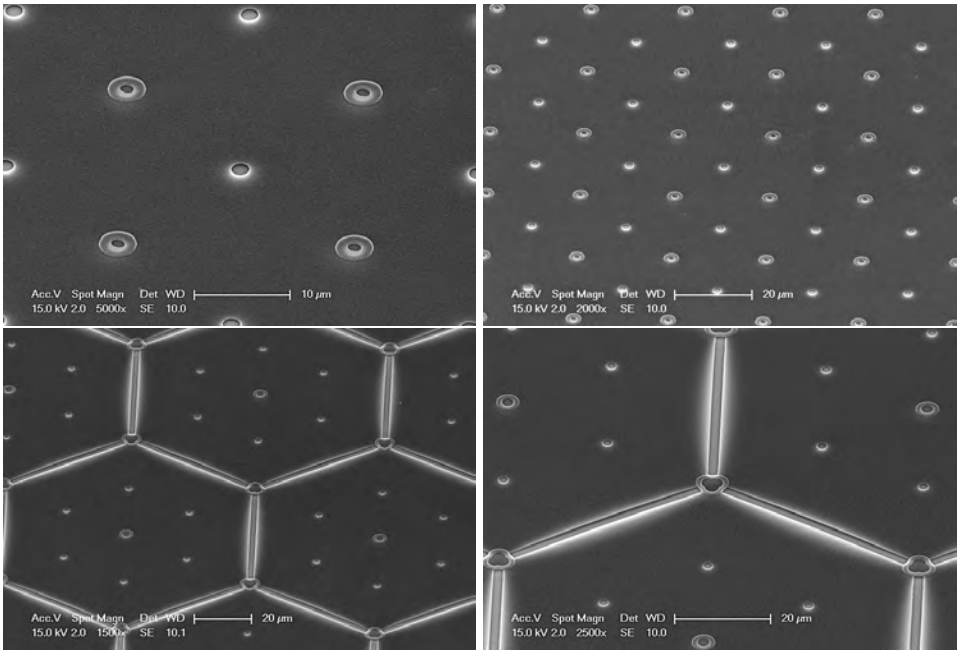

Figure 5.21: SEM imaging of the flat membrane by tensiling.

membrane to the wafer. Figure 5.23 shows the resulting spectral reflectance of the area. An optical design similar to the design used in Figure 5.22 (Design 1) but without the air-gap layer were used. As shown in Figure 5.23 the curve is in agreement with the measurement results. These results revealed that that a $77\ nm$ thick polysilicon layer has remained on the membrane layers. Although that the result seem counter-intuitive, as the polysilicon is the sacrificial material, closer investigation of the membranes reveal a very thin (less than $10\ nm$) SiO_2 layer (native oxide) on top of the polysilicon passivation layer. This layer protected the

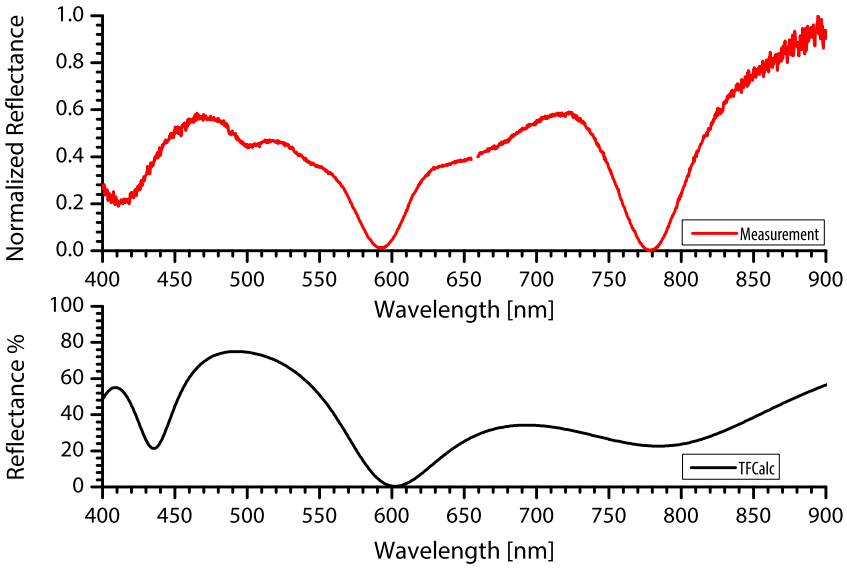

Figure 5.22: Top curve: The reflectance plot of the areas shown in Figure 5.21. Bottom curve: The reflectance modeled reproduced by TFCalc.

Table 5.6: Layer listing of reproduced best-fit curve of the measured reflectance.

Layers	Model 1: Thickness [nm]	Model 2: Thickness [nm]
SiO_2	135	135
Air (gap)	100	0
SiO_2	70	70
Polysilicon	77	77

polysilicon from etching during the sacrificial etch.

Figure 5.24 shows the SEM images of the thin SiO_2 residue that remained on the boundary of the flat areas. A thin fractured layer can be seen over the wavy area. It is expected that the same layer is present and covers part of the membrane area, thus protecting the polysilicon layer. The Young's modulus of the polysilicon layer (about $169 \pm 6\ GPa$ [19]) is about two times as high as that of the SiO_2 (about $81.5\ GPa$ [20]). Therefore, the compound membrane has become stiffer (i.e. more resistant to the deformations). These results indicate that, even though the stress gradient in the ultra-thin membranes is significant, flat membranes are nevertheless obtainable via this special straining method. Therefore, implementation of higher-order optical designs can also be used to obtain higher stiffness in the membranes.

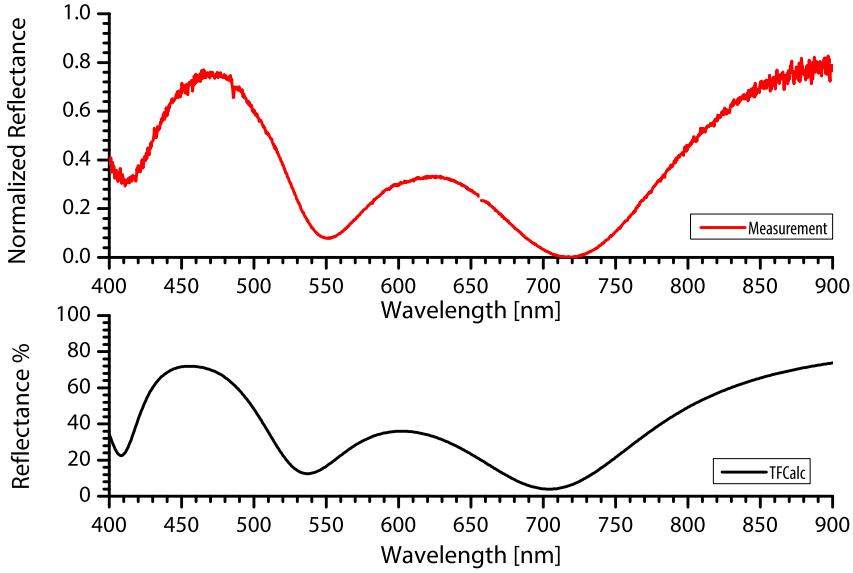

Figure 5.23: Top curve: Spectral reflectance of an area in which the membrane is intentionally damaged to snapped to the wafer. Bottom curve: The expected reflectance reproduced by TFCalc.

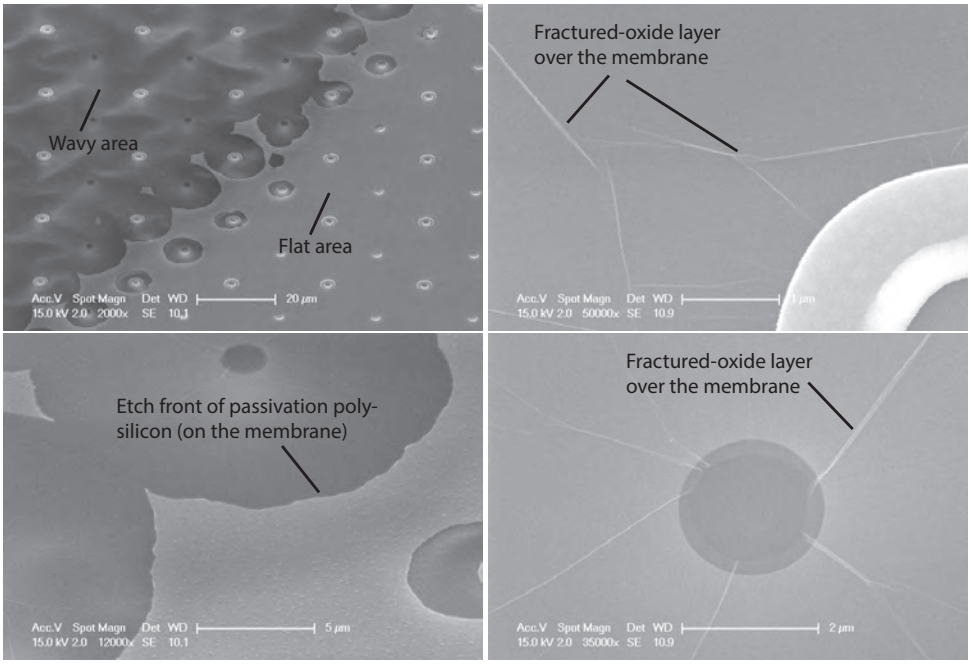

Figure 5.24: The boundary between flat area and wavy area of the membranes. A very thin and fractured layer can be seen at the wavy areas.

5.8. Higher-order and compound-membrane designs

The fabrication results presented in the previous section have led to the conclusion that a single quarter-wave optical design based on silicon-oxide layers is not suitable for the large-area optical application. According to the fabrication roadmap of Section 5.2, high-order designs using 3 quarter-wave thick membranes are highly promising. Furthermore, the compound membranes, such as oxide-polysilicon membranes, as discussed in the previous chapter are worthwhile to consider. However, polysilicon is not a suitable optical material for the UV spectrum, due to its optical properties. Furthermore, polysilicon functions as the sacrificial material in the fabrication of these airgap structures. Silicon-nitride is a suitable choice to replace the polysilicon layer in a compound membrane design.

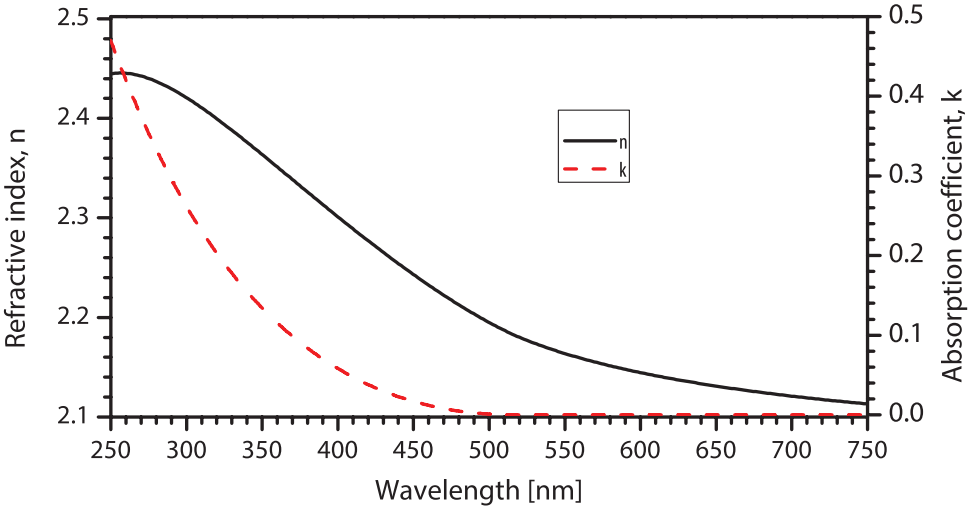

Figure 5.25: Refractive index of PECVD silicon-nitride measured and analyzed by VASE.

The Young's modulus of Silicon-nitride is significantly higher than that of oxide (about $200\ GPa$ for PECVD deposited films [21]). While the as-deposited residual stress of silicon-nitride films was measured to be equal to $-200\ MPa$ (compressive), the residual stress increased to about $1\ GPa$ (tensile) after an annealing cycle at 600^oC. Furthermore, the etch rate of silicon-nitride in TMAH is very low [22], thus can be used as a membrane material. The residual stress in silicon-nitride layers deposited using PECVD or LPCVD can also be tuned to be tensile. The only disadvantage of silicon-nitride is its high absorption coefficient in the UV range. However, using a thin silicon-nitride layer would not significantly degrade the optical response in the UV. The refractive index data of PECVD silicon-nitride was measured using ellipsometry and used for the analysis (see Figure 5.25). This approach is similar to the implementation of a nitride layer in the oxide membranes for compensating the compressive stress of oxide membranes used for thermal detectors [23]. Table 5.7 lists various membrane designs based on the conclusions on the mechanical properties of the materials and optical designs. Figure 5.26 shows and compares

the optical response of the different designs as listed in the Table 5.7.

Table 5.7: List of the high order and compound-membrane designs. The designs correspond to DBRs with 1QWOT airgap layer. The reflectance bandwidth corresponding to each design is also shown.

Order	Membrane composition	N	Bandwidth [nm]
a.	3 QWOT SiO_2	1	132.9
b.	3 QWOT SiO_2	2	97.1
c.	1 QWOT SiN	1	192.1
d.	3 QWOT SiN	1	121.1
e.	1 QWOT SiN + 2 QWOT SiO_2	1	160.4

According to Figure 5.26, all five designs result in a comparatively similar spectral response at the center wavelength of $400\ nm$. The designs **a** and **b** are composed of three-quarter-wave thick oxide membranes, with a different number of DBR periods of one and two, respectively. Thus the stacked membrane design of **b**, as compared to design **a**, resulted in an increase in the expected peak reflectance from 73% to about 87%. Designs **c** and **d** are composed of the single-quarter and three-quarter-wave thick nitride membranes. A single quarter-wave nitride layers, due to the higher refractive index, is thinner than a single quarter-wave of oxide. However, the Young modulus of nitride layers is about three times higher. Thus the fabrication of such a design is challenging but possible. Design **d** is based on a three-quarter-wave nitride membrane which, although the most stable mechanical design, is not very promising optically. The absorption coefficient of nitride (see Figure 5.25) in a thick membrane results in a degraded optical response, as compared to design **c**. Therefore, design **d** is not very suitable for multiple-membrane DBR designs.

Finally, design **e** presents a compound membrane designed using compound silicon nitride and silicon oxide layers in the membrane. This design benefits from multiple characteristics gathered by the mechanical and optical properties of its comprising materials. This design is based on the three-quarter wave design (**a**), where the first quarter-wave thick part is replaced with a nitride layer. The single quarter-wave nitride layer at the bottom interface mechanically increases the effective Young's modulus of the membrane. Furthermore, the residual stress of PECVD nitride layers strongly affects the total residual stress of the compound membrane. The effective optical properties of nitride and oxide layer result in a higher peak reflectance and a wider bandwidth, as compared to designs **a** and **b**. A single membrane DBR ($N = 1$) of design **e** would result in a bandwidth of $160\ nm$ and peak reflectivity of 82%. These characteristics make design **e** the most promising structure both from mechanical and optical perspectives.

Stacked layers according to the designs **a** to **e** were deposited on bare silicon wafers ($10\ cm$, <100>, P-type). The structuring was carried out according to the previous process flow. Several samples were etched and went through the stiction-free drying using CO_2 critical point drying. Different etch durations was chosen to study the membranes before the complete release. This is also used

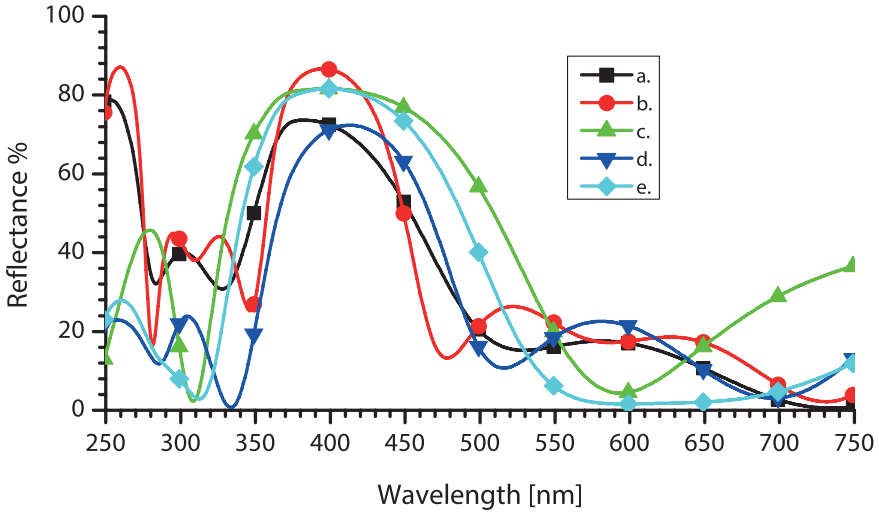

Figure 5.26: The optical response of various higher order designs as listed in Table 5.7.

to identify the maximum length the membrane can sustain the various forces on the membrane, such as the strain forces due to the factors such as the residual stress, the turbulent flow of liquids during the etching due to the bubble formation between the membranes and turbulent flow of liquids during the drying procedure. The design spectrum in these devices were chosen in such a way that any flaw in the devices results in a significant spectral shift in the visible spectrum. Therefore, microscope imaging and spectral reflectance analysis of the samples provides a comprehensive indication of the condition of the devices and was used as such in this study. In the next sections, the fabrication results of the five designs are presented, and the results are discussed.

5.8.1. Fabrication of 3 QWOT oxide membranes

According to the fabrication roadmap shown before, a $1Q3Q$ is the most promising compromise between processing limitations and optical specifications for the interested optical spectrum. A fabrication process based on the optical design was carried out. A stack of 3QWOT SiO_2 and 1QWOT air (sacrificial polysilicon) layers has been deposited and characterized using VASE. The remainder of the fabrication process was carried out similar to the process discussed before.

Design a: N=1

Figure 5.27 shows the microscope image of several released membranes of design **a** after the sacrificial release and drying. Various colors are recognizable in the microscope images. These areas correspond to released membranes (green-purple), unreleased membranes (yellow-green), and membranes snapped to the substrate due to the stiction (bright purple). The optical investigation qualitatively shows that the released membranes are optically flat. Figure 5.28 shows the SEM images of

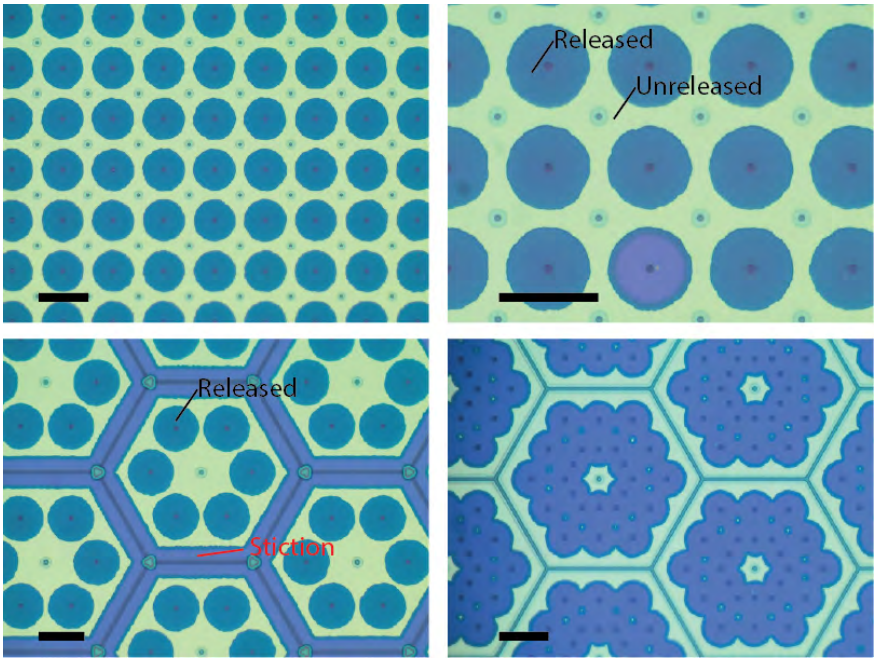

Figure 5.27: The microscope images of various partially under-etched sturctures of design **a**. The released, unreleased, and snapped area are visually recognizable. The scale bar in each image is $25\ \mu m$.

the same structures. The tilted SEM images also indicate that the membranes are optically flat and free-standing.

Figure 5.29 presents the expected optical response of this design as simulated using the transfer matrix method (TFCalc, software spectra). The reflectance of the structure for the unreleased structure and the released, but snapped membranes (due to stiction) are also presented in the figure. Accordingly, a significant shift in the spectral reflectance occurs from unreleased membranes to the released membranes.

The normal incidence reflectance of the samples was analyzed using the measurement setup shown in Section 5.5. It must be noted that the reflection setup measures the reflectance over a large area of the sample size. This area is determined by the core diameter of the fiber ($200\ \mu m$), its numerical aperture (0.22), and the distance from the sample surface ($0.5-2\ mm$). Based on these factors, the reflectance probe measures the spectral reflectance over a surface area of about $1-3\ mm^2$. Therefore, the measured spectral reflectance is a weighted combination of the reflectance curves of the released areas, the unreleased parts, the anchor pins, and the sacrificial openings.

Figure 5.30 shows the large-area reflectance of several samples. As expected, the measured reflection spectrum in the fabricated samples shows a combined reflectance spectrum of the released and unreleased membranes. While both of these

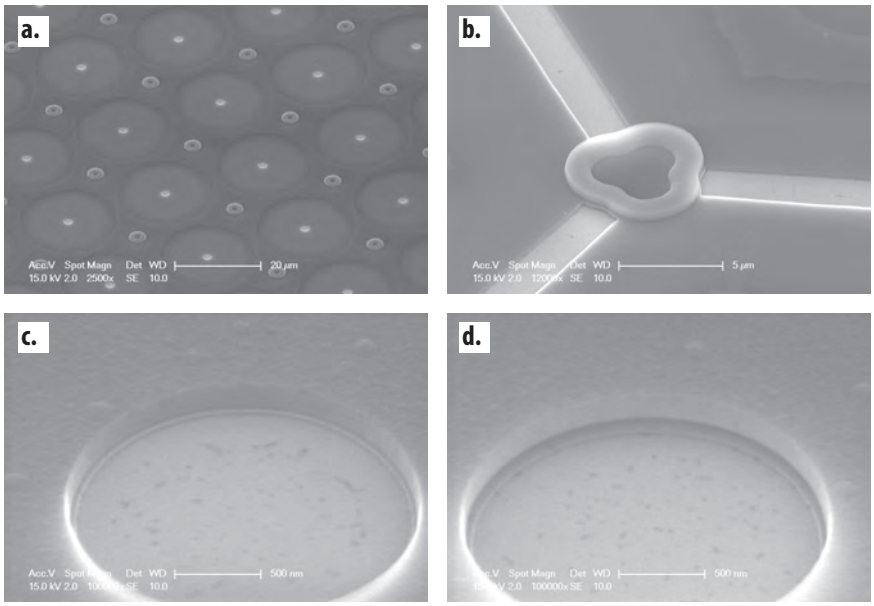

Figure 5.28: The tilted SEM images of various partially under-etched devices. The released and snapped membrane can be seen by comparing the images *c.* and *d.*

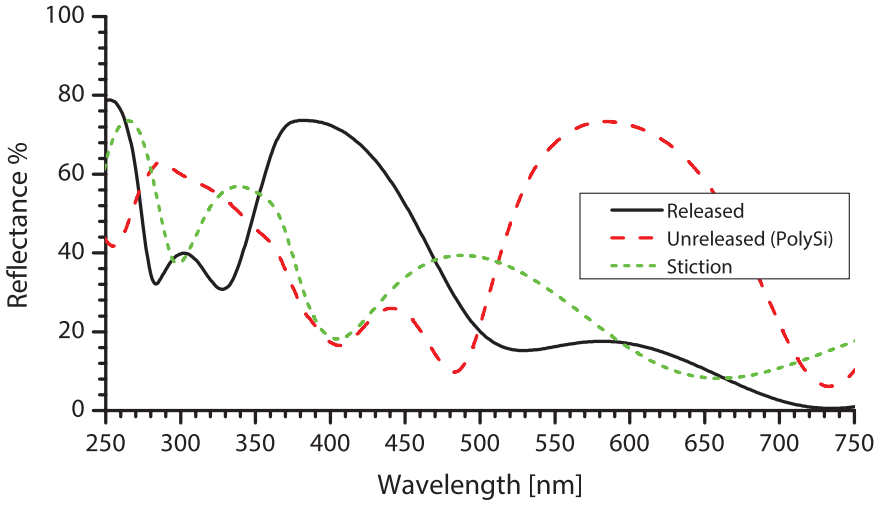

Figure 5.29: The expected reflectance of design **a** samples, before releasing, after releasing and snapped membranes.

peaks are present in the measured reflection spectrum, the ratio of the reflected intensity indicates the ratio of the area of the released membranes to the unreleased area. Based on a visual estimation, the fill factor of the released structures

varied from about 10% to 60% in the samples. By increasing the fill factor of the released structures, the peak centered at $400\ nm$ intensifies, while the peak corresponding to the unreleased parts decreases. Therefore, the measurement is in good agreement with the optical modeling.

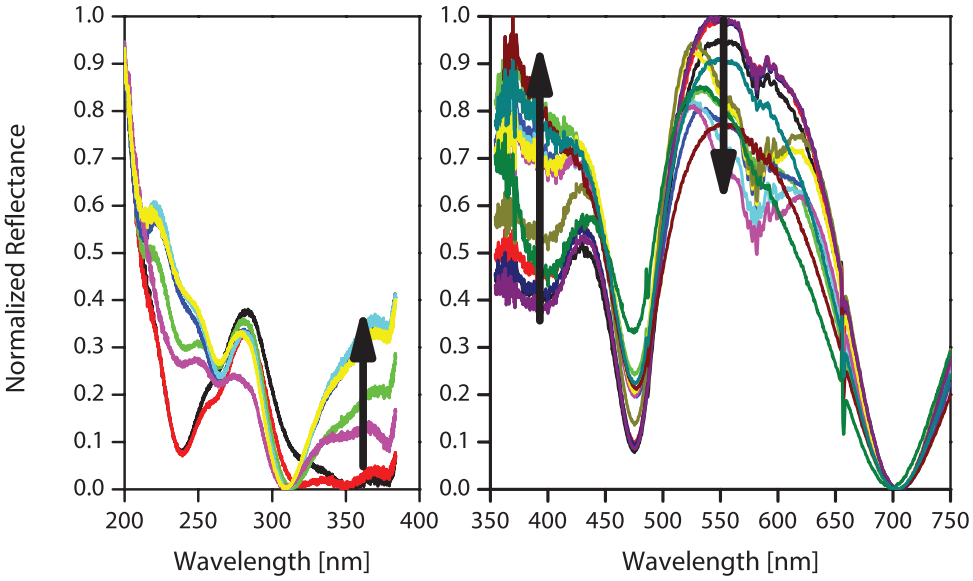

Figure 5.30: The measured reflectance spectra of design **a** samples. As the peak at $400\ nm$ intensifies, the peak at about $550\ nm$ decreases. The spectral reflectance over UV and over visible was measured using dedicated spectrometer modules and normalized separately, thus the data is not continuous in this figure.

Design b: N=2

Samples with two stacked three-quarter wave thick oxide membranes separated by a single quarter-wave airgap layer were fabricated. Figures 5.31 and 5.32 shows the microscope images and 45^o tilted SEM images of the released structure. Similar to the previous case, the free-standing area is recognizable and presents an optically flat surface. SEM images also show that the membranes are separated by the nominal distance of $100\ nm$.

Based on the visual estimation, the fill factor in this samples varies from 10% to about 80%. Figure 5.33 shows the expected reflectance of the structure for different scenarios. For instance, the case where the membranes are snapped together but are separated from the substrate (as shown in SEM photo 5.32-c.), is considered. Spectral reflectance analysis over a large area ($1 - 3\ mm^2$) is shown in Figure 5.34. The spectral response of these samples shows a similar behavior between the released area and the relative height of the peak at $400\ nm$ to the peak at $500\ nm$ (according to expected peaks represented in Figure 5.33). It must be noted that the process yield for the double membrane is lower than for the structures with a single membrane.

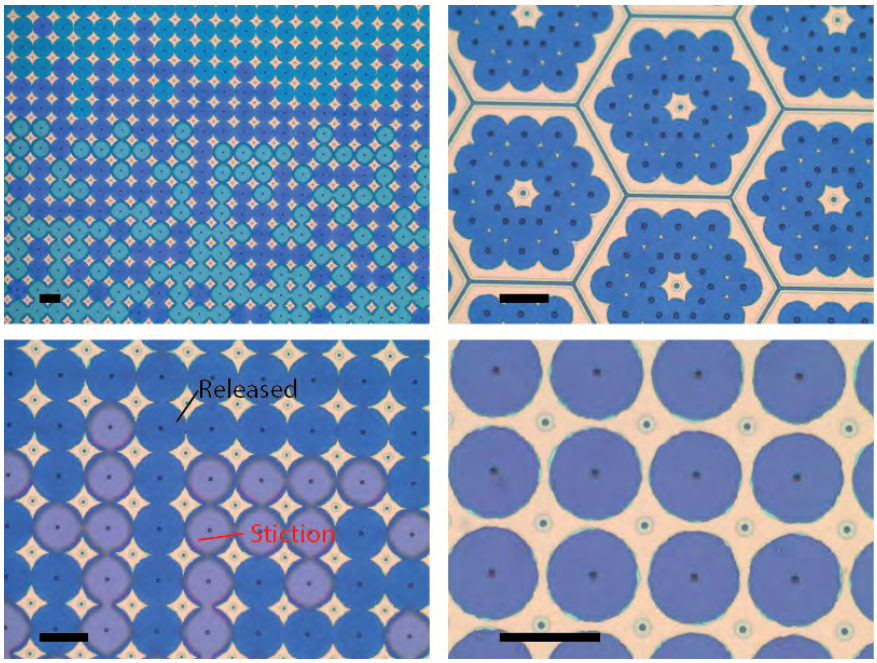

Figure 5.31: The microscope images of various partially under-etched devices of design **b**. The released, unreleased, and stiction area are visually recognizable. The scale bar in each image is $25\ \mu m$.

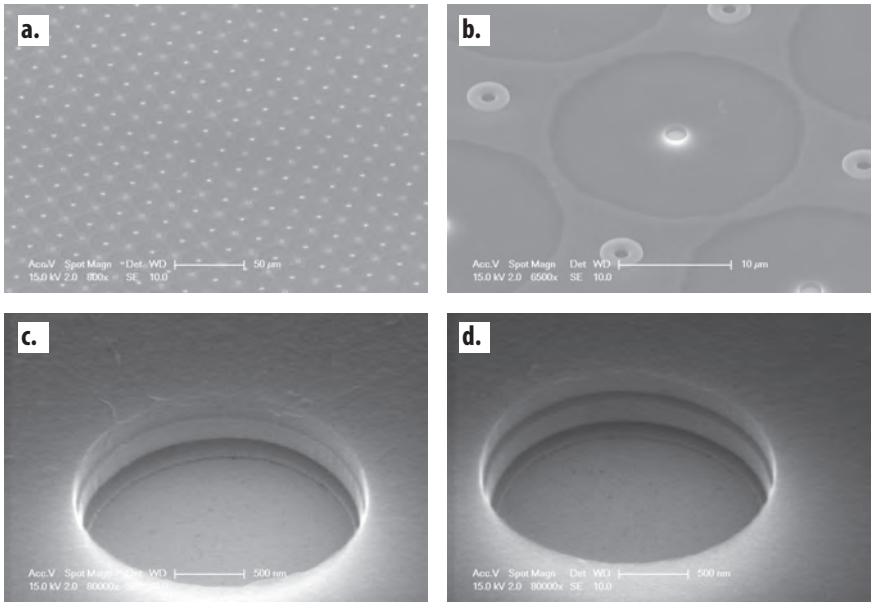

Figure 5.32: The tilted SEM images of various partially under-etched devices of design **b**. The released and snapped membrane can be seen by comparing the images *c* and *d*.

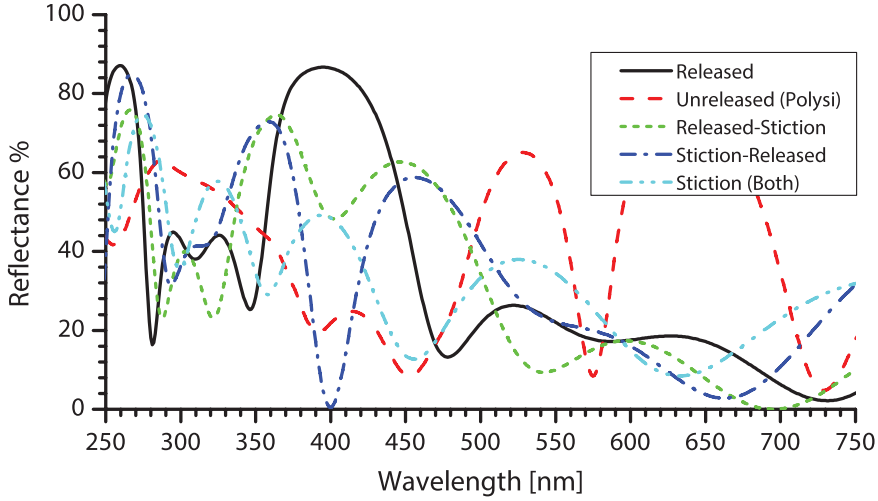

Figure 5.33: The expected reflectance of design **b** samples, before releasing, after releasing and snapped membranes (different stiction cases are also considered).

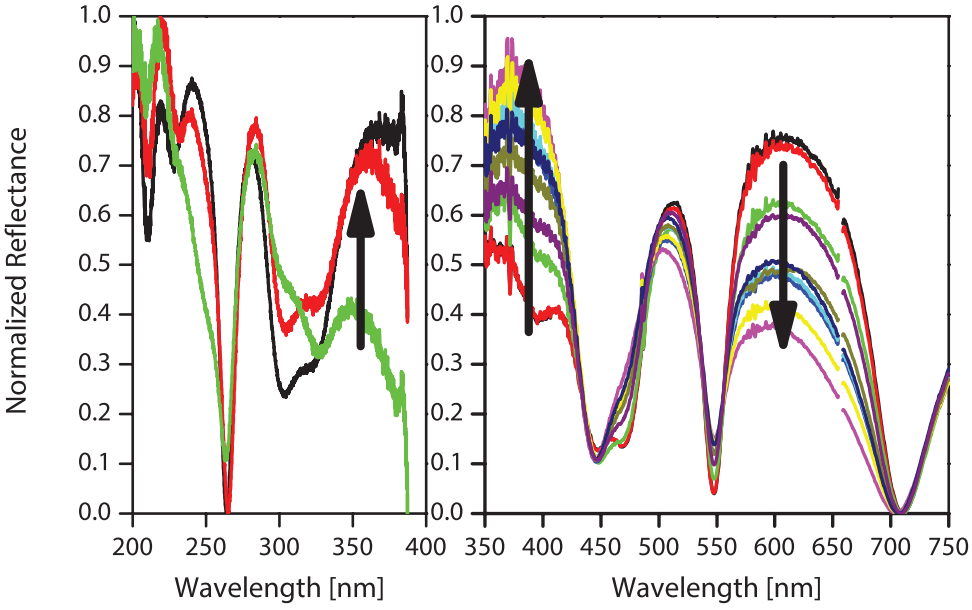

Figure 5.34: The measured reflectance spectra of design **b** samples. As the peak at $400\ nm$ intensifies, the peak at about $600\ nm$ decreases. The spectral reflectance over UV and over visible was measured using dedicated spectrometer modules and normalized separately, thus the data is not continuous in this figure.

5.8.2. 1 QWOT and 3 QWOT nitride membrane fabrication

Design c

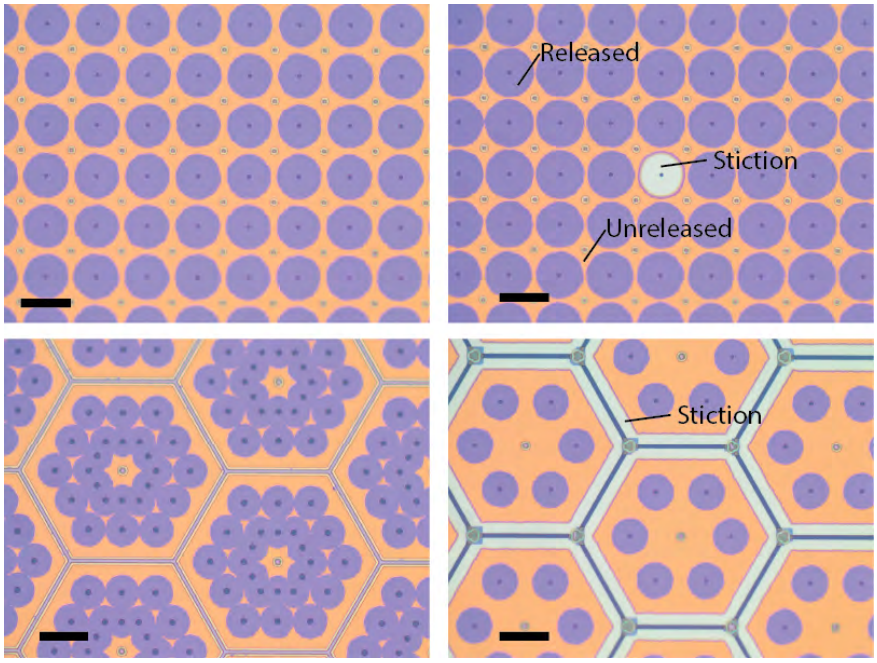

Figure 5.35: The microscope images of various partially under-etched devices of design **c**. The released, unreleased, and stiction area are visually recognizable. The scale bar in each image is $25\ \mu m$.

Several structures of design **c** were fabricated and characterized. These structures use a one quarter-wave silicon-nitride layer as the membrane material. Therefore, these membranes have a diameter-to-thickness ratio of more than 500, which is the highest among all designs. Figure 5.35 and 5.36 show the microscope images and 45^o tilted SEM images of the partially released membranes. Measured reflectance curves, as shown in Figure 5.38, clearly follow the expected spectral reflectance of various cases shown in Figure 5.37. A pronounced spectral reflectance at $400\ nm$, corresponding to the released membranes (about 90% fill factor), is noticeable in Figure 5.38.

Although the extinction coefficient of silicon-nitride is significant, the nitride-based designs are still highly interesting. This stems from the higher refractive index of silicon-nitride, as compared to the silicon-oxide designs. The higher refractive index of nitride results in a considerable increase in the refractive index contrast. Furthermore, for the same reason, a QWOT of silicon-nitride is thinner, thus the intensity loss due to the absorption is smaller.

Design d

The structures of design **d**, which are composed of a three-quarter-wave nitride membranes, were fabricated, and the results are shown in Figure 5.39 and 5.40.

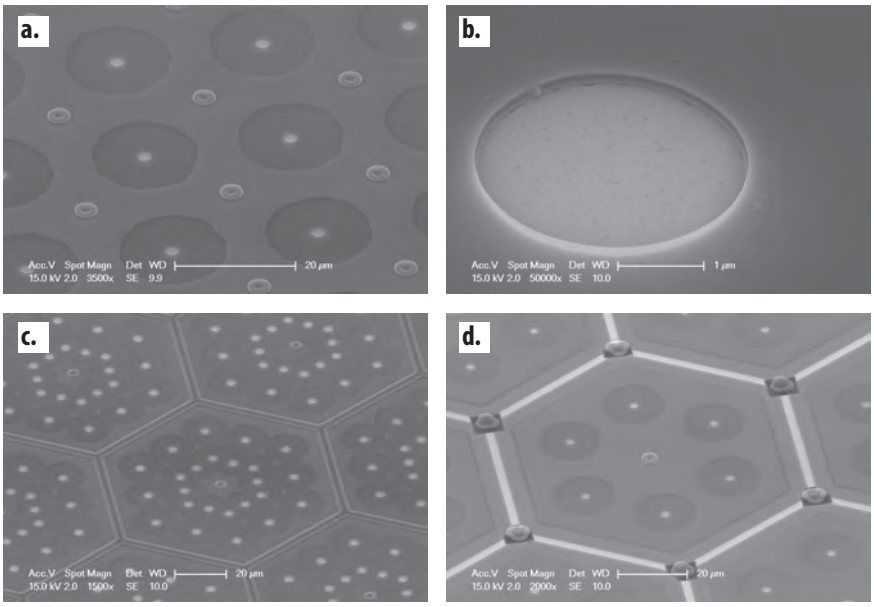

Figure 5.36: The tilted SEM images of various partially under-etched devices of design **c**.

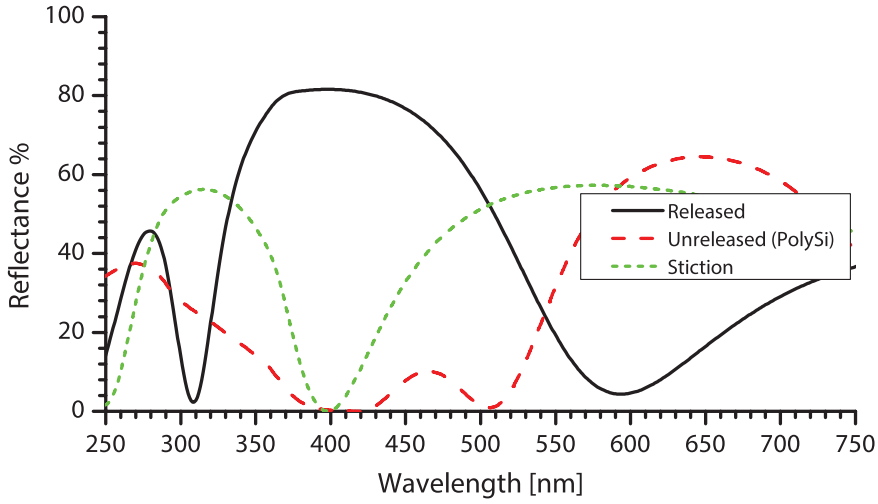

Figure 5.37: The expected reflectance of design **c** samples, before releasing, after releasing and snapped membranes (different stiction cases are also considered).

Due to the higher Young's modulus (than oxide) and thicker membrane (compared to design **c**), these structures were mechanically more stable, and the fabrication process resulted in a higher yield. The large-area spectral reflectance of these structures is also can be seen in Figure 5.42. The height of the peaks at $400\ nm$

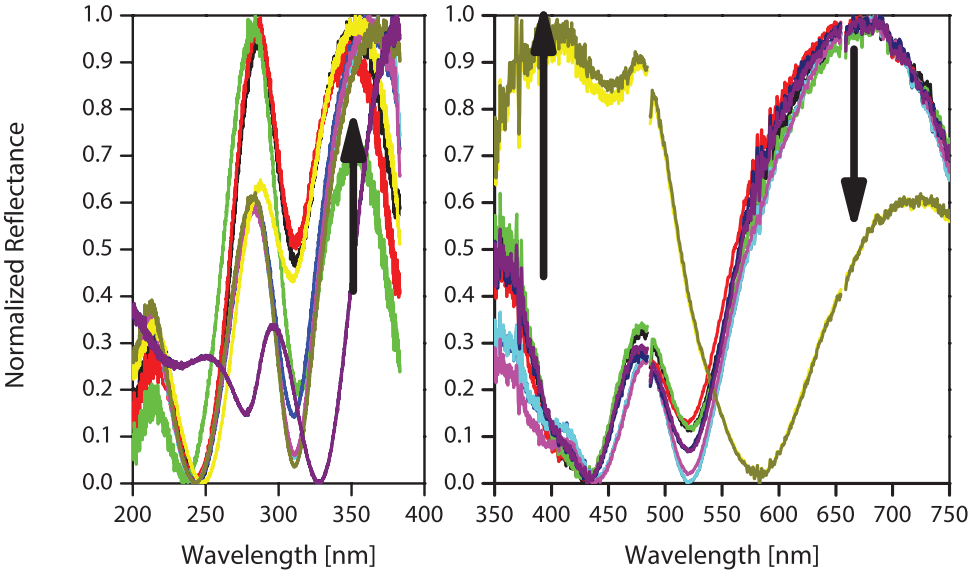

Figure 5.38: The measured reflectance spectra of design **c** samples. As the peak at $400\ nm$ intensifies, the peak at about $650\ nm$ diminishes. The spectral reflectance over UV and over visible was measured using dedicated spectrometer modules and normalized separately, thus the data is not continuous in this figure.

and $550\ nm$, corresponding to the released and unreleased structures, respectively, varies by an increase in the fill factor of the released structures from about 10% to 60%.

5.8.3. Nitride-oxide compound membrane

Design e

Finally, the compound nitride-oxide membranes were also fabricated and released. The optical result obtained from these membranes resulted in a similar response as the previous designs. Figure 5.43 shows the microscope images of the fabricated free-standing membranes. Tilted SEM images are also shown in Figure 5.44. Accordingly, a maximum fill factor of about 75% was achieved. The measured large area spectral response of the samples are also shown in Figure 5.46. The results are in agreement with the expected reflectance (based on the fill factor estimation) presented in Figure 5.45

It is worthwhile to mention that the released membranes of this design represent a distinct and pure purple-colored reflectance. This is especially interesting when compared with the design **c** which also results in a similar reflection band at $400\ nm$ (See Figure 5.26 and Table 5.7). However, the spectral response of design **e** results of a suppressed and minimal reflectance at longer wavelengths, while the reflectance of other designs also includes a reflectance at the $600\ nm$ and higher wavelengths (corresponding to the color red). This result is highly promising for applications in which an out-of-band rejection outside the spectrum is required.

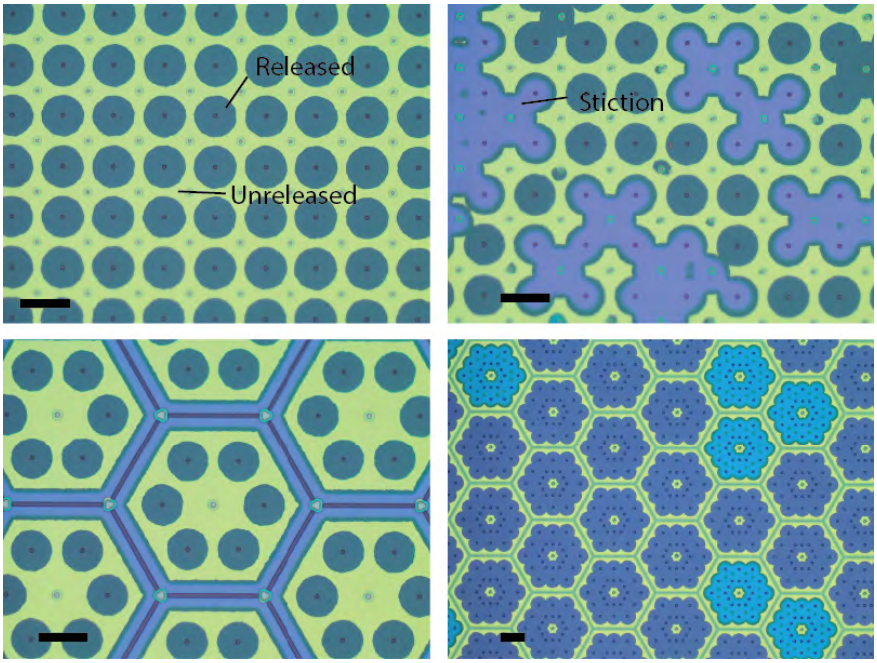

Figure 5.39: The microscope images of various partially under-etched devices of design **d**. The released, unreleased, and stiction area are visually recognizable. The scale bar in each image is $25\ \mu m$.

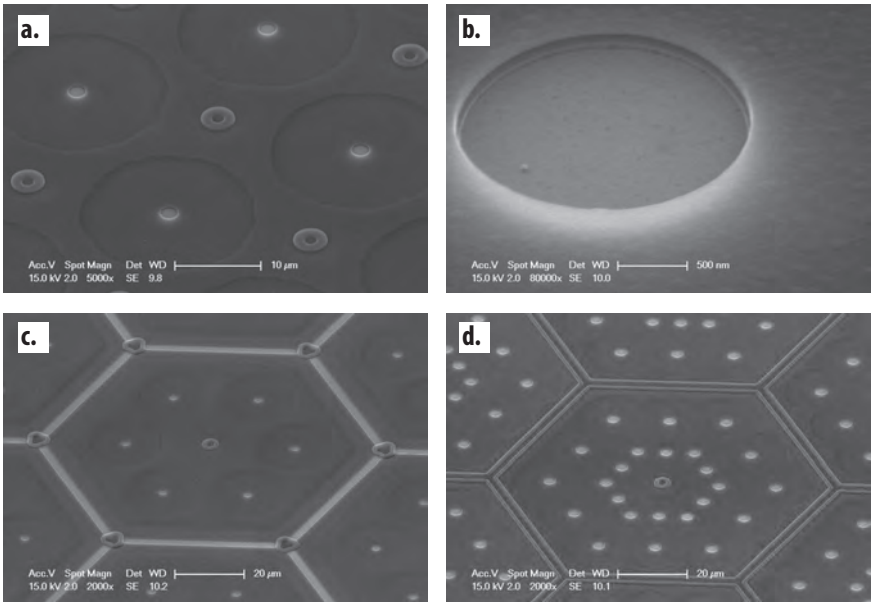

Figure 5.40: The tilted SEM images of various partially under-etched devices of design **d**.

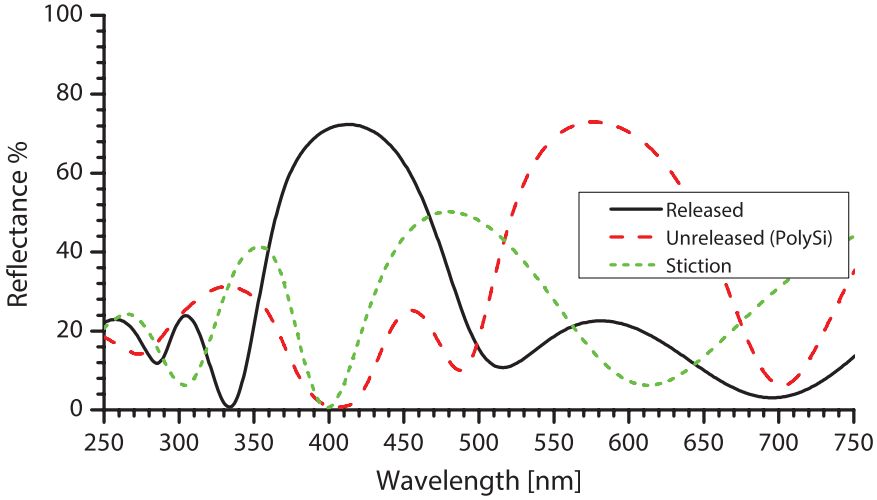

Figure 5.41: The expected reflectance of design **d** samples, before releasing, after releasing and snapped membranes (different stiction cases are also considered).

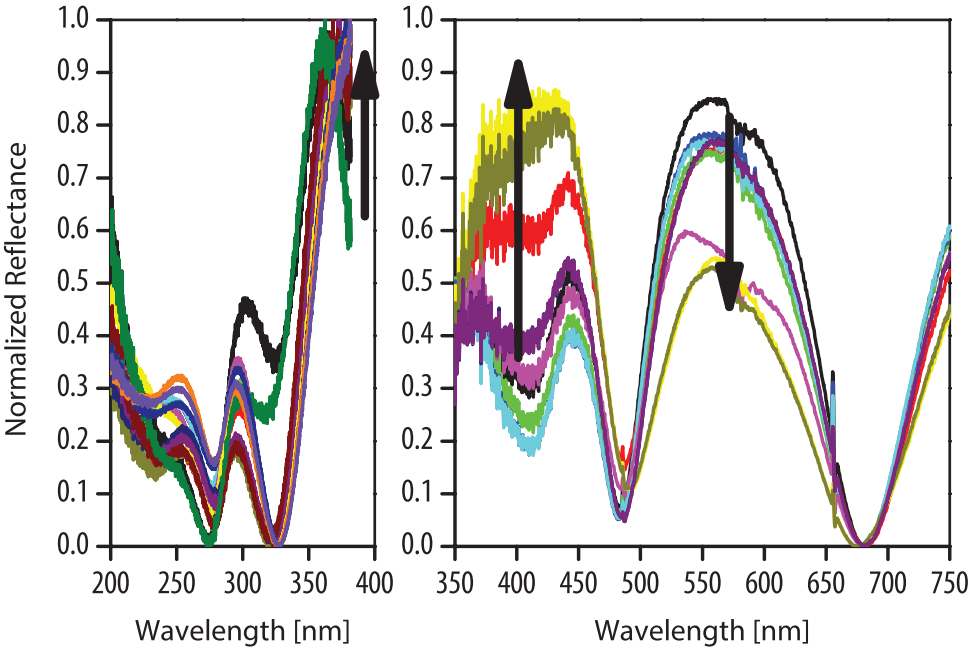

Figure 5.42: The measured reflectance spectra of design **d** samples. As the peak at $400\ nm$ intensifies, the peak at about $550\ nm$ decreases. The spectral reflectance over UV and over visible was measured using dedicated spectrometer modules and normalized separately, thus the data is not continuous in this figure.

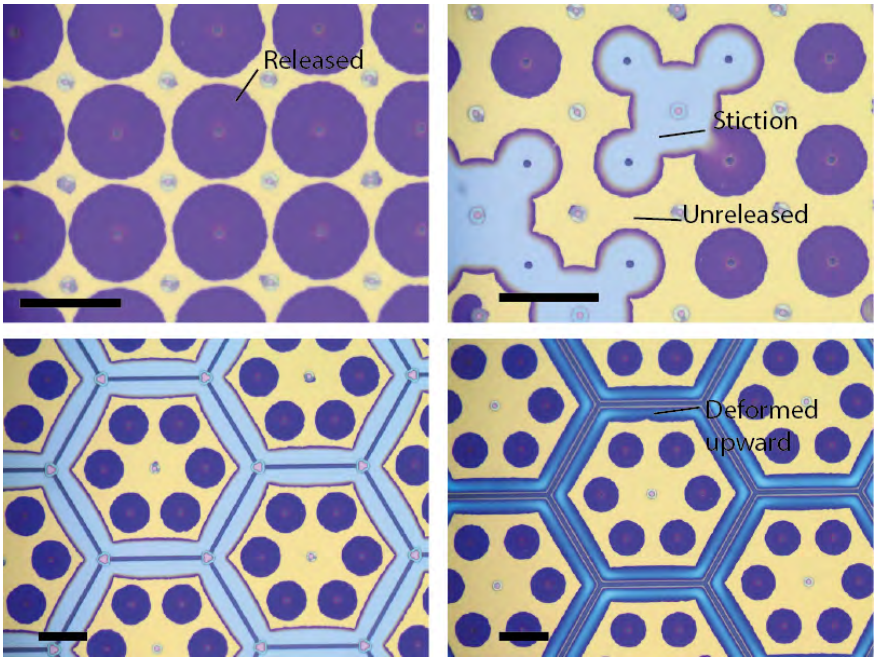

Figure 5.43: The microscope images of various partially under-etched devices of design **e**. The released, unreleased, and stiction area are visually recognizable. The scale bar in each image is $25\ \mu m$.

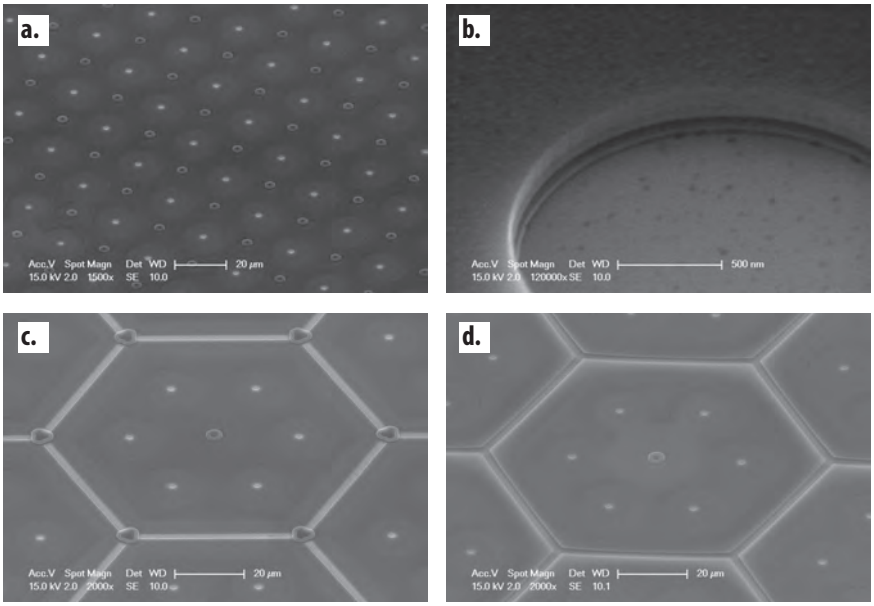

Figure 5.44: The tilted SEM images of various partially under-etched devices of design **e**.

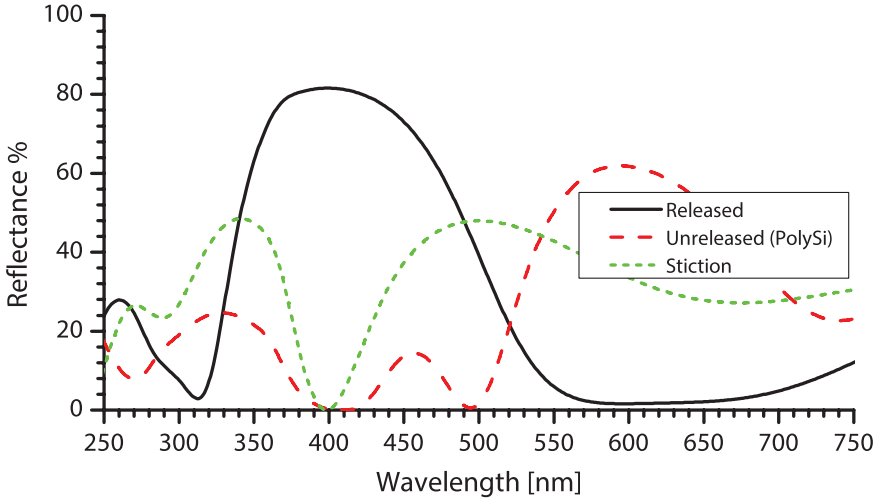

Figure 5.45: The expected reflectance of design **e** samples, before releasing, after releasing and snapped membranes (different stiction cases are also considered).

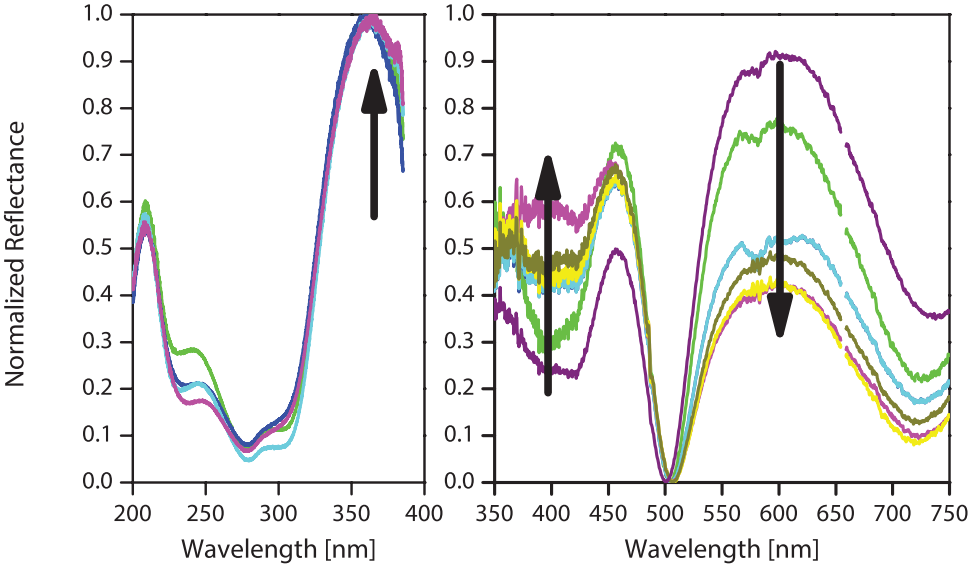

Figure 5.46: The measured reflectance spectra of design **e** samples. As the peak at $400\ nm$ intensifies, the peak at about $600\ nm$ decreases. The spectral reflectance over UV and over visible was measured using dedicated spectrometer modules and normalized separately, thus the data is not continuous in this figure.

References

[1] M. Strassner, J. C. Esnault, L. Leroy, J. L. Leclercq, M. Garrigues, and I. Sagnes, *Fabrication of ultrathin and highly flexible InP-based membranes for microoptoelectromechanical systems at 1.55 μm,* IEEE Photonics Technology Letters **17**, 804 (2005).

[2] C. J. Tay, C. Quan, H. Liu, M. Gopal, and R. Akkipeddi, *Stress gradient of a micro-optoelectromechanical systems Fabry–Perot cavity based on InP,* Journal of Micro/Nanolithography, MEMS, and MOEMS **9**, 023010 (2010).

[3] M. Garrigues, J. Danglot, J. L. Leclercq, and O. Parillaud, *Tunable high-finesse InP/air MOEMS filter,* IEEE Photonics Technology Letters **17**, 1471 (2005).

[4] F. Römer, C. Prott, S. Irmer, J. Daleiden, A. Tarraf, H. Hillmer, and M. Strassner, *Tuning efficiency and linewidth of electrostatically actuated multiple air-gap filters,* Applied Physics Letters **82**, 176 (2003).

[5] D. Chen and J. Han, *High reflectance membrane-based distributed Bragg reflectors for GaN photonics,* Applied Physics Letters **101**, 221104 (2012), http://dx.doi.org/10.1063/1.4768806.

[6] A. Altoukhov, J. Levrat, E. Feltin, J.-F. Carlin, A. Castiglia, R. Butté, and N. Grandjean, *High reflectivity airgap distributed Bragg reflectors realized by wet etching of AlInN sacrificial layers,* Applied Physics Letters **95**, 191102 (2009), http://dx.doi.org/10.1063/1.3259720.

[7] R. Sharma, E. D. Haberer, C. Meier, E. L. Hu, and S. Nakamura, *Vertically oriented GaN-based air-gap distributed Bragg reflector structure fabricated using band-gap-selective photoelectrochemical etching,* Applied Physics Letters **87**, 051107 (2005), http://dx.doi.org/10.1063/1.2008380.

[8] R. Tao, M. Arita, S. Kako, and Y. Arakawa, *Fabrication and optical properties of non-polar III-nitride air-gap distributed Bragg reflector microcavities,* Applied Physics Letters **103**, 201118 (2013), http://dx.doi.org/10.1063/1.4832069.

[9] TFCalc, *Version 3.5. 15 user's manual, software spectra,* (2009).

[10] M. Garrigues, J. Leclercq, and P. Viktorovitch, *III-V semiconductor based MOEMS devices for optical telecommunications,* Microelectronic Engineering **61–62**, 933 (2002), micro- and Nano-Engineering 2001.

[11] T. Kusserow, R. Zamora, J. Sonksen, N. Dharmarasu, H. Hillmer, T. Nakamura, T. Hayakawa, and B. Vengatesan, *Monolithic integration of a tunable photodetector based on InP/air-gap Fabry-Perot filters,* in *Optical MEMS and Nanophotonics, 2008 IEEE/LEOS Internationall Conference on* (2008) pp. 134–135.

[12] T. Enomoto, M. Suzuki, T. Iwaki, H. Wado, and Y. Takeuchi, *Infrared absorption sensor for multiple gas sensing. Development of a Fabry–Perot spectrometer with ultrawide wavelength range,* Electronics and Communications in Japan **96**, 50 (2013).

[13] M. Tuohiniemi, A. Näsilä, A. Akujärvi, and M. Blomberg, *MOEMS Fabry–Perot interferometer with point-anchored Si-air mirrors for middle infrared,* Journal of Micromechanics and Microengineering **24**, 095019 (2014).

[14] R. A. B. Devine, D. Mathiot, W. L. Warren, and B. Aspar, *O interstitial generation and diffusion in high temperature annealed Si/SiO_2/Si structures,* Journal of Applied Physics **79**, 2302 (1996).

[15] V. V. Afanas'ev and A. Stesmans, *Thermally induced si(100)/sio_2 interface degradation in poly- si/sio_2/si structures evidence for a hydrogen-stimulated process,* Journal of The Electrochemical Society **148**, G279 (2001), http://jes.ecsdl.org/content/148/5/G279.full.pdf+html .

[16] F. Maseeh and S. D. Senturia, *Proceedings of the 5th international conference on solid-state sensors and actuators and eurosensors iii plastic deformation of higly doped silicon,* Sensors and Actuators A: Physical **23**, 861 (1990).

[17] M. Ghaderi, N. P. Ayerden, G. de Graaf, and R. F. Wolffenbuttel, *Minimizing stress in large-area surface micromachined perforated membranes with slits,* Journal of Micromechanics and Microengineering **25**, 074010 (2015).

[18] M. Tuohiniemi, A. Nasila, J. Antila, H. Saari, and M. Blomberg, *Micromachined Fabry-Perot interferometer for thermal infrared,* in *SENSORS, 2013 IEEE* (2013) pp. 1–4.

[19] W. Sharpe, B. Yuan, R. Vaidyanathan, and R. L. Edwards, *Measurements of young's modulus, poisson's ratio, and tensile strength of polysilicon,* in *Micro Electro Mechanical Systems, 1997. MEMS '97, Proceedings, IEEE., Tenth Annual International Workshop on* (1997) pp. 424–429.

[20] J. Thurn and R. F. Cook, *Stress hysteresis during thermal cycling of plasma-enhanced chemical vapor deposited silicon oxide films,* Journal of Applied Physics **91**, 1988 (2002).

[21] C. A. Zorman, R. C. Roberts, and L. Chen, *MEMS Materials and Processes Handbook*, edited by R. Ghodssi and P. Lin (Springer US, Boston, MA, 2011) Chap. Additive Processes for Semiconductors and Dielectric Materials, pp. 37–136.

[22] M. Paranjape, A. Pandy, S. Brida, L. Landsberger, M. Kahrizi, and M. Zen, *Dual-doped TMAH silicon etchant for microelectromechanical structures and systems applications,* Journal of Vacuum Science & Technology A **18**, 738 (2000).

[23] J. Laconte, D. Flandre, and J. Raskin, *Micromachined Thin-Film Sensors for SOI-CMOS Co-Integration* (Springer US, 2006) Book section 3, pp. 47–103.

6

Conclusion

6.1. Optical filters for the ultraviolet spectral range

Interference-based optical filters, which can be designed for the transmission or reflection of selected parts of the spectrum of light, are essential components in optical MEMS devices. These filters are composed of a stack of layers of alternating high and low index materials. The spectral response of the filter can be tuned by varying the optical thickness of the layers in the stack. Both the real and imaginary parts of the refractive index of the thin films have a significant impact on the performance of the filter. Firstly, the spectral absorption limits the applicability of the materials for use in optical filters. Most materials have absorption peaks in the ultraviolet spectrum, which limits the number of materials available for an optical filter. Secondly, a large ratio between the real parts of the refractive index of the high and low index layers is required for the implementation of a demanding spectral filtering function.

In the fabrication of integrated optical MEMS, the optical components are often the least compatible ones compared to the rest of the device. This is mostly due to the limitation of optically suitable materials that can be used in conventional CMOS fabrication. Furthermore, the number of layers required in an optical filter, such as a DBR, often exceeds the typical layer number required for conventional 'electro-mechanical' MEMS. Implementation of air as an optical material in airgap-based optical filters provides a solution, since air has a relatively high refractive index contrast when combined with CMOS compatible dielectrics and the optical absorption can be disregarded for wavelengths down to $200\ nm$. Furthermore, surface micromachining techniques, which are routinely used in MEMS fabrication processes, can be utilized for the fabrication of thin membranes separated with airgaps.

Therefore, optical filters with a significantly higher performance can be fabricated as compared to all-dielectric realizations, while maintaining CMOS compatibility, which is of paramount importance in the mass production of low cost MEMS devices. The CMOS compatibility of the process allows optical filters to be integrated with silicon photo-detectors that are integrated in a CMOS process, thus enabling wafer processing with all the low unit cost advantages that have been the main drivers of IC technologies for decades.

Airgap-based optical filters (mainly DBRs and Fabry-Perot filters) with high spectral selectivity and optical performance have been fabricated for a wide spectral range: from infrared to ultraviolet. Historically, the optical filters operating in the infrared spectrum ($1 - 10\ \mu m$) have been the first optical filters exploiting airgap structures [1]. Especially, WDM and VCSEL systems with high wavelength selectivity have been fabricated for telecommunication applications [2]. CMOS compatible Fabry-Perot filters have been also studied for infrared MEMS spectrometers [3]. Following the trend in the infrared, ultraviolet filters that increase the light extraction efficiency of blue LEDs have also been studied [4]. However, the fabrication of these devices is mainly based on non-CMOS, III-V semiconductor materials and processes. The fabrication of thin membranes studied and presented in this work provide a tool for high performance optical filters for CMOS compatible devices. The CMOS compatible fabrication opens a vast range of opportunities in the fabrication

of low cost devices.

The refractive index contrast, Δ, is a dimensionless parameter between 0 and 0.5, and is a highly suitable quality factor in the assessment of interference-based optical filters. For optical filters with similar complexity, in terms of the number of layers and operating order of the resonator, a set of materials with a higher refractive contrast results in a significantly sharper spectral response. The physical principles and the design of airgap-based optical filters have been discussed in Chapter 2. In the distributed Bragg reflectors (DBRs), in particular, the peak reflectance and the bandwidth both increase with the refractive contrast. The refractive index contrast of the available CMOS compatible materials that are suitable for the ultraviolet, is typically limited to about 0.25 (using $Si_3N_4|SiO_2$ and down to $300\ nm$) and 0.16 (using $Al_2O_3|SiO_2$ for below $300\ nm$). Consequently, obtaining an adequate optical response would necessitate either the use of non-CMOS compatible materials (and processes) or the introduction of novel optical structures. With air as the low index material, a refractive index contrast of 0.28 (for $SiO_2|$air) and 0.35 (for $Al_2O_3|$air) can be achieved. The airgap-based optical filters bring the high refractive index contrast together with CMOS compatible fabrication capability.

An airgap-based optical filter is composed of a stack of membranes in which the optical interference in the layers determines the spectral response (both the reflectance and transmittance mode) of the structure. A surface micromachining process for the fabrication of CMOS compatible, large-area optical filters operating in the ultraviolet-visible spectrum was presented in this dissertation. SiO_2 was chosen as the high index optical material and the mechanical material, for reasons such as: (1) availability of various deposition methods, (2) possibility of tuning the physical parameters of the deposited films, and (3) compatibility with other CMOS materials and processes.

Typically, sub-$100\ nm$ thick airgaps and sacrificial layers are required for operation in the ultraviolet-visible spectral range. The PECVD method was selected for the deposition of the SiO_2 layers, because of the advantages over similar methods such as low deposition temperature and the possibility of varying the deposition recipe to tune the physical characteristics of the deposited films. Similar to the case of free-standing structures in MEMS, a slight tensile residual stress in the thin films is required in the oxide layers of the airgap-based optical filters. The effects of varying the deposition parameters on the residual stress of the deposited thin films were studied in Chapter 3. It was shown that a higher incorporation of residual hydrogen atoms (Si-O-H / silanol bonds) changes the stress level of the film toward higher tensile stress values. Furthermore, thermal annealing of these layers results in a higher (tensile) residual stress in the films. This increase in the residual stress is related to the void formation due to the transformation of Si-O-H bonds into Si-O bonds. Finite element modeling was implemented to study the forces acting on the membrane structure caused by an average residual stress. The resulting residual stress concentration located at the anchor pins and sacrificial windows makes the membranes susceptible to fractures. Therefore, the stress level must remain low in the membranes.

The refractive index of the layers was also analysed using ellipsometry and was

presented in Chapter 3. It was shown that annealing effectively decreases the refractive index of the thin-films. This decrease is consistent with the bond transformation due to annealing.

Maintaining a well-defined, predictable, and uniform optical response over the entire structure is the main challenge in the fabrication of the airgap optical filters. The fabrication tolerances thus impose a limit to the highest achievable finesse in these filters. The limitation is also directly related to the operating wavelength. Therefore, the impact of fabrication tolerances on the optical response of the filter become more critical in the ultraviolet, as compared to visible and infrared systems. The very thin sacrificial layers must be removed with a good selectivity to the remaining membrane material. At the same time, the optical flatness criteria in the thinner membranes become more restrictive, due to the increased scattering of given surface roughness/waviness with increasing wavelength. Three main factors were considered: (1) the etch selectivity, (2) the deposition uniformity, and (3) the deformation of the released membranes. The finesse formulation was implemented to quantify the impact of the fabrication tolerances on the optical response of a Fabry-Perot filter structure.

The uniformity of the deposition of the structural and sacrificial layers must be considered for precise optical filter fabrication. However, both PECVD and LPCVD methods result in a (non-)uniformity of about 1% over a $10\ cm$ wafer. Furthermore, a finite etch selectivity between the sacrificial and structural/optical layers results in an over-etching of the membranes, hence local changes in the optical thicknesses over the area of the filter. The etch selectivity of alkaline-based wet etching processes (e.g. KOH and TMAH) were compared in Chapter 4. A maximum selectivity of about 10^2 can be obtained using conventional solutions. However, a selectivity of better than 10^3 was obtained using a doped-TMAH solution. This selectivity results in an etch length of more than $10\ \mu m$ (as compared to an etch length of only $1\ \mu m$) while keeping the membrane over-etch length under $1\ nm$.

The presence of a residual stress gradient in the film affects the flatness of the released membranes. Therefore, in Chapter 4 the deformation pattern of the free-standing membranes due to a stress gradient along the thickness was analysed. Several stress measurements at different film thicknesses were carried out, and the residual stress profile in the PECVD layers was evaluated. The PECVD oxide films reveal a linear stress gradient of 0.17 to $0.67\ MPa/nm$ along the thickness. Finite element modeling (FEM) was used to study the resulting deformation pattern in the membranes after the release. The FEM-generated deformation was then used as the input for a finite-difference time-domain (FDTD) analysis to study the effect of the stress gradient on the optical response of the filter. The optical analysis showed a lower optical performance due to the presence of the residual stress gradient in the membranes. Therefore, avoiding membrane deformation due to the residual stress gradient is the main challenge in the fabrication of optical filters.

A CMOS compatible fabrication process was presented in Chapter 5, and the results were discussed. The fabrication was based on a polysilicon SiO_2 layer system, which was characterized in the previous chapters. The polysilicon (LPCVD deposited at $570^o\ C$) and SiO_2 (PECVD deposited at $400^o\ C$) layers were deposited according

to the optical design. The thickness of the polysilicon layers was chosen equal to the airgap layers in the optical design. Maintaining optical flatness is the main challenge for obtaining an operational optical filter. The deformation of a free-standing membrane depends on the stiffness. The stiffness of a membrane increases with t^3, thus the deformation of the thin film membranes decreases when increasing the thickness. Therefore, higher order optical filter designs were considered. In these filters, $3\lambda/4n$ (or $5\lambda/4n$) layers, instead of $1\lambda/4n$ layers, were used as the membranes. Although this choice limits the functional bandwidth of the filter, the peak transmission (FWHM and peak transmittance) remains unaffected. Furthermore, the process allows for the fabrication of membranes with a higher level of rigidity and lower deformation.

The mechanical structure of the device was realized with several patterning, deposition, and etching steps. In this process, a $500\ nm$ PECVD SiO_2 layer is deposited and used as an anchoring layer to hold the membranes using pin-shaped anchoring structures. Finally, the polysilicon layers were etched in a 5% TMAH-based wet etching process. Following the etching process, the structures were released in a stiction-free drying process using super-critical CO_2 drying.

6.2. Suggestions for the future work

The process discussed in this thesis is fully developed, although it is still at an experimental stage and designedto continue investigating the challenges in the fabrication of extreme optical structures in CMOS fabrication processes. Although a specific structure (e.g. a Bragg reflector) was studied, the results are applicable to the wide range of novel optical microstructures. These microstructures range from fixed and tunable DBRs, Fabry-Perot filters, linear variable optical filters (LVOFs), dielectric-based metamaterials [5], and photonic crystal structures [6].

The optical properties of the layers must be carefully optimized and tuned for the intended spectrum. The residual stress is also an essential factor in any design for extreme requirements, where a large-area membrane with a specific pattern of anchoring and cut-outs is of importance.

The intended application of this work is in gas composition measurement using absorption spectroscopy [7]. Historically, the infrared and visible spectrum were the driving force in the optical spectroscopy market. Fuels such as natural gas (i.e. hydrocarbons) have absorption peaks in the infrared [8]. Mid-infrared optical MEMS spectrometers using tunable Fabry-Perot filters have been reported by Tuohiniemi *et al.* at VTT Finland [3]. Compact CMOS compatible and high resolution optical filters have also been investigated [8, 9]. However, the infrared spectrum is crowded with many overlapping peaks. Furthermore, the complex absorption spectrum of water vapor (H_2O) contaminates the measurement in the infrared.

The ultraviolet spectrum, on the other hand, has been investigated far less extensively. However, a MEMS sensor operating in the ultraviolet has several advantages:

- Firstly, a number of different gases have absorption peaks in the ultraviolet. Exhaust gases (e.g. NO, NO_2, SO_2 and O_3) emitted as a result of the com-

bustion of different fuels have peaks in the ultraviolet and visible spectrum ($200\ nm$ to about $500\ nm$). Although the typical absorption coefficient of these gases is generally lower than their peaks in the infrared (if available), the spectrum is less crowded and unaffected by the absorption effect of the water molecules.

- Secondly, typically the absorption peaks are much wider in the ultraviolet (in contrast to the highly crowded spectrum in the infrared), so a far less spectral resolution is required to distinguish between similar molecules (e.g. NO and NO_2).
- Finally, the silicon technology offers a huge advantage by providing low cost and reliable detectors that can operate in the ultraviolet-visible spectrum.

Therefore, the absorption spectroscopy of the gases in ultraviolet, in combination with high resolution infrared sensors, provides reliable detection of both fuel and exhaust gases. Furthermore, the detection of pollutant gases has a high potential in health related topics [10]. An additional challenge of ultraviolet spectroscopy is the smaller peak values of the absorption coefficients of a gas when compared to the infrared.

The spectral filtering of light has potential for the biological analysis of tissues. In the narrow band imaging (NBI) technique, spectral imaging of tissues at certain spectra, such as $415\ nm$ for hemoglobin absorption, provides a more reliable sensing performance for *in vivo* studies [11]. The implementation of such optical filters in medical devices has been studied and presented by Silva *et al.* [11].

The suggested future work should consider two aspects. At the fabrication level, new deposition techniques should be studied. Atomic layer deposition (ALD) is a well-known method to deposit (grow) layers of high quality with excellent accuracy. The use of ALD layers has not been considered thus far, because of limited access to the deposition machine. Furthermore, new material combinations for sacrificial and optical layers, such as Al_2O_3, SiO_2, SiN, and polymers, provide the possibility of applying new sacrificial release techniques such as isotropic plasma etching and vapour-phase etching to avoid the stiction effect in layers with narrow airgaps in between.

At the device level, novel optical structures can be fabricated. The lateral design in typical CMOS compatible designs is limited to lithography technology (critical dimension-CD). Vertical air-gap-based photonic structures with dimensions in the order of tens of nanometers can be fabricated using these techniques without having to resort to nanofabrication techniques. This opens up a wide range of opportunities and applications in CMOS compatible devices.

References

[1] N. P. Siwak, X. Z. Fan, and R. Ghodssi, *Fabrication challenges for indium phosphide microsystems,* Journal of Micromechanics and Microengineering **25**, 043001 (2015).

[2] M. Garrigues, J. Leclercq, and P. Viktorovitch, *III-V semiconductor based MOEMS devices for optical telecommunications,* Microelectronic Engineering **61–62**, 933 (2002), micro- and Nano-Engineering 2001.

[3] M. Tuohiniemi, A. Näsilä, A. Akujärvi, and M. Blomberg, *MOEMS Fabry–Perot interferometer with point-anchored Si-air mirrors for middle infrared,* Journal of Micromechanics and Microengineering **24**, 095019 (2014).

[4] R. Sharma, Y.-S. Choi, C.-F. Wang, A. David, C. Weisbuch, S. Nakamura, and E. L. Hu, *Gallium-nitride-based microcavity light-emitting diodes with air-gap distributed Bragg reflectors,* Applied Physics Letters **91**, 211108 (2007), http://dx.doi.org/10.1063/1.2805028.

[5] S. Jahani and Z. Jacob, *All-dielectric metamaterials,* Nat Nano **11**, 23 (2016), review.

[6] F. Priolo, T. Gregorkiewicz, M. Galli, and T. F. Krauss, *Silicon nanostructures for photonics and photovoltaics,* Nat Nano **9**, 19 (2014), review.

[7] J. Hodgkinson and R. P. Tatam, *Optical gas sensing: a review,* Measurement Science and Technology **24**, 012004 (2013).

[8] M. Ghaderi, N. P. Ayerden, A. Emadi, P. Enoksson, J. H. Correia, G. d. Graaf, and R. F. Wolffenbuttel, *Design, fabrication and characterization of infrared LVOFs for measuring gas composition,* Journal of Micromechanics and Microengineering **24**, 084001 (2014).

[9] N. P. Ayerden, G. de Graaf, and R. F. Wolffenbuttel, *Compact gas cell integrated with a linear variable optical filter,* Opt. Express **24**, 2981 (2016).

[10] G. Dooly, C. Fitzpatrick, and E. Lewis, *Optical sensing of hazardous exhaust emissions using a UV based extrinsic sensor,* Energy **33**, 657 (2008).

[11] M. Silva, J. Rodrigues, M. Ghaderi, L. Goncalves, G. de Graaf, R. Wolffenbuttel, and J. Correia, *Nbi optical filters in minimally invasive medical devices,* Selected Topics in Quantum Electronics, IEEE Journal of **PP**, 1 (2016).

Acknowledgements

First and foremost, I would like to express my deepest gratitude to my supervisor (and copromoter) Dr. Reinoud Wolffenbuttel for the continued support of my PhD study and related research, for his patience, encouragement, and vast knowledge. Reinoud has given me the freedom to explore on my own, yet he supported and guided me whenever my steps faltered. He guided me throughout my research and the writing of this thesis. I could not have wished for a better advisor and mentor for my PhD study.

Besides my supervisor, I would like to thank my promoter Prof. Albert Theuwissen for his encouragement and insightful comments, as well as his critical questions which inspired me to broaden my research scope. I would also like to sincerely thank all the members of my doctoral committee, Professors Gleb Vdovine, Paddy French, Hamid Latifi, Peter Enoksson, and Jose Higino Correia for their helpful feedback and suggestions.

I would like to especially thank my fellow PhD student and colleague, Pelin, for the stimulating discussions, collaborations, and for all the fun we had in the last four years. I am grateful to the group members, both current and former, especially to Dr. Ger de Graaf and Dr. Arvin Emadi. Dr. Ger de Graaf's insightful comments and constructive criticism at different stages of my research were thought-provoking and they helped me focus on my ideas. I am specially indebted to Dr. Arvin Emadi. Arvin helped me with various technical (and non-technical) complications during the first few months of my PhD.

I am also grateful to Prof. Latifi, who was my supervisor during my Master study, for introducing me to a high research standard and a rigorous attitude to research. I would also like to thank my doctoral mentor, Prof. Said Hamdioui, for all his support and advices during early stages of my PhD study.

During my PhD research I was fortunate to be able to work in four different laboratories, Electronic Instrumentation lab (EI Lab- which was my home), the cleanroom facilities at DIMES (now Else Kooi Laboratory), the cleanroom facilities at Kavli Institute of Nanoscience Delft, and the cleanroom facilities at Nanofabrication Laboratory at Chalmers University of Technology (MC2). I am grateful to all the colleagues and staff in these four laboratories, especially to all the supporting staff at EKL where the fabrication mainly took place. Without their valuable support it would not be possible to conduct this research. In particular I am grateful to Silvana (my cleanroom mentor), Gregory, Tom, Johan, and Mario for their time, for all the technical discussions, and for all their assistance in the processing. I am thankful to the technical staff at Kavli, especially Roel Mattern who gave me access to the laboratory and helped me with the critical-point drying process. I am grateful to Göran Alestig for the access to the cleanroom facilities at MC2, and to Henrik Frederiksen for teaching me many things about sputtering processes. I am thankful to

all the members of EI lab and especially Prof. Kofi Makinwa for the friendly and warm research environment. I am grateful to the technical staff in EI lab, Ron van Puffelen for making the special sample holder, Antoon Frehe for all his the help with various computer issues in running different simulation tools, Lukasz Pakula, Zu-yao Chang, and Jeroen Bastemeijer. Finally, I would like to thank Joyce Siemers and Karen van Busschbach for their administration support.

During my PhD I was lucky to have many colleagues and friends with whom I enjoyed spending time and from whom I have learnt a lot. I would like to thank Manuel (now dr. Silva), Filipe, and Marino for all the scientific, technical, and non-technical discussions. I am glad that I have met all of you. I enjoyed all the great time we had together. I am thankful to Ehsan for all his friendship, his scientific insight, and collaborations (especially on FDTD simulations). I would like to also thank Giuseppe Lacerenza and Accel Abarca Prouza for collaboration during their master thesis projects.

I would also like to thank my friends especially Iman, Mauricio, Beatrix, Victoria, Maryam, Hassan, Saleh, Bahman, and many others. I greatly value their friendship and I deeply appreciate their belief in me. I also thank all my officemates especially Chao and Johan (for all the lunch-time discussions).

Last, but most certainly not least, I would like to thank my mother, father, and brothers (Omid and Amin) for all their love and encouragement. I dedicate this thesis to To my parents, who raised me with a love of science and supported me in all my pursuits.

This research has been funded by the Dutch Technology Foundation STW under grant DEL.11476. I am grateful for their support that made my PhD work possible.

Thank you all!

Mohammadamir Ghaderi
Delft, June 2016

Curriculum Vitæ

Mohammadamir Ghaderi

22-09-1886 Born in Birjand, Iran.

Education

2004 – 2008 Undergraduate in Physics
University of Birjand
Birjand, Iran.

2008 – 2011 Master of science in Laser Physics and Optics
Shahid Beheshti University
Tehran, Iran.
Thesis: Design and Fabrication of Polymer-based Cantilevers
Promotor: Prof. dr. H. Latifi

2012 – 2016 PhD. Electrical Engineering
Delft University of Technology
Delft, the Netherlands.
Thesis: Airgap-based MEMS optical filters
Promotor: Prof. dr. Albert J.P. Theuwissen
Copromotor: Dr. ir. Reinoud F. Wolffenbuttel

About the Author

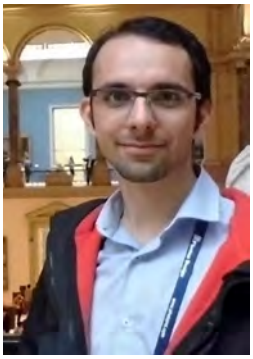

Mohammadamir Ghaderi was born in *Birjand*, *Iran* on 22 September 1986. He received his bachelor's degree in physics from *Birjand University* in 2008. Afterwards, Amir was admitted into a master degree program at *Shahid Beheshti University* in *Tehran*, where he studied laser physics and optics. During his masters, Amir carried out his project on the fabrication of various polymer-based MEMS components for optical applications. After obtaining the master's degree, Amir stayed in Laser and Plasma Research Institute at *Beheshti University* as a research assistant until January 2012. In February 2012, Amir joined the Electronic Instrumentation Laboratory in Microelectronics department at *Delft University of Technology* and started working towards the PhD degree on the *"microsystem for gas analysis"* project.

During his PhD, Amir was involved in the development of fabrication process for infrared linear variable optical filters (IR-LVOF), large area infrared detector arrays and thermal conductivity detectors, and on the advanced airgap-based optical filters for ultraviolet and visible spectrum. His work on the airgap-based MEMS optical filter was to develop high refractive index contrast dielectric-airgap structures with high fill-factor and using silicon-based technology. The fabrication process of these optical structures was carried out at *Else Kooi Laboratory* and *Kavli Nanolab* both at the *Delft University of Technology*. Amir has been a member of *IEEE* and *SPIE* societies, and also severed as a reviewer for several MEMS related journals such as *Journal of Micromechanics and Microengineering (JMM)* and *Sensor and Actuators A*.

List of Publications

Scientific Journals

8. **M Ghaderi** and RF Wolffenbuttel, *Optical performance of airgap-based MEMS optical filter for ultraviolet and visible range*, Optics Express **in preparation**

7. **M Ghaderi** and RF Wolffenbuttel, *Design and fabrication of ultraviolet-visible airgap-based MEMS optical filters*, Journal of Micrelectromechanical Systems (JMEMS) **in preparation**

6. **M Ghaderi**, G de Graaf, and RF Wolffenbuttel, *Thermal annealing of thin PECVD silicon-oxide films for airgap-based optical filters*, Journal of Micromechanics and Microengineering **Accepted for publication**, (2016)

5. M Silva, J Rodrigues, **M Ghaderi**, L Goncalves, G de Graaf, RF Wolffenbuttel, and JH Correia, *NBI Optical Filters in Minimally Invasive Medical Devices*, IEEE Journal of Selected Topics in Quantum Electronics **22**, (2016)

4. NP Ayerden, **M Ghaderi**, P Enoksson, G de Graaf, and RF Wolffenbuttel *A miniaturized optical gas-composition sensor with integrated sample chamber*, Sensors and Actuators B: Chemical, (2016)

3. **M Ghaderi**, NP Ayerden, G de Graaf, and RF Wolffenbuttel, *Minimizing stress in large-area surface micromachined perforated membranes with slits*, Journal of Micromechanics and Microengineering **25**, 074010 (2015)

2. **M Ghaderi**, NP Ayerden, A Emadi, P Enoksson, JH Correia, G De Graaf, and RF Wolffenbuttel, *Design, fabrication and characterization of infrared LVOFs for measuring gas composition*, Journal of Micromechanics and Microengineering **24**, 084001 (2014)

1. MS Cheri, H Latifi, F Aghbolagh, OR Naeini, M Taghavi, and **M Ghaderi**, *Fabrication, characterization, and simulation of a cantilever-based airflow sensor integrated with optical fiber*, Applied optics **14**, 3420-3427 (2013).

Conference Proceedings

14. **M Ghaderi**, G de Graaf, and RF Wolffenbuttel, *Fabrication of ultrathin large-area dielectric membrane stacks for use as interference filters*, Eurosensors 2016, (2016)

13. **M Ghaderi**, EK Shahmarvandi, G de Graaf, and RF Wolffenbuttel, *Analysis of the effect of stress-induced waviness in airgap-based optical filters*, SPIE Photonics Europe, **98890A-98890A-9** (2016)

12. **M Ghaderi**, G de Graaf, and RF Wolffenbuttel, *Design and fabrication of ripple-free CMOS-compatible stacked membranes for airgap optical filters for UV-visible spectrum* SPIE Photonics Europe, **98880R-98880R-8** (2016)

11. EK Shahmarvandi, **M Ghaderi**, NP Ayerden, G de Graaf, and RF Wolffenbuttel, *CMOS-compatible metamaterial-based wideband mid-infrared absorber for microspectrometer applications*, SPIE Photonics Europe, **988309-988309-9** (2016)

10. **M Ghaderi**, NP Ayerden, G De Graaf, and RF Wolffenbuttel, *Vapour HF release of airgap-based UV-visible optical filters*, Eurosensors 2015, Procedia Engineering **120**, 816-819 (2015)

9. **M Ghaderi**, NP Ayerden, G De Graaf, and RF Wolffenbuttel, *Optical characterization of MEMS-based multiple air-dielectric blue-spectrum distributed Bragg reflectors*, Proc. SPIE 9517, Smart Sensors, Actuators, and MEMS VII; and Cyber Physical Systems, **95171M**, (May 21, 2015)

8. NP Ayerden, **M Ghaderi**, G De Graaf, and RF Wolffenbuttel, *Optical design and characterization of a gas filled MEMS Fabry-Perot filter*, Proc. SPIE 9517, Smart Sensors, Actuators, and MEMS VII; and Cyber Physical Systems, **95171N**, (May 21, 2015)

7. NP Ayerden, **M Ghaderi**, G De Graaf, and RF Wolffenbuttel, *A miniaturized optical sensor with integrated gas cell*, Eurosensors 2015, Procedia Engineering **120**, 392-395 (2015)

6. **M Ghaderi**, NP Ayerden, G De Graaf, and RF Wolffenbuttel, *Surface-micromachined Bragg Reflectors Based on Multiple Airgap/SiO_2 Layers for CMOS-compatible Fabry-perot Filters in the UV-visible Spectral Range*, Eurosensors 2014, Procedia Engineering **87**, 1533-1536 (2014)

5. NP Ayerden, **M Ghaderi**, G De Graaf, and RF Wolffenbuttel, *A Lossy Fabry-perot Based Optical Filter for Natural Gas Analysis*, Eurosensors 2014, Procedia Engineering **87**, 1410-1413 (2014)

4. MF Silva, JA Rodrigues, MJ Oliveira, AR Fernandes, S Pereira, CG Costa, **M Ghaderi**, P Ayerden, LM Goncalves, G De Graaf, RF Wolffenbuttel, and JH Correia, *Optical Filter for Providing the Required Illumination to Enable Narrow Band Imaging*, Eurosensors 2014, Procedia Engineering **87**, 1414-1417 (2014)

3. **M Ghaderi** and RF Wolffenbuttel, *Design and fabrication of multiple airgap-based visible filters*, Proc. SPIE 9130, Micro-Optics 2014, **913005**, (May 2, 2014)

2. MF Silva, **M Ghaderi**, LM Goncalves, G de Graaf, RF Wolffenbuttel, and JH Correia, *A blue optical filter for narrow-band imaging in endoscopic capsules*, Proc. SPIE 9129, Biophotonics: Photonic Solutions for Better Health Care IV, **912915**, (May 8, 2014)

1. NP Ayerden, **M Ghaderi**, MF Silva, A Emadi, P Enoksson, JH Correia, G De Graaf, and RF Wolffenbuttel, *Design, fabrication and characterization of LVOF-based IR microspectrometers*, Proc. SPIE 9130, Micro-Optics 2014, **91300T**, (May 2, 2014)